OULU 2017
C 625

ACTA UNIVERSITATIS OULUENSIS

Ville-Valtteri Visuri

MATHEMATICAL MODELLING OF CHEMICAL KINETICS AND RATE PHENOMENA IN THE AOD PROCESS

UNIVERSITY OF OULU GRADUATE SCHOOL;
UNIVERSITY OF OULU,
FACULTY OF TECHNOLOGY

ACTA UNIVERSITATIS OULUENSIS
C Technica 625

VILLE-VALTTERI VISURI

MATHEMATICAL MODELLING OF CHEMICAL KINETICS AND RATE PHENOMENA IN THE AOD PROCESS

Academic dissertation to be presented with the assent of the Doctoral Training Committee of Technology and Natural Sciences of the University of Oulu for public defence in Kuusamonsali (YB210), Linnanmaa, on 17 November 2017, at 12 noon

UNIVERSITY OF OULU, OULU 2017

Acta Univ. Oul. C 625, 2017

Supervised by
Professor Timo Fabritius
Associate Professor Mika Järvinen

Reviewed by
Professor Johannes Schenk
Associate Professor Anders Tilliander

Opponent
Professor Lauri Holappa

ISBN 978-952-62-1670-6 (Paperback)
ISBN 978-952-62-1671-3 (PDF)

ISSN 0355-3213 (Printed)
ISSN 1796-2226 (Online)

Cover Design
Raimo Ahonen

JUVENES PRINT
TAMPERE 2017

Visuri, Ville-Valtteri, Mathematical modelling of chemical kinetics and rate phenomena in the AOD Process.
University of Oulu Graduate School; University of Oulu, Faculty of Technology
Acta Univ. Oul. C 625, 2017
University of Oulu, P.O. Box 8000, FI-90014 University of Oulu, Finland

Abstract

Argon-oxygen decarburisation (AOD) is the most common unit process for refining stainless steel. The AOD process consists of multiple stages, in which the rate of processing is determined by complex reaction mechanisms. The main objective of this work was to study the chemical rate phenomena in selected process stages. For this purpose, an extensive literature review was conducted to clarify the main assumptions of the existing reaction models. Based on the literature review, a new categorisation of the models was proposed. In addition, a literature review was conducted to identify the main phenomena that affect the reaction kinetics in the AOD process.

In this work, based on the law of mass action, a novel kinetic approach and its application for modelling of parallel mass transfer controlled reactions were studied. The developed approach enables the simultaneous solution of the chemical equilibrium and mass transfer rate which controls it. A simplified reaction model was employed for studying the effect of mass transfer rates and residual affinity on the constrained equilibrium at the reaction interface.

An earlier-proposed AOD model was extended with two phenomenon-based sub-models. The top-blowing model is based on the assumption that reactions take place simultaneously at the surface of the cavity formed by the momentum of the gas jet and on the surface of the metal droplets caused by the shear force of the gas jet. The reduction model describes the reactions during the reduction stage of the AOD process by assuming that all reactions take place between the metal bath and emulsified slag droplets. The results obtained with the models were in good agreement with the measurement data collected from a steel plant. Owing to their phenomenon-based structure, the developed models are well-suited for the analysis of both existing and new production practices.

Keywords: AOD process, chemical kinetics, mathematical modelling, stainless steelmaking, transport phenomena

Visuri, Ville-Valtteri, Kemiallisen kinetiikan ja nopeusilmiöiden matemaattinen mallintaminen AOD-prosessissa.
Oulun yliopiston tutkijakoulu; Oulun yliopisto, Teknillinen tiedekunta
Acta Univ. Oul. C 625, 2017
Oulun yliopisto, PL 8000, 90014 Oulun yliopisto

Tiivistelmä

Argon-happimellotus (AOD) on yleisin ruostumattoman teräksen valmistamiseen käytettävä yksikköprosessi. AOD-prosessi koostuu useista vaiheista, joissa prosessointinopeutta määrittävät monimutkaiset reaktiomekanismit. Tutkimuksen päätavoitteena oli tutkia kemiallisia nopeusilmiöitä valituissa prosessivaiheissa. Tähän liittyen tehtiin kattava kirjallisuuskatsaus, jonka tavoitteena oli tunnistaa olemassa olevien reaktiomallien pääoletukset. Kirjallisuuskatsauksen pohjalta esitettiin uusi mallien kategorisointi. Lisäksi tehtiin kirjallisuuskatsaus, jonka tavoitteena oli tunnistaa tärkeimmät reaktiokinetiikkaan vaikuttavat ilmiöt AOD-prosessissa.

Tässä työssä tutkittiin uudenlaista massavaikutuksen lakiin perustuvaa lähestymistapaa sekä sen soveltamista rinnakkaisten aineensiirron rajoittamien reaktioiden mallinnukseen. Kehitetty lähestymistapa mahdollistaa kemiallisen tasapainotilan sekä sitä rajoittavan aineensiirron samanaikaisen ratkaisun. Aineensiirtonopeuksien ja jäännösaffiniteetin vaikutusta reaktiopinnalla vallitsevaan rajoitettuun tasapainotilaan tutkittiin käyttämällä yksinkertaistettua reaktiomallia.

Aiemmin kehitettyä AOD-mallia laajennettiin kahdella ilmiöpohjaisella alimallilla. Lanssipuhallusmalli perustuu oletukseen, että reaktiot tapahtuvat samanaikaisesti kaasusuihkun liikemäärän muodostaman tunkeuman ja kaasusuihkun leikkausvoiman aiheuttamien metallipisaroiden pinnalla. Pelkistysmalli kuvaa AOD-prosessin pelkistysvaiheen aikana tapahtuvia reaktioita olettaen, että kaikki reaktiot tapahtuvat terässulan ja emulgoituneiden kuonapisaroiden välillä. Malleilla saadut tulokset vastasivat hyvin terästehtaalta kerättyä mittausaineistoa. Ilmiöpohjaisen rakenteensa ansiosta kehitetyt mallit soveltuvat hyvin sekä olemassa olevien että uusien tuotantopraktiikoiden analysoimiseen.

Asiasanat: AOD-prosessi, kemiallinen kinetiikka, matemaattinen mallinnus, nopeusilmiöt, ruostumattoman teräksen valmistus

In memory of my grandfather

Viljo Visuri

(1926 – 2017)

Acknowledgements

This research was carried out at the Process Metallurgy Research Unit, University of Oulu from 2011 to 2017. The research was conducted within the Energy and Lifecycle-efficient Metal Processes (ELEMET) and System Integrated Metals Processing (SIMP) research programmes coordinated by DIMECC Oy and funded by the Finnish Funding Agency for Technology and Innovation (TEKES). The execution of this work was enabled by the funding of Outokumpu Stainless Oy and the national-level Graduate School in Chemical Engineering. In addition, the research has been supported by grants awarded by the Finnish Foundation for Technology Promotion, the Finnish Science Foundation for Economics and Technology, the Graduate School in Chemical Engineering, the Tauno Tönning Foundation, and the Technology Industries of Finland Centennial Foundation.

It is an honour to acknowledge the support of my supervisors, co-authors, and colleagues, who have facilitated the completion of this work. First, I would like to acknowledge my supervisors Professor Timo Fabritius and Associate Professor Mika Järvinen for their inspiring guidance and support through my doctoral studies. Secondly, I am grateful to my colleagues Dr Petri Sulasalmi, Aki Kärnä, and Docent Eetu-Pekka Heikkinen not only for their co-authorship, but also for the numerous edifying discussions we have had during our daily research work. As for the execution of the experimental heats, I thank Pentti Kupari and Jari Savolainen, my co-authors at Outokumpu Stainless Oy, who gave me many practical insights into the AOD process. I also wish to acknowledge Docent Cataldo De Blasio and Sauli Pisilä for their co-authorship and Tommi Kokkonen for his technical assistance. Professor Johannes Schenk from Montanuniversität Leoben and Associate Professor Anders Tilliander from KTH Royal Institute of Technology are gratefully appreciated for the pre-examination of this thesis and their constructive comments.

During the execution of this study, I have benefited greatly from cooperation and discussions with experts in other organisations. I would like to extend my warm thanks to Professor Herbert Pfeifer for the opportunity to conduct a research visit at the Department of Industrial Furnaces and Heat Engineering, RWTH Aachen University in 2014. Likewise, I thank Dr Osmo Kauppila and Professor Jaakko Kujala for the opportunity to participate in teaching at the Department of Industrial Engineering,

University of Oulu from 2011 to 2013. Kevin Christmann, Tim Haas, Professor Rauf Hürman Eriç, Seppo Ollila, and Pekka Tanskanen are acknowledged for their valuable comments to the manuscripts. In addition to those already mentioned, I thank Dr Nils Andersson, Dr Nils Giesselmann, Dr Paavo Hooli, Topi Ikäheimonen, Veikko Juntunen, Ari Kruskopf, Gunnar Lindstrand, Dr Helge Mees, Professor Hans-Jürgen Odenthal, Mika Pylvänäinen, Dr Jan Reichel, and Dr Antje Rückert for valuable discussions regarding this work.

I thank the staff of the Process Metallurgy Research Unit for a great working environment, in which humour was not spared. In particular, my colleagues Tuomas Alatarvas, Dr Matti Aula, Matias Hultgren, Dr Mikko Iljana, and Olli Peltosaari are acknowledged for the ludicrous conversations we had during our frequent visits to Humus-kuppila. During my doctoral studies, I have instructed a fair number of people working on their Bachelor's and Master's theses and on this occasion, I would like to thank them for introducing me to diverse topics ranging from hot metal desulphurisation to hot rolling.

I am grateful to my friends, parents, and siblings for providing an essential counterbalance to work. Finally, I thank my beloved wife Paula Tegelberg for her invaluable support in this endeavour.

Oulu, October 16, 2017 Ville-Valtteri Visuri

List of abbreviations and symbols

Abbreviations

AC	Alternating current
ANN	Artificial neural network
ASM	Argon secondary melting
AOD	Argon-oxygen decarburisation
BOF	Basic oxygen furnace
CAS-OB	Composition adjustment by sealed argon bubbling – oxygen blowing
CFD	Computational fluid dynamics
CLU	Creusot-Loire Uddeholm
CRE	Carbon removal efficiency
CSTR	Continuous stirred tank reactor
DIN	Deutsches Institut für Normung e.V.
EAF	Electric arc furnace
EC	Electrical conductivity
FVRM	Finite volume reaction model
GOR	Gas oxygen refining
K-BOP	Kawasaki basic oxygen process
KCB-S	Krupp combined blowing-stainless
LIBS	Laser-induced breakdown spectroscopy
MAE	Mean absolute error
MLM	Machine learning model
LA	Light absorption
LMA	Law of mass action
MRP	Metal refining process
NRE	Nitrogen removal efficiency
OES	Optical emission spectrometry
PMM	Process mechanism model
PFR	Plug flow reactor
REM	Reaction equilibrium model
RH	Ruhrstahl-Heraeus
RMSE	Root-mean-square error

RRS	Rosin-Rammler-Sperling
SFEMM	System free energy minimisation model
SM	Statistical model
SRIM	Simple reaction interface model
SST	Stainless steel
STB	Sumimoto top and bottom blowing process
TMBI	Top mixed bottom inert
UIP	Unified interaction parameter
VCR	Vacuum converter refiner
VOD	Vacuum-oxygen decarburisation
VODC	Vacuum oxygen decarburisation converter
XRD	X-ray diffraction
XRF	X-ray fluorescence

Latin symbols

A	Area [m^2]
A	Frequency factor in Eqs. 178 and 179
A_b	Total surface area between gas bubbles and the metal bath [m^2]
A_{eff}	Effective surface area [m^2]
A_i	Parameter of the Kronig-Brink solution (Eq. 144)
A_n	Constant in Eq. 11
A_V	Reaction surface area per unit volume [m^2/m^3]
a	Activity
B	Constant
b	Constant
C	Constants in Eqs. 118 and 119
C_{IP}	Substance specific constant
C_S	Sulphide capacity of slag
c	Molar concentration [mol/m^3]
c_p	Specific heat capacity at constant pressure [J/(kg·K)]
D	Mass diffusivity [m^2/s]
D^t	Oxygen dissolved in the liquid metal [kg]
d_c	Crucible diameter [m]
d_{cav}	Top diameter of the cavity [m]
d_{limit}	Limiting diameter of the metal droplets [m]

d_{plume}	Diameter of the plume at the metal–slag interface [m]
$d_{\text{tuyère}}$	Tuyère diameter [m]
d_{32}	Sauter mean diameter [m]
$\overline{d}$	Mean diameter [m]
E_{a}	Activation energy [J]
e	Electron
F	Force [N]
f	Activity coefficient (wt-% basis)
f	Predicted variable in Eqs. 97–99
f_i	Mass fraction of size class i in Eq. 252
$\overline{f}$	Mean of predicted variables in Eq. 97
$\overline{f}$	Partial fugacity in Eq. 174
f°	Fugacity at the standard state
ΔG	Change in Gibbs free energy of reaction [J/mol]
ΔG°	Change in standard Gibbs free energy of reaction [J/mol]
ΔG_{conv}	Conversion factor [J/mol]
g	Standard gravity [m/s^2]; $g \approx 9.80665$ m/s^2
ΔH_{a}	Enthalpy of activation [J/mol]
ΔH°	Change in standard enthalpy of reaction [J/mol]
h	Height of the top of plume above the surface slag [m] in Eq. 278
h	Planck constant [J·s]; $h \approx 6.626070040 \cdot 10^{-34}$ J·s
h_{cav}	Depth of the cavity [m]
h_{lance}	Distance of lance from the surface of the metal bath [m]
h_{slag}	Height of the slag layer [m]
h_{I}	Distance between slag–metal interface and nozzle tip [m]
h_{I}^*	Transitional value of h_{I} [m]
Δh	Change in specific enthalpy of reaction [J/kg]
Δh_{dis}	Specific enthalpy of dissolution into liquid iron [J/kg]
I	Conductance parameter [1/s]
K	Equilibrium constant
K	Constant in Eq. 245 [kg·h^2·cm^4·(Nm^3)$^{-3}$]
K_{c}	Equilibrium constant expressed in terms of concentrations
k	Time constant [1/s] or rate parameter [1/s]
k_{B}	Boltzmann constant [J/K]; $k_{\text{B}} \approx 1.38064852 \cdot 10^{-23}$ J/K
k_{b}	Backward reaction rate coefficient

k_f	Forward reaction rate coefficient
$k_\mathrm{[N],dis}$	Velocity constant of the nitrogen dissolution reaction [m/s]
$\overline{k}_\mathrm{mix}$	Average time constant of mixing [1/s]
L	Characteristic length [m]
L	Partition ratio
L	Penetration depth [m]
l_m	Latent heat of melting [J/kg]
M	Molar mass [kg/mol]
$\dot{M}_\mathrm{d}$	Dimensionless momentum flow rate
$\dot{M}_\mathrm{h}$	Dimensionless momentum flow rate
m	Mass [kg]
m''	Mass flux [kg/(m^2·s)]
$\dot{m}$	Mass flow [kg/s]
$\dot{m}_\mathrm{md}$	Metal droplet generation rate [kg/s]
$\dot{m}_\mathrm{md,eff}$	Effective metal droplet generation rate [kg/s]
N_A	Avogadro constant [1/mol]; $N_\mathrm{A} \approx 6.022140857 \cdot 10^{23}$ 1/mol
$\dot{N}_\mathrm{sd}$	Slag droplet generation rate [1/s]
$\tilde{\mathrm{N}}_\mathrm{B}$	Blowing number [m^3/(h·cm^2)] as defined in Eq. 244
n	Amount of substance [mol]
n''	Molar flux [mol/(m^2·s]
$\dot{n}$	Molar flow rate [mol/s]
n	Distribution exponent of the RRS distribution
n	Order of reaction in Eq. 11
n_lance	Number of exit ports in a nozzle (top lance)
P	Steric factor
p	Partial pressure [atm]
p_amb	Ambient pressure [Pa]
p_atm	Atmospheric pressure [Pa]; p_atm = 101325 Pa.
p_d	Dynamic pressure [Pa]
p_exit	Pressure at nozzle exit [Pa]
p_G	Total gas pressure [atm]
p_0	Stagnation pressure at upstream part of the top lance [Pa]
p°	Standard pressure [atm]
Q	Reaction quotient
Q_L	Circulation flow rate of metal into the bottom-blowing zone [kg/s]

Q^t	Oxygen supply per time step [kg/s]
R	Gas constant [J/(mol·K)]; $R \approx 8.3144598$ J/(mol·K)
R^t	Oxygen consumed by reactions [kg]
R^2	Correlation coefficient
R''	Reaction rate [kg/(m^2·s)]
$\tilde{R}$	Reaction rate [mol/s]
$\tilde{R}''$	Reaction rate [mol/(m^2·s)]
$R_{i,j}$	Ratio of species i to be reduced by species j in Eq. 85
r	Radius [m]
r_b	Bubble radius [m]
r_c	Crucible radius [m]
r_cav	Top radius of the cavity [m]
RF	Cumulative weight-fraction
S_a	Specific surface area [m^2/m^3]
ΔS_a	Entropy of activation [J/(mol·K)]
ΔS°	Change in standard entropy of reaction [J/(mol·K)]
s	Surface renewal rate [1/s] in Eq. 113
s_1	Rate parameter [1/s] defined in Eq. 83
s_1	Rate parameter [1/s] defined in Eq. 84
T	Temperature [K]
T^*	Interfacial temperature [K]
T_C	Kinetic time constant [s]
T_G	Temperature of the gas film [K]
T_m	Melting temperature [K]
t	Time [s]
t_c	Contact time [s]
$t_{\mathrm{md},i}$	Residence time of metal droplet size class i [s]
$\bar{t}_\mathrm{md}$	Average residence time of the metal droplets [s]
$\bar{t}_\mathrm{mix}$	Average mixing time [s]
$\bar{t}_\mathrm{sd}$	Average residence time of the slag droplets [s]
$\bar{t}_\mathrm{sd,max}$	Maximum average residence time of the slag droplets [s]
U	Dimensionless velocity
u	Velocity [m/s]
u	Mass-averaged velocity [m/s] in Eqs. 89–91
u_b	Terminal velocity of the gas bubbles [m/s]

u_{exit}	Gas velocity at the nozzle exit [m/s]
u_{i}	Interfacial velocity [m/s]
u_τ	Turbulent shear stress velocity [m/s]
$\overline{u}_{\text{md}}$	Average terminal velocity of the metal droplets [m/s]
$\overline{u}_{\text{sd}}$	Average terminal velocity of the slag droplets [m/s]
V	Volume [m^3]
$\dot{V}$	Volumetric rate [m^3/s]
$\dot{V}'$	Modified volumetric rate [m^3/s]
X	Cation fraction
x	Mole fraction
x	Oxygen distribution ratio in Eq. 79
x	Position [m] in Eqs. 110, 111, and 136
y	Mass fraction
y	Measured variable in Eqs. 97–99
$\overline{y}$	Mean of measured variables in Eq. 97
y^*	Interfacial mass fraction
Z_{AB}	Collision frequency between molecules A and B [$1/(s \cdot m^3)$]

Greek symbols

α	Heat transfer coefficient [$W/(m^2 \cdot K)$]
α	Interaction energy [J]
α	Phase volume fraction in Eq. 26
β	Mass transfer coefficient [m/s]
β_{tot}	Overall mass transfer coefficient [m/s]
Γ	Binary operator
γ	Activity coefficient (molar basis)
γ	Distribution ratio of oxygen
γ	Isentropic expansion factor
δ_{N}	Thickness of the (Nernst) diffusion boundary layer [m]
δ_{Pr}	Thickness of the (Prandtl) thermal boundary layer [m]
ε	First-order molar interaction parameter
ε	Interaction coefficients in Eqs. 296–299
$\dot{\varepsilon}$	Specific stirring energy [W/kg]
η	Dimensionless parameter defined in Eq. 247.
η	Microkinetic efficiency

η	Utilisation ratio
θ	Inclination angle of the gas jets [°]
θ	Correction factor for high mass transfer rates in Eq. 42
λ	Thermal conductivity [W/(m·K)]
λ_i	Parameter of the Kronig-Brink solution (Eq. 144)
μ	Dynamic viscosity [Pa·s]
ν	Kinematic viscosity [m^2/s]
ν	Stoichiometric coefficient
$\overline{\nu}$	Mass-based stoichiometric coefficient
ξ	Geometry parameter in Eq. 41
ξ	Mixing time criterion in Eq. 102
ρ	Density [kg/m^3]
σ	Interfacial or surface tension [N/m]
τ_m	Melting time [s]
ϕ	Surface factor

Subscripts

a	Additions
b	Bubble
bath	Metal bath
c	Continuous phase
cav	Cavity or cavity interface
crit	Critical
d	Dispersed phase
e	Equilibrium
eff	Effective
equiv	Equivalent
G	Gas phase
gas	Bulk gas
H	Henrian standard state
H	Heat transfer
in	Input
inert	Inert
jet	Gas jet
L	Liquid metal phase

lance	Top lance
M	Mass transfer
md	Metal droplet
mix	Mixing
out	Output
R	Raoultian standard state
res	Residence
S	Slag phase
sd	Slag droplet or slag droplet interface
slag	Top slag
solvent	Solvent
t	Turbulent
tot	Total
tuyère	Tuyère
(l)	Liquid state
(s)	Solid state
1 wt-%	1 wt-% standard state at the Henrian activity line

Indices

B	Bulk phase
i	Size class
i, j, k	Species
k	Iteration number
n	Number of species
p	Reaction products
r	Number of reactions
r	Reactants
ψ	Phase
ω	Reaction interface

Mathematical and chemical notations

$\mathbf{J}$	Jacobian matrix; $\mathbf{J}_{ij} = \frac{\partial f_i}{\partial x_j}$
$\Delta\mathbf{x}$	Correction vector
$\mathbf{f}$	Residual vector
$\|\mathbf{x}\|_1$	l_1-norm (Taxicab norm)

$\|\mathbf{x}\|_2$	l_2-norm (Euclidian norm)
$\|\mathbf{x}\|_\infty$	l_∞-norm (Chebyshev norm)
$\rightleftharpoons$	Reversible chemical reaction
$[i]$	Species i dissolved in liquid iron
$\{i\}$	Species i in the gas phase
(i)	Species i in the slag phase

Dimensionless numbers

E	Equilibrium number; $\mathrm{E} = \left\|1 - \frac{Q}{K}\right\|$
Eo	Eötvös number; $\mathrm{Eo} = \frac{g\Delta\rho d^2}{\sigma}$
F	Fractional equilibrium; $\mathrm{F} = \frac{x_0 - x}{x_0 - x^*}$
$\mathrm{Fo_H}$	Fourier number (heat transfer); $\mathrm{Fo_H} = \frac{\lambda t}{c_\mathrm{p}\rho L^2}$
$\mathrm{Fo_M}$	Fourier number (mass transfer); $\mathrm{Fo_M}] = \frac{Dt}{L^2}$
Fo′	Modified Fourier number; $\mathrm{Fo}' = \frac{D_\mathrm{eff} t}{L^2}$
Fr′	Modified Froude number; $\mathrm{Fr}' = \frac{\rho_\mathrm{G} u_\mathrm{G}^2}{g(\rho_\mathrm{L} - \rho_\mathrm{G}) d_\mathrm{tuyère}}$
$\overline{\mathrm{Gr}}$	Mean Grashof number; $\overline{\mathrm{Gr}} = \mathrm{Gr_M} + \mathrm{Gr_H}\left(\frac{\mathrm{Sc}}{\mathrm{Pr}}\right)^{1/2}$
$\mathrm{Gr_H}$	Grashof number (heat transfer); $\mathrm{Gr_H} = \frac{g\rho_\mathrm{G}^2 L^3 \Delta T}{T_\mathrm{G}\mu_\mathrm{G}^2}$ (ideal gas)
$\mathrm{Gr_M}$	Grashof number (mass transfer); $\mathrm{Gr_M} = \frac{g\rho_\mathrm{G} L^3 \Delta\rho_i}{\mu_\mathrm{G}^2}$ (ideal gas)
Mo	Morton number; $\mathrm{Mo} = \frac{g\mu^4\Delta\rho}{\rho^2\sigma^3}$
$\mathrm{N_B}$	Blowing number; $\mathrm{N_B} = \frac{\rho_\mathrm{G} u_\mathrm{G}}{2\sqrt{\sigma_\mathrm{L}\rho_\mathrm{L} g}}$
$\mathrm{N_B'}$	Modified blowing number; $\mathrm{N_B} = \frac{p_\mathrm{d}}{\sqrt{\sigma_\mathrm{L}\rho_\mathrm{L} g}}$
Nu	Nusselt number; $\mathrm{Nu} = \frac{\alpha L}{\lambda}$
$\mathrm{Pe_H}$	Péclet number (heat transfer); $\mathrm{Pe_H} = \frac{u\rho L c_\mathrm{p}}{\lambda} = \mathrm{RePr}$
$\mathrm{Pe_M}$	Péclet number (mass transfer); $\mathrm{Pe_M} = \frac{uL}{D} = \mathrm{ReSc}$
Pr	Prandtl number; $\mathrm{Pr} = \frac{\mu c_\mathrm{p}}{\lambda}$
Re	Reynolds number; $\mathrm{Re} = \frac{uL}{\nu}$
Sc	Schmidt number; $\mathrm{Sc} = \frac{\nu}{D}$
Sh	Sherwood number; $\mathrm{Sh} = \frac{\beta L}{D}$
We	Weber number; $\mathrm{We} = \frac{\rho u^2 L}{\sigma}$
Φ	Dimensionless concentration gradient; $\Phi = \frac{x - x^*}{x_0 - x^*}$

List of original articles

This work is based on the following peer-reviewed articles, which are referred to in the text by their Roman numerals (I–VI):

I Visuri V-V, Järvinen M, Kärnä A, Sulasalmi P, Heikkinen E-P, Kupari P & Fabritius T (2017) A Mathematical Model for Reaction During Top-Blowing in the AOD Process: Derivation of the Model. Metall. Mater. Trans. B 48(3): 1850–1867

II Visuri V-V, Järvinen M, Kärnä A, Sulasalmi P, Heikkinen E-P, Kupari P & Fabritius T (2017) A Mathematical Model for Reactions During Top-Blowing in the AOD Process: Validation and Results. Metall. Mater. Trans. B 48(3): 1868–1884

III Visuri V-V, Järvinen M, Sulasalmi P, Heikkinen E-P, Savolainen J & Fabritius T (2013) A Mathematical Model for the Reduction Stage of the AOD Process. Part I: Derivation of the Model. ISIJ Int. 53(4): 603–612

IV Visuri V-V, Järvinen M, Savolainen J, Sulasalmi P, Heikkinen E-P & Fabritius T (2013) A Mathematical Model for the Reduction Stage of the AOD Process. Part II: Model Validation and Results. ISIJ Int. 53(4): 613–621

V Järvinen M, Visuri V-V, Pisilä S, Kärnä A, Sulasalmi P, Heikkinen E-P & Fabritius T (2013) Advanced Methods in Modelling of Metallurgical Unit Operations. Mater. Sci. Forum 762: 236–241

VI Järvinen M, Visuri V-V, Heikkinen E-P, Kärnä A, Sulasalmi P, De Blasio C & Fabritius T (2016) Law of Mass Action Based Kinetic Approach for the Modelling of Parallel Mass Transfer Limited Reactions: Application to Metallurgical Systems. ISIJ Int. 56(9): 1543–1552

Contribution of the author

Articles I–IV	The author of this thesis prepared the research plan, conducted the literature review, designed and programmed the models, conducted the validation experiments together with the co-authors, analysed the validation material, simulated the studied cases, analysed the results together with co-authors, and wrote the manuscript.
Articles V–VI	The author of this thesis took part in preparing the research plan, conducted part of the literature review, took part in designing the models, took part in simulating the studied cases, co-analysed the results, and co-authored the manuscript.

Other publications by the author cited in this work

1. Kruskopf A & Visuri V-V (2017) A Gibbs Energy Minimization Approach for Modeling of Chemical Reactions in a Basic Oxygen Furnace. Metall. Mater. Trans. B, DOI: 10.1007/s11663-017-1074-x
2. Heikkinen E-P, Visuri V-V, Suopajärvi H, Kemppainen A, Aula M, Sulasalmi P & Fabritius T (2017) Selected research focus areas for energy and material improvements in reduction and refining metallurgy. In: Proc. 2nd ISIJ-VDEh-Jernkontoret Joint Symposium, pp. 24–33. Jernkontoret, Stockholm, Sweden
3. Sulasalmi P, Visuri V-V, Kärnä A, Järvinen M, Ollila S & Fabritius T (2016) A Mathematical Model for the Reduction Stage of the CAS-OB Process. Metall. Mater. Trans. B 47(6): 3544–3556
4. Visuri V-V, Isohookana E, Kärnä A, Haas T, Eriç RH & Fabritius T (2016) A Physical Modelling Study of Mixing in an AOD Vessel. In: Proc. 5th International Conference on Process Development in Iron and Steelmaking. Swerea MEFOS, Luleå, Sweden
5. Haas T, Visuri V-V, Isohookana E, Kärnä A, Sulasalmi P, Eriç RH, Pfeifer H & Fabritius T (2016) Physical Modelling of the Effect of Top Slag on Mixing in the AOD Process. In: Reddy RG, Chaubal P, Pistorius PC & Pal U (eds.) Proc. 10th International Conference on Molten Slags, Fluxes, and Salts, pp. 999–1008. The Minerals, Metals and Materials Society, Seattle, WA, USA
6. Sulasalmi P, Visuri V-V, Kärnä A & Fabritius T (2015) Simulation of the effect of steel flow velocity on the slag droplet distribution and interfacial area between steel and slag. Steel Res. Int. 86(3): 212–222.
7. Järvinen M, Kärnä A, Visuri V-V, Sulasalmi P, Heikkinen E-P, Pääskylä K, De Blasio C, Ollila S & Fabritius T (2014) A Novel Approach for Numerical Modeling of the CAS-OB Process: Process Model for the Heat-Up Stage. ISIJ Int. 54(10): 2263–2272
8. Visuri V-V, Järvinen M, Pääskylä K, Kärnä A, Sulasalmi P, De Blasio C, Ollila S & Fabritius T (2014) Preliminary validation of a numerical model for the CAS-OB process. In: Proc. 7th European Oxygen Steelmaking Conference. Czech Metallurgical Society, Třinec, Czech Republic
9. Sulasalmi P, Visuri V-V & Fabritius T (2013) Effect of Interfacial Tension on the Emulsification – Considerations on the CFD Modelling of Dispersion. Mater. Sci. Forum 762: 242–247.
10. Visuri V-V, Heikkinen E-P, Järvinen M, Kupari P & Fabritius T (2012) Phenomena-based model in AOD process improvement. In: Proc. 4th International Conference on Process Development in Iron and Steelmaking, volume 1, pp. 225–235. Swerea MEFOS, Luleå, Sweden
11. Järvinen M, Pisilä S, Kärnä A, Visuri V-V, Fabritius T, Ikäheimonen T & Kupari P (2011) Fundamental Mathematical Modelling of AOD Process. In: Proc. 4th International Conference on Modelling and Simulation of Metallurgical Processes in Steelmaking. Stahlinstitut VDEh, Düsseldorf, Germany

Contents

1 Introduction

Steel is one of the most important materials of modern society. The definition of steel covers a wide-variety of ferrous alloys which contain less than 2.1 wt-% carbon and are deformable in a solid state [1]. The term *stainless steel* refers to steel grades that are designed to resist corrosion, rust, and stains; they contain at least 10.5 wt-% chromium and a maximum of 1.2 wt-% carbon [2, 3]. Stainless steels can be divided into four categories based on their crystal structure [4, 5]:

1. *ferritic*: body-centred cubic,
2. *austenitic*: face-centred cubic,
3. *martensitic*: body-centred tetragonal, and
4. *duplex*: austenitic-ferritic.

In addition, precipitation-hardening martensitic stainless steels are sometimes considered as a fifth category [5]. The aforementioned steel grades differ in physical properties, such as their ferromagnetism, corrosion resistance, and hardness. In the crystal lattice, the alloying elements can either replace the iron atoms or dissolve in the interstial spaces between them [6]. Therefore, carbon, alloying elements, and inclusions can be used to modify the properties of the alloy. A typical range of chemical compositions is shown in Table 1.

Table 1. Chemical composition of stainless steels [4].

	Composition [wt-%]						
Grade	C	Si	Mn	Cr	Ni	Mo	Other elements
Ferritic	≤ 0.1	≤ 1	≤ 1	15–18	< 1	≤ 2	Nb, Ti, Al
Martensitic	0.1–1.2	≤ 1	≤ 1.5	12–18	≤ 2.5	≤ 1.2	V, S
Austenitic	≤ 0.1	≤ 1	≤ 2	17–26	7–26	≤ 5	Cu, Nb, Ti, N, S
Duplex	≤ 0.1	≤ 1	≤ 2	24–28	4–7.5	≤ 2	Nb

Although chromium was discovered already in 1797 by Louis Vauquelin [3], it was not before the early 20th century that parallel metallurgical research in Great Britain, Germany, and the USA lead to the discovery, patenting, and commercialisation of the main stainless steel grades [3, 7]. The first commercial use of stainless steel is commonly credited to Harry Brearley, a self-taught metallurgist from Sheffield, who melted commercial stainless steel for cutlery blades in 1913 and later obtained patents in

the USA, France, and Canada [3, 7]. In 1912, Benno Strauß and Eduard Maurer from the Friedrich Krupp Works in Essen, in Germany, were the first to patent two stainless steel alloys: a martensitic grade V1M and an austenitic grade V2A [3, 7]. The pioneers of stainless steels in the USA were Elwood Haynes, Frederick Becket, and Christian Dantsizen; Haynes is known for his work on martensitic stainless steels, while Becket and Dantsizen are credited for their development of non-hardenable ferritic stainless steels [3, 7].

The main technical attributes contributing to the increasing use of stainless steels are their relatively high strength, corrosion resistance, and suitability for hygienic applications [3]. Owing to the increasing demand for stainless steel, the melt shop production of stainless steel has increased from approximately 1 million metric tonnes in 1950 [4] to 46 million metric tonnes in 2016 [8]. In recent years, the melt shop production has remained stagnant or has slightly declined both in Europe and in the Americas, while the output from China has risen to account for roughly half of the global stainless steel melt shop production (see Fig. 1).

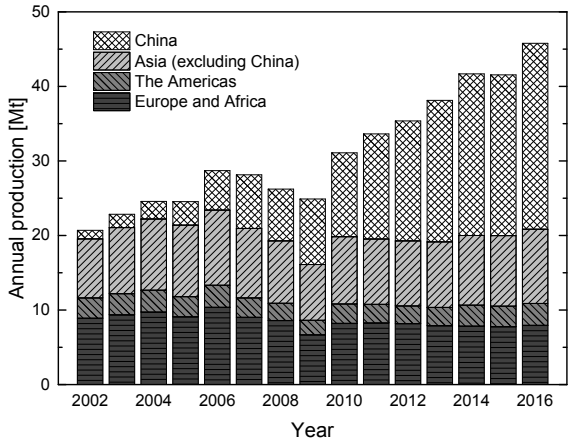

Fig 1. Stainless steel melt shop production from 2002 to 2016. Adapted from [8].

1.1 Metallurgy of stainless steelmaking

The refining of stainless steel in its liquid state takes place in a meltshop, while the treatments in its solid state are conducted in hot and cold rolling mills [9]. The melt

metallurgy of stainless steelmaking begins with the *electric arc furnace* (EAF), in which electric energy is used to melt scrap, alloys, and other charge materials to produce a batch of hot metal for further refining [10, 11]. Typical *alternating current* (AC) furnaces have three electrodes and operate with power levels in the 20–200 MW range [11]. The EAF process accounts for most chromium losses during stainless steelmaking [12]. Although the oxidised chromium can be reduced back to the melt by the addition of reducing agents, the reduction of chromium oxides in the EAF vessel is relatively slow [13, 14]. For this reason, modern vessels can be equipped with water-cooled oxyfuel burners and lances for the injection of oxygen, lime, and carbon, as well as electromagnetic stirring or inert gas injection to improve mixing characteristics [11, 15, 16].

Until the rapid adoption of the *argon-oxygen decarburisation* (AOD) process in the 1970s, it was common to carry out both melting and decarburisation in an EAF with treatment times between two and four hours [5, 17, 18]. In modern meltshops, the technological function of the EAF has changed from a combined melting and refining process to a melting process [16, 19]. In the *duplex* production route, the raw materials are melted in an EAF, while the refining is conducted in a separate converter process [5, 9, 19, 20]; an illustration is shown in Fig. 2. In comparison to refining in an EAF only, the duplex production route enables higher use of stainless and carbon steel scrap, low-cost ferrochromium, and materials with higher sulphur content [5, 18, 21].

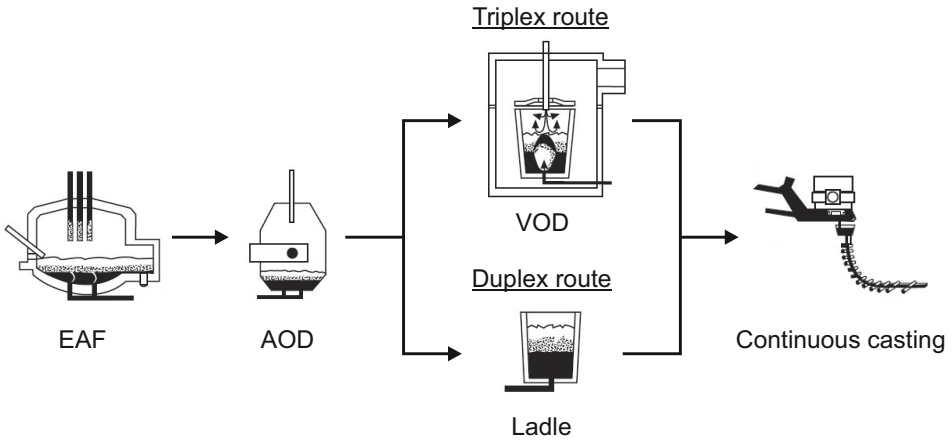

Fig 2. Comparison of duplex and triplex production routes. Adapted from [5].

The main objective of the converter processes is to decarburise the molten metal

to make steel by means of oxygen-blowing. Additional objectives of the converter processes include desulphurisation and alloying. One of the main factors supporting the immense growth in stainless steel production was the invention and commercialisation of the AOD process [3, 22], in which inert gases are employed for diluting the gas mixture [5, 22]. Following the separation of melting and refining, other equipment manufacturers soon introduced similar concepts [5], which differ mainly with respect to the employed gases and method of gas injection [5, 23, 24]. A compilation of the developed processes and their characteristics is shown in Table 2. The most common types of stainless steelmaking converters are AOD, KCB-S, K-BOP/K-OBM-S, MRP, and CLU [5]. An exhaustive description of the AOD process is provided in Chapter 2 and is not repeated here.

The final adjustment of the melt is conducted in ladle treatments. The main objectives of ladle treatments are mixing, homogenisation, alloying, degassing, and heating of steel. [4]. If the final product has very low carbon and nitrogen specifications, it may be necessary to operate a vacuum system [5], such as ladle vacuum, *Ruhrstahl-Heraus* (RH) or *vacuum oxygen decarburisation* (VOD) [25].[1] Because the decarburisation rate in the VOD process is inherently slower than in the AOD process [4, 24], EAF, AOD, and VOD are often used in combination as a *triplex* production route [5], as shown in Fig. 2.

After the specified composition, properties, and temperature of the metal bath have been obtained, the melt is transferred to the casting station. Despite some early attempts, continuous casting of stainless steels became commonplace only after the development of the AOD and VOD processes [30]. In continuous casting, molten metal is solidified into semi-finished billets, blooms, or slabs in sequences of several ladles. A tundish acts as a buffer and transforms the discontinuous flow from the ladle in a continuous flow to the mold [31]. In the mold, the outer surface of the steel starts to solidify and the desired slab dimensions are obtained [32]. Continuous casting machines can be categorised based on the orientation of the casting, type of mold, and number of bending points [32]. In order to avoid re-oxidation, the casting process for stainless steel takes place under a protective cover from the ladle via the tundish to the mold [30].

[1] The reaction mechanisms in the VOD process are quite similar to the AOD process [26–28], with the exception of reduced atmospheric pressure and different fluid flow patterns due to bottom-blowing (see Wei and Zeng [29]).

Table 2. Converter processes for stainless steelmaking.

Process	Developer(s)	Country	Gas injection	Notes	References
AOD	Union Carbide Corporation	USA	Side (+ top)	Top lance included in AOD-L.	[5, 17, 23, 24]
AOD-VCR	Daido Steel	Japan	Side	Operated as a conventional AOD down to 0.08 – 0.10 wt-% C, after which a vacuum lid is employed for the remainder of the treatment.	[5, 33]
ASM	MAN Gutehoffnungshütte	Germany	Side (+ top)	Top lance included in ASM-L.	[5, 23, 24]
CLU	Creusot-Loire / Uddeholm	France / Sweden	Bottom	Argon is substituted with steam.	[5]
GOR	National Metallurgical Academy of Ukraine	Ukraine	Bottom	Features a tapping hole in the sidewall.	[34]
K-BOP	Kawasaki Steel	Japan	Bottom + top	Tuyères are protected by injection of propane. Possible to inject powdered lime via tuyères.	[5, 23, 24, 35]
K-OBM-S	Voest-Alpine Industrieanlagenbau	Austria	Bottom + top / Side + top	Bottom- and side-blowing variants. Tuyères are protected by injection of hydrocarbons, *e.g.* natural gas or propane.	[5, 36]
KCB-S	Krupp Stahl	Germany	Side + top	Top lance employed down to 0.15 wt-% C.	[5, 23, 24]
MRP	Mannesmann Demag Hüttentechnik	Germany	Bottom (+top)	Oxygen-blowing is not diluted by inert gases. Top lance included in MRP-L.	[5, 23, 24, 37]
STB	Sumitomo Metal Industries	Japan	Bottom + top		[5, 38]
TMBI	Allegheny Ludlum Corporation	USA	Bottom + top	Bottom-blowing employed only for injection of inert gases.	[5]
VODC	Thyssen	Germany	Bottom + top	Operated under vacuum.	[5, 23, 24]

Abbreviations: AOD = argon-oxygen decarburisation; VCR = vacuum converter refiner; ASM = Argon secondary melting; CLU = Creusot-Loire Uddeholm; GOR = Gas oxygen refining; K-BOP = Kawasaki basic oxygen process, K-OBM-S = Kombiniert oxygen bottom Maxhütte stainless; KCB-S = Krupp combined blowing stainless; MRP = metal refining process; STB = Sumitomo top and bottom blowing process; TMBI = Top mixed bottom inert; VODC = vacuum oxygen decarburisation converter.

1.2 Mathematical modelling as a research method

Mathematical models play an important role in process optimisation and control [39]. According to Velten [40], mathematical models can be defined as a triad of 1) the observed system, 2) a question relating to the system, and 3) a set of mathematical statements, which answer the question. The objective of a mathematical model is to provide a quantitative description for the purpose of representation and prediction of a phenomenon of interest within a confined system.

Fig. 3 provides an simplified illustration of the modelling process. The formulation of the model depends on the chosen approach and may include statistical, mechanistic, and empirical elements. An important notion is that the term *model* as opposed to *law* implies that the description is not exact, but approximate in nature [39]. Consequently, the validation and verification are one of the main steps of the modelling process. *Conceptual validation* aims to determine whether the conceptual model provides an acceptable level of agreement for the domain of intended application, while *computerised model verification* refers to the substantiation that the computerised model represents the conceptual model [41, 42]. *Operative validation* denotes the substantiation that the computerised model is sufficiently accurate for its intended application [41, 42].

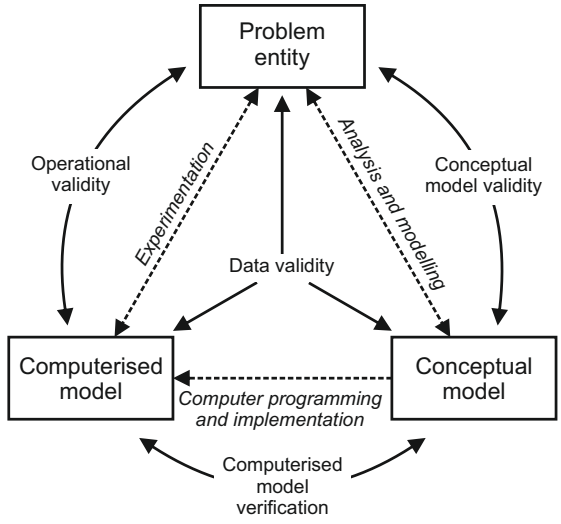

Fig 3. Schematic illustration of the modelling process. Reproduced from [42].

The context of this work is defined by the application of mathematical modelling to study chemical kinetics and rate phenomena in the AOD process. A distinction can be made between *transport phenomena* and *chemical or physicochemical phenomena*: the former category denotes the transport of momentum, heat, and mass, while the latter category covers the transformation of species and the interaction of species and phases [43]. Although the scope of this work encompasses topics from both categories, discussion will focus on chemical rate phenomena. In recent years, significant advances have been made in mechanistic mathematical modelling of unit processes in the metallurgy of steelmaking, based on thermodynamic and kinetic fundamentals. This has been enabled not only by more sophisticated mathematical methods and higher computational resources, but also by the accumulating scientific foundation laid down by experimental and numerical modelling studies.

1.3 Aims of the present study

The long-term vision of this work is to develop a holistic process simulator, which is able to predict the effect of the main physico-chemical phenomena on the chemical composition of the molten metal during different process stages. As a first step towards this vision, Järvinen *et al.* [44] proposed a mathematical model for reactions during side-blowing in the AOD process. This model was validated by Pisilä *et al.* [45] with plant data. In a continuation of this work, the following aims were laid out for the present study:

1. review of the existing reaction models for the AOD process,
2. review of the treatment of chemical kinetics relevant to the AOD process,
3. derivation and validation of a mathematical model for reactions during top-blowing,
4. derivation and validation of a mathematical model for reactions during the reduction stage, and
5. derivation of a mathematical approach for modelling parallel mass transfer controlled reactions.

The main research work is presented in six original articles. In Articles I–IV, two mathematical models were developed and validated for reactions during top-blowing and the reduction stage. In Articles V and VI, a novel approach for modelling of parallel mass transfer controlled reactions based on the law of mass action was studied. The contribution of the original articles to the research aim is summarised in Table 3.

Table 3. Contribution of original articles to the research aim.

Original article	Contribution to the research aim
Article I A Mathematical Model for Reactions During Top-Blowing in the AOD Process: Derivation of the Model	Derivation of a mathematical model, which describes reactions between top-blown oxygen and metal bath by assuming that reactions take place simultaneously at the surface of the cavity and splashed metal droplets.
Article II A Mathematical Model for Reactions During Top-Blowing in the AOD Process: Validation and Results	Validation of the top-blowing model proposed in Article I. A series of experimental heats was conducted in order to isolate the contribution of top-blowing on the overall decarburisation rate.
Article III A Mathematical Model for the Reduction Stage of the AOD Process. Part I: Derivation of the Model	Derivation of a mathematical model for reactions during the reduction stage. The novelty of the model is that it combines the emulsification of top slag and the kinetics of reduction reactions between the metal bath and slag droplets.
Article IV A Mathematical Model for the Reduction Stage of the AOD Process. Part II: Model Validation and Results	Validation of the reduction model proposed in Article III with experimental data. The sensitivity of model predictions to various parameters was also studied.
Article V Advanced Methods in Modelling of Metallurgical Unit Operations	Discussion on the application of a law of mass action based rate expression for modelling of unit processes in the metallurgy of steelmaking. The modelling approach is illustrated with examples from modelling of the AOD and CAS-OB processes.
Article VI Law of Mass Action Based Kinetic Approach for the Modelling of Parallel Mass Transfer Limited Reactions: Application to Metallurgical Systems	A detailed description of a law of mass action based rate expression for mass transfer controlled reversible reactions. A simple test model was derived for illustrating parallel oxidation of silicon, chromium and carbon under conditions relevant to the AOD process. Literature review of competing methods.

The structure of the thesis and its link to the original articles is illustrated in Fig. 4. Following the introduction (Chapter 1), Chapter 2 presents the main characteristics of the AOD process. To establish an understanding of the state of the art, Chapter 3 presents a review and categorisation of the reaction models proposed for the AOD process, while Chapter 4 provides a review of the treatment of the chemical kinetics relevant to the AOD process. The research methods employed and the results obtained are presented in Chapters 5, 6, and 7. Here, the content of the original articles has been supplemented with additional material and results. Finally, the conclusions of this work are provided in Chapter 8.

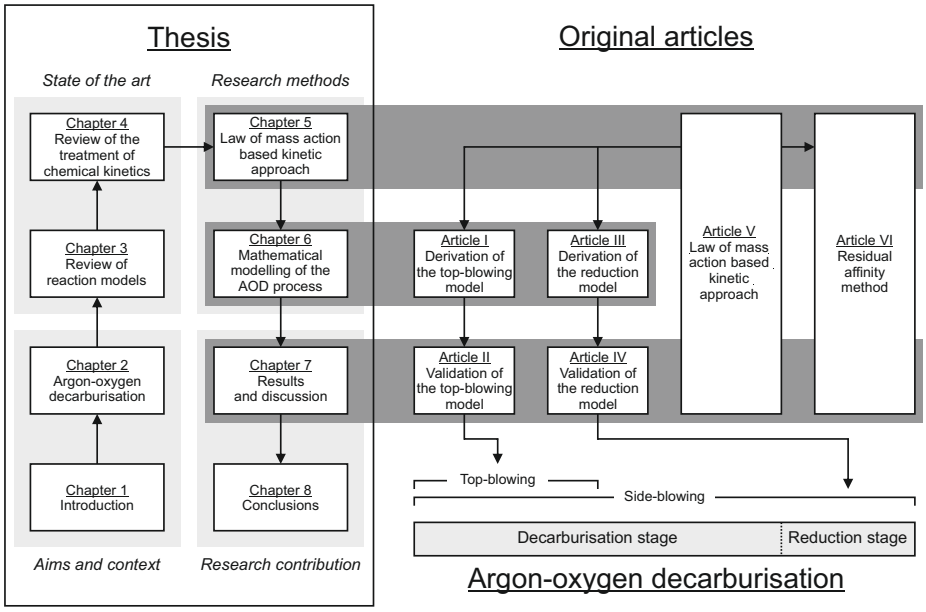

Fig 4. Structure of the thesis and the relation of the original articles to the main stages of the AOD process.

2 Argon-oxygen decarburisation

The tests that eventually lead to the conception of argon-oxygen decarburisation were conducted at Union Carbide from 1954 to 1955 [17]. Subsequently, a patent application was submitted by William A. Krivsky in 1956 [46]. Initially, two different tuyère injection designs were tested: the first design combined injection of both oxygen and argon through tuyères, while the second design employed the separate injection of oxygen through a top lance and used tuyères for delivering the argon [47]. The experiments pointed out that the combined injection design was a simpler and more reliable design, and thus it was selected as a basis for the first 15 t commercial installation at the Joslyn Fort Wayne plant in 1968 [17, 47].

Following the success of the first commercial installation, the AOD process was adopted throughout the world in the 1970s [5, 18, 19, 21, 48] and became the dominating refining process already in the early 1980s [5]. Nowadays, the AOD process accounts for approximately three quarters of the total world production of stainless steel [9, 49]. The advent of the AOD process marked a breakthrough in converter technology: a high chromium yield could be achieved with a significantly lower consumption of reductants [5, 10, 17, 47, 50]. The carbon content could be reduced to below 50 ppm without vacuum treatments [51]. Additional advantages over the preceding processes include:

– high cleanness of steel [48, 52],
– relatively low sulphur content of steel [52],
– good predictability of the process [48], and
– the ability to use inexpensive charge materials [21].

In addition to refining, part of the alloying of stainless steel is conducted in the AOD process. Typical alloying additions include, but are not limited to, high carbon ferrochrome, stainless steel scrap, carbon steel scrap, nickel, iron, high carbon ferromanganese, and molybdenum oxide [5]. Minor alloying elements such as molybdenum, vanadium, and tungsten can be added either as ferroalloys or as oxides [53]. The total weight of the additions varies in the range of 5–30% of the tap weight [5]. Alloying additions can also be used for cooling the metal bath [54]. The alloying additions during the reduction stage primarily serve this aim [55].

2.1 Equipment

A schematic illustration of a typical geometry is shown in Fig. 5. The vessel is attached to its foundations via a supporting structure which allows the tilting of the vessel for charging and tapping. Owing to the high blowing rates, the AOD process provides highly efficient mixing characteristics [56–58]. One of the drawbacks of high gas injection rates is that the resulting fluid flows can bring the whole vessel into an oscillating motion [59–61], causing wear of the support bearings, structural steelwork, and foundations [62–64]. The oscillation behaviour is dominated by blowing procedure and is most intense during the reduction stage or at the end of the decarburisation stage [62, 65–67].[2]

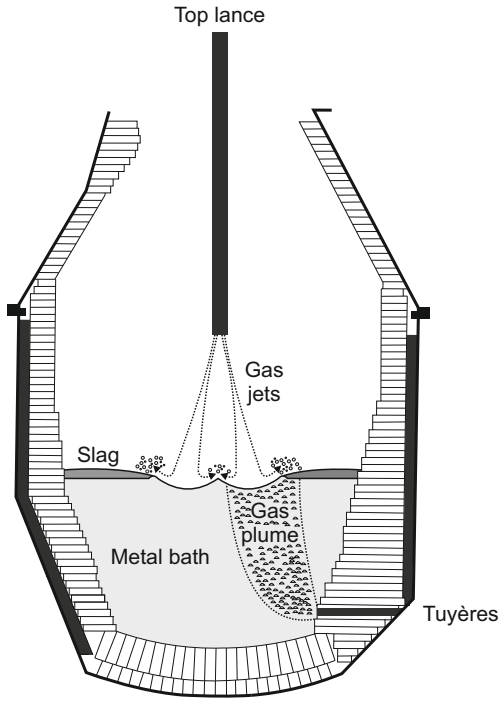

Fig 5. Schematic illustration of an AOD vessel. Reproduced from Article I by permission of Springer Nature.

The AOD vessel is lined with refractory materials in order to protect the steel shell from the high temperatures prevailing in the process. Magnesia-chrome and dolomite

[2]Dampening systems have been proposed as a solution for reducing the vessel oscillation [64].

have been the most common refractory materials since the first AOD furnace, although rebonded and semi-bonded bricks have replaced direct-bonded bricks [68]. In general, magnesia-chrome stones have a better durability with acid slags, while dolomite is better suited for basic slag practice [69]. In terms of temperature, the chemical potential of reactions and fluid flows, the most wearing circumstances are found at the tuyère wall and the trunnion area [70–72]. Dolomite refractories typically last for approximately 100–150 operating hours [69].

The off-gas consists mainly of carbon monoxide and inert gases [55]. Its composition changes during the processing so that the CO content is proportional to the decarburisation rate [55]. The main mechanisms of dust formation are the ejection of metal droplets, ejection of slag droplets, entrainment of solids, and vaporisation of metal [73]. Experimental evidence suggests that the ejection of metal and slag droplets are the most important of the aforementioned mechanisms [73]. The solid oxide particles found in the off-gas amount to 5–8 kg per ton of metal on average [55], and consist mainly of FeO, Cr_2O_3, MnO, and CaO [55, 74].

Because the attachment of the flue structure to the converter mouth is not air-tight, the oxygen contained in the leakage air may react with CO to form CO_2, thus heating up the flue gas [75]. Numerical calculations suggest that during simple side-blowing post-combustion takes place primarily in the AOD flue and is sensitive to outlet fan gauge pressure [75, 76]. If the pressure in the ventilation hood rises, most of the gas exits to the atmosphere through the gap between the vessel and the hood [77]. However, the intrusion of cold air into the vessel appears to be impossible under normal operating conditions [78].

2.1.1 Tuyères

Most AOD vessels feature two to nine horizontally aligned tuyères along the converter wall [5]. Fig. 6 illustrates a typical double-tube structure: the gas mixture is injected through a coaxial inner stainless steel tube, while inert gas (N_2 or Ar) is injected through the outer copper tube in order to cool the tuyère [62, 68, 79]. The total flow rates through the central pipe and the outer tube are typically 0.80–1.25 $Nm^3/(t \cdot min)$ and 0.05–0.08 $Nm^3/(t \cdot min)$, respectively [80].

Owing to limited measurements available from actual AOD vessels, the effectiveness of side-blowing has been subject to numerous physical and numerical modelling studies [58–63, 65, 67, 79, 81–104]. Physical modelling studies suggests that the penetration

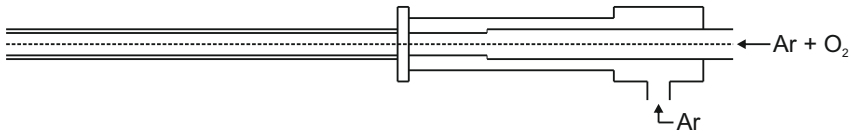

Fig 6. Schematic illustration of an AOD tuyère. Adapted from [68].

depth is independent of the bath height [92] and increases with the increasing momentum of the gas mixture [62, 67]. Some estimates on the penetration depth in an actual vessel have also been obtained through *computational fluid dynamics* (CFD) modelling: Odenthal *et al.* [62] reported that the penetration depths were in the range of 0.35 to 0.4 m in a 120-tonne vessel (7 tuyères; total flow rate of 120 Nm^3/min). Some authors [62, 101, 105] have found that a reasonable agreement with CFD calculations can be obtained using the penetration depth correlation proposed by Hoefele and Brimacombe [106]:

$$L = 10.7 \left(\mathrm{Fr}'\right)^{0.46} d_{\text{tuyère}} \left(\frac{\rho_\mathrm{G}}{\rho_\mathrm{L}}\right)^{0.35}, \tag{1}$$

where L is the penetration depth, Fr' is the modified Froude number, $d_{\text{tuyère}}$ is the diameter of the tuyère, ρ_G is the density of the gas phase, and ρ_L is the density of the liquid phase. It should be bore in mind that Eq. 1 does not account for the interaction of the gas jets [65].

2.1.2 Top lance

The experiences from refining of stainless steels in top-blowing *basic oxygen furnace* (BOF) vessels indicated that although top-blowing enabled a high oxygen injection rate, the vessel was ill-suited for efficient mixing of slag during silicon reduction [107]. Relatively soon after the introduction of the AOD process, steel producers in Germany [108, 109] and Japan [35, 110–112] conducted tests on the use of combined top- and side-blowing for refining of stainless steels. Following the success of these attempts, it has become common to equip AOD vessels with a top lance, which is employed usually only in the early part of the decarburisation stage [5, 22, 80]. The gas flow rate through the top lance is typically 1.0–1.6 Nm^3/min per ton of molten metal [80]. Similarly to side-blowing, the top-blowing gas mixture can be diluted with N_2 or Ar [55, 80], often

up to an oxygen-inert ratio of 1:1 in the final combined-blowing step [80].

Both sonic/subsonic and supersonic lances can be employed [5, 55]. Supersonic lances are always water-cooled and positioned one to four meters from the metal bath surface, while subsonic lances are placed closer to the bath and are not necessarily water-cooled [5, 55]. The advantages of supersonic lances in comparison to subsonic lances are the increased oxygen delivery rate and improved penetrability of the gas jet [5]. On the other hand, subsonic lances enable more post-combustion, which improves the energy efficiency of the process [5]. The supersonic gas jet is obtained with a de Laval nozzle [113, 114], which can feature one or more exit ports [114]. For a properly designed nozzle, the gas velocity at the nozzle exit can be calculated from [115]:

$$u_{\text{exit}} = \sqrt{\left(\frac{2}{\gamma-1}\right)\frac{\gamma p_0}{\rho_0}\left[1-\left(\frac{p_{\text{exit}}}{p_0}\right)^{\left(\frac{\gamma-1}{\gamma}\right)}\right]}, \tag{2}$$

where γ is the isentropic expansion factor, ρ_0 is the density of the gas at supply condition (p_0 and T_0), p_0 is the supply pressure, and p_{exit} is the pressure at nozzle exit. After exiting the nozzle, the gas jet forms a potential core, which has a length of approximately six times the nozzle exit diameter [114]. In this region, ambient pressure and temperature have only a small effect on the spread and decay of the gas jet [114, 116, 117]. Upon entering the converter atmosphere, the gas jet becomes subject to ambient conditions, which have a considerable effect on its behaviour [114, 117–120]. The length of the supersonic region is affected greatly by the ambient temperature in the converter: if the ambient temperature increases from room temperature to 1923 K (1650 °C), the length of the supersonic region of an oxygen jet increases from 10–20 to 20–35 times the nozzle exit diameter [114]. The effect of ambient pressure (p_{amb}) on the expansion phenomena of a supersonic gas jet can be summarised as follows [113, 114, 118, 119, 121]:

– If the exit pressure is lower than the ambient pressure, *over-expansion* occurs and overlapping compression and expansion waves cause a diamond-shaped pattern, which occurs periodically until the jet becomes subsonic (Fig. 7a).
– If the exit pressure is equal to the ambient pressure, the expansion of the gas jet is optimal; this is the design point of the de Laval nozzles (Fig. 7b).
– If the exit pressure is higher than the ambient pressure, *under-expansion* occurs: expansion waves are formed after the nozzle exit and overlapping compression waves continue until the jet the end of the supersonic region (Fig. 7c).

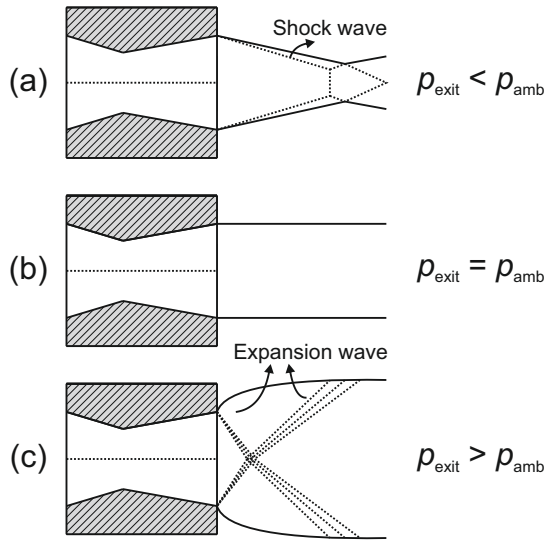

Fig 7. Expansion behaviour of a supersonic gas jet: (a) over-expansion, (b) optimal expansion, and (c) under-expansion. Adapted from [119].

Operating outside the design point may lead to increased equipment wear or decreased productivity [122]. For this reason, typical de Laval lances can be designed for only one gas flow rate [123]. Variable gas flow rates can be obtained with the help of adaptive top lances: these lances have a variable cross-section of the lance head and can maintain the design point at different blowing rates [122, 123]. Under typical operating conditions, the gas jet impacts the surface of the metal bath at subsonic velocity (see *e.g.* [124]) After the potential core, the gas jet behaves similarly to an incompressible flow [116] and starts to spread rapidly; the radial velocity distribution follows a Gaussian error function [117, 125]. The total pressure and total momentum of the gas jet are virtually constant at any cross section of the gas jet [116]. The entrainment of gases from the ambient atmosphere affects the gas jet by decreasing its velocity, increasing its mass flow, and – if the ambient temperature is higher than that of the gas jet – by increasing its temperature [126]. Upon impact, the momentum of the gas jet forms a cavity on the bath surface [114], while the liquid steel outside the cavity is pushed towards the refractory walls of the vessel in the radial direction [98]. In the case of reduced ambient pressure, the momentum transferred by the gas jet to the surface of the bath is higher than in the case of atmospheric pressure [127].

2.2 Operating practice

A typical blowing practice consists of a decarburisation stage and a reduction stage, which includes desulphurisation and alloying [5, 61]. An example of a stepwise blowing practice for a 120-tonne vessel is shown in Fig. 8. The objective of the decarburisation stage is to reach the target carbon content of the melt and thus the treatment is usually continued until the target content is reached. Typically, a sample is taken at the end of the decarburisation stage to fine-tune the end point calculations [55]. After the decarburisation stage, the top slag contains approximately 30–40 wt-% Cr_2O_3, and consequently a high degree of chromium reduction must be achieved in the reduction stage for the process to be economical [128].

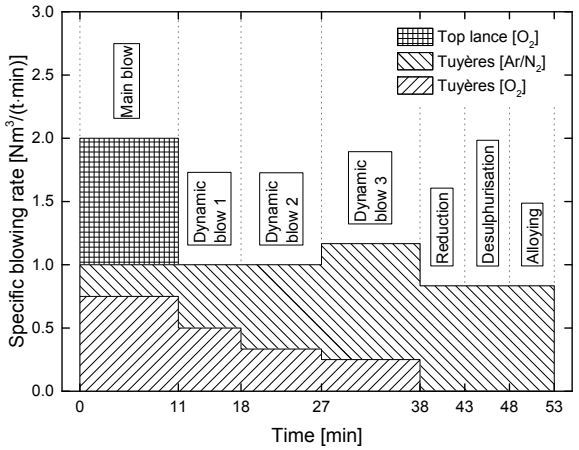

Fig 8. Typical blowing practice for a 120-tonne AOD vessel [61]. Steel grade: AISI 304. Reproduced from Article II by permission of Springer Nature.

The total blowing time depends on the employed equipment, operating practice, starting carbon content, and the target carbon content. For a typical heat with a starting carbon content of 1.5–2.5 wt-%, and a target carbon content of 0.04 wt-%, the duration of the decarburisation varies from 20 to 35 minutes [5]. For a given refining practice, the length of the decarburisation stage depends mainly on the starting and target carbon contents [5]. In comparison to the decarburisation stage, the reduction stage is much shorter and lasts only 5 to 8 minutes [10].

In 1967, the total blowing time of the first complete AOD heat with start carbon

content of 0.29 wt-% and end carbon content of 0.021 wt-% was 51 minutes [17]. An improvement in process control was brought about by computer-based techniques in the early 1970s [129], while the introduction of top-blowing alongside side-blowing in the late 1970s and early 1980s [35, 108–112] marked a considerable increase in the total gas injection rate. Further improvements were brought by the optimisation of the gas injection equipment, such as the number and arrangement of the tuyères (see *e.g.* [130]) or the type of top lance employed (see *e.g.* [131]). Owing to advances in refining practices, total treatment times of less than 30 minutes can be obtained in modern meltshop practice (see Table 4).

Table 4. Reported total blowing times in the AOD process.

		Nominal	Blowing time [min]		
Year	Reference	capacity [t]	Austenitic	Ferritic	Gas injection
1976	Gorges *et al.* [18]	80	77	80	Side
1977	Hodge [48]	55	82	–	Side
1978	Gorges *et al.* [108]	80	37*	41*	Side+top
1984	Tohge *et al.* [111]	60	75	–	Side
1984	Tohge *et al.* [111]	70	61	–	Side+top
1996	Neuschütz *et al.* [132]	80	33	–	Side+top
2011	Pisilä *et al.* [45]	150	37	–	Side+top
2016	Stebner *et al.* [133]	180	> 30	–	Side+top

Notes: * decarburisation only.

2.2.1 Decarburisation

The decarburisation stage consists of multiple steps, the number of which depends on the produced steel grade [20]. If the vessel is fitted with a top lance, combined top- and side-blowing can be employed in order to maximise oxygen delivery [4, 10, 20, 108–110, 132, 134, 135]. Typically, combined-blowing is employed only in the early part of the decarburisation until a carbon content of approximately 0.1–0.5 wt-% has been reached [10, 108, 109, 134, 136]. The combined top- and side-blowing is characterised by the large reaction areas formed by the gas bubbles, cavity, and metal droplets [4, 134, 137].

The combined-blowing decarburisation steps are followed by side-blowing decarburisation, in which the dilution of the blowing mixture is increased stepwise or continuously towards the end of the decarburisation [4, 20]. During the side-blowing decarburisation stage, reactions take place primarily between the gas plume and the

metal bath [10, 44]. Fig. 9 illustrates typical changes in composition and temperature during the AOD process.

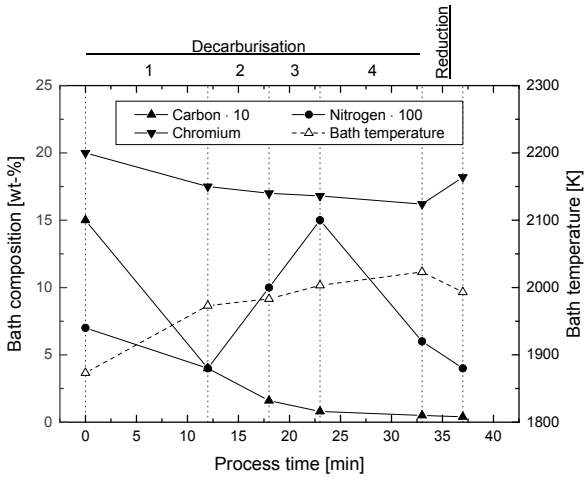

Fig 9. Typical changes in bath composition and temperature during the refining of austenitic steel grades in the AOD process. Adapted from [45, 138].

The main decarburisation reaction in the metal bath is the exothermic oxidation of dissolved carbon to carbon monoxide [4, 139]. The direct oxidation reaction can be expressed by [4, 139]:

$$[\mathrm{C}] + \frac{1}{2}\{\mathrm{O_2}\} \rightleftharpoons \{\mathrm{CO}\}\,. \tag{3}$$

The dissolution of oxygen into the metal bath, and the direct oxidation reactions of Fe, Cr, Mn, and Si can be expressed according to Eqs. 4, 5, 6, 7, and 8, respectively [10, 139]. The indirect oxidation reactions of Fe, Cr, Mn, and Si can be formulated simply by combining Eq. 4 with Eqs. 5, 6, 7, and 8, respectively.

$$\{\mathrm{O_2}\} \rightleftharpoons 2\,[\mathrm{O}]\,. \tag{4}$$

$$\mathrm{Fe_{(l)}} + \frac{1}{2}\{\mathrm{O_2}\} \rightleftharpoons (\mathrm{FeO})\,. \tag{5}$$

$$[\mathrm{Cr}] + \frac{3}{2}\{\mathrm{O_2}\} \rightleftharpoons (\mathrm{Cr_2O_3})\,. \tag{6}$$

$$[\mathrm{Mn}] + \frac{1}{2}\{\mathrm{O_2}\} \rightleftharpoons (\mathrm{MnO})\,. \tag{7}$$

$$[\mathrm{Si}] + \{\mathrm{O_2}\} \rightleftharpoons (\mathrm{SiO_2})\,. \tag{8}$$

The relation of carbon and chromium oxidation can be described by the following endothermic overall reaction [4, 10]:

$$(\mathrm{Cr_2O_3}) + 3[\mathrm{C}] \rightleftharpoons 2[\mathrm{Cr}] + 3\{\mathrm{CO}\}\,. \tag{9}$$

The equilibrium constant of Eq. 9 *at equilibrium* is given by [4, 10]:

$$K = \frac{\left(a^{\mathrm{H}}_{[\mathrm{Cr}]}\right)^2 p^3_{\mathrm{CO}}}{a^{\mathrm{R}}_{(\mathrm{Cr_2O_3})}\left(a^{\mathrm{H}}_{[\mathrm{C}]}\right)^3} = \exp\left(-\frac{88704}{T} + 56.67\right)\,. \tag{10}$$

where $a^{\mathrm{H}}_{[\mathrm{Cr}]}$ is the Henrian activity (1 wt-% standard state) of chromium, p_{CO} is the partial pressure of CO, $a^{\mathrm{R}}_{(\mathrm{Cr_2O_3})}$ is the Raoultian activity of $\mathrm{Cr_2O_3}$, $a^{\mathrm{H}}_{[\mathrm{C}]}$ is the Henrian activity (1 wt-% standard state) of carbon, and T is the temperature. The ability to influence $a^{\mathrm{H}}_{[\mathrm{Cr}]}$ are limited and $a^{\mathrm{H}}_{[\mathrm{C}]}$ decreases along with the decreasing carbon content [10]. Therefore, the basic measures for shifting the reaction equilibrium from left to right are the dilution of the blowing mixture to *decrease* the p_{CO}, adjustment of the slag basicity to *increase* $a^{\mathrm{R}}_{(\mathrm{Cr_2O_3})}$, and high operating temperatures to *increase* K [10]. However, the effect of a change in p_{CO} is greater than that of a change in T or $a^{\mathrm{R}}_{(\mathrm{Cr_2O_3})}$ [140]. The decarburisation rate can be expressed according to the following differential equation [141, 142]:

$$\frac{\mathrm{d}[\%\mathrm{C}]}{\mathrm{d}t} = A_n[\%\mathrm{C}]^n\,, \tag{11}$$

where A_n is a constant and n is the order of reaction. It has been established that in the high carbon region, the decarburisation rate is independent of the carbon content and follows a zeroth order reaction scheme ($n = 0$), but as the carbon content falls below a so-called *critical carbon content*, the mass transfer rate of carbon starts to control the reaction rate and the decarburisation proceeds according to a first order reaction scheme ($n = 1$) [26, 49, 141–143]. Schürmann and Rosenbach [141] proposed that the decarburisation rate follows an n-th order reaction scheme below 0.05 wt-% C, but this finding has not been confirmed in subsequent studies. The decarburisation behaviour observed in plant practice deviates to some extent from the simplified theoretical description presented above. As illustrated in Fig. 10, four regions of decarburisation rate can be identified [142]:

Region 1 In the first minutes of the treatment, the blown oxygen reacts primarily with silicon, manganese and chromium, thus hindering the decarburisation rate [10, 72, 144].

Region 2 After the silicon and manganese contents have decreased, the majority of the oxygen injected is consumed by the decarburisation reaction [10, 72]. The decarburisation rate is constant for a given rate of oxygen injection, *i.e.* directly proportional to the rate of oxygen injection [26, 49, 141–143].

Region 3 This period of refining is characterised by the formation of a solid chromium oxide phase [142, 145], thereby limiting a further increase in the activity of chromium oxides. Because the activity of carbon continues to decrease as its content decreases, an increasing share of oxygen is consumed for oxidising other dissolved elements, particularly chromium and manganese [10, 72, 142, 144].

Region 4 Below the critical carbon content, the decarburisation rate is directly proportional to the carbon gradient and the reaction rate is characterised by 1st order kinetics [26, 49, 141–143]. More specifically, the decarburisation rate is limited by the mass transfer of carbon in the diffusion boundary layer [26, 49, 142]. It has been suggested that the critical carbon content is different for side- and top-blowing conditions [144] and higher in the case of higher specific oxygen injection rate [142].

The efficiency of oxygen use is commonly assessed with the concept of *carbon removal efficiency* (CRE), which, as defined in Eq. 12, is the ratio of oxygen used for decarburisation to the total amount of oxygen blown [10, 146]. It should be noted that the definition of CRE does not account for top slag as a possible source of oxygen. For this reason, some authors [146] have questioned its purposefulness in evaluating the efficiency of decarburisation.

$$\mathrm{CRE}\,[\%] = \frac{\text{amount of oxygen reacting with carbon}}{\text{total added oxygen}} \cdot 100\,. \tag{12}$$

The oxidation of carbon and other alloying elements produces a large amount of heat, which is much larger than the heat losses due to the radiation of heat through the mouth of the converter, convection of heat with the flue gas, or heat transport through the refractory lining and metal shell of the vessel [54]. For this reason, the bath temperature needs to be adjusted so that the maximum allowed temperature of the refractory lining is not exceeded [54].

In the original concept, argon was used to dilute the partial pressure of CO, but in

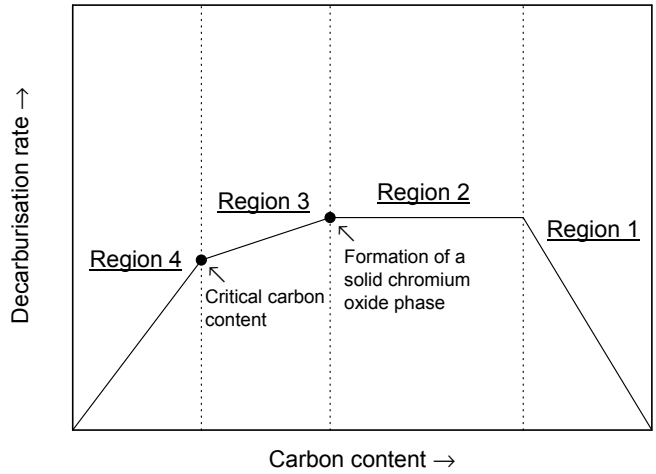

Fig 10. Schematic illustration of the decarburisation rate as a function of the carbon content of the metal bath. Adapted from [142].

modern practice nitrogen is often used alongside argon as an inexpensive substitute [147]. However, nitrogen – unlike argon – has a relatively high solubility in stainless steel melts. Table 5 shows a compilation of the effect of certain parameters on the solubility of nitrogen in stainless steel melts. Although nitrogen causes detrimental effects to the properties of most steel grades [138, 148], it can improve the properties of certain special steel grades, such as high nitrogen austenitic steels [148–150].

Table 5. Effect of certain parameters on the solubility of nitrogen in stainless steel melts.

Parameter	Effect on solubility	Reference
Al, Cr, Co, Mn, Mo, Ta, V	Increasing	[148, 151, 152]
Co, Cu, N, Ni, Si, Sn	Decreasing	[149, 151]
Partial pressure of nitrogen	Increasing	[148, 150]
Temperature	Decreasing	[148, 149, 152]

During decarburisation, the nitrogen content of austenitic steel grades rises to a level of 1000–1500 ppm [138]. The contribution of top-blowing to the nitrification of steel is very limited in comparison to side-blowing [134].[3] The level of dissolved nitrogen decreases during later stages, in which nitrogen is replaced by argon (see Fig. 9).

[3]Scheller and Wahlers [134] studied the nitrification in the low carbon region (0.5 to 0.2 wt-% C) and found that the efficiency of nitrogen dissolution for the tuyère gas was 23%, but less than 1% for the top-blown gas.

The absorption reaction at the gas–metal interface consists of three sequential steps: adsorption, dissociation, and dissolution [153]. The rate of nitrogen desorption follows a mixed control mechanism consisting of a desorption reaction at the interface and mass transfer in the molten metal [154]. The absorption of nitrogen in the early part of decarburisation follows a dual-site mechanism (*i.e.* second-order kinetics), while the desorption of nitrogen in the later part of the decarburisation stage follows a single-site mechanism (*i.e.* first-order kinetics) [138]. The latter mechanism takes place when surface active elements (such as oxygen) hinder the movement of absorbed nitrogen atoms on the surface [138, 155].

2.2.2 Reduction

The reduction of slag is conducted by adding reductants and employing vigorous argon stirring to promote good mixing conditions and emulsification of the top slag [55, 128]. After the reduction stage, the Cr_2O_3 content of the top slag is typically 0.1–5 wt-% [73, 128, 156–158]. Consequently, chromium yields in excess of 95% are achievable (see Table 6). The yields of manganese and other metallics are of the same order of magnitude.

Table 6. Typical consumptions of an 80-tonne AOD vessel. Adapted from [5].

Indicator	Unit	Typical	Best
Argon	Nm^3/t	12	9
Nitrogen	Nm^3/t	9–11	9
Oxygen	Nm^3/t	25–32	–
Lime	kg/t	50–60	42
Fluorspar	kg/t	3	2
Aluminium	kg/t	2	1
Silicon	kg/t	8–9	6
Brick	kg/t	5–9	2
Decarburisation metallics	kg/t	135	NA
Charge to tap time	min	50–80	40
Total Cr yield	%EAF/AOD	96–97	99.5
Total Mn yield	%EAF/AOD	88	95
Total Metallic yield	%EAF/AOD	95	97

Notes: AISI 304 steel grade, start carbon content 1.8 wt-%.

Typical reductants include silicon-containing alloys (FeSi, SiMn, SiCr) [156–159] and aluminium [159]; the choice of reductant depends mainly on the specified target composition of the steel. The main reaction during FeSi reduction is the reduction of Cr_2O_3 by silicon (Eq. 13), while the corresponding main reaction during aluminium reduction is the reduction of Cr_2O_3 by aluminium (Eq. 14). A mixed FeSi–Al reduction can be described simply as a combination of the two reactions.

$$(Cr_2O_3) + \frac{3}{2}[Si] \rightleftharpoons 2[Cr] + \frac{3}{2}(SiO_2)\,. \tag{13}$$

$$(Cr_2O_3) + 2[Al] \rightleftharpoons 2[Cr] + (Al_2O_3)\,. \tag{14}$$

2.2.3 Desulphurisation

The charged liquid metal batch produced by the EAF contains roughly 100–300 ppm of sulphur [157]. The desulphurisation of the liquid metal batch is conducted largely in the AOD process. As virtually no desulphurisation takes place during the decarburisation stage (see *e.g.* [157]), the desulphurisation is carried out as a part of the reduction stage. The desulphurisation reaction can be described by the following ion exchange reaction [159, 160]:

$$[S] + \frac{1}{2}\{O_2\} \rightleftharpoons \frac{1}{2}\{S_2\} + [O]\,. \tag{15}$$

Owing to the difficulty of determining the partial pressure of sulphur, the concept of a *sulphur partition ratio* can be used to relate the distribution of sulphur between metal and slag to the desulphurisation capacity of the slag [159]:

$$L_S = \frac{(\%S)}{[\%S]} = K\frac{C_S f^H_{[S]}}{a^H_{[O]}}\,, \tag{16}$$

where K is the equilibrium constant and C_S is the sulphide capacity of the slag, while f^H and a^H denote the Henrian activity coefficient (1 wt-% standard state) and the Henrian activity (1 wt-% standard state), respectively. Typically, the value of L_S increases with a higher basicity of the slag [161, 162] and – owing to a lower oxygen potential – with a higher Si content of the metal [161]. The concept of sulphide capacity was defined by Richardson and Fincham [163, 164] as follows:

$$C_S = [\%S]\left(\frac{p_{O_2}}{p_{S_2}}\right)^{1/2} = K\left(\frac{a^H_{(O^{2-})}}{f^H_{(S^{2-})}}\right), \quad (17)$$

where p denotes the partial pressure. Some models [165–169] employ the concept of *optical basicity* [170] to relate slag composition to its sulphide capacity. Other approaches include the *Flory polymerisation model* [171] and the *ion and molecule coexistence theory* [172, 173], while the so-called KTH model is based on computational thermodynamics [174–177].

2.2.4 Slag practice

Table 7 shows typical chemical compositions of AOD slags after the decarburisation stage and after the reduction stage. It can be seen that the main constituents of the AOD slag are CaO, SiO_2, and Cr_2O_3, most of which is reduced during the reduction stage. It should be noted that X-ray fluorescence (XRF) analyses, such as those shown in Table 7, do not account for the different oxidation states of the oxide species. For example, chromium may be present in both divalent (CrO) and trivalent (Cr_2O_3) oxidation states. The fraction of CrO decreases with increasing total chromium content, increasing basicity, increasing oxygen partial pressure, and decreasing temperature [178, 179]. With respect to basicity, the constituents of the AOD slag can be categorised into basic oxides (CaO, CrO, Cr_2O_3, FeO, MnO, MgO), acid oxides (SiO_2), amphoteric oxides (Al_2O_3, Fe_2O_3), and salts (CaF_2, CaS) [160, 180, 181].

Table 7. Typical chemical composition of AOD slags. Adapted from [73].

	Composition [wt-%]						
Sample	CaO	SiO_2	MgO	Cr_2O_3	Fe_2O_3	MnO	NiO
After the decarburisation stage	35.5	4.6	4.0	25.0	26.9	0.6	0.9
After the reduction stage	60.9	27.7	7.1	0.6	1.0	0.1	0.2

Note: austenitic grade 1.4301 (18 wt-% Cr, 8.5 wt-% Ni).

Table 8 shows the reported phases and minerals in solidified AOD slags [156, 158]. The decarburisation slags consist mainly of a chrome-spinel phase, a silicate matrix, and metal droplets [156, 158]. The silicate matrix is based on networks of silicon tetrahedra, which consist of Si cations surrounded by four oxygen anions [180, 182]. The silicon tetrahedra are connected to each other by bridging oxygens, which can also connect other cations with tetrahedral coordination (*e.g.* Al^{3+} and Fe^{3+}) and can be broken

by network-modifying cations (*e.g.* Fe^{2+}, Ca^{2+}, and Mg^{2+}) to form non-bridging oxygens [180, 182]. The chrome-spinel phase is reduced in the reduction stage and the resulting final slag consists mainly of dicalciumsilicate [156, 158]. Because the $\beta \rightarrow \gamma$ dicalciumsilicate transformation causes a volume increase, it is necessary to use stabilising compounds, typically boron, to avoid disintegration of the slag in storage [183].

Table 8. Phases and minerals in solidified AOD slags.

Slag type	Mineral group	Mineral	Chemical formula
Rubens and co-authors [156, 158]			
	Chrome-spinel	Picrochromite	$MgO{\cdot}Cr_2O_3$
Carry-over	Silicate matrix	Merwinite	$3CaO{\cdot}MgO{\cdot}2SiO_2$
	Metal alloy		
	Chrome-spinel	Picrochromite	$MgO{\cdot}Cr_2O_3$
Decarburisation	Chrome-spinel	Calcium chromite	$CaO{\cdot}Cr_2O_3$
	Silicate matrix	β-Dicalciumsilicate	$2CaO{\cdot}SiO_2$
	Metal alloy		
	Silicate matrix	Merwinite	$3CaO{\cdot}MgO{\cdot}2SiO_2$
	Silicate matrix	γ-Dicalciumsilicate	$2CaO{\cdot}SiO_2$
Reduction	Other	Fluorspar	CaF_2
	Other	Calciowüstite	(Ca,Fe)O
	Other	Periclase	MgO
	Other	Cuspidine	$3CaO{\cdot}2SiO_2{\cdot}CaF_2$
Ternstedt *et al.* [184]			
	Chrome-spinel	Calcium chromite	$CaO{\cdot}Cr_2O_3$
Decarburisation	Garnet	Uvarovite	$3CaO{\cdot}Cr_2O_3{\cdot}3SiO_2$
	Silicate matrix	Rankinite	$3CaO{\cdot}2SiO_2$
	Amorphous phase		
	Metal alloy		
Lindstrand *et al.* [185]			
	Chrome-spinel	Calcium chromite	$CaO{\cdot}Cr_2O_3$
	Silicate matrix	Dicalciumsilicate	$2CaO{\cdot}SiO_2$
	Silicate matrix	Rankinite	$3CaO{\cdot}2SiO_2$
Decarburisation	Metal oxide	Various	Cr_2O_3, Fe_xO_y, and Mn_xO_y with parts of CaO and/or MgO
	Amorphous phase		
	Metal alloy		

One of the objectives of the slag practice during the decarburisation stage is to minimise chromium oxide solubility in the slag [10]. On the other hand, refractory lining wear is a considerable cost factor in AOD processing and therefore it is necessary to ensure that the slag practice and the employed refractory lining material are compatible [156, 186]. In order to meet these two goals, the basicity of the slag is adjusted with the addition of basic oxides, particularly lime [10, 139, 186]. The recommended basicity ratios for decarburisation slags are shown in Table 9. The total amount slag former additions are typically in the range of 3–7% of total bath weight [5]. The dissolution of lime in decarburisation slags is hindered by the formation of a calcium silicate layer, which surrounds the lime particles [156, 158]. For example, Münchberg *et al.* [158] suggested a dissolution time of at least 16 minutes.

Table 9. Basicity ratios for decarburisation slags. Adapted from [186].

Basic oxide addition	Minimum ratios for refractory combatibility
Typical steel grades *	
Lime addition only	$\frac{(\%CaO)}{(\%SiO_2)} \leq 1.6$
Doloma or doloma/lime	$\frac{(\%CaO) + (\%MgO)}{(\%SiO_2)} \leq 2.0$
Special steel grades **	
Doloma or doloma/lime	$\frac{(\%CaO) + (\%MgO)}{(\%SiO_2) + (\%Al_2O_3) + (\%Nb_2O_5)} \leq 2.0$
Basic oxide addition	**Recommended ratios for solid slag practice**
Typical steel grades *	
Lime addition only	$\frac{(\%CaO)}{(\%SiO_2)} \leq 2.0$
Doloma or doloma/lime	$\frac{(\%CaO)}{(\%SiO_2)} \leq 2.0$ or $\frac{(\%CaO) + (\%MgO)}{(\%SiO_2)} \leq 3.33$
Special steel grades **	
Doloma or doloma/lime	$\frac{(\%CaO) + (\%MgO)}{(\%SiO_2) + (\%Al_2O_3) + (\%Nb_2O_5)} \leq 3.33$

* low Al_2O_3 and Nb_2O_5; ** high Al_2O_3 and Nb_2O_5. All concentrations in weight-percent.

Earlier it was common to have separate slags for both reduction of slag and subsequent desulphurisation, but modern plants employ a single slag practice, in which desulphurisation takes place during the reduction stage [147, 159]. The advantages of the single slag practice include higher chromium yields, decreased refractory lining

wear, as well as reductions in process time and lime additions [4, 158].

Because the viscosity of the AOD slag increases with increasing chromium oxide content [187], it becomes highly viscous towards the end of the decarburisation stage. For this reason, the basicity and viscosity of the slag are adjusted by additions of fluxes and slag formers to provide sufficient preconditions for efficient reduction of slag and desulphurisation [55]. Nevertheless, it has been suggested that even after the reduction stage the slag can have a small amount of solid $CaO{\cdot}Cr_2O_3$ precipitates [162]. According to Song *et al.* [161], the slag basicity should be adjusted to $(\%CaO/\%SiO_2) > 2$ for efficient reduction of slag and desulphurisation. Furthermore, it was recommended that the metal bath temperature should be higher than 1943 K (1670 °C) to increase slag fluidity [161].

A common flux employed in the AOD process is calcium fluoride (CaF_2), also known as fluorspar, which is an efficient flux, but very aggressive towards the refractory lining [188]. Moreover, it may leach fluor, which contaminates ground water [189]. The melting point of the slag can also be reduced with the addition of bauxite, which is an aluminium ore consisting mainly of gibbsite, boehmite, and diaspore minerals mixed with goethite and hematite [188]. In normal operating practice the removal of phosphorous is inefficient. However, laboratory experiments [190] suggest that lime-based slags can be modified with BaO and NaF to improve their phosphate capacity.

3 Review of reaction models

Optimisation of the AOD process is hindered by the lack of continuous composition and temperature measurements during operation. Instead, the process must be halted for sampling and temperature measurements, which decreases the productivity of the process. Unless the vessel is fitted with a separate sub lance for sampling, the vessel has to be tilted before the samples can be taken. Online off-gas measurements are available, but provide only secondary information on the composition of the steel and their accuracy can be affected by intrusion of air from the atmosphere. For these reasons, the ability to predict the changes in composition and temperature with reasonable accuracy is of paramount importance.

Computer-based techniques for the optimisation of the AOD process first came into use already in the early 1970s [129], only a few years after the first commercial installation in 1968 [17, 47]. The first thermodynamic decarburisation models [143, 191–193] were published soon afterwards. The early models were focussed on chemistry and relied on major simplifications to avoid the description of the kinetic parameters. Since then, the models have evolved from simplistic depictions to complex process models, which provide descriptions for the dominating physical phenomena. As shown in Fig. 11, modern process models may include several thermodynamic-kinetic reaction models of selected phenomena [194, 195]. A critical review of the proposed reaction models is provided in the following.[4]

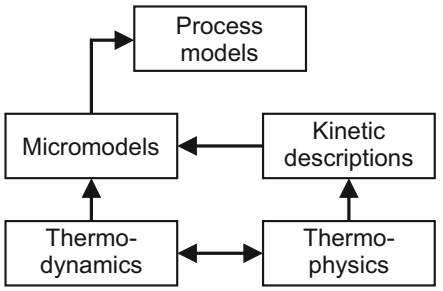

Fig 11. Process model based on micromodels. Adapted from [194].

[4] An exhaustive review of the parallel development of CFD models for the AOD process is available in [196].

3.1 Categorisation of the models

In this work, a new categorisation of reaction models was devised based on the earlier categorisations available in the literature [27, 39, 57]. The proposed categorisation is shown in Fig. 12. The main line of division lies between fundamental and data-based models.[5] The former type of models are based on the physical, chemical, and technical fundamentals of the process [39, 197], while the latter type of models are based on the analysis of empirical measurement data [197]. In comparison to data-based models, fundamental models provide a deeper understanding of the process, a lower number of parameters to be estimated, and a higher transferability of results, but tend to have a lower degree of predictive accuracy and require more extensive research [197].

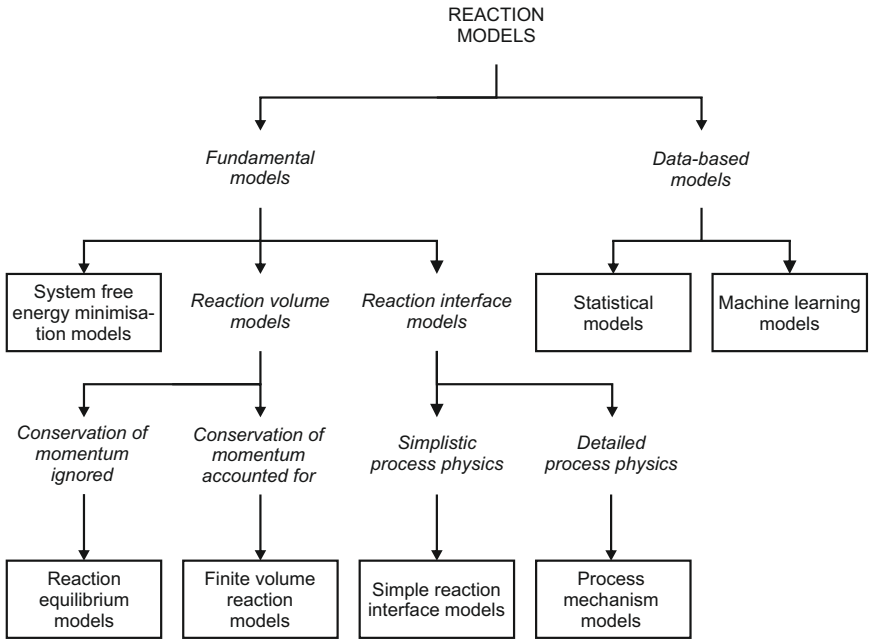

Fig 12. Categorisation of the reaction models.

Three main categories of fundamental models were identified: system free energy minimisation models, reaction volume models, and reaction interface models. The

[5] This distinction is, in essence, analogous to the common division between theoretical and empirical models.

subcategories of the reaction volume models are reaction equilibrium models and finite volume reaction models, while the subcategories of the reaction interface models are simple reaction interface models and process mechanism models. Furthermore, two main categories of data-based models were identified: statistical models and machine learning models.[6] The description of model categories, as well as the categorisation and description of the models proposed in the literature is presented in the following.

3.1.1 System free energy minimisation models

System free energy minimisation models deduce the reaction extent from the minimisation of the Gibbs free energy at the reaction zone [27]. More specifically, the reaction extent is not explicitly expressed as a function of time, but as a function of the amount of species in the system. System free energy minimisation models are often based computational thermodynamics software; examples of software suitable for metallurgical applications include FactSage [199], HSC Chemistry [200], MTDATA [201], PANDAT [202], and Thermo-Calc [203].

Swinbourne and co-authors (2012)

In a three-part series Swinbourne and co-authors employed HSC chemistry thermodynamic software for modelling EAF [15], VOD [204], and AOD [145] processes. The model for the AOD process [145] was based on substantial simplifications, including a lack of kinetic factors, ideal behaviour of slag species, constant activity coefficients of species in the metal phase, and a constant temperature during each processing stage. Despite these shortcomings, the model provides a good overall picture of the process for educational contexts. One of the main advantages of this model is the extensive thermodynamic database of the HSC Chemistry software.

[6]The proposed sub-categories of data-based models are intended to encompass only those proposed for reaction modelling. However, other types of models have also been proposed. For example, Wang *et al.* [198] proposed a case-based reasoning model for prediction of the endpoint temperature of the metal bath in the AOD process.

3.1.2 Reaction equilibrium models

Reaction equilibrium models assume that reactions reach an equilibrium in a specified reaction zone or volume [27]. Unlike detailed finite volume reaction models, zone-based mathematical models aim to provide a computationally light simulation tool, which is a simplified description of the main characteristics of the observed process [205]. These types of models focus on the conservation of species, mass, and energy, while the conservation of momentum is usually not solved for. The bulk composition is updated through the mass exchange between the bulk phase and the observed reaction volume [27]. One of the advantages of the reaction equilibrium models is the ability to use Gibbs free energy minimisation routines for equilibrium calculation (see *e.g.* [206]). The conservation of mass in the reaction volume is generally of the form

$$\underbrace{\frac{\mathrm{d}m}{\mathrm{d}t}}_{\text{accumulation}} = \underbrace{\dot{m}_{\text{in}}}_{\text{input}} - \underbrace{\dot{m}_{\text{out}}}_{\text{output}} + \underbrace{S}_{\substack{\text{source}\\ \text{term}}} . \tag{18}$$

It should be noted that under steady-state conditions the accumulation term is zero.

Semin and co-authors (1983)

Semin *et al.* [207] made partial use of the assumption of a constant oxygen potential in the metal bath, but discarded previous assumptions of a constant chromium content and temperature. In the first series of calculations, it was assumed that all excess oxygen would be consumed by chromium, but in later calculations iron oxidation loss was taken as a constant at 1.5% to provide better results. Two decarburisation regimes were taken into consideration:

1. In high carbon region, all oxygen was assumed to be consumed by the oxidation of carbon.
2. At high silicon content levels, 80% of the supplied oxygen was used to oxidise silicon, while the remaining 20% was distributed between carbon and chromium.

Görnerup and Sjöberg (1999)

Görnerup and Sjöberg [159] published a model for reduction and desulphurisation in AOD and CLU processes.[7] As discussed in Section 3.1.5 (p. 74), this model was essentially a sub-model of the AOD model proposed earlier by Sjöberg [209]. The objective of the reduction and desulphurisation model was to determine optimal slag composition and calculate the necessary material additions to achieve it. In this regard, the modelling approach was fundamentally different from the main decarburisation model. The three main assumptions of the model are summarised below:

1. The observed system reaches a thermodynamic equilibrium at the end of the desulphurisation.
2. The injected oxygen not consumed by CO and SiO_2 during decarburisation is reduced completely by the reductant additions.
3. The heat losses are constant during the reduction stage.

The sulphur partition ratio L_S was defined as a function of temperature, sulphide capacity, and bath composition according to Eq. 19.

$$\log_{10} L_S = -\frac{935}{T} + 1.375 + \log C_S + \log f^H_{[S]} - \log a^H_{[O]}\,, \tag{19}$$

where C_S is the sulphide capacity of the top slag, $f^H_{[S]}$ is the Henrian activity coefficient (1 wt-% standard state) of dissolved sulphur, and $a^H_{[O]}$ is the Henrian activity (1 wt-% standard state) of dissolved oxygen. The activity coefficient of dissolved sulphur was determined according to the Wagner formalism, while the activity of the dissolved oxygen was calculated from the silicon-silica equilibrium.

The main assumptions of the model leave some room for criticism. As pointed out by Wei and Zhu [49], it is unlikely that a thermodynamic equilibrium can be reached and established in the whole metal bath during the reduction stage. The modelling results obtained in Article IV support this criticism. Furthermore, as admitted by Görnerup and Sjöberg [159] themselves, the second assumption is not in keeping with typical slag end compositions, which contain a small residual amount of chromium, iron, and manganese oxides. While the third assumption does not cause inaccuracy *per se*, it means that the heat losses need to be re-assessed if the duration of the reduction stage is changed.

[7] See also [208].

Kikuchi and co-authors (2002/2004)

Kikuchi *et al.* [210, 211] proposed a mathematical model for the decarburisation of stainless steel in a combined-blowing converter in the low carbon range. In their study, the top lance was not employed for decarburisation, but for stirring the bath with nitrogen. Three reaction zones were considered in the model: 1) the free surface created by the nitrogen gas jet, 2) the slag–metal interface, and 3) the bottom-blowing zone. In the free surface, the reaction rate is determined by the mass transfer rates of carbon and oxygen; their mass transfer coefficients were assumed to be equal. At the metal–slag interface, the oxygen content in the metal bath equilibriates with the oxygen content of the slag, which is determined by the oversaturated Cr_2O_3. Consequently, the reduction of Cr_2O_3 supplies the metal bath with dissolved oxygen. In the bottom-blowing zone, the injected oxygen is consumed first by the available carbon, after which the remainder is consumed by oxidation of chromium. The overall differential equations for carbon, oxygen, and chromium contents were expressed as follows [211]:

$$\begin{aligned}
\frac{\mathrm{d}[\%\mathrm{C}]}{\mathrm{d}t} &= -\frac{100}{m_{\mathrm{bath}}}\left(\dot{m}_{[\mathrm{C}],1}+\dot{m}_{[\mathrm{C}],3}\right) \\
&= -\frac{100}{m_{\mathrm{bath}}}\left(A_{\mathrm{G}}R''_{[\mathrm{C}],1}+229\dot{V}_{\mathrm{O}_2}\frac{[\%\mathrm{C}]}{100}\right), \qquad (20)\\
\frac{\mathrm{d}[\%\mathrm{O}]}{\mathrm{d}t} &= -\frac{100}{m_{\mathrm{bath}}}\left(-\dot{m}_{[\mathrm{O}],2}-\dot{m}_{[\mathrm{O}],3}+\frac{16}{12}\dot{m}_{[\mathrm{C}],1}\right) \\
&= -\frac{100}{m_{\mathrm{bath}}}\left\{\left[\alpha\left(\dot{m}_{[\mathrm{O}],\mathrm{lance}}-\dot{m}_{[\mathrm{O}],\mathrm{bottom}}\right)-Q_{\mathrm{L}}\right]\frac{([\%\mathrm{O}]-[\%\mathrm{O}]_{\mathrm{sat}})}{100}\right. \\
&\quad \left.+\frac{16}{12}\dot{m}_{[\mathrm{C}],1}\right\}, \qquad (21)\\
\frac{\mathrm{d}[\%\mathrm{Cr}]}{\mathrm{d}t} &= -\frac{100}{m_{\mathrm{bath}}}\left(\dot{m}_{[\mathrm{Cr}],3}-\dot{m}_{[\mathrm{Cr}],2}\right), \qquad (22)
\end{aligned}$$

where $\dot{m}_{[\mathrm{C}]}$, $\dot{m}_{[\mathrm{O}]}$, and $\dot{m}_{[\mathrm{Cr}]}$ are the mass transfer rates of carbon, oxygen, and chromium, respectively. The subscripts 1, 2, and 3 denote the three reaction zones, $\dot{m}_{[\mathrm{O}],\mathrm{lance}}$ is the oxygen transfer rate between slag and metal induced by top-blowing, $\dot{m}_{[\mathrm{O}],\mathrm{bottom}}$ is the oxygen transfer rate between slag and metal induced by bottom-blowing, A_{G} is the gas–metal interfacial area, $R''_{[\mathrm{C}],1}$ is the decarburisation rate at the free surface, α is the liquid phase fraction of the slag, Q_{L} is the circulation flow rate of metal into the bottom-blowing zone, and $[\%\mathrm{O}]_{\mathrm{sat}}$ is the oxygen content in equilibrium with the

chromium oxide saturated in the slag.

3.1.3 Finite volume reaction models

The fundamental basis of the finite volume reaction models is the numerical solution of fluid flows in discrete control volumes. The general equation of continuity in a control volume is expressed by [116]:

$$\underbrace{\frac{\partial \rho}{\partial t}}_{\substack{\text{rate of} \\ \text{change of } \rho}} = \underbrace{-\nabla \cdot (\rho \mathbf{u})}_{\substack{\text{divergence} \\ \text{of } \mathbf{u}}}, \tag{23}$$

where $\mathbf{u}$ is the velocity vector. In principle, the chemical reaction rates can be given as source terms without any interaction with the fluid flow field. In more complex models, chemical reaction rates are calculated based on the conditions of the fluid flow field.

Kärnä and co-authors (2008)

Kärnä *et al.* [212] proposed a CFD-based reaction model for nitrogen transfer in the AOD process during side-blowing. The isothermal, three-dimensional fluid flow field was solved using the ANSYS Fluent software by employing an Eulerian multiphase approach and the realizable k-ε turbulence model. Nitrogen absorption and desorption were calculated based on a time-averaged flow field according to Eqs. 24 and 25, respectively.

$$\frac{\mathrm{d}c_{[\mathrm{N}]}}{\mathrm{dt}} = -\beta_1 \frac{A}{V_{\mathrm{bath}}} \left(c_{[\mathrm{N}]} - c_{[\mathrm{N}],\mathrm{e}}\right), \tag{24}$$

$$\frac{\mathrm{d}c_{[\mathrm{N}]}}{\mathrm{dt}} = -\beta_2 \frac{A}{V_{\mathrm{bath}}} \left(c^2_{[\mathrm{N}]} - c^2_{[\mathrm{N}],\mathrm{e}}\right), \tag{25}$$

where c denotes the molar concentration, β_1 is the mass transfer coefficient of the absorption reaction, A is the interfacial area, V_{bath} is the volume of the metal bath, and β_2 is the mass transfer coefficient of the desorption reaction. The model was applied for simulation of a single heat. The calculated nitrogen content as a function of time was in reasonably good agreement with the measured data.

Andersson and co-authors (2012/2013)

Andersson *et al.* [213–217] proposed a reaction model, which coupled a CFD model of an AOD converter with Thermo-Calc computational thermodynamics software. The CFD model – implemented with the PHOENICS software – was used to calculate a steady-state flow field, which was employed for the reaction calculations [214].[8] The transport of species ϕ_i^k of phase i was defined according to [214]:

$$\underbrace{\frac{\mathrm{d}\left(\alpha_i \rho_i \phi_i^k\right)}{\mathrm{d}t}}_{\substack{\text{temporal}\\ \text{change}}} + \underbrace{\nabla\left(\alpha_i \rho_i v_i \phi_i^k\right)}_{\substack{\text{convective}\\ \text{mass transport}}} = \underbrace{\nabla\left[\alpha_i \rho_i \left(D_0^k + \frac{\mu_t}{\rho_i \mathrm{Sc_t}}\right) \nabla \phi_i^k\right]}_{\substack{\text{diffusive}\\ \text{mass transport}}}, \tag{26}$$

where α_i is the phase volume fraction, ρ_i is the phase density, v_i is the phase velocity vector, D_0^k is the diffusion coefficient of species k, μ_t is the turbulent dynamic viscosity, and $\mathrm{Sc_t}$ is the turbulent Schmidt number. The effect of top slag on the metallostatic pressure in the metal bath was calculated assuming a smooth bath surface [215]. A significant shortcoming of the model is that that the metal and slag temperatures were calculated using a linear temperature equation, which was determined based on regression data and included both the heat produced by the reactions and the cooling effects of gas and slag [214]. Furthermore, the temperature was assumed to be constant for the whole computational domain [214]. This assumption appears to be quite rough and ignores the different heat transfer processes taking place in the bath, particularly the heat transfer phenomena in the gas injection area and in the gas plume.

So far, the model has been validated only by comparison with the TimeAOD2 model, which is based on the model proposed by Sjöberg [209] (see p. 74). Nevertheless, the model has been used for an in-depth analysis of the early decarburisation stage [213] and for sensitivity studies regarding the effect of chromium oxide separation [215] and bath temperature [216] on the decarburisation reaction. Based on the results obtained, it was proposed that a higher amount of liquid slag as well as higher separation of chromium oxide to the liquid slag have a decreasing effect on the decarburisation rate [215].

Song and co-authors (2014)

Song *et al.* [75] studied post-combustion phenomena in the AOD process using a CFD-based reaction model. The fluid flow field was solved using commercial ANSYS Fluent

[8] This approach is essentially similar as in the BOF model proposed earlier by Ersson *et al.* [218].

software by employing Reynolds-averaged Navier-Stokes equations for decomposing the instantaneous Navies-Stokes equations into average fluctuation components and using the realizable k-ε model for turbulence modelling [75]. The transport and reaction of oxygen were calculated with species transport model. More specifically, it was assumed that the reaction rate is controlled either by the Arrhenius rate or the turbulence mixing rate [75].

3.1.4 Simple reaction interface models

The theoretical basis for simple reaction interface models is constituted by the boundary layer theory [219]. More specifically, it is assumed that the reactions establish an equilibrium at the reaction interfaces and that the reaction rates are determined by mass transfer onto and from the interface [27]. For example, in the case of slag–metal reactions the reaction rate of species i can be calculated simply as [220]:

$$\frac{\mathrm{d}c_i}{\mathrm{d}t} = -\beta \frac{A}{V} (c_i - c_i^*) = -k (c_i - c_i^*) \,, \tag{27}$$

where c_i is the molar concentration of species i, t is the time, β is the mass transfer coefficient, A is the interfacial area, V is the volume, c_i^* is the molar concentration of species i at the interface, and k is the time constant. It should be noted that the formulation shown in Eq. 27 excludes the presence of bulk motion. In general, simple reaction interface models do not provide mathematical descriptions of the time constant k, but employ fixed values derived from plant data. As discussed later in Section 4.1 (p. 97), the physical significance of Eq. 27 is limited by the fact that it is strictly valid for dispersed systems only when the average residence time of the particles approaches zero.

Watanabe and Tohge (1973)

Watanabe and Tohge [221] proposed a model for the decarburisation phenomena of liquid stainless steel under reduced pressure. The model was based on the assumption that the blown oxygen is first transferred to the metal bath via Eqs. 28 and 29, and then reacts with dissolved carbon according to Eq. 30.

$$x[\mathrm{M}] + \frac{y}{2}\{\mathrm{O_2}\} \rightleftharpoons (\mathrm{M}_x\mathrm{O}_y) \,. \tag{28}$$

$$(\mathrm{M}_x\mathrm{O}_y) \rightleftharpoons x[\mathrm{M}] + y[\mathrm{O}]\,. \tag{29}$$

$$[\mathrm{C}] + [\mathrm{O}] \rightleftharpoons \{\mathrm{CO}\}\,. \tag{30}$$

The carbon content was obtained by integrating the first-order differential equation for decarburisation:

$$\frac{[\%\mathrm{C}]_\mathrm{t} - [\%\mathrm{C}]_\mathrm{e}}{[\%\mathrm{C}]_0 - [\%\mathrm{C}]_\mathrm{e}} = \exp\left[-\frac{A}{V_\mathrm{bath}}\left(\frac{D}{\delta}\right)t\right]\,, \tag{31}$$

where $[\%\mathrm{C}]$ is the carbon content, $[\%\mathrm{C}]_\mathrm{e}$ is the carbon content at equilibrium, A is the reaction area, V_bath is the volume of the metal bath, D is the mass diffusivity, δ is the thickness of the diffusion boundary layer, and t is the time. The ratio D/δ corresponds to the definition of the mass transfer coefficient and was taken as a velocity parameter of the decarburisation reaction. The model was validated with a series of heats, in which pure O_2, Ar–O_2, CO_2, and Fe_2O_3 additions were employed for the decarburisation of the melt under reduced pressure. The start carbon contents were 0.2 – 0.3 wt-%. Based on the validation data, the velocity parameter was evaluated to be $D/\delta = 1.41 \cdot 10^{-4}$ m/s.

Asai and Szekely (1974)

Asai and Szekely [191] proposed a mathematical decarburisation model for laboratory scale results. This initial model assumed that dissolved oxygen reacts either with dissolved carbon or dissolved chromium. Oxidation of Fe was excluded as FeO was considered purely an intermediary product. The differential oxygen, carbon, and chromium balances were written as:

$$\frac{\mathrm{d}y_{[\mathrm{O}]}}{\mathrm{d}t} = I(y_{[\mathrm{O}],\mathrm{e}} - y_{[\mathrm{O}]}) + \frac{\dot{m}_{[\mathrm{O}]}}{m_\mathrm{bath}}\,, \tag{32}$$

$$\frac{\mathrm{d}y_{[\mathrm{C}]}}{\mathrm{d}t} = I(y_{[\mathrm{C}],\mathrm{e}} - y_{[\mathrm{C}]})\,, \tag{33}$$

$$\frac{\mathrm{d}y_{[\mathrm{Cr}]}}{\mathrm{d}t} = I(y_{[\mathrm{Cr}],\mathrm{e}} - y_{[\mathrm{Cr}]})\,, \tag{34}$$

where y denotes the mass fraction, I is the conductance parameter (1/s) which incorporates all the mass transfer resistances, and $\dot{m}_{[\mathrm{O}]}$ is the feed rate of oxygen (kg/s). For the calculations, Eqs. 32, 33, and 34 were converted into a dimensionless form and a dimensionless conductance parameter was used as a fitting parameter. The activity coefficients of oxygen, carbon, and chromium were determined using Wagner's

formalism, considering only the main interactions in the Fe–Cr–C–O system. The activity of Cr_2O_3 was taken as $a_{(Cr_2O_3)} = 1$. The model was employed for simulating laboratory-scale experiments, which included top- or bottom-blowing.

In later work, Szekely and Asai [192] modified the model for non-isothermal industrial practice. This model considered a reaction system, where the side-blown oxygen could either react with C, Cr, and Si (thus forming CO, Cr_2O_3, and SiO_2, respectively), or accumulate in the melt. In relation to the silicon-silica equilibrium, the activity coefficients of Si and SiO_2 were taken as 1 and 0.01, respectively.

A comparison of the model predictions to plant data from a 40 t electric furnace showed that despite strong simplifications, the model was able to predict the correct carbon, chromium, and temperature trajectories with good accuracy [192], but as the model was applied for only one heat, it remains unclear whether the same level of accuracy level could be achieved with a larger amount of data. The studied heat started at a carbon content of 0.892 wt-%, which is above the critical carbon contents reported for side-blowing [26, 144]. One of the key deficiencies of the model is that it did not take into account that the mass transfer of carbon is not rate-limiting for decarburisation at high carbon content levels.

Fruehan (1976/1976)

In 1975, Fruehan [222] published a study on nitrification and decarburisation of stainless steels. It was postulated that both the mass transfer of nitrogen in the liquid steel and the chemical reaction at the interface could control the nitrogen pick-up rate. Combining these two mechanisms, the following rate equation was proposed:

$$\frac{[\%\mathrm{N}]_\mathrm{e} - [\%\mathrm{N}]_\mathrm{t}}{[\%\mathrm{N}]_\mathrm{e} - [\%\mathrm{N}]_0} = \frac{k_\alpha}{k_\alpha - k_\beta} \exp(-k_\beta t) - \frac{k_\beta}{k_\alpha - k_\beta} \exp(-k_\alpha t)\,, \tag{35}$$

where k_α is the rate parameter of nitrogen mass transfer and k_β is the rate parameter for the solution of nitrogen into the metal bath. In the same study, Fruehan [222] suggested that the injected oxygen primarily oxidises chromium and iron at the tuyère zone. It was assumed that FeO would be reduced rapidly primarily by chromium, thus rendering it as an intermediate product. The decarburisation reaction would then take place between dissolved carbon and the chromium oxide particles rising with the gas bubbles towards the surface of the metal bath:

$$\mathrm{Cr_2O_{3\,(s)}} + 3[\mathrm{C}] \rightleftharpoons 2[\mathrm{Cr}] + 3\{\mathrm{CO}\}\,. \tag{36}$$

In 1976, Fruehan [143] published a reaction model based on the earlier findings. This model established many of the basic principles that have been employed in later models. It was assumed that the decarburisation rate would be controlled by oxygen supply rate at high carbon range and by liquid-phase mass transfer of carbon to the bubble surface at the low carbon range. Therefore, the decarburisation rate at a given moment is defined simply by the mechanism, which provides a slower rate:

$$\frac{\mathrm{d}[\%\mathrm{C}]}{\mathrm{d}t} = \max\left(\underbrace{-\frac{200 M_\mathrm{C} \dot{n}_{\mathrm{O_2}}}{m_\mathrm{bath}}}_{\substack{\text{oxygen}\\ \text{supply control}}}, \underbrace{-k\left([\%\mathrm{C}] - [\%\mathrm{C}]_\mathrm{e}\right)}_{\substack{\text{carbon mass}\\ \text{transfer control}}}\right), \tag{37}$$

where M_C is the molar mass of carbon, $\dot{n}_{\mathrm{O_2}}$ is the molar flow rate of oxygen, m_bath is the mass of the metal bath, k is a rate parameter fitted to the measurement data, $[\%\mathrm{C}]$ is the time-dependent average carbon content in the metal bath, and $[\%\mathrm{C}]_\mathrm{e}$ is the average carbon content at the bubble surface in equilibrium with the average chromium content and the CO partial pressure in the gas bubbles. The equilibrium carbon content ($[\%\mathrm{C}]_\mathrm{e}$), the partial pressure of CO (p_CO), and the molar flow rate of CO ($\dot{n}_\mathrm{CO}$) were calculated as follows:

$$[\%\mathrm{C}]_\mathrm{e} = \frac{a_{[\mathrm{Cr}]}^{2/3}}{K^{1/3}} \frac{100 M_\mathrm{C}}{M_\mathrm{Fe} \gamma_{[\mathrm{C}]}} p_\mathrm{CO}\,, \tag{38}$$

$$p_\mathrm{CO} = \frac{\dot{n}_\mathrm{CO}}{\dot{n}_\mathrm{CO} + \dot{n}_\mathrm{Ar}} p_\mathrm{G}\,, \tag{39}$$

$$\dot{n}_\mathrm{CO} = \frac{\mathrm{d}[\%\mathrm{C}]}{\mathrm{d}t} \frac{m_\mathrm{bath}}{100 M_\mathrm{C}}\,, \tag{40}$$

where $a_{[\mathrm{Cr}]}$ is the activity of dissolved chromium, M_Fe is the molar mass of iron, $\gamma_{[\mathrm{C}]}$ is the activity coefficient of dissolved carbon (molar basis), K is the equilibrium constant,[9] $\dot{n}_\mathrm{Ar}$ is the molar flow rate of argon, and p_G is the average total pressure in the metal bath. The activity coefficient of carbon was determined in the Fe–Cr–C system using the Wagner formalism.

Having identified the reduction of chromium oxides with dissolved carbon as the main decarburisation mechanism, Fruehan [223] undertook experiments to study the

[9] Corresponding to reaction $\mathrm{Cr_2O_3(s)} + 3[\mathrm{CO}] \rightleftharpoons 2[\mathrm{Cr}] + 3\{\mathrm{CO}\}$.

rate-controlling step in the reduction of Cr_2O_3 by carbon. Experiments were conducted with both solid carbon and carbon dissolved in Fe–Cr–C melts. In the previous case, it was found that the overall reaction is controlled by the mass transfer of CO away from the reaction surface. In the latter case, the decarburisation rate was found to be controlled by the diffusion of dissolved carbon into the liquid Cr_2O_3 surface.

All in all, the work carried out by Fruehan [143, 222, 223] in 1970s was instrumental not only in identifying the main mechanism of decarburisation during side-blowing operations through experiments, but also in formulating a mathematical description. As shown by Irving *et al.* [224], the reaction model proposed by Fruehan [143] is sufficiently simple to be incorporated in a control model. However, as pointed out by Deb Roy and Robertson [225], some seemingly rough assumptions were related to the equilibrium composition at the reaction interface:

1. the equilibrium carbon content at the interface was taken as zero for isothermal decarburisation at low carbon content,
2. the equilibrium chromium concentration at the interface was taken as equal to the bulk chromium concentration, and
3. the model did not account for the effect of the variation of CO partial pressure with bath height.

Ohno and Nishida (1977)

Ohno and Nishida [193] introduced an AOD model, which employed gas bubble geometry. Similarly to Fruehan [143], it was assumed that the decarburisation rate was controlled by the liquid-phase mass transfer of carbon. The generation of CO was expressed by

$$\frac{\mathrm{d}n_{\mathrm{CO}}}{\mathrm{d}t} = \beta_{[\mathrm{C}]}\xi V_{\mathrm{bath}}^{2/3}\frac{\rho_{\mathrm{L}}}{100M_{\mathrm{C}}}\left([\%\mathrm{C}]-[\%\mathrm{C}]_{\mathrm{e}}\right), \tag{41}$$

where $\beta_{[\mathrm{C}]}$ is the mass transfer of dissolved carbon, ξ is a geometry parameter, V_{bath} is the volume of the metal bath, and ρ_{L} is the density of liquid metal. The mass transfer coefficient was calculated according to the Higbie [226] correlation by employing bubble geometry. As pointed out by Wei and Zhu [49], a considerable deviation from reality was caused by the assumption that the activities of the dissolved species were taken as being equal to unity.

Deb Roy and co-authors (1978)

In 1978, Deb Roy and Robertson [225] proposed a mathematical reaction model for argon–oxygen steam mixtures under isothermal conditions and studied decarburisation in AOD and CLU processes. This model assumed that most of the blown oxygen first oxidises Cr to Cr_2O_3, which oxidises carbon in the metal bath. Gas- and liquid-side mass transfer resistance as well as the effect of partial pressure on the gas-side mass transfer coefficient were accounted for. The effects of variation of reduced top pressure, oxygen-argon ratio of the blowing mixture and steam injection on the oxidation of carbon and chromium were also considered. The mass transfer of gaseous species i was calculated according to the penetration theory and accounted for the effect of bulk motion (Eq. 42). The rate expressions of the dissolved species C, Cr, O, and H were defined according to Eq. 43.

$$n''_{i,\mathrm{G}} = \underbrace{\theta_i \frac{\beta_{i,\mathrm{G}}}{(p_\mathrm{G} RT)^{1/2}} (p_i^* - p_i)}_{\text{mass transport}} + \underbrace{\frac{p_i^*}{p_\mathrm{G}} \sum_{j=1}^{n} n''_{j,\mathrm{G}}}_{\text{bulk motion}}, \tag{42}$$

$$n''_{i,\mathrm{L}} = \underbrace{\beta_{i,\mathrm{L}} (c_i - c_i^*)}_{\text{mass transport}}, \tag{43}$$

where θ is the correction factor for high mass transfer rates, p_G is the total gas pressure, p is the partial pressure, p^* is the partial pressure at the interface, n'' is the molar flux, β is the mass transfer coefficient, c is the molar concentration, and c^* is the molar concentration at the interface. Based on the initial results, it was suggested that reduced top pressure has an increasing effect on the decarburisation rate, but that the effect is more pronounced at higher carbon contents [225]. The use of steam as a substitute for argon was also studied and the hydrogen level in the end composition of the metal bath was found to be comparable to the saturation solubility of hydrogen in liquid iron [225].

In a subsequent paper, Deb Roy *et al.* [227] extended the model for non-isothermal conditions and assumed that all the oxygen blown from the tuyères would react to Cr_2O_3, SiO_2, and MnO in proportion to their molar concentrations. Thereafter, the oxides rising upwards with gas bubbles would react with the dissolved species in the metal phase. The activity coefficients of the dissolved species were calculated using the Wagner formalism. The model was compared to plant data from six heats.

Tohge and co-authors (1984)

Tohge *et al.* [111] proposed a new scheme for process control of combined top- and side-blowing decarburisation. The oxidation ratio of each element due to top-blowing was related to the Gibbs free energy of the corresponding oxide. However, a fixed molar Cr/Fe oxidation ratio of 4.6 was assumed based on slag analysis. The effects of the additions were considered in the mass and heat balance. The change in carbon content and the molar rate of carbon removal are obtained from Eqs. 44 and 45, respectively.

$$\frac{\mathrm{d}[\%\mathrm{C}]}{\mathrm{d}t} = -\frac{1200\dot{n}_{[\mathrm{C}]}}{m_{\mathrm{bath}}} - \frac{[\%\mathrm{C}]}{m_{\mathrm{bath}}}\frac{\mathrm{d}m_{\mathrm{bath}}}{\mathrm{d}t}, \tag{44}$$

$$\dot{n}_{[\mathrm{C}]} = \frac{m_{\mathrm{bath}} A_V \beta_{[\mathrm{O}]}([\%\mathrm{O}] - [\%\mathrm{O}]_{\mathrm{e}})}{1600}, \tag{45}$$

where A_V is the reaction surface area per unit volume and $\beta_{[\mathrm{O}]}$ is the mass transfer coefficient of oxygen. The apparent volumetric mass transfer coefficient $A_V\beta_{[\mathrm{O}]}$ was determined based on plant data. The obtained volumetric mass transfer coefficients were presented as a function of the carbon content and were essentially the same for side-blowing and combined side- and top-blowing. The predictions of the proposed model were not compared to experimental data.

Vercruyssen and co-authors (1994)

Vercruyssen *et al.* [37] proposed a model for the MRP process. The model considered three reaction interfaces: metal–slag, metal–gas, and slag–gas. At the metal–slag interface, metal oxidation and dissolution of oxides was assumed to take place according to Eq. 46. At the metal–gas interface, direct oxidation of carbon was described according to Eqs. 47–49, while dissolution of oxygen was expressed according to Eq. 50. At the slag–gas interface, the reduction of oxides was formulated according to Eq. 51.

$$[\mathrm{Me}] + x[\mathrm{O}] \rightleftharpoons (\mathrm{MeO}_x)\,. \tag{46}$$

$$[\mathrm{C}] + \{\mathrm{CO}_2\} \rightleftharpoons 2\{\mathrm{CO}\}\,. \tag{47}$$

$$[\mathrm{C}] + [\mathrm{O}] \rightleftharpoons \{\mathrm{CO}\}\,. \tag{48}$$

$$[\mathrm{C}] + 2[\mathrm{CO}] \rightleftharpoons \{\mathrm{CO}_2\}\,. \tag{49}$$

$$\{O_2\} \rightleftharpoons 2[O]\,. \tag{50}$$

$$\{MeO_x\} + x\,(CO) \rightleftharpoons [Me] + x\,(CO_2)\,. \tag{51}$$

The total molar flux of species i in the metal and slag phases was calculated according to Eqs. 52 and 53, respectively, while the total molar flux of species i in the gas phase was calculated according to Eq. 54.

$$n''_{i,L} = \beta_{i,L}\, c_L\, (x_{i,e} - x_{i,bath})\,, \tag{52}$$

$$n''_{i,S} = \beta_{i,S}\, c_S\, \left(x_{i,e} - x_{i,slag}\right)\,, \tag{53}$$

$$n''_{i,G} = \beta_{i,G}\, c_G\, \left(x_{i,e} - x_{i,gas}\right) + x_{i,e} \sum_{j=1}^{n} n''_{j,G}\,, \tag{54}$$

where c_L, c_S, and c_G are the molar concentrations of the metal, slag, and gas phases, respectively. The equilibrium mole fractions $x_{i,e}$ were calculated from the equilibrium constants of the reactions considered. The activity coefficients of elements dissolved in the metal phase were described using the Wagner formalism, while the activity coefficients of slag species were assumed to be constant. It should be noted that all the species in one phase were assumed to have the same mass transfer coefficient. The interfacial areas for metal–slag ($A_{L–S}$), metal–gas ($A_{L–G}$), and slag–gas ($A_{S–G}$) reactions were assumed to be adjustable variables.

Reichel and Szekely (1995)

Reichel and Szekely [26] presented a mathematical model for decarburisation in AOD and VOD processes. The approach shared many similarities with their earlier-proposed control models for the KCB-S [228] and VOD processes [229]. The AOD model was combined with an on-line gas analysis to determine the optimal rate of oxygen supply at a given moment.

The main assumption of the model is that the decarburisation rate in the high carbon region is directly proportional to the oxygen flow rate and proceeds according to the zeroth order differential equation, but as the carbon content decreases below a critical value, the decarburisation rate becomes limited by the mass transfer of carbon and proceeds according to the first order differential equation. Combining these regimes, the

decarburisation rate can be expressed as follows:

$$\frac{\mathrm{d}[\%\mathrm{C}]}{\mathrm{d}t} = \begin{cases} \underbrace{-\frac{100}{m_{\mathrm{bath}}}\frac{12}{11.2}\dot{V}_{\mathrm{O_2,C}}}_{\substack{\text{oxygen}\\ \text{supply control}}} & \text{when} \quad [\%\mathrm{C}] > [\%\mathrm{C}]_{\mathrm{crit}}\,, \\ \underbrace{-k\left([\%\mathrm{C}]-[\%\mathrm{C}]_{\mathrm{e}}\right)}_{\substack{\text{carbon mass}\\ \text{transfer control}}} & \text{when} \quad [\%\mathrm{C}] \leq [\%\mathrm{C}]_{\mathrm{crit}}\,, \end{cases} \tag{55}$$

where $\dot{V}_{\mathrm{O_2,C}}$ is the oxygen flow rate consumed for CO formation and k is the overall oxygen exchange coefficient. The formulation shown in Eq. 55 essentially similar to that of Eq. 37. Reichel and Szekely [26] suggested that $1/k$ is practically constant for the low-carbon region below the critical carbon content. The statistical analysis of production data for an AOD converter with a top lance suggested a value of $1/k = 6.7$ min. However, it should be noted that k is constant only for a specific vessel and blowing practice.

Scheller and Wahlers (1996)

Scheller and Wahlers [134] studied nitrification during combined top- and side-blowing decarburisation in the low carbon region. The studied 1st order reaction mechanism is a diffusion-controlled case, while the 2nd order reaction mechanism is controlled by the chemical reaction at the interface:

$$\frac{\mathrm{d}[\%\mathrm{N}]}{\mathrm{d}t} \approx \beta_1 \frac{A}{V} f_{[\mathrm{N}]}\left([\%\mathrm{N}]_{\mathrm{e}} - [\%\mathrm{N}]\right) \qquad \text{(1st order reaction)}\,, \tag{56}$$

$$\frac{\mathrm{d}[\%\mathrm{N}]}{\mathrm{d}t} \approx \beta_2 \frac{A}{V} f^2_{[\mathrm{N}]}\left([\%\mathrm{N}]^2_{\mathrm{e}} - [\%\mathrm{N}]^2\right) \qquad \text{(2nd order reaction)}\,, \tag{57}$$

where β_1 is the mass transfer coefficient of the 1st order reaction, A is the reaction area, V is the volume of the metal bath, $f_{[\mathrm{N}]}$ is the activity coefficient of nitrogen, $[\%\mathrm{N}]_{\mathrm{e}}$ is the equilibrium content of nitrogen, and β_2 is the mass transfer coefficient of the 2nd order reaction. The corresponding rate constants k_1 and k_2 were defined by Eqs. 58 and 59, respectively.

$$k_1 = \beta_1 \frac{A}{V} = \frac{1}{t f_{[\mathrm{N}]}} \ln \frac{[\%\mathrm{N}]_{\mathrm{e}} - [\%\mathrm{N}]_0}{[\%\mathrm{N}]_{\mathrm{e}} - [\%\mathrm{N}]}\,. \tag{58}$$

$$k_2 = \beta_2 \frac{A}{V} = \frac{1}{t f_{[\mathrm{N}]}^2} \frac{50}{[\%\mathrm{N}]_\mathrm{e}} \left(\ln \frac{[\%\mathrm{N}]_\mathrm{e} - [\%\mathrm{N}]_0}{[\%\mathrm{N}]_\mathrm{e} + [\%\mathrm{N}]_0} + \ln \frac{[\%\mathrm{N}]_\mathrm{e} + [\%\mathrm{N}]}{[\%\mathrm{N}]_\mathrm{e} - [\%\mathrm{N}]} \right) . \qquad (59)$$

In order to differentiate the contributions of side- and top-blowing to nitrification, the validation heats were conducted as follows: when an O_2–N_2 mixture was blown via tuyères, an O_2–Ar mixture was blown via a top lance and *vice versa*. The ratio of O_2 to N_2 or Ar was $\leq$ 1:1. The start and end carbon contents of the studied stages were approximately 0.5 wt-% and 0.2 wt-%, respectively. Based on the experimental heats, it was found that the efficiency of nitrification was found to be approximately 23% for side-blown nitrogen and $\leq$ 1% for top-blown nitrogen. The first-order rate constants (k_1) were approximately 0.35–0.45 min^{-1} for side-blowing and 0.006–0.013 min^{-1} for top-blowing. The corresponding second-order rate constants (k_2) were approximately 400–700 min^{-1} and 15–35 min^{-1}, respectively.[10] These results suggest that the top-blowing of nitrogen plays practically no role in the nitrification of steel during the AOD process.

Kleimt and co-authors (2006/2007)

Kleimt *et al.* [230–232] proposed a thermodynamic decarburisation model, which is largely similar to other reaction interface models. The decarburisation rate in the low carbon region was defined according to [230]:

$$\frac{\mathrm{d}[\%\mathrm{C}]}{\mathrm{d}t} = -\frac{1}{T_\mathrm{C}} \left([\%\mathrm{C}] - [\%\mathrm{C}]_\mathrm{e} \right) , \qquad (60)$$

where T_C is a kinetic time constant. The equilibrium carbon content was defined by

$$[\%\mathrm{C}]_\mathrm{e} = \frac{\left(f_{[\mathrm{Cr}]} [\%\mathrm{Cr}]_\mathrm{e} \right)^{2/3}}{f_{[\mathrm{C}]}} \frac{K_\mathrm{Cr}^{1/3}}{K_\mathrm{C}} \frac{1}{a_{(\mathrm{Cr_2O_3})}^{1/3}} p_\mathrm{CO} = F_\mathrm{CO} p_\mathrm{CO} , \qquad (61)$$

where f is the Henrian activity coefficient (wt-% scale), $[\%\mathrm{Cr}]_\mathrm{e}$ is the equilibrium chromium content, K_Cr is the equilibrium constant,[11] K_C is the equilibrium constant of the reaction $[\mathrm{C}] + [\mathrm{O}] \rightleftharpoons \{\mathrm{CO}\}$, $a_{(\mathrm{Cr_2O_3})}$ is the activity of Cr_2O_3, and F_CO is a parameter which equals the carbon equilibrium at the CO partial pressure p_CO of 1 bar. The partial

[10] The 1st order rate reaction shown in Eq. 56 is similar to a typical expression of decarburisation with low carbon contents. Assuming that the surface area available for oxygen and nitrogen is the same, the reported k_1 coefficients can be employed for side- and top-blowing decarburisation.

[11] Corresponding to reaction $2[\mathrm{Cr}] + 3[\mathrm{O}] \rightleftharpoons (\mathrm{Cr_2O_3})$.

pressure of CO was calculated on the basis of CO gas generation and the injection of inert gases. Here, it was assumed that the total pressure and the partial pressure of CO corresponded to a value near the bath surface. The activity coefficients of species dissolved in the metal bath were solved using the Wagner formalism.

Riipi and co-authors (2009)

The mathematical model proposed by Riipi *et al.* [138] focuses on the absorption and desorption of nitrogen during the AOD process. The rate equations were formulated as follows:

$$\frac{\mathrm{d}c_{[\mathrm{N}]}}{\mathrm{d}t} = -\beta_1 \frac{A_{\mathrm{eff}}}{V_{\mathrm{bath}}} \left(c_{[\mathrm{N}]} - c_{[\mathrm{N}],\mathrm{e}}\right) \qquad \text{(absorption)}, \tag{62}$$

$$\frac{\mathrm{d}c_{[\mathrm{N}]}}{\mathrm{d}t} = -\beta_2 \frac{A_{\mathrm{eff}}}{V_{\mathrm{bath}}} \left(c^2_{[\mathrm{N}]} - c^2_{[\mathrm{N}],\mathrm{e}}\right) \qquad \text{(desorption)}, \tag{63}$$

where β_1 is the mass transfer coefficient of the absorption reaction, A_{eff} is the effective surface area, and β_2 is the mass transfer coefficient of the desorption reaction. The effective surface area for nitrogen absorption and desorption were calculated according to Eqs. 64 and 65.

$$A_{\mathrm{eff}} = \left(1 - 1.8 \times 10^{-4} t - 0.57\right) A_{\mathrm{b}} \qquad \text{(absorption)}, \tag{64}$$

$$A_{\mathrm{eff}} = \left(-4.8 \times 10^{-5} t + 0.19\right) A_{\mathrm{b}} \qquad \text{(desorption)}, \tag{65}$$

where t is the time and A_{b} is the total surface area between gas bubbles and the metal bath. The employed equation for the equilibrium nitrogen content (Eq. 66) represents a regression equation of the results obtained using the FactSage thermodynamic software.

$$[\%\mathrm{N}]_{\mathrm{e}} = \Big[\left(-11.786 y^2_{[\mathrm{Cr}]} + 1.8136 y_{[\mathrm{Cr}]} - 0.2325\right) y_{[\mathrm{Ni}]} + 9.6786 y^2_{[\mathrm{Cr}]} - 1.1532 y_{[\mathrm{Cr}]} + 0.1518 \Big] p^{1/2}_{\mathrm{N_2}}. \tag{66}$$

3.1.5 Process mechanism models

Process mechanism models assume that chemical reactions take place only at the reaction interface, and make use of the boundary layer theory [219] to derive the rate. In

contrast to simple reaction interface models, process mechanism models aim to provide a description of the oxygen–bulk contact mechanism, such as the oxygen impact area and shape and oxygen–bulk contact time [27]. The process mechanism models often account for several reaction resistances; the overall resistance is then similar to resistors in series as suggested by the Lewis-Whitman film theory [233]. In many cases, the interfacial area is calculated using experimental correlations or simplistic mathematical models to avoid excess complexity. In principle, the reaction interface can also be calculated with the control volume method provided that the interface is tracked (see *e.g.* [234–236]).

Sjöberg (1994)

Sjöberg [209] proposed a reaction model for bottom- and side-blowing stainless steelmaking converters.[12] The model included descriptions for decarburisation, reduction of slag, and desulphurisation. The description of the reduction and desulphurisation model is provided along with other reaction equilibrium models in Section 3.1.2 (p. 59) and is not repeated here. As for the decarburisation stage, the total amount of carbon removed during a time step was calculated as follows:

$$n_{\mathrm{[C],\,tot}} = \underbrace{n_{\mathrm{[C],tuyère}}}_{\substack{\text{tuyère}\\ \text{zone}}} + \underbrace{\int_0^{H_0} \left(\frac{\mathrm{d}n_{\mathrm{[C],plume}}}{\mathrm{d}h}\right)_h \mathrm{d}h}_{\substack{\text{gas plume}\\ \text{above the tuyères}}} . \tag{67}$$

The first term on the right-hand side of Eq. 67 describes the oxidation of carbon at the tuyère zone, in which oxygen was assumed be consumed by C, Cr, Mn, Si, and Fe proportional to their molar concentration in the metal bath. The second term on the right-hand side of Eq. 67 expresses the decarburisation rate (mol/m) at height h above the tuyère and is defined according to Eq. 68.

$$\left(\frac{\mathrm{d}n_{\mathrm{[C],plume}}}{\mathrm{d}h}\right)_h = -k_\alpha \left[\frac{(n_{\mathrm{CO},h} + n_{\mathrm{inert}})RT}{p_{\mathrm{tot},h}}\right]^{5/12} \cdot \left[1 + k_\beta \frac{p_{\mathrm{tot},h}^{13/12}}{T^{7/12}} \frac{1}{(n_{\mathrm{CO},h} + n_{\mathrm{inert}})^{1/12}} \frac{1}{K_{\mathrm{CO}} a_{\mathrm{[O]}} f_{\mathrm{[C]}}}\right]^{-1} [\%\mathrm{C}]_{\mathrm{bath}} \left(1 - \frac{p_{(\mathrm{CO,\,B}),h}}{p_{\mathrm{CO,\,e}}}\right), \tag{68}$$

[12] See also the earlier publication by Wijk and Sjöberg [139].

where k_α and k_β are constants to be evaluated based on plant data, $n_{\mathrm{CO},h}$ is the number of moles of CO at height h, n_{inert} is the number of moles of diluting gas at height h, $p_{\mathrm{tot},h}$ is the total pressure at height h, K_{CO} is the equilibrium constant of the reaction $[\mathrm{C}] + \frac{1}{2}\{\mathrm{O_2}\} \rightleftharpoons \{\mathrm{CO}\}$, R is the gas constant, T is the temperature, $a_{[\mathrm{O}]}$ is the activity of dissolved oxygen, $f_{[\mathrm{C}]}$ is the activity coefficient of dissolved carbon, $[\%\mathrm{C}]_{\mathrm{bath}}$ is the carbon content in the metal bath, $p_{(\mathrm{CO,\,B}),h}$ is the partial pressure of carbon monoxide in the gas bulk phase at height h, and $p_{\mathrm{CO,\,e}}$ is the partial pressure of carbon monoxide at equilibrium. The remaining oxygen not consumed by decarburisation ($n_{[\mathrm{O}],\mathrm{rem}}$) was divided between Cr, Mn, Si, and Fe in proportion to their hypothetical driving force:

$$n_{[\mathrm{O}],k} = \frac{\Delta G'_k}{\sum_{k=1}^{r} \Delta G'_k} n_{[\mathrm{O}],\mathrm{rem}} \quad \text{where} \quad \Delta G'_k = K_k \frac{\prod_r a_r^{\nu_r}}{\prod_p a_p^{\nu_p}} \,. \tag{69}$$

The activity coefficients of the species in the metal phase were determined according to the Wagner formalism. The activity of silica was determined according to a regression equation, while the activities of the other oxides were taken as unity. The behaviour of nitrogen in the AOD vessel was defined through the concept of *nitrogen removal efficiency* (NRE), which was defined as a function of dissolved oxygen and sulphur contents:

$$\mathrm{NRE} = (1 + 28.4 \cdot [\%\mathrm{O}] + 5.34 \cdot [\%\mathrm{S}])^{-2} \,. \tag{70}$$

In comparison to the models proposed before it, the model proposed Sjöberg [209] was arguably the first to provide a comprehensive description of the entire side-blowing AOD process by combining a decarburisation model with nitrification, reduction, and desulphurisation sub-models. However, it did not provide a description for top-blowing. The original model evolved later into two commercial models: *TimeAOD* [237] and *UTCAS* [238]. The latest version of the TimeAOD model (TimeAOD2) is coupled with the ThermoCalc® thermodynamic software [237]. Detailed descriptions of these models, however, are not available in the open literature.

Wei and co-authors (2002/2007/2011)

In 2002, Wei and Zhu [49, 239] proposed a reaction model for side-blowing operations. Two sets of reaction equilibria were considered: Eqs. 71–74 describe the reactions with FeO as an oxidant, while Eqs. 75–78 describe the decarburisation reactions.

$$[\mathrm{C}] + (\mathrm{FeO}) \rightleftharpoons \{\mathrm{CO}\} + [\mathrm{Fe}]\,. \tag{71}$$

$$2[\mathrm{Cr}] + 3(\mathrm{FeO}) \rightleftharpoons (\mathrm{Cr_2O_3}) + 3[\mathrm{Fe}]\,. \tag{72}$$

$$[\mathrm{Si}] + 2(\mathrm{FeO}) \rightleftharpoons (\mathrm{SiO_2}) + 2[\mathrm{Fe}]\,. \tag{73}$$

$$[\mathrm{Mn}] + (\mathrm{FeO}) \rightleftharpoons (\mathrm{MnO}) + [\mathrm{Fe}]\,. \tag{74}$$

$$(\mathrm{FeO}) + [\mathrm{C}] \rightleftharpoons [\mathrm{Fe}] + \{\mathrm{CO}\}\,. \tag{75}$$

$$(\mathrm{Cr_2O_3}) + 3[\mathrm{C}] \rightleftharpoons 2[\mathrm{Cr}] + 3\{\mathrm{CO}\}\,. \tag{76}$$

$$(\mathrm{SiO_2}) + 2[\mathrm{C}] \rightleftharpoons [\mathrm{Si}] + 2\{\mathrm{CO}\}\,. \tag{77}$$

$$(\mathrm{MnO}) + [\mathrm{C}] \rightleftharpoons [\mathrm{Mn}] + \{\mathrm{CO}\}\,. \tag{78}$$

The distribution of blown oxygen among the elements in the metal matrix was based on the Gibbs free energies of their oxidation reactions at the interface. The distribution ratio of oxygen to reactant i was defined according to

$$x_i = \frac{\frac{1}{\nu_{i,\mathrm{O}}}\Delta G_i}{\Delta G_{[\mathrm{C}]} + \frac{1}{3}\Delta G_{[\mathrm{Cr}]} + \frac{1}{2}\Delta G_{[\mathrm{Si}]} + \Delta G_{[\mathrm{Mn}]}}\,, \tag{79}$$

where ΔG is the Gibbs free energy and $\nu_{i,\mathrm{O}}$ is the stoichiometric coefficient of oxygen in the oxide of species i. The activities of species in the liquid metal were calculated using the WLE formalism, while the activities of the slag species were calculated using an empirical slag model, which was based on the slag model proposed in [240]. Later, the model was extended with a description for top-blowing [137, 241]. Two reaction areas were defined under the following assumptions:

1. Reactions between the top-blown gas and the metal bath were assumed to occur both on the interface of the cavity and on the surface of the splashing metal droplets. Moreover, it was assumed that the geometry of the cavity corresponds to a paraboloid of revolution and that the volume of the metal droplets equals the displaced volume of the cavity. The cavity depth and radius correlations were taken from [242] and [243], respectively. The surface area of the metal droplets was calculated by determining the average size of a single droplet, which was employed as a fitting parameter.
2. Reactions between the side-blown gas and the metal bath were assumed to occur on the interface of the rising gas bubbles and the surrounding molten steel. The average bubble size was taken from [85].

The decarburisation rate was defined separately for high and low carbon regions:

$$\frac{\mathrm{d}[\%\mathrm{C}]}{\mathrm{d}t} = \begin{cases} -\dfrac{100M_\mathrm{C}}{m_\mathrm{bath}} \dfrac{2\left(\eta_1 \dot{V}_\mathrm{G,tuyère} + (\eta_2 - \eta_\mathrm{CO})\dot{V}_\mathrm{G,lance}\right)}{22400} x_{[\mathrm{C}]} & \text{if} \quad [\%\mathrm{C}] > [\%\mathrm{C}]_\mathrm{crit} \\ \underbrace{-\dfrac{A_\mathrm{L–G}}{m_\mathrm{bath}} \rho_\mathrm{L} \beta_{[\mathrm{C}]} \left([\%\mathrm{C}] - [\%\mathrm{C}]_\mathrm{L–G}\right)}_{\text{side-blowing}} & \\ \underbrace{-\dfrac{A_\mathrm{L–S}}{m_\mathrm{bath}} \rho_\mathrm{L} \beta_{[\mathrm{C}]} \left([\%\mathrm{C}] - [\%\mathrm{C}]_\mathrm{L–S}\right)}_{\text{top-blowing}} & \text{if} \quad [\%\mathrm{C}] \leq [\%\mathrm{C}]_\mathrm{crit} \end{cases}, \tag{80}$$

where η_1 is the total utilisation ratio of side-blown oxygen, η_2 is the total utilisation of top-blown oxygen, η_CO is the post-combustion ratio for top-blown oxygen, $\dot{V}_\mathrm{G,tuyère}$ is the side-blowing rate, $\dot{V}_\mathrm{G,lance}$ is the top-blowing rate, $A_\mathrm{L–G}$ is the surface area of the molten metal – gas bubble interface, $\beta_{[\mathrm{C}]}$ is the mass transfer coefficient of carbon, $[\%\mathrm{C}]$ is the mass percent of carbon in the metal bath, $[\%\mathrm{C}]_\mathrm{L–G}$ is the mass percent of carbon at the molten metal – gas bubble interface, $A_\mathrm{L–S}$ the surface area of the molten metal – slag interface, and $[\%\mathrm{C}]_\mathrm{L–S}$ is the mass percent of carbon at the molten metal – slag interface. At both interfaces, the mass transfer coefficient of carbon was calculated according to the equation proposed by Baird and Davidson [244]:

$$\beta_{[\mathrm{C}]} = 0.8 r_\mathrm{b}^{-1/4} D_{[\mathrm{C}]}^{1/2} g^{1/4}, \tag{81}$$

where r_b is the equivalent radius of the gas bubble, $D_{[\mathrm{C}]}$ is the mass diffusivity of carbon, and g is the standard acceleration due to gravity. In 2011, Wei *et al.* [245] modified the model with an improved heat analysis and revalidated it with 28 heats. One of the main drawbacks of the model is the necessity to pre-define the oxygen utilisation ratios based on plant data.

Chen and co-authors (2006/2007)

Chen *et al.* [246] modified the model proposed by Wei and Zhu [49, 239] by adding a description for reactions during top-blowing. It was assumed that all the oxidation-reduction reactions took place simultaneously and reached a combined equilibrium at the liquid–gas interface during side-blowing and in the impingement zone during

top-blowing. The distribution of oxygen to the species in the metal bath was calculated based on the Gibbs free energies of the considered reactions. Moreover, it was assumed that the unabsorbed oxygen escaped the bath and formed CO_2 with the CO in the exhaust gas. The decarburisation rate was calculated according to [246]:

$$\frac{\mathrm{d}[\%\mathrm{C}]}{\mathrm{d}t} = \begin{cases} \underbrace{-\frac{200 M_\mathrm{C} \dot{V}_{\mathrm{O}_2} \eta}{22.4 m_\mathrm{bath}} \lambda_{[\mathrm{C}],\text{tuyère}}}_{\text{side-blowing}} \\ \underbrace{-\frac{M_\mathrm{C}}{2 m_\mathrm{bath}} \dot{n}_{[\mathrm{O}]} \lambda_{[\mathrm{C}],\text{lance}}}_{\text{top-blowing}} & \text{if} \quad [\%\mathrm{C}] > [\%\mathrm{C}]_\text{crit} \\ \underbrace{-\frac{1}{2}\left(s_{1,\text{tuyère}} + \sqrt{s_{1,\text{tuyère}}^2 + s_{2,\text{tuyère}}}\right)}_{\text{side-blowing}} \\ \underbrace{-\left(s_{1,\text{lance}} + \sqrt{s_{1,\text{lance}}^2 + s_{2,\text{lance}}}\right)}_{\text{top-blowing}} & \text{if} \quad [\%\mathrm{C}] \leq [\%\mathrm{C}]_\text{crit} \end{cases}, \tag{82}$$

where $\lambda_{[\mathrm{C}],\text{tuyère}}$ and $\lambda_{[\mathrm{C}],\text{lance}}$ are the distribution ratios of oxygen to carbon at the gas–metal interface during side-blowing and in the impingement zone, respectively, η is the oxygen utilisation ratio, and $\dot{n}_{[\mathrm{O}]}$ is the molar transfer rate of oxygen into metal bath. The rate parameters s_1 and s_2 were defined according to Eqs. 83 and 84, respectively.

$$\begin{aligned} s_1 = &-\frac{100 M_\mathrm{C}}{m_\mathrm{bath}} \frac{\dot{V}_{\mathrm{O}_2}(1-\eta) + \dot{V}_\text{inert}}{22400} \\ &+ \frac{A \rho_\mathrm{L} \beta_{[\mathrm{C}]}}{m_\mathrm{bath}} \left[[\%\mathrm{C}] - \frac{p_\mathrm{G}}{f_{[\mathrm{C}]}} \left(\frac{a_{[\mathrm{Cr}]}^2}{a_{(\mathrm{Cr_2O_3})} K_{\mathrm{Cr–C}}} \right)^{1/3} \right], \end{aligned} \tag{83}$$

$$s_2 = 4 \frac{A \rho_\mathrm{L} \beta_{[\mathrm{C}]}}{m_\mathrm{bath}} [\%\mathrm{C}] \frac{100 M_\mathrm{C}}{m_\mathrm{bath}} \frac{\dot{V}_{\mathrm{O}_2}(1-\eta) + \dot{V}_\text{inert}}{22400}, \tag{84}$$

where $\dot{V}_\text{inert}$ is the volumetric flow rate of inert gases, A is the reaction area, $K_{\text{Cr-C}}$ is the equilibrium constant,[13] and p_G is the total pressure of gas in a bubble. During the reduction stage, the reduction rate of oxide i by species j in the metal bath was calculated as:

[13] Corresponding to reaction $3[\mathrm{C}] + (\mathrm{Cr_2O_3}) \rightleftharpoons 3\{\mathrm{CO}\} + 2[\mathrm{Cr}]$.

$$\frac{\mathrm{d}(\%i)}{\mathrm{d}t} = -\frac{M_i A \rho_\mathrm{L}}{100 m_\mathrm{slag}} \sum_j \left[\frac{z_{MO_{z,j}} \beta_j}{M_j} \left([\%j] - [\%j]_{j-i,\mathrm{eq}} \right) R_{i,j} \right] , \tag{85}$$

where $R_{i,j}$ is the ratio of species i to be reduced by species j. The model proposed by Chen *et al.* [246] also featured a description for absorption and removal of nitrogen; a detailed description of this model is found in [247]. Two possible limiting steps for nitrogen absorption were accounted for: mass transfer of nitrogen in the boundary layer and the chemical reaction at the reaction interface [246]. At equilibrium, the reaction rates of both mechanisms were considered to be equal and the total absorption rate was obtained from Eq. 86 [246].

$$\left(\frac{\mathrm{d}[\%\mathrm{N}]}{\mathrm{d}t} \right)_\mathrm{absorption} = -\frac{1}{\left(\dfrac{1}{\beta_{[\mathrm{N}]}} + \dfrac{1}{k_{[\mathrm{N}],\mathrm{dis}}} \right)} \left(\frac{A}{V_\mathrm{bath}} \right) \left([\%\mathrm{N}] - [\%\mathrm{N}]_\mathrm{e} \right) , \tag{86}$$

where $\beta_{[\mathrm{N}]}$ is the mass transfer coefficient of nitrogen in the boundary layer, $k_{[\mathrm{N}],\mathrm{dis}}$ is the velocity constant of the nitrogen dissolution reaction, and V_bath is the volume of the metal bath. As with the absorption of nitrogen, the mass transfer of nitrogen in liquid metal and the chemical reaction rate at the interface were considered as two limiting steps for the nitrogen removal rate [246]:

$$\begin{aligned} \left(\frac{\mathrm{d}[\%\mathrm{N}]}{\mathrm{d}t} \right)_\mathrm{removal} &= -\beta_{[\mathrm{N}]} \left(\frac{A}{V_\mathrm{bath}} \right) \\ &\cdot \left[[\%\mathrm{N}] + \frac{1}{2k_{[\mathrm{N}],\mathrm{dis}}} \left(\beta_{[\mathrm{N}]} - \sqrt{\beta_{[\mathrm{N}]}^2 + 4k_{[\mathrm{N}],\mathrm{dis}} \left(\beta_{[\mathrm{N}]} [\%\mathrm{N}] + k_{[\mathrm{N}],\mathrm{dis}} [\%\mathrm{N}]_\mathrm{e}^2 \right)} \right) \right] . \end{aligned} \tag{87}$$

The description for the velocity constant of the nitrogen dissolution reaction was taken from Ban-Ya *et al.* [248]:

$$k_{[\mathrm{N}],\mathrm{dis}} = \frac{9}{1 + 300 a_{[\mathrm{O}]} + 130 a_{[\mathrm{S}]}} , \tag{88}$$

where $a_{[\mathrm{O}]}$ and $a_{[\mathrm{S}]}$ are the activities of dissolved oxygen and dissolved sulphur, respectively.

Järvinen and co-authors (2009)

Järvinen *et al.* [249] proposed a bubble model for a single gas bubble in the metal bath. The model considered the oxidation reactions of Fe, C, Cr, Mn, and Si as well as the

dissolution reaction of O_2. The system of conservation equations was solved using a control volume method by dividing the gas bubble and surrounding metal bath into small cells in a radial direction. The conservation equations for mass, species, and energy were expressed according to Eqs. 89, 90, and 91, respectively.

$$\underbrace{\frac{\partial \rho}{\partial t}}_{\substack{\text{temporal}\\ \text{change}}} = -\frac{1}{r^2}\frac{\partial}{\partial r}\underbrace{\left(u\rho r^2\right)}_{\text{advection}}, \tag{89}$$

$$\underbrace{\frac{\partial y_i}{\partial t}}_{\substack{\text{temporal}\\ \text{change}}} = -\frac{1}{r^2}\frac{\partial}{\partial r}\left(\underbrace{u r^2 y_i}_{\text{advection}} - \underbrace{D_i r^2 \frac{\partial y_i}{\partial r}}_{\text{diffusion}}\right), \tag{90}$$

$$\underbrace{\rho c_\mathrm{p}\frac{\partial T}{\partial t}}_{\substack{\text{temporal}\\ \text{change}}} = -\frac{1}{r^2}\frac{\partial}{\partial r}\left(\underbrace{u\rho r^2 h}_{\text{advection}} - \underbrace{\lambda r^2 \frac{\partial T}{\partial r}}_{\text{conduction}}\right), \tag{91}$$

where u is the mass-averaged velocity and h is the specific enthalpy. The model employed a law of mass action based method for the treatment of parallel mass transfer controlled reactions. The activity coefficients of the liquid species were calculated using the Wagner formalism and the variation of the gas pressure was taken into account by summing the ferrostatic pressure and surface tension force, while ignoring inertial and viscous forces.

The results of the study illustrated the transient and local chemical rate phenomena both inside and outside the gas bubble during decarburisation. The model captures the effect of the oxygen content of the gas bubble on the selectivity of oxygen. Furthermore, the model automatically accounts for the variations in the thickness and composition of the gas- and liquid-side diffusion boundary layers.

Wang and co-authors (2010)

Wang *et al.* [250] proposed a model for reactions between gas bubbles and the metal bath. The model was applied for an experimental setup, in which oxygen was injected through a submerged lance into liquid metal containing C and Cr [250, 251]. The molar rate of the mass transfer (mol/s) of species i in phase ψ was formulated according to

$$\dot{n}_i = \frac{\beta_i \rho_\psi A}{100 M_i} \left([\%i] - [\%i]^* \right) = \beta_i A \left(c_i - c_i^* \right) , \tag{92}$$

where A is the reaction area. The mass transfer coefficients for C and Cr in liquid metal were calculated according to the Ranz-Marschall correlation [252, 253]. The same correlation was assumed to be valid also for the gas species. It should be noted that because the Ranz-Marschall correlation is applicable for viscous mass transfer around rigid spheres, it is likely to underestimate the mass transfer rate.

Järvinen and co-authors (2011)

Based on the experiences with the earlier-proposed bubble model [249], Järvinen *et al.* [44] proposed a new model for reactions during side-blowing. In comparison to other models proposed in the literature, their model provides a more detailed description of the local chemical rate phenomena during side-blowing. In particular, it accounts for the vertical variation of properties.

All the reactions during side-blowing were assumed to take place in the gas plume, which was modelled as a three-phase *plug flow reactor* (PFR). The PFR was divided into a predefined number of computational cells in the vertical direction. Here, the considered reactions included the oxidation of Fe, C, Cr, Mn, and Si as well as the dissolution of O_2. After leaving the gas plume, the three phases separate so that the gas phase exits the system, the metal phase returns to the metal bath, and the slag phase is deposited in the top slag. The metal bath was represented by a *continuous stirred tank reactor* (CSTR), in which the steel composition and temperature are homogenised at every time step.

In the PFR, gas, metal, and slag phases rise from lowest to highest cell. In each cell, the gas, metal, and slag species establish a joint equilibrium at the surface of the rising gas bubbles. The main properties, including the compositions and temperatures as well as thermodynamic and transport properties, were determined locally in each cell. Owing to vertical discretisation, the effect of varying ferrostatic pressure is also accounted for. The conservation of species i in the gas plume was expressed according to

$$\frac{\mathrm{d}m_i}{\mathrm{d}t} = \underbrace{\int_{z=0}^{h} S_i(z) S_\mathrm{a}(z) \, \mathrm{d}V}_{\text{analytic form}} \approx \underbrace{\sum_{\omega} S_{i,\omega} S_{\mathrm{a},\omega} V_\omega}_{\text{discretised form}} , \tag{93}$$

where $S_{i,\omega}$, $S_{\mathrm{a},\omega}$, and V_ω denote the source term of species i, the specific reaction

area, and the volume in cell ω, respectively. The conservation of species i in cell ω was determined according to

$$\underbrace{m''_{i,\omega}}_{\text{mass flux}} + \underbrace{S_{i,\omega}}_{\text{reactions}} = 0\,, \tag{94}$$

where $m''_{i,\omega}$ is the mass flux of species i in cell ω, which was determined according to

$$m''_{i,\omega} = \sum_{\psi} \Gamma_{i,\psi} \left(\underbrace{m''_{\psi,\omega} \frac{y_{i,\omega}}{y_{\psi,\omega}}}_{\text{bulk motion}} + \underbrace{\beta_{\psi,\omega} \rho_{\psi,\omega} \frac{(y_{i,\omega} - y^*_{i,\omega})}{y_{\psi,\omega}}}_{\text{mass transport}} \right), \tag{95}$$

where ψ denotes the phase, and m'', y, β, ρ, and y^* are the net mass flux, mass fraction, mass transfer coefficient, density, and interfacial mass fraction, respectively. $\Gamma_{i,\psi}$ is a binary operator, which is 1 if species i is present in phase ψ and otherwise zero. The source terms of species in cell ω were determined according to

$$S_{i,\omega} = \sum_{k=1}^{r} R''_{k,\omega} \overline{\nu}_{i,k}\,, \tag{96}$$

where R'' is the reaction rate and $\overline{\nu}_{i,k}$ is the mass-based stoichiometric coefficient. The reaction rate fluxes were determined according to the law of mass action based method described in Chapter 5 (p. 133). The numerical solution is obtained with a Newton-like method, in which derivatives are determined only with respect to the free variables themselves. The activity coefficients of species in the metal and slag phases were calculated employing the *unified interaction parameter* (UIP) formalism [254] and the activity model presented by Wei and Zhu [49], respectively. The adsorption and desorption of nitrogen were taken into account by employing a sub-model proposed by Riipi *et al.* [138].

In later work, the model was employed for studying conditions in the gas plume by Järvinen *et al.* [255] and Visuri *et al.* [256]. Their results suggest that most of the oxidising reactions near the tuyères, where the partial pressure of oxygen is the highest [255, 256]. Similarly, the removal rate of nitrogen was found to be higher deeper in the metal bath [255]. The temperature drop induced by additions of slag formers and scrap was found to reduce the rate of decarburisation [256]. Subsequently, the model has been improved with detailed descriptions for physical properties.

Patra and co-authors (2017)

Patra *et al.* [135] proposed a mathematical model for predicting of the nitrogen content in the AOD process. The description of the main oxidation and reduction reactions was adopted from Wei and Zhu [49]. A kinetic sub-model was derived for predicting the nitrogen content of the metal bath. The solubility of nitrogen in Fe–Cr and Fe–Cr–Mn alloys was calculated based on the WLE formalism, while a regression equation proposed by Riipi *et al.* [138] was employed for calculating the equilibrium nitrogen content in Fe–Cr–Ni alloys. Likewise, the kinetic description for the absorption and desorption rate of nitrogen was adopted from Riipi *et al.* [138]. Similarly to Riipi *et al.* [138], the effective surface area for nitrogen absorption and desorption were calculated according to Eqs. 64 and 65, respectively (see p. 73).

Certain criticisms arise from the modelling assumptions related to the use of Eqs. 64 and 65. Firstly, Patra *et al.* [135] did not take into account that that Eqs. 64 and 65 are simple regression equations, which are strictly applicable only for the data of Riipi *et al.* [138]. Secondly, the value of the total surface area A was taken from CFD calculations specific to a 150 t AOD vessel [212], although Patra *et al.* [135] studied a much smaller vessel with a nominal capacity of 50 t.

3.1.6 Machine learning models

Machine learning models employ learning algorithms for solution of an optimisation problem. The algorithm can be based, for example, on biological neural networks (artificial neural networks) or natural selection (generic algorithms) [257]. Unlike statistical models, machine learning models do not rely on rules-based programming.

Deo and Srivastava (2003)

Deo and Srivastava [258] developed a control model for the low-carbon regime of the decarburisation stage in the AOD process. The reaction model was based on two main assumptions: 1) the decarburisation rate is controlled by the Cr_3O_4 present in the top slag, and 2) all the oxygen left after the decarburisation reaction is consumed by chromium. Fitting parameters α, β, and κ were incorporated in the expressions for the decarburisation rate, chromium oxidation rate, and cooling rate, respectively. As a novel feature, the parameters α, β, and κ were optimised for plant data by a genetic algorithm.

The main assumptions of the employed optimisation routine can be summarised as follows:

– The objective function for the genetic algorithm was written so that carbon, chromium, and temperature terms have approximately equal weighting.
– A Roulette wheel method for probabilistic generation was used as a selection procedure.
– The structures were treated as rings, choosing two crossover points and exchanging the section between these points.
– The initial population was taken as 100 and the gene length was 30.

Deo and Kumar (2013)

Deo and Kumar [259] compared three separate approaches to create a dynamic control model of the AOD process. The employed models were as follows:

1. a linear regression model, which was derived by statistical analysis of the plant data. The input variables were selected through backward elimination,
2. an *artificial neural network* (ANN) model, which was created by selection of appropriate input variables through training exercises, pre-processing of the data in order to assess the extent of coverage of training data and designing the optimal neural network architecture through training and learning exercises, and
3. a dynamic model, which was based on the main assumption that all blown oxygen oxidises dissolved C, Cr, Si, and Mn simultaneously and that the rate of decarburisation is controlled by the mass transfer of carbon in the metal bath. The mass transfer rate of carbon was related to the combined inert gas flow rate and CO production by two kinetic parameters, which were determined with a genetic algorithm so that the resulting prediction error was minimised. Moreover, it was assumed that the composition and temperature of the metal bath are uniform at every instant and that all the Si is oxidised during the first decarburisation period.

3.2 Summary and statistical comparison

A summary of the studies on the modelling of reactions in the AOD process is presented in Table 10 (p. 86–87). It can be seen that the principal subject of interest in the early as well as later modelling studies has been the decarburisation stage.

The main reaction product of the decarburisation reaction is carbon monoxide, which may react further to carbon dioxide. However, injected oxygen does not react only with carbon, but also with other dissolved elements, particularly chromium. Therefore, it is necessary to consider multiple reactions in order to achieve a sufficient accuracy in predicting the changes in the carbon content. For this aim, virtually all of the proposed models have relied on established thermodynamic principles for determining the driving force. As the observed reactions are controlled mainly by mass transport, the understanding of the related transport phenomena and physical properties is of great importance [9]. This is reflected as a general trend towards more complex models, which are based on the actual physico-chemical phenomena taking place in the vessel. A similar trend towards more detailed models has been reported by Ma *et al.* [260].

Table 10. Summary of studies on modelling of reactions in converter processes for stainless steelmaking.

			Gas injection		Studied phenomena				
Year	Study	Type	Top	Side	Decarb.	Post-comb.	Nitrification	Reduction	Desulph.
1973	Watanabe and Tohge [221]	SRIM	X	X	X	–	–	–	–
1974	Asai and Szekely [191, 192]	SRIM	X	X	X	–	–	–	–
1975	Fruehan [222]	SRIM	–	X	–	–	X	–	–
1976	Fruehan [143]	SRIM	–	X	X	–	–	–	–
1977	Ohno and Nishida [193]	SRIM	–	X	X	–	–	–	–
1977	Fruehan [223]	SRIM	–	X	X	–	–	–	–
1978	Deb Roy *et al.* [225, 227]	SRIM	–	X	X	–	–	–	–
1983	Semin *et al.* [207]	REM	–	X	X	–	–	–	–
1984	Tohge *et al.* [111]	SRIM	X	X	X	–	–	–	–
1994	Vercruyssen *et al.* [37]	SRIM	X	X	X	–	–	X	–
1994	Sjöberg [209]	PMM	–	X	X	–	X	X	X
1995	Reichel and Szekely [26]	SRIM	X	X	–	–	–	–	–
1996	Scheller and Wahlers [134]	SRIM	X	X	–	–	X	–	–
1999	Görnerup and Sjöberg [159]	SREM	–	X	–	–	–	X	X
2002	Wei and Zhu [49, 239]	PMM	X	X	X	–	–	X	–
2002	Kikuchi *et al.* [210]	REM	X	X	X	–	–	X	–
2003	Deo and Srivastava [258]	MLM	–	X	X	–	–	–	–
2003	Teng *et al.* [261]	SRIM	X	X	X	–	–	X	–
2004	Tang *et al.* [77]	FVRM	–	X	–	–	X	–	–

FVRM = finite volume reaction model; MLM = machine learning model; PMM = process mechanism model; REM = reaction equilibrium model; SFEMM = system free energy minimisation model; SM = statistical model; SRIM = simple reaction interface model.

Table 10. (Continued)

Year	Study	Type	Gas injection		Studied phenomena				
			Top	Side	Decarb.	Post-comb.	Nitrification	Reduction	Desulph.
2006/2007	Kleimt *et al.* [230–232]	SRIM	X	X	X	–	X	X	–
2006/2007	Chen *et al.* [246, 247]	SRIM	X	X	X	–	X	X	–
2007	Zhu *et al.* [137, 144]	PMM	X	X	X	–	–	X	–
2008	Kärnä *et al.* [212]	FVRM	–	X	–	–	X	–	–
2008	Engholm *et al.* [238]	SRIM	–	X	X	–	–	–	–
2008	Ternstedt *et al.* [237]	SRIM	–	X	X	–	–	–	–
2009	Järvinen *et al.* [249]	PMM	–	X	X	–	–	–	–
2009	Riipi *et al.* [138]	SRIM	–	–	–	–	X	–	–
2010	Wang *et al.* [251]	PMM	–	X	X	–	–	–	–
2011	Wei *et al.* [245]	PMM	X	X	X	–	–	X	–
2011	Järvinen *et al.* [44, 45]	PMM	–	X	X	–	X	–	–
2012	Swinbourne *et al.* [145]	SFEMM	X	X	X	–	–	X	–
2012/2013	Andersson *et al.* [213–216]	FVRM	–	X	X	–	–	–	–
2013	Visuri *et al.* [262, 263]	PMM	–	X	–	–	–	X	–
2013	Deo and Kumar [259]	MLM	X	X	X	–	–	X	–
2014	Song *et al.* [75]	FVRM	–	X	–	X	–	–	–
2017	Patra *et al.* [135]	PMM	–	X	X	–	X	X	–
2017	Visuri *et al.* [136, 264]	PMM	X	X	X	–	–	–	–

FVRM = finite volume reaction model; MLM = machine learning model; PMM = process mechanism model; REM = reaction equilibrium model; SFEMM = system free energy minimisation model; SM = statistical model; SRIM = simple reaction interface model.

A statistical analysis of the model predictions was conducted in order to provide a comparison of the models. The employed statistical indicators consist of a correlation coefficient (R^2), root-mean-square error (RMSE), and mean absolute error (MAE), which were calculated according to Eqs. 97, 98, and 99, respectively [265]. It should be noted that the expression given in Eq. 97 defines R^2 as the square of the Pearson product-moment correlation coefficient.

$$R^2 = \left[\frac{\sum_{i=1}^{n} (f_i - \overline{f})(y_i - \overline{y})}{\sqrt{\sum_{i=1}^{n} (f_i - \overline{f})^2 (y_i - \overline{y})^2}} \right]^2 , \tag{97}$$

$$\mathrm{RMSE} = \sqrt{\frac{1}{n} \sum_{i=1}^{n} (y_i - f_i)^2} , \tag{98}$$

$$\mathrm{MAE} = \frac{1}{n} \sum_{i=1}^{n} |y_i - f_i| , \tag{99}$$

where f_i is the predicted variable, $\overline{f}$ is the mean of the predicted variables, y_i is the measured variable, and $\overline{y}$ is the mean of the measured variables.

The model proposed by Fruehan [143] was validated with metal samples from the manufacturing of 409 grade stainless steel. Considering the simplicity of the model, the predictions agreed well with the measured values. As for Deb Roy *et al.* [227], the decarburisation data included an initial sample, two intermediary samples and a final sample for each heat. As seen from Table 11, the predicted carbon contents are in reasonably good agreement with the measured values. The absolute error in predicted carbon contents decreases as the carbon content decreases, while the opposite is true for the relative error. The absolute errors in the predicted chromium content and bath temperature are virtually independent from the carbon content. The model by Semin *et al.* [207] was validated using five heats from the experimental data published by Deb Roy *et al.* [227]. As seen from Table 11, the statistical agreement is comparable to that of the model proposed by Deb Roy *et al.* [227].

The model by Vercruyssen *et al.* [37] was validated against measurement data from a 100 t MRP converter. The oxygen was injected via a top lance at a rate of 1.6 $\mathrm{Nm^3/(min{\cdot}t)}$, while inert gas (nitrogen or argon) was injected via porous plugs at a rate of 0.03 $\mathrm{Nm^3/(min{\cdot}t)}$. The mass transfer coefficients and interfacial areas were defined as follows: $\beta_\mathrm{L} = 1.5 \cdot 10^{-4}$ m/s, $\beta_\mathrm{S} = 1 \cdot 10^{-4}$ m/s, $\beta_\mathrm{G} = 0.1$ m/s, $A_{\mathrm{L–S}} = 200$ m^2, $A_{\mathrm{L–G}} =$

100 m^2, and $A_{S–G}$ = 100 m^2. The predictions were in very good agreement with the measured metal bath composition and temperature.

The model proposed by Sjöberg [209] was validated with production data from a 58 t converter. Table 11 shows the calculated statistical indicators for the model predictions. The extension for desulphurisation proposed by Görnerup and Sjöberg [159] was validated with ten heats. The MAE of the predicted sulphur content was approximately 6 ppm, which represents a satisfactory degree of accuracy.

The model by Wei and Zhu [239] was validated with production data from an 18 t AOD vessel. As seen in Table 11, the predicted carbon contents and bath temperatures are in excellent agreement with the measured values. The improved model, which featured a description for top-blowing, was validated with the design specifications of a 120 t AOD converter [144, 241]. The further improved model by Wei *et al.* [245] was validated with 28 heats, for which steel samples were taken after the decarburisation stage and after the reduction stage. The predicted carbon content and bath temperature are in excellent agreement with the measured values and in this regard the model is more accurate than most reaction models proposed for the AOD process. The predicted chromium content exhibits more variation.

The model proposed by Kleimt *et al.* [230–232] was validated with samples from the medium-to-high ($[\%C] \geq 0.1$ wt-%) and low carbon regions ($[\%C] < 0.1$ wt-%). Based on validation with industrial heats, it was reported that the standard deviation of error in the predicted end carbon content was 0.011 wt-% when $[\%C] < 0.1$ and 0.135 wt-% when $[\%C] > 0.1$ wt-%. The standard deviation of error in the predicted bath temperature was 16.5 K.

The model proposed by Järvinen *et al.* [44] was validated by Pisilä *et al.* [45] with industrial data from two AOD converters with nominal capacities of 95 and 150 tonnes, respectively. The validation data considers the last side-blowing decarburisation step, in which the initial carbon content is typically in the order of 0.1–0.2 wt-%. The agreement of the model predictions with the measured values of carbon and chromium was reasonably good (see Table 11). However, the predicted carbon contents were consistently above the measured values, while the predicted chromium contents were higher than the measured values. In some experiments, a period of argon-blowing was conducted prior to the studied decarburisation stage and it was found that the top slag can oxidise carbon in the metal bath. Therefore, it is likely that part of the deviation can be attributed to the fact that reactions between the top slag and metal bath were not considered by the model.

A comparison of the statistical indicators for the three models studied by Deo and Kumar [259] are shown in Table 11. In the first decarburisation stage, the R^2 and the RMSE were the largest for the ANN model and the lowest for the dynamic model. Except for temperature, the best overall accuracy in the second decarburisation stage was obtained with the dynamic model, although the results of all the models are relatively good. In the third decarburisation stage, the highest R^2 and RMSE values were obtained with the linear regression and ANN models.

The model proposed by Patra *et al.* [135] was validated with production data obtained from a 50 t AOD converter equipped with a top lance and five tuyères. The employed data covers steel grades 304L, 204Cu, and 18Cr–18Mn–0.5N; the measured final nitrogen contents of these grades were approximately 440–550 ppm, 1600–1900 ppm, and 5000–5800 ppm, respectively. As can be seen in Table 11, the agreement between the predicted and measured nitrogen contents was better in the case of steel grades 304L and 204Cu than in the case of 18Cr–18Mn–0.5N.

Table 11. Statistical indicators for the predictions.

	Range of studied variables				Statistical indicators			
Stage	Variable	Start	End	Unit	*n*	R^2	RMSE	MAE
Fruehan [143]								
D	[C]	0.8 – 1.2	0.07 – 0.6	wt-%	56	0.89	0.042	0.031
Deb Roy *et al.* [227]								
D	[C]	0.8 – 1.2	0.2 – 0.5	wt-%	6	0.63	0.089	0.076
	[Cr]	16.7 – 17.8	16.1 – 17.5	wt-%	6	0.74	0.27	0.25
	T	1708 – 1778	1913 – 1963	wt-%	6	0.64	12.4	11.2
D	[C]	0.2 – 0.5	0.1 – 0.2	wt-%	6	0.22	0.028	0.024
	[Cr]	16.1 – 17.5	15.9 – 17.2	wt-%	6	0.83	0.30	0.23
	T	1913 – 1963	1975 – 2003	wt-%	6	0.01	23.0	16.3
D	[C]	0.1 – 0.2	0.03 – 0.05	K	6	0.06	0.020	0.016
	[Cr]	15.9 – 17.2	15.5 – 17.1	K	6	0.57	0.35	0.23
	T	1975 – 2003	1998 – 2023	K	6	0.11	17.9	13.3
Semin *et al.* [207]								
D	[C]	0.8 – 1.2	0.2 – 0.5	wt-%	5	0.51	0.078	0.056
	[Cr]	16.7 – 17.8	16.1 – 17.4	wt-%	5	0.80	0.37	0.31
	T	1708 – 1778	1913 – 1963	K	5	0.90	11.5	10.6
D	[C]	0.2 – 0.5	0.1 – 0.2	wt-%	5	0.27	0.032	0.028
	[Cr]	16.1 – 17.4	15.9 – 17.1	wt-%	5	0.65	0.26	0.20
	T	1913 – 1963	1975 – 2003	K	5	0.10	19.8	16.4
D	[C]	0.1 – 0.2	0.03 – 0.05	wt-%	5	0.31	0.022	0.019
	[Cr]	15.9 – 17.1	15.5 – 16.6	wt-%	5	0.78	0.21	0.19
	T	1975 – 2003	1998 – 2013	K	5	0.38	32.5	31.2
Vercruyssen *et al.* [37]								
D	[C]	1.8	0.24	wt-%	1	–	0.004	0.004
	[Cr]	18.7	16.6	wt-%	1	–	0.03	0.03
	[Si]	0.3	0.05	wt-%	1	–	0.03	0.03
	T	1786	2012	K	1	–	1.4	1.4
R	[C]	0.24	0.22	wt-%	1	–	0.008	0.008
	[Cr]	16.6	17.8	wt-%	1	–	0.01	0.01
	[Si]	0.05	0.05	wt-%	1	–	0.02	0.02
	T	2012	1950	K	1	–	2.9	2.9
Sjöberg [209]								
D+R	[C]	–	0.01 – 0.4	wt-%	37	0.94	0.025	0.021

Notes: D = decarburisation; R = reduction.

Table 11. (Continued)

	Range of studied variables				Statistical indicators			
Stage	Variable	Start	End	Unit	*n*	R^2	RMSE	MAE
Görnerup and Sjöberg [159]								
R	[S]	–	5 – 43	ppm	10	0.78	6.8	5.6
Wei and Zhu [239]								
D	[C]	–	0.1 – 0.2	wt-%	32	0.99	0.004	0.003
	T	–	1945 – 2046	K	32	0.95	8.2	6.8
D	[C]	0.1 – 0.2	0.03 – 0.06	wt-%	32	1.00	0.001	0.001
	T	1945 – 2046	2013 – 2067	K	32	0.97	3.8	2.6
Kleimt *et al.* [230]								
D	[C]	–	0.1 – 0.5	wt-%	26	0.38	0.137	0.119
		–	0.005 – 0.08	wt-%	24	0.99	0.011	0.009
Kärnä *et al.* [212]								
D+R	[N]	380	290	ppm	1	–	27	27
Wei *et al.* [245]								
D	[C]	–	0.04 – 0.2	wt-%	28	1.00	0.003	0.002
	[Cr]	–	14.6 – 17.9	wt-%	28	0.94	0.19	0.12
	T	–	1927 – 2056	K	28	0.98	5.5	3.0
D+R	[C]	0.04 – 0.2	0.03 – 0.06	wt-%	28	1.00	0.000	0.000
	[Cr]	14.6 – 17.9	15.93 – 20.0	wt-%	28	0.60	0.44	0.17
	T	1927 – 2056	1974 – 2062	K	28	0.97	3.9	2.5
Pisilä *et al.* [45]								
D	[C]	0.1 – 0.2	0.004 – 0.04	wt-%	6	0.83	0.014	0.013
	[Cr]	10.9 – 20.5	9.6 – 18.9	wt-%	6	1.00	0.31	0.25
Deo and Kumar [259], Linear regression model								
D	[C]	2.2	0.4	wt-%	–	0.53	0.42	–
	[Cr]	–	–	wt-%	–	0.36	0.048	–
	[Mn]	–	–	wt-%	–	0.57	0.22	–
	T	–	–	K	–	0.30	17.0	–
D	[C]	0.3 – 0.4	0.11 – 0.15	wt-%	–	0.58	0.037	–
	[Cr]	–	–	wt-%	–	0.77	0.38	–
	[Mn]	–	–	wt-%	–	0.72	0.18	–
	T	–	–	K	–	0.44	15.4	–

Notes: D = decarburisation; R = reduction.

Table 11. (Continued)

	Range of studied variables				Statistical indicators			
Stage(s)	Variable	Start	End	Unit	n	R^2	RMSE	MAE
Deo and Kumar [259], Linear regression model (continued)								
D	[C]	0.10 – 0.15	0.07 – 0.09	wt-%	–	0.52	0.018	–
	[Cr]	–	–	wt-%	–	0.92	0.25	–
	[Mn]	–	–	wt-%	–	0.49	0.14	–
	T	–	–	K	–	0.35	17.2	–
Deo and Kumar [259], Dynamic model								
D	[C]	2.2	0.4	wt-%	–	0.158	0.151	–
	[Cr]	–	–	wt-%	–	0.03	1.67	–
	[Mn]	–	–	wt-%	–	0.00	0.77	–
	T	–	–	K	–	0.10	48.5	–
D	[C]	0.3 – 0.4	0.11 – 0.15	wt-%	–	0.366	0.028	–
	[Cr]	–	–	wt-%	–	0.72	0.40	–
	[Mn]	–	–	wt-%	–	0.66	0.19	–
	T	–	–	K	–	0.05	26.1	–
D	[C]	0.10 – 0.15	0.07 – 0.09	wt-%	–	0.012	0.021	–
	[Cr]	–	–	wt-%	–	0.70	0.38	–
	[Mn]	–	–	wt-%	–	0.29	0.26	–
	T	–	–	K	–	0.00	22.3	–
Deo and Kumar [259], Artificial neural network model								
D	[C]	2.2	0.4	wt-%	–	0.38	0.047	–
	[Cr]	–	–	wt-%	–	0.53	0.34	–
	[Mn]	–	–	wt-%	–	0.44	0.24	–
	T	–	–	K	–	0.54	11.6	–
D	[C]	0.3 – 0.4	0.11 – 0.15	wt-%	–	0.37	0.025	–
	[Cr]	–	–	wt-%	–	0.53	0.40	–
	[Mn]	–	–	wt-%	–	0.11	0.22	–
	T	–	–	K	–	0.35	11.5	–
D	[C]	0.10 – 0.15	0.07 – 0.09	wt-%	–	0.43	0.010	–
	[Cr]	–	–	wt-%	–	0.63	0.36	–
	[Mn]	–	–	wt-%	–	0.30	0.17	–
	T	–	–	K	–	0.40	14.5	–
Patra *et al.* [135]								
D+R	[N]	≈ 500	440 – 548	ppm	10	0.55	19	17
		≈ 300	1625 – 1930	ppm	12	0.92	29	26
		≈ 300	4951 – 5821	ppm	3	0.92	417	213

Notes: D = decarburisation; R = reduction.

4 Review of the treatment of chemical kinetics

In metallurgical processes, reactions such as decarburisation, dephosphorisation, desulphurisation, or nitrogen removal are operated typically far away from their equilibrium [266]. *Chemical rate phenomena* denotes the study of factors, which influence the rates of chemical reactions. The description of the complex chemical rate phenomena is enabled by the knowledge of the individual phenomena, whose theoretical description can be divided into theory of chemical equilibria and theory of transport phenomena [267].

Chemical rate phenomena are induced by the existence of a *driving force*, which seeks to remove potential energy gradients from the system [116, 268]. A distinction can be made between velocity, temperature, and chemical potential gradients [116, 268]; the last category includes concentration gradients, pressure gradients, and external force differences [268]. An equilibrium state is reached when the driving forces vanish. For chemical rate phenomena, the equilibrium of primary interest is the equilibrium of chemical potentials, *i.e.* the chemical equilibrium.

The velocity at which the system moves towards to its equilibrium state is described by *kinetics* [1]. A further distinction is made between *macrokinetics* and *microkinetics* [1, 269, 270]. In the metallurgical context, the term macrokinetics is used to denote the overall kinetics of the observed system [1, 269]. In the case of heterogeneous reactions, microkinetics refers to the rate phenomena, which take place in the velocity, temperature, and concentration boundary layers between phases [1]. In dispersion systems microkinetics describes the kinetics of a single particle, droplet, or bubble [1, 269, 270]. Fig. 13 represents a synthesis of the framework of chemical rate phenomena based on the division between kinetic factors and driving forces.

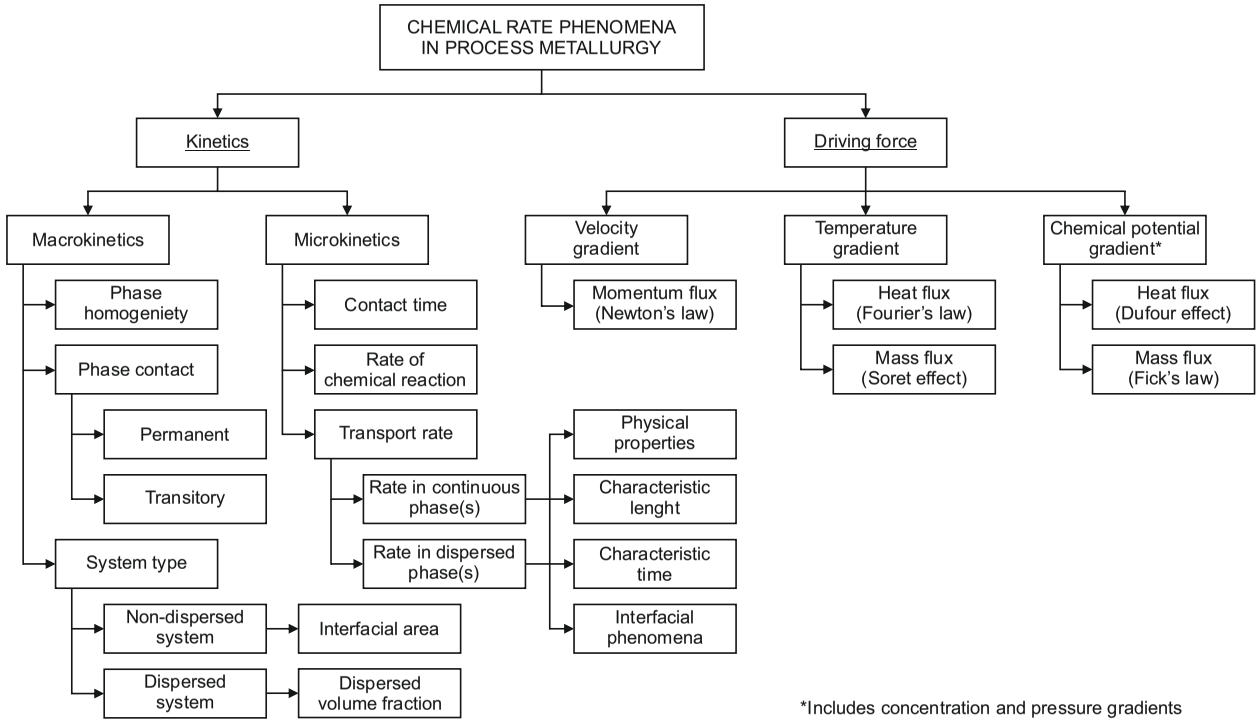

Fig 13. Chemical rate phenomena in process metallurgy.

4.1 Macrokinetics

Arguably the most important macrokinetic factor is the system type, *i.e.* the division into *non-dispersed* and *dispersed* systems [1]. In both cases, a distinction can be made between *permanent* and *transitory* phase contacts [1, 270–273]. Reactions between liquid metal and slag phases take place through a permanent phase contact [1, 270, 272]. On the other hand, gas injection constitutes an example of a transitory phase contact [1, 270, 272]. Transitory phase contact enables a high extraction efficiency, because the extractive phase is completely emulsified and its initial composition is constant [1].

4.1.1 Bath mixing

In reaction modelling, the inhomogeneity of the metal bath can often be ignored provided that large-scale mixing is far more efficient than small-scale mixing [1]. The validity of this assumption is discussed in the following. Assuming first-order kinetics, the average time constant of mixing can be expressed as follows:

$$\bar{k}_{\mathrm{mix}} = -\frac{1}{\bar{t}_{\mathrm{mix}}} \ln \Phi_{\mathrm{mix}} = -\frac{1}{\bar{t}_{\mathrm{mix}}} \ln \left(1 - \mathrm{F}_{\mathrm{mix}}\right) , \tag{100}$$

where Φ_{mix} is the dimensionless gradient, $\bar{t}_{\mathrm{mix}}$ is the average mixing time, and $\mathrm{F}_{\mathrm{mix}}$ is the fractional equilibrium. The dimensionless gradient Φ_{mix} can defined as follows:

$$\Phi_{\mathrm{mix}} = 1 - \mathrm{F}_{\mathrm{mix}} = \frac{x - x^*}{x_0 - x^*} , \tag{101}$$

where x denotes the measured variable. Depending on the method employed, the measured variable can be, for example, electrical conductivity, light absorption, or pH. The mixing time is can be defined in several ways. In some studies, it is defined as the time required for the measured value to change from $x = x_0$ to $x = x^* \pm (1 - \xi) x^*$, where x^* is the equilibrium value of x, and ξ denotes the mixing time criterion. In other studies, $\mathrm{F}_{\mathrm{mix}}$ is employed as the criterion, and the mixing time is defined as the time required for the measured value to change from $x = x_0$ to $x = (1 - \mathrm{F}_{\mathrm{mix}})(x_0 - x^*) + x^*$. The relation of these criteria is exemplified by Eq. 102.

$$F_{mix} = \begin{cases} 1 - \dfrac{(1-\xi)x^*}{x_0 - x^*} & \text{if} \quad x_0 > x^* \\ 1 + \dfrac{(1-\xi)x^*}{x_0 - x^*} & \text{if} \quad x_0 < x^* \end{cases} . \tag{102}$$

The AOD process is characterised by efficient mixing due to high gas injection rates [58, 85, 94, 99, 102, 103, 274]. On the basis of physical modelling studies, it has been established that the mixing time is shorter with a smaller diameter of the vessel [94], a higher gas flow rate through the tuyères [58, 82, 85, 99, 102, 103, 274, 275], a lower gas flow rate through a top lance [58, 85, 102, 275], and a lower amount of top slag [102]. The mixing time is affected also by the height-to-fill ratio [99] and angle of the tuyères [58, 85, 274, 275]; the optimal tuyère angle appears to depend on the number of tuyères [58, 275].

Table 12 shows a compilation of mixing times reported on the basis of physical modelling studies of the AOD vessel. The tabulated studies cover a broad range of different modelling setups for simple side-blowing and combined-blowing with and without a top phase. As the variations between different studies as well as within studies are relatively large, the results must be interpreted carefully.

Table 12. Mixing times in physical modelling studies of the AOD process.

Reference	Model scale	Measured property	Criterion [%]	Gas injection	$\bar{t}_{mix}$ [s]	$\bar{k}_{mix}$ [1/min]
Wei *et al.* [85]	1:3	EC	95	Side	10 – 21	9 – 19
Wei *et al.* [275]	1:4	EC	95	Side	29 – 50	4 – 6
				Side + top	43 – 61	3 – 4
Ternstedt *et al.* [94]	–	EC	95	Side	7 – 23	8 – 25
Wei *et al.* [58]	1:4	EC	95	Side	18 – 50	4 – 10
				Side + top	18 – 61	3 – 10
Odenthal *et al.* [62]	1:4	LA	95	Side	37 – 54	3 – 5
Wuppermann *et al.* [99]	1:4	LA	95	Side	33 – 44	4 – 5
Zhou *et al.* [276]	1:6	EC	97.5	Side	60	4
Visuri *et al.* [103]	1:9	pH	97.5	Side	7 – 26	9 – 33
Haas *et al.* [102]	1:9	pH	97.5	Side	11 – 17	13 – 19
				Side + top	12 – 40	6 – 18

Notes: EC = electrical conductivity; LA = light absorption; $\bar{k}_{mix}$ is calculated by setting F_{mix} as equal to the mixing time criterion.

The analysis of the time constants of mixing is complicated by the varying criteria

for the mixing time. In some cases, the calculation of $\bar{k}_{\mathrm{mix}}$ would require the knowledge of the absolute values of the measured variables. However, from Eq. 102 it can be seen that $\mathrm{F}_{\mathrm{mix}} \geq \xi$ if $x_0 \neq x^*$. Therefore, setting $\mathrm{F}_{\mathrm{mix}} = \xi$ yields the smallest possible value for the average time constant of mixing. The results of this calculation are shown in Table 12. It can be seen that the calculated average time constants of mixing varied from 3 to 33 1/min. These values are one to two decades higher than the reported time constants of decarburisation for the AOD process. Reichel and Szekely [26] suggested an overall time constant of $k_{\mathrm{tot}} \approx 0.15$ 1/min for a combined-blowing vessel. Reichel and Rose [277] reported that k_{tot} varies from 0.11 to 0.14 1/min for side-blowing vessels and from 0.15 to 0.20 1/min for combined-blowing vessels. The values estimated on the basis of the top-blowing data presented in Article II are of the same magnitude as those reported in [26, 277].[14] In conclusion, it can be stated that the overall rate of decarburisation in the AOD process appears to be controlled almost entirely by small-scale mixing under typical operating conditions.

4.1.2 Macrokinetics in non-dispersed systems

In non-dispersed systems with permanent phase contact, the participating phases are completely separated and mass exchange takes place through their interfacial area. The mass change of species i in phase ψ is given by the following kinetic expression [220]:

$$\left(\frac{\mathrm{d}m_i}{\mathrm{d}t}\right)_{\text{non-dispersed}} = -\underbrace{\beta_{i,\mathrm{tot}}\rho_\psi A}_{\substack{\text{mass}\\ \text{transport}}}\underbrace{(y_i - y_{i,\mathrm{e}})}_{\substack{\text{driving}\\ \text{force}}}, \tag{103}$$

where $\beta_{i,\mathrm{tot}}$ is the overall mass transfer coefficient, ρ_ψ is the density of phase ψ, A is the interfacial area, y_i is the mass fraction of species i, and $y_{i,\mathrm{e}}$ is the equilibrium mass fraction of species i. It should be noted that Eq. 103 assumes no bulk motion; this assumption is also known as the stationary medium approach [279]. In the case of temporary phase contact, the composition variable y_i is treated as constant and equal to the initial content, *viz.* $y_i = y_{i,0}$ [1]. The overall mass transfer coefficient can

[14] The time constants of mixing for BOF converters are of the same magnitude as those shown in Table 12. The numerical results of Odenthal *et al.* [121] for a 210-ton BOF vessel with pure bottom stirring correspond to a time constant of $\bar{k}_{\mathrm{mix}} \approx 9$–$17$ 1/min. Even in ladle metallurgy, where the gas injection rates are considerably much smaller, the time constants of mixing are relatively large compared to those of chemical reactions. For example, the numerical results of Liu *et al.* [278] for an industrial scale ladle correspond to $\bar{k}_{\mathrm{mix}} \approx 0.6$–$1.0$ 1/min.

be determined with the help of the Lewis-Whitman [233] two film model, which is essentially an extension of the Nernst boundary layer model [219].

4.1.3 Macrokinetics in dispersed systems

In dispersed systems, the emulsification mechanism determines the volume, surface area, size distribution,[15] and residence time of the dispersed phase [1]. In order to determine the changes in bath composition, the mass balance needs to be coupled with the reaction rate in the dispersed phase. Mathematical expressions for the macrokinetic rate in metallurgical emulsification systems are available in the literature [1, 269, 270]. The mathematical treatment is slightly different if the metal phase is dispersed in an extracting phase than if the extracting phase is dispersed in the metal phase [1]. In the case of permanent phase contact, the macrokinetic rate of species i in the dispersed phase (d) can be expressed as follows [1]:

$$\left(\frac{\mathrm{d}m_i}{\mathrm{d}t}\right)_{\text{dispersed}} = -\underbrace{\frac{m_\mathrm{d}}{\bar{t}_\mathrm{res}}}_{\text{macrokinetics}} \cdot \underbrace{\overline{\eta}_\mathrm{M}}_{\text{microkinetics}} \cdot \underbrace{(y_i - y_{i,\mathrm{e}})}_{\text{driving force}}, \tag{104}$$

where m_d is the mass of the dispersed phase, $\bar{t}_\mathrm{res}$ is the average residence time, and $\overline{\eta}_\mathrm{M}$ is the average microkinetic efficiency. It should be that Eq. 104 assumes no net change in the mass of the dispersed phase. If the phase contact is permanent, the dispersed phase is completely emulsified and the variable y_i is treated as $y_i = y_{i,0}$ [1]. The microkinetic efficiency can be defined as follows [1]:

$$\overline{\eta}_\mathrm{M} = \frac{y_0 - y}{y_0 - y^*} = 1 - \frac{y - y^*}{y_0 - y^*} = 1 - \exp\left[-\beta_{i,\mathrm{tot}}\left(\frac{A}{V}\right)_\mathrm{d}\bar{t}_\mathrm{res}\right]. \tag{105}$$

In Eq. 105, the average residence time of the dispersed phase ($\bar{t}_\mathrm{res}$) denotes the maximum contact time available for mass exchange. For the conservation of species i in the dispersed phase, the following limits are obtained for the relation of expressions for non-dispersed and dispersed systems:

[15] A broad variety of particle size distributions relevant to process metallurgy can be described with the Rosin-Rammler-Sperling distribution function, including metal droplets induced by top-blowing [280, 281], metal droplets generated by bubble bursting [282], slag droplets generated due to bottom-blowing [236], and desulphurisation reagent powders [283]. The distribution of gas bubbles in liquid metals has been suggested to follow a log-normal distribution [284].

$$\lim_{\bar{t}_{\mathrm{res}}\to 0}\frac{\left(\frac{\mathrm{d}m_i}{\mathrm{d}t}\right)_{\text{non-dispersed}}}{\left(\frac{\mathrm{d}m_i}{\mathrm{d}t}\right)_{\text{dispersed}}}=\frac{-\beta_{i,\mathrm{tot}}\rho_{\mathrm{d}}A_{\mathrm{d}}\left(y_i-y_{i,\mathrm{e}}\right)}{-\frac{m_{\mathrm{d}}}{\bar{t}_{\mathrm{res}}}\left\{1-\exp\left[-\beta_{i,\mathrm{tot}}\left(\frac{A}{V}\right)_{\mathrm{d}}\bar{t}_{\mathrm{res}}\right]\right\}\left(y_i-y_{i,\mathrm{e}}\right)}=1\,, \tag{106}$$

$$\lim_{\bar{t}_{\mathrm{res}}\to \infty}\frac{\left(\frac{\mathrm{d}m_i}{\mathrm{d}t}\right)_{\text{non-dispersed}}}{\left(\frac{\mathrm{d}m_i}{\mathrm{d}t}\right)_{\text{dispersed}}}=\frac{-\beta_{i,\mathrm{tot}}\rho_{\mathrm{d}}A_{\mathrm{d}}\left(y_i-y_{i,\mathrm{e}}\right)}{-\frac{m_{\mathrm{d}}}{\bar{t}_{\mathrm{res}}}\left\{1-\exp\left[-\beta_{i,\mathrm{tot}}\left(\frac{A}{V}\right)_{\mathrm{d}}\bar{t}_{\mathrm{res}}\right]\right\}\left(y_i-y_{i,\mathrm{e}}\right)}=\infty\,. \tag{107}$$

As discussed by Oeters [1, 269, 270], the limits shown in Eqs. 106 and 107 can be interpreted as follows:

1. If the residence time is long, the dispersed phase will be able to react to its equilibrium composition before returning back to the bulk phase [1, 269]. The microkinetic efficiency $\overline{\eta}_{\mathrm{M}}=1$ and the emulsification rate becomes rate controlling [1].
2. If the residence time is short, only a small part of the extraction capacity will be utilised during the residence time and hence microkinetic efficiency $\overline{\eta}_{\mathrm{M}}\ll 1$ [1]. The emulsification affects the reaction rates primarily through the increase in mass exchange area [1, 269].

Similar behaviour is found when the mass transfer rates calculated with the two approaches are compared. Here, the reaction rate is expressed as relative to the theoretical maximum rate defined by the conservation of mass:

$$\text{relative reaction rate }[\%]=100\cdot\frac{\bar{t}_{\mathrm{res}}}{m_{\mathrm{d}}}\left|\frac{\mathrm{d}m_i}{\mathrm{d}t}\right|\,. \tag{108}$$

Fig. 14 shows the relative reaction rate as a function of the average microkinetic efficiency. As expected, the two approaches converge as $\overline{\eta}_{\mathrm{M}}\to 0\%$ and diverge as $\overline{\eta}_{\mathrm{M}}\to 100\%$. The relative error in the reaction rate arising from treating the emulsified system as a non-emulsified system – labelled here as the *surface area approach* – is given by

$$\text{relative error }[\%]=100\cdot\left[-\frac{\ln\left(1-\overline{\eta}_{\mathrm{M}}\right)}{\overline{\eta}_{\mathrm{M}}}-1\right]\,. \tag{109}$$

The relative error of the surface area approach is less than 10% only up to $\overline{\eta}_{\mathrm{M}}\approx 18\%$. It should be highlighted that the relation of the approaches is not affected by the mass transfer rate, interfacial area, or particle size if $\overline{\eta}_{\mathrm{M}}$ remains constant.

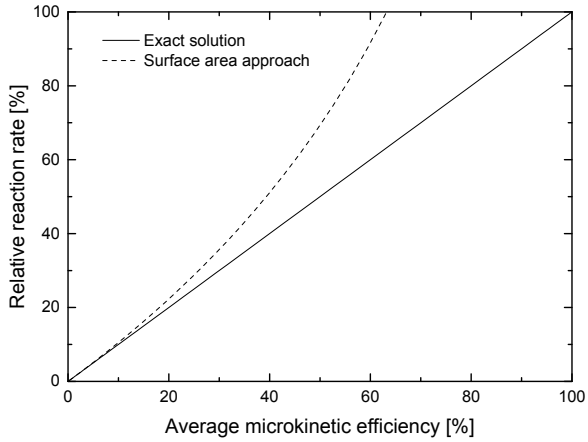

Fig 14. Mass transfer rate as a function of average microkinetic efficiency.

A special case and an exception to the mathematical treatment presented above is constituted by systems in which the reaction product dissolves neither in the dispersed nor the continuous phase. Consequently, the reaction product accumulates on the surface of the dispersed phase, forming an additional reaction resistance.[16] This effect is in many ways analogous to the effect of solid shell formation on melting of ferroalloys, *q.v.* Section 6.4.1 (p. 180).

4.2 Microkinetics of non-dispersed systems

Several theoretical models are available for description of mass transfer on free surfaces. The model proposed by Higbie [226] assumes that the reaction interface is renewed by volume elements, which originate from a semi-infinite bulk media with an initial concentration of c_0 [1, 286, 287]; for this reason, the model is also known as the surface renewal model. During the contact time at the reaction surface, the concentration of the volume element c approaches the interfacial concentration c^* according to Fick's 2nd Law in a one-dimensional form [1, 286]:

$$\frac{\partial c}{\partial t} = D\frac{\partial^2 c}{\partial x^2}\,, \tag{110}$$

where x represents the position and D is the mass diffusivity. The expression for

[16] A well-known example is the formation of CaS layer on the surface of CaO particles in hot metal desulphurisation [269, 285].

fractional equilibrium is obtained with the help of a Laplace transformation and the given boundary conditions [1, 226, 268, 286]:

$$\frac{c - c^*}{c_0 - c^*} = -\mathrm{erf}\left(\frac{x}{2\sqrt{Dt}}\right). \tag{111}$$

It can be shown [1, 226, 288] that the correlation for the Sherwood number is then

$$\mathrm{Sh} = \frac{2}{\sqrt{\pi}}\mathrm{Re}^{1/2}\mathrm{Sc}^{1/2}. \tag{112}$$

From Eq. 112 it can be deduced that the Sherwood number is independent from the viscosity of the continuous phase. In the model proposed by Danckwerts [289], the surface is renewed by volume elements similar to the Higbie model. However, the residence time of the fluid elements at the interface is not considered identical, but independent from the time it had already resided at the interface [287, 289]. The Danckwerts model can be expressed in terms of Sherwood number according to

$$\mathrm{Sh} = L\sqrt{\frac{s}{D}}, \tag{113}$$

where L is the characteristic length and s is the surface renewal rate. In the case of turbulent mass transfer at a free surface, the damping of the fluid velocity is affected by the surface tension of the fluid. In the Levich model [290], the diffusion boundary layer thickness is defined by [287]:

$$\delta_\mathrm{N} = \sqrt{\frac{D\sigma_\mathrm{equiv}}{0.41\rho u_\tau^3}}, \tag{114}$$

where u_τ is the turbulent shear stress velocity and σ_equiv is the equivalent interfacial tension.[17] The corresponding correlation for the Sherwood number [287] is given by

$$\mathrm{Sh} = 0.32\sqrt{\frac{\rho u_\tau^3}{D\sigma_\mathrm{equiv}}}. \tag{115}$$

By comparing Eqs. 112 and 115 it can be seen that according to the Levich model $\mathrm{Sh} \propto u_\tau^{3/2}$, while the surface renewal model suggests that $\mathrm{Sh} \propto u^{1/2}$.

[17] The constant 0.41 is known as the *von Kármán constant* and is considered to be universal [1].

4.2.1 Liquid metal and gas jet

Mass transfer between gas jets and solid surfaces is relatively well understood [279, 291–293], but despite extensive efforts [124, 294–304], much less is known about the mass transfer between an impinging gas jet and a liquid phase, particularly under the high-temperature conditions of converter processes. Experimental studies have been conducted with CO_2 jets and liquid iron [298], oxygen jets and liquid silver [299, 302, 303], and air jets and water [296, 297].

The most comprehensive analysis is available from experiments with oxygen jets and liquid silver. Wakelin and co-authors [294, 295] found that the mass transfer rates measured from experiments with oxygen jets and liquid silver were in good accordance with the those predicted using surface renewal theory. Similar results were presented also by Chatterjee *et al.* [301]. In their experiments, the mass transfer rate was found to be higher at lower lance heights and a higher gas jet momentum [301]. In a later study, Herbertson *et al.* [303] used an oxygen-diluent jet and liquid silver to study the interfacial phenomena during top-blowing in the non-splashing regime. It was found that surface tension driven convection developed spontaneously during desorption, whereas the interface remained stable during absorption [303].

Lohe *et al.* [297] studied gas phase mass transfer between an impinging air jet and water. In their experiments the range of momentum of the gas jet was generally below the splashing region. A correlation corresponding to their data was proposed by Oeters [1] and is shown in Eq. 116. It can be seen that the proportionality of Sh and Re varied from $\mathrm{Sh} \propto \mathrm{Re}^{0.51}$ at a moderate Re range to $\mathrm{Sh} \propto \mathrm{Re}^{0.75}$ at a high Re range.[18]

$$\mathrm{Sh} = \begin{cases} 1.41\mathrm{Re}^{0.51}\mathrm{Sc}^{0.33} & \text{when} \quad 2\times10^3 \leq \mathrm{Re} \leq 3\times10^4 \\ 0.41\mathrm{Re}^{0.75}\mathrm{Sc}^{0.33} & \text{when} \quad 3\times10^4 \leq \mathrm{Re} \leq 2\times10^5 \end{cases} . \tag{116}$$

The direct measurement of the gas phase mass transfer coefficients in an actual vessel is hindered to a great extent by the harsh conditions, as well as by the difficulty of isolating the gas phase mass transfer rate from the overall rate. For this reason, only numerical estimates [124, 304] are available for mass transfer coefficients of oxygen gas jets under the high temperature conditions of steelmaking. Kärnä *et al.* [304] derived a mass transfer correlation based on CFD calculations for top-blowing in the CAS-OB process. With the gas flow rate and the boundary temperature held constant,

[18] These proportionalities are keeping with mass correlations for gas jets impinging on solid surfaces [291].

the dependency of the mass transfer coefficient on the lance height (h_{lance}) was almost linear. Eq. 117 expresses the proposed correlation in terms of Sh and is applicable for a boundary temperature of 2000 K (1727 °C).

$$\text{Sh} = (-0.213 h_{\text{lance}} + 1.014)\,\frac{L}{D}\,, \tag{117}$$

4.2.2 Liquid metal and top slag

In comparison to metal–gas mass transfer, metal–slag mass transfer is affected to greater extent by viscous forces. Riboud and Olette [305] proposed an experimental expression for the mass transfer coefficient in the case of metal–slag reactions. The proposed correlation – expressed here in terms of Sh – relates the mass transfer rate to the cross-sectional gas flow rate [305]:

$$\text{Sh} = \frac{\beta d_{\text{bath}}}{D} = C\left(D\frac{\dot{V}_{\text{G}}}{A_{\text{bath}}}\right)^{1/2}\frac{d_{\text{bath}}}{D}\,, \tag{118}$$

where β is the mass transfer coefficient, d_{bath} is the diameter of the metal bath, D is the mass diffusivity, C is a fitting parameter, $\dot{V}_{\text{G}}$ is the volumetric gas flow rate, and A_{bath} is the cross-sectional area of the metal bath. A wide range of plant data concerning ladle desulphurisation and converter dephosphorisation could be reproduced well by C = 500 $\text{m}^{-0.5}$ [305].[19] As pointed out by Oeters [1], Eq. 118 should be used with caution, because the emulsification of slag and thereby the surface area available for mass exchange increase as the gas injection rate increases.

Hirasawa *et al.* [306] studied the metal-side mass transfer in a slag–metal reaction system during gas stirring. More specifically, the model studies focussed on the oxidation of Si in a molten slag–Cu reaction system at 1523 K (1250 °C), aqueous solution–amalgam system at room temperature, and molten salt–molten Pb system at 723 K (450 °C). Based on the results obtained in [306], Hirasawa *et al.* [307] proposed the following correlations for metal-side mass transfer:

[19] A roughly similar value of C = 570 $\text{m}^{-0.5}$ was reported for slag–Cu system at 1523 K (1250 °C), while higher values have been reported for aqueous solution–amalgam (C = 790–970 $\text{m}^{-0.5}$) and molten salt–molten Pb (C = 930 $\text{m}^{-0.5}$) systems at low temperatures [306].

$$\mathrm{Sh} = \frac{\beta d_\mathrm{c}}{D} = \begin{cases} C_3 \times \left[\mathrm{Pe}^{C_\alpha} \left(\frac{\rho_\mathrm{L} g d_\mathrm{c}^2}{\sigma} \right)^{C_\beta} \left(\frac{h_\mathrm{I}}{d_\mathrm{c}} \right) \left(\frac{h_\mathrm{slag}}{d_\mathrm{c}} \right) \right]^{1/2} & \text{when} \quad h_\mathrm{I} < h_\mathrm{I}^* \\ C_4 \times \left[\mathrm{Pe}^{C_\alpha} \left(\frac{\rho_\mathrm{L} g d_\mathrm{c}^2}{\sigma} \right)^{C_\beta} \left(\frac{d_\mathrm{b} \mathrm{Re}^{-1/3}}{d_\mathrm{c}} \right) \left(\frac{h_\mathrm{slag}}{d_\mathrm{c}} \right) \right]^{1/2} & \text{when} \quad h_\mathrm{I} > h_\mathrm{I}^* \end{cases}, \tag{119}$$

where d_c is the crucible diameter, d_b is the bubble diameter, h_I is the distance between slag–metal interface and nozzle tip, h_slag is the height of the slag layer, h_I^* is the transitional value of h_I, while C_3, C_4, C_α, and C_β are constants. The studied range of gas injection rates ($\dot{V}_\mathrm{G}$) were divided into three regions. In Region I, where the proportionality of the mass transfer coefficient to the gas injection rate was expressed by $\beta \propto \dot{V}_\mathrm{G}^{1/2}$, the model parameters were reported to be $C_3 = 1$, $C_4 = 6$, $C_\alpha = 1$, and $C_\beta = 1$. In the case of Region II, the effect of $\dot{V}_\mathrm{G}$ on β was much smaller than in Region I, and values of $C_3 = 100$, $C_4 = 600$, $C_\alpha = 0.425$, and $C_\beta = 0.654$ were reported. The effect of $\dot{V}_\mathrm{G}$ on β increases again in Region III, but no correlation was proposed for this region. Furthermore, Eq. 119 was applied for ladle desulphurisation and the calculated mass transfer coefficients were found to be in reasonably good accordance with those calculated with Eq. 118.

Making use of the integral profile method, Oeters and Xie [308] derived the following correlations for metal–slag mass transfer under conditions of non-zero interfacial velocity:

$$\mathrm{Sh} = \frac{\beta r_\mathrm{c}}{D} = 1.15 \left[U + \frac{1}{2} \frac{\delta_\mathrm{N,L}}{\delta_\mathrm{Pr,L}} (1-U) \right]^{1/2} \mathrm{Re}^{1/2} \mathrm{Sc}^{1/2} \qquad \text{(metal phase)}, \tag{120}$$

$$\mathrm{Sh} = \frac{\beta r_\mathrm{c}}{D} = 0.787 U^{1/2} \mathrm{Re}^{1/2} \mathrm{Sc}^{1/3} \qquad \text{(slag phase)}, \tag{121}$$

where r_c is the crucible radius, U is the dimensionless velocity defined by Eq. 122, and $\frac{\delta_\mathrm{N,L}}{\delta_\mathrm{Pr,L}}$ is the ratio of diffusion and thermal boundary layer thicknesses in the liquid metal defined by Eq. 123.

$$U = \left(\frac{\rho_\mathrm{L}}{\rho_\mathrm{S}} \right)^{1/2} \left(\frac{\rho_\mathrm{S} \mu_\mathrm{L}}{\rho_\mathrm{L} \mu_\mathrm{S}} \right)^{1/3} \left[(1-U)^2 (1-1.5U) \right]^{1/3}. \tag{122}$$

$$\frac{\delta_\mathrm{N,L}}{\delta_\mathrm{Pr,L}} = \left(\frac{2}{5} \frac{1+1.5U}{U + \frac{1}{2} \frac{\delta_\mathrm{N,L}}{\delta_\mathrm{Pr,L}} (1-U)} \right)^{1/2} \left(\frac{\mu_\mathrm{L}}{\rho_\mathrm{L} D_\mathrm{L}} \right)^{-1/2}. \tag{123}$$

The following limits of Eq. 120 are of interest [308]:

- for a free surface, $U = 1$ and Eq. 120 reduces to Sh = 1.15 $Re^{1/2}Sc^{1/2}$, which is in close agreement with the penetration model defined by Eq. 112.
- for a solid wall, $U = 0$ and Eq. 120 reduces to Sh = 0.787 $Re^{1/2}Sc^{1/3}$. The exact solution of the Navier-Stokes equations and the diffusion boundary layer equations yield a pre-factor of 0.664 instead of 0.787. In view of the simplifications of the integral profile method, the agreement is reasonably good.

In [309], the mass transfer coefficients obtained with Eqs. 120 and 121 were found to be in excellent agreement with experimental results for mass transfer of Mn and Si between liquid iron and slags. In [310] it was found that in the case of the reduction of FeO by Si dissolved in liquid Fe, the mass transfer coefficient of Si was approximately 2.5 times the nominal value obtained from Eq. 120 due to interfacial convection.

4.3 Microkinetics of dispersed systems

In dispersed systems, microkinetics denotes the processes which govern mass transport for individual droplets, bubbles, and particles [1]. Indeed, the AOD process features several emulsification mechanisms, including the break-up of side-blown gas jets into bubbles, the detachment of slag droplets due to the shear force of the fluid flow, as well as generation of metal droplets due to top-blown gas jet and the bursting of ascending gas bubbles at the surface of the metal bath. The modelling efforts of this work have focused on the generation of metal droplets during top-blowing and the generation of slag droplets during the reduction stage.

The main factors affecting the microkinetics are the rate of the surface reaction, the mass transfer in the dispersed phase (*internal mass transfer*) and the mass transfer in the continuous phase (*external mass transfer*) [1, 257, 288, 311, 312]. As shown Fig. 15, four limiting cases of the solute concentration profiles can be identified:

Case 1 The interfacial reaction is much slower than the mass transport in the dispersed and continuous phases. In the AOD process, an example of a reaction of this type is the removal of nitrogen in the presence of high amounts of surface elements, such as dissolved oxygen.

Case 2 Mass transfer in the continuous phase is much slower than the interfacial reaction or mass transfer in the dispersed phase. Most reactions between gas bubbles and the metal bath are likely to fall into this category. The main factors

contributing to the efficient mass transfer within the bubbles are the high mass diffusivity of the gas phase and the internal circulation caused by the forces acting on the rising gas bubbles. The micro-slag formed as a result of the reactions may attach to the rising gas bubbles [313] and react with the surrounding metal phase. It has been suggested [314] that the microslag is then swept to the base of the bubble so that a fresh metal–gas interface is left on the top surface.

Case 3 Mass transfer in the dispersed phase is much slower than the interfacial reaction or mass transfer in the continuous phase. An example of this category are reactions between the metal bath and slag droplets during the reduction stage. The slag phase has a low diffusivity, and a high viscosity, which hinders the formation of internal circulation within the droplet.

Case 4 Mass transfer rates in the dispersed and continuous phases are comparable and much slower than the interfacial reaction. An example of this category are the reactions between the top slag and metal droplets, which are formed *e.g.* due to top-blowing or bubble bursting. The properties of the metal droplets are such that both internal and external mass transfer control come into question depending on the size of the droplet: large metal droplets generally exhibit internal circulation, while small droplets tend to behave similar to rigid spheres [1]. Therefore, both internal and external mass transfer resistance become relevant if the whole droplet size distribution is considered.

The overall efficiency of mass transfer can be characterised with the fractional equilibrium F and the dimensionless concentration gradient Φ [288]:

$$\mathrm{F} = \frac{x_0 - x}{x_0 - x^*} = \frac{y_0 - y}{y_0 - y^*} = 1 - \Phi\,, \tag{124}$$

$$\Phi = \frac{x - x^*}{x_0 - x^*} = \frac{y - y^*}{y_0 - y^*} = 1 - \mathrm{F}\,. \tag{125}$$

The microkinetic efficiency is defined by $\eta_\mathrm{M} = \mathrm{F} = 1 - \Phi$. Employing dimensionless groups for mass transfer, F can be calculated as follows [288, 315]:

$$\mathrm{F} = 1 - \exp\left(-\frac{3}{2}\overline{\mathrm{Sh}}\mathrm{Fo}_\mathrm{M}\right)\,, \tag{126}$$

where $\overline{\mathrm{Sh}}$ is the time-averaged Sherwood number and Fo_M is the Fourier number for mass transfer. Typically, the Sherwood number is a function of the Reynolds number (Re) and the Schmidt number (Sc), while the product ReSc is also known as the Péclet

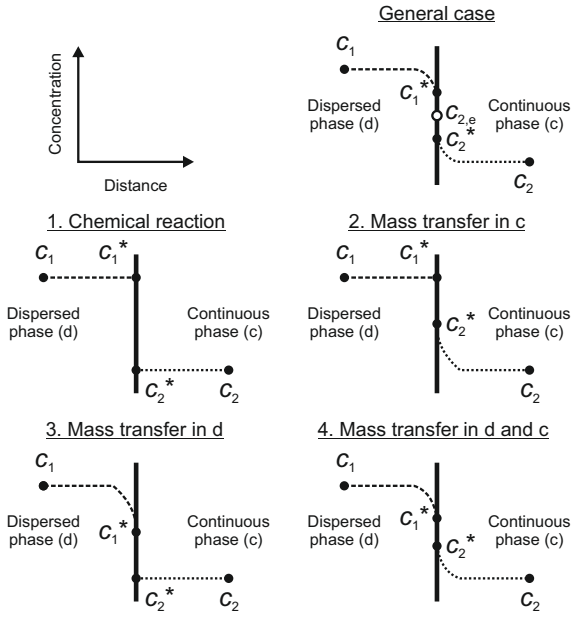

Fig 15. Schematic illustration of solute concentration profiles across the interface between dispersed and continuous phases in different limiting cases. Adapted from [312].

number for mass transfer ($\mathrm{Pe_M}$). The definitions of Sh, $\mathrm{Fo_M}$, Re, Sc, and $\mathrm{Pe_M}$ are given below for convenience [43, 288]:

$$\mathrm{Sh} = \frac{\beta d_\mathrm{p}}{D} = \frac{\text{total mass transfer}}{\text{diffusive mass transfer}}, \tag{127}$$

$$\mathrm{Fo_M} = \frac{4Dt}{d_\mathrm{p}^2} = \frac{\text{diffusive mass transfer}}{\text{storage rate}}, \tag{128}$$

$$\mathrm{Re} = \frac{u d_\mathrm{p} \rho}{\mu} = \frac{\text{inertial force}}{\text{viscous force}}, \tag{129}$$

$$\mathrm{Sc} = \frac{\mu}{\rho D} = \frac{\text{momentum diffusivity}}{\text{mass diffusivity}}, \tag{130}$$

$$\mathrm{Pe_M} = \frac{u d_\mathrm{p}}{D} = \frac{\text{bulk mass transfer}}{\text{diffusive mass transfer}} = \mathrm{ReSc}, \tag{131}$$

where β is the mass transfer coefficient, d_p is the particle diameter, D is the mass diffusivity, t is the characteristic time, u is the characteristic velocity, ρ is the density,

and μ is the dynamic viscosity.[20]

The mass transfer resistances of the dispersed and continuous phases vary greatly depending on the shape regime of the dispersed phase. For this reason, the general factors affecting the shape regimes are introduced before a more detailed discussion on the characteristics of mass transfer in the dispersed and continuous phases. A rough estimate of the relative mass transfer resistances of the dispersed and continuous phases can be obtained using the rules shown in Table 13.

Table 13. Limiting cases of mass transfer to spheres. Adapted from [288].

	Continuous phase resistance	
Dispersed phase resistance	Negligible	Significant
Negligible	Case 1	Case 3 Short times: $L\sqrt{D_\mathrm{d}/D_\mathrm{c}} \gg 1$ Long times: $LD_\mathrm{d}/D_\mathrm{c} \gg \mathrm{Sh}$
Significant	Case 2 Short times: $L\sqrt{D_\mathrm{d}/D_\mathrm{c}} \ll 1$ Long times: $LD_\mathrm{d}/D_\mathrm{c} \ll \mathrm{Sh}$	Case 4

Notes: $L = c_\mathrm{d}/c_\mathrm{c}$ = partition coefficient.

4.3.1 Shape regimes of the dispersed phase

The shape regimes of bubbles and droplets rising or falling freely in infinite media can be described with the Eötvös number (Eo), Morton number (Mo), and Reynolds number (Re) [288]. The definitions of the Eo and Mo are given below in Eqs. 132 and 133 [288].

$$\mathrm{Eo} = \frac{g\Delta\rho d_\mathrm{p}^2}{\sigma} = \frac{\text{gravitational force}}{\text{surface tension force}}, \tag{132}$$

$$\mathrm{Mo} = \frac{g\mu_\mathrm{c}^4\Delta\rho}{\rho_\mathrm{c}^2\sigma^3}, \tag{133}$$

where σ is the interfacial tension and c denotes the continuous phase. In the following, the shape regimes of metal droplets in slag, slag droplets in metal, and gas bubbles in metal are studied briefly. The properties of the studied systems are shown in Table 14. The value of Re was calculated based on terminal velocity. Assuming

[20]It should be noted that in the aforementioned definitions the characteristic length for calculation of Sh, Re, and $\mathrm{Pe_M}$ is the particle diameter, *i.e.* $L = d_\mathrm{p}$, while in the case of $\mathrm{Fo_M}$ the characteristic length is the particle radius, *i.e.* $L = r_\mathrm{p} = \frac{1}{2}\,d_\mathrm{p}$ [288, 316].

rigid sphere behaviour, the terminal velocities of metal and slag droplets were solved numerically from force balance using the drag coefficient correlation proposed by Hu and Kintner [317], while the terminal velocity of gas bubbles was calculated according to Mendelson [318] (see Appendix 1).

Table 14. Dimensionless representation of dispersions in steelmaking.

Dispersed phase	Continuous phase	d [mm]	Eo	$\log_{10}$Mo	Re
Metal	Slag	1	0.04	–10.4	28
Metal	Slag	10	3.9	–10.4	1876
Slag	Metal	1	0.04	–12.3	129
Slag	Metal	10	3.9	–12.3	6041
Gas	Metal	10	4.6	–12.6	4244
Gas	Metal	40	73.2	–12.6	25469

Employed physical properties: μ_L = 0.005 Pa·s; μ_S = 0.01 Pa·s; ρ_L = 7000 kg/m^3; ρ_S = 3000 kg/m^3; ρ_G = 0.2 kg/m^3; σ_{L-S} = 1.0 N/m; σ_L = 1.5 N/m.

Fig. 16 illustrates the shape regimes presented by Clift *et al.* [288] along with the above mentioned metallurgical systems. Although Fig. 16 is not applicable for extreme density or viscosity ratios, it provides general guidelines for the shapes of bubbles and droplets. It can be seen that small metal or slag droplets (d = 1 mm) are expected to behave similarly to rigid spheres. Larger droplets (d = 10 mm) are likely to exhibit wobbling behaviour similarly to gas bubbles of same size. Fig. 16 suggests that small gas bubbles (d = 10 mm) should rise as wobbling ellipsoids, while large gas bubbles (d = 40 mm) should rise as spherical caps. The expected behaviour of gas bubbles is in keeping with the numerical results of Xu *et al.* [319, 320] and Wang *et al.* [321]. As will be demonstrated later, these conclusions are in reasonably good accordance with mass transfer rates observed in the aforementioned metallurgical systems.

4.3.2 Mass transfer in the dispersed phase

Table 16 (p. 117) shows a compilation of correlations for mass transfer in the dispersed phase. The correlations are represented in terms of Sh. The properties of the continuous and dispersed phases are indicated with subscripts c and d, respectively. Under conditions of negligible external resistance the value of the Sherwood number is defined by [288]:

$$\mathrm{Sh} = \frac{2}{3\,(1-\mathrm{F})}\,\frac{\mathrm{dF}}{\mathrm{dFo_M}} = \frac{2}{3\Phi}\,\frac{\mathrm{d}(1-\Phi)}{\mathrm{dFo_M}}\,. \tag{134}$$

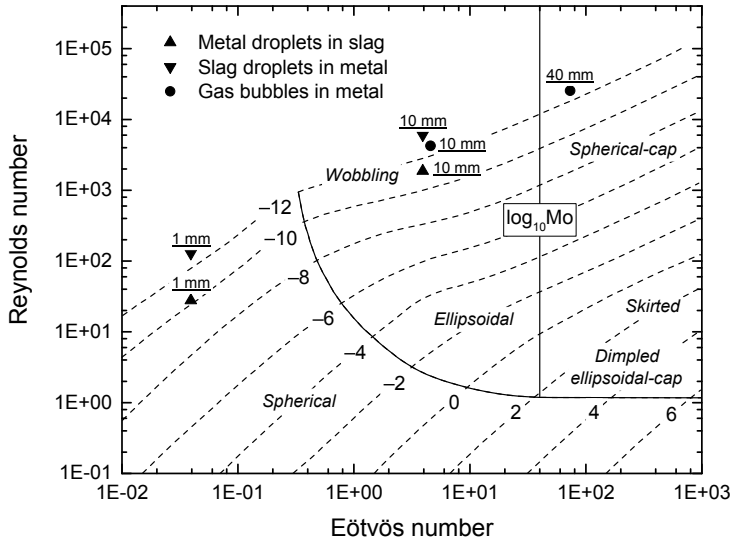

Fig 16. Shape regimes for bubbles and droplets in unhindered gravitational motion through liquids. Modified after [288].

The time-averaged Sherwood number is then obtained from [288, 315]:

$$\overline{\mathrm{Sh}} = -\frac{2\ln(1-\mathrm{F})}{3\mathrm{Fo_M}} = \frac{2\ln\Phi}{3\mathrm{Fo_M}}\,. \tag{135}$$

In a stagnant sphere (Re = 0, $\mathrm{Pe_M}$ = 0) mass transfer takes place solely by molecular diffusion [1, 288, 322]. The concentration change with respect to time is described by the Fick's 2nd law for spherical coordinates [1]:[21]

$$\frac{\partial c}{\partial t} = D\left[\frac{\partial^2 c}{\partial x^2} + \frac{2}{x}\frac{\partial c}{\partial x}\right], \tag{136}$$

where x denotes the distance from the midpoint of the sphere. A series expansion for the solution of the average concentration from Eq. 136 is known as the Newman [323] solution, which is expressed in terms of Sh in Eq. 141 (Table 16). The steady-state asymptotic value of the Newman solution is [1, 288, 324]:

$$\lim_{\mathrm{Fo_M}\to\infty} \mathrm{Sh} = \frac{2\pi^2}{3} \approx 6.58\,. \tag{137}$$

[21] Here, the mass diffusivity (D) is taken as a constant in space.

If the dispersed phase is in motion relative to the continuous phase, the external flow can induce internal circulation or oscillation, which decrease the dispersed mass transfer resistance considerably [1, 116, 288, 322, 325, 326]. The characteristic time variation of the Sherwood number in the dispersed phase in a creeping flow is illustrated in Fig. 17. The time variations are caused by Hill's vortex [327], whose intensity is controlled by the continuity of the velocity and the viscous shear stress at the interface [324].

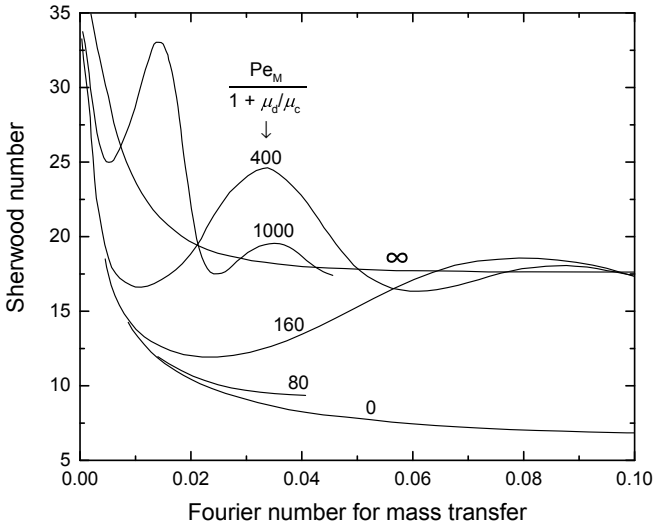

Fig 17. Variation of instantaneous overall Sh number in a creeping flow with negligible external resistance. Redrawn after [288].

Kronig and Brink [328] proposed a mathematical solution, which describes laminar diffusion with circulation induced by viscous forces (see Eq. 144 in Table 16). The first seven values for the parameters A_i and λ_i in Eq. 144 are shown in Table 15.

Table 15. Parameters of the Kronig and Brink solution. Adapted from [329].

	i						
Parameter	1	2	3	4	5	6	7
A_i	1.33	0.60	0.36	0.35	0.28	0.22	0.16
λ_i	1.678	8.48	21.10	38.5	63.0	89.8	123.8

The Kronig-Brink solution is based on the assumption that surfaces of uniform concentration coincide with the Hadamard-Rybczynski streamlines [330, 331], which

describe the laminar flow past a fluid sphere in the Stokes flow regime ($Re \ll 1$) [288, 325, 326, 328]. In terms of dimensionless numbers, the solution is thus applicable for the special case of $Re \to 0$ and $Pe_M \to \infty$ [288, 324]. Despite its limited theoretical applicability, experimental studies have shown that the Kronig-Brink solution gives a reasonably good prediction of the mass transfer coefficient even at Reynolds numbers well above those corresponding to creeping flows [288, 325, 332]; the resulting error is then $O(Pe^{-0.5})$ [333]. Johns and Beckmann [334] have suggested that for practical purposes the Hadamard stream function may be extended to systems for which $Re < 10$. The steady-state asymptotic value of the Kronig-Brink solution is given by [324]:

$$\lim_{Fo_M \to \infty} Sh = \frac{32}{3}\lambda_1 \approx 17.9\,, \tag{138}$$

which indicates that laminar circulation should increase the internal mass transfer rate by a factor of 2.7 in comparison to rigid sphere behaviour. In the case of heat transfer within a sphere, the asymptotic value of Nu is within 5% of the Newman solution for $Pe_H/(1-\frac{\mu_d}{\mu_c}) < 10$ and within 5% of the Kronig-Brink solution for $Pe_H/(1-\frac{\mu_d}{\mu_c}) > 250$ [288, 326]. Fig. 18 shows the numerical results by Juncu [326] in comparison to the Newman and Kronig-Brink solutions.

A somewhat simpler expression for mass transfer in a droplet with internal circulation was proposed by Calderbank and Korchinski [335]. Employing the approximate Vermeulen [336] empirical approach (Eq. 143 in Table 16) as the basis of their analysis, they considered the effect of internal circulation on effective diffusivity by multiplying the value of molecular diffusivity (Eq. 142 in Table 16). The steady-state asymptotic value of their correlation is

$$\lim_{Fo_M \to \infty} Sh = \frac{3\pi^2}{2} \approx 14.8\,, \tag{139}$$

which suggests that the effective mass diffusivity during internal circulation is 2.25 times the molecular value [335]. It should be noted that neither the Kronig-Brink nor the Calderbank-Korchinski solution reproduce the time oscillations shown in Fig. 17.

It is well known that internal circulation can be inhibited or even suppressed by surface active elements [1, 288, 325, 337–339], and that the tendency for this phenomenon grows with increasing droplet size [1, 338]. In a moving bubble or drop the surfactants are swept to the aft and the resulting concentration gradient induces a surface tension gradient and a tangential stress, which opposes the direction of movement [339]. Henschke and Pfennig [340] showed that the effect of surface instability on the internal

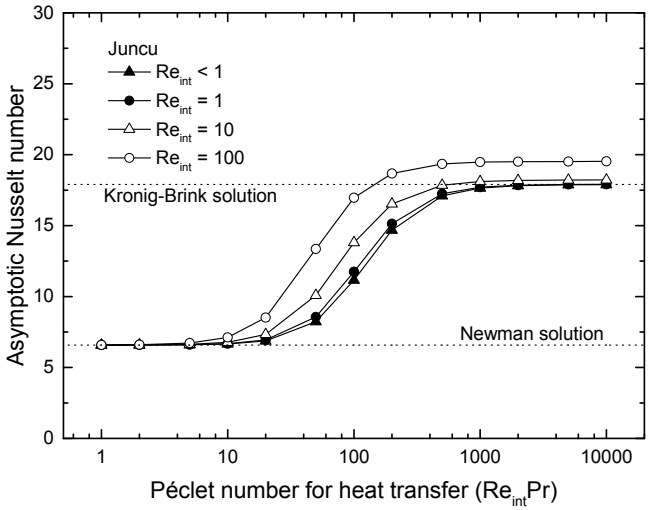

Fig 18. Asymptotic Nu values for different Pe_H and Re_{int} values in a liquid–liquid system. Comparison of numerical results of Juncu [326] with the Newman [323] and Kronig-Brink [328] solutions.

circulation can be described by the Newman solution by replacing the mass diffusivity with effective diffusivity:

$$D_{\text{eff}} = D + \frac{u d_{\text{p}}}{C_{\text{IP}} \left(1 + \frac{\mu_{\text{d}}}{\mu_{\text{c}}}\right)}, \tag{140}$$

where C_{IP} is a substance specific constant which accounts for transient effects at the interface, while μ_{d} and μ_{c} denote the dynamic viscosity of the dispersed and continuous phases, respectively. The corresponding correlation for the Sherwood number is shown in Eq. 145 (Table 16). Later it has been shown that C_{IP} is not only substance specific, but also a function of concentration [316].

A mathematical solution for internal circulation at larger Re values was proposed by Handlos and Baron [341] (Eq. 146 in Table 16), who assumed eddy diffusion between internal toroidal lines of a moving drop. The solution assumes a constant spherical shape of the drop [315], and suggests that Sh is a function of ReSc, *i.e.* Pe_{M}, and the viscosity ratio of the dispersed and continuous phases. The value of λ_1 in Eq. 146 was reported to be 2.88 [341], but was later more accurately recalculated to be 2.866 by Wellek and Skelland [342]. Because only the first term in the series solution was used,

the Handlos-Baron solution is inaccurate at small contact times [315, 343, 344].

Olander [343] modified the Handlos-Baron solution to be applicable for the entire range of contact times (Eq. 147 in Table 16). Another modification of the Handlos-Baron solution was proposed by Wegener and Paschedag [345] (Eq. 148 in Table 16), who introduced a concentration dependent parameter α to describe the influence of the initial solute concentration on Marangoni convection. However, as the internal mass transfer is usually not the rate limiting step at high Pe_M values, mass transfer correlations of the type shown in Eqs. 146, 147, and 148 have found little use in the metallurgical literature.

Table 16. Mass transfer correlations for dispersed phase.

Reference	Application	Equation
Newman [323]	Molecular diffusion in a stagnant drop (Re = 0, Pe_M = 0)	$\mathrm{Sh} = \frac{2\pi^2}{3} \frac{\sum_{i=1}^{\infty} \left[\exp\left(-i^2\pi^2 \mathrm{Fo_M}\right)\right]}{\sum_{i=1}^{\infty} \left[\frac{1}{i^2} \exp\left(-i^2\pi^2 \mathrm{Fo_M}\right)\right]}$ (141)
Calderbank and Korchinski [335]	Effective molecular diffusion in a drop	$\mathrm{Sh} = \frac{3\pi^2}{4} \frac{\exp\left(-\frac{9\pi^2}{4}\mathrm{Fo_M}\right)}{\mathrm{F}(1-\mathrm{F})}$ (142) where $\mathrm{F} = \left[1 - \exp\left(-\frac{9\pi^2}{4}\mathrm{Fo_M}\right)\right]^{1/2}$ (143)
Kronig and Brink [328]	Laminar diffusion with circulation induced by viscous forces between a moving drop and continuous phase (Re $\to$ 0, $Pe_M \to \infty$)	$\mathrm{Sh} = \frac{32}{3} \frac{\sum_{i=1}^{\infty} \left[A_i^2 \lambda_i \exp\left(-16\lambda_i \mathrm{Fo_M}\right)\right]}{\sum_{i=1}^{\infty} \left[A_i^2 \exp\left(-16\lambda_i \mathrm{Fo_M}\right)\right]}$ (144)
Henschke and Pfennig [340]	Effective mass transfer in a drop in the presence of transient instability	$\mathrm{Sh} = \frac{2\pi^2}{3} \frac{\sum_{i=1}^{\infty} \left[\exp\left(-i^2\pi^2 \mathrm{Fo'_M}\right)\right]}{\sum_{i=1}^{\infty} \left[\frac{1}{i^2} \exp\left(-i^2\pi^2 \mathrm{Fo'_M}\right)\right]}$ (145)

Notes: Eqs. 141, 142, and 144 are taken from [288], [346], and [324], respectively; $\mathrm{F} = \frac{x_0 - x}{x_0 - x^*}$ = fractional equilibrium. $\mathrm{Fo'_M} = \frac{4 D_{\mathrm{eff}} t}{d_p^2}$ = modified $\mathrm{Fo_M}$.

Table 16. (Continued)

Reference	Application	Equation	
Handlos and Baron [341]	Eddy diffusion between internal toroidal stream lines of a moving drop	$\mathrm{Sh} = \frac{\lambda_1}{128} \frac{\mathrm{ReSc}}{1+\frac{\mu_d}{\mu_c}}$	(146)
Olander [343]	Eddy diffusion between internal toroidal stream lines of a moving drop	$\mathrm{Sh} = 0.972 \left(\frac{\lambda_1}{128} \frac{\mathrm{ReSc}}{1+\frac{\mu_d}{\mu_c}} \right) + \frac{0.3}{\mathrm{Fo_M}}$	(147)
Wegener and Paschedag [345]	Eddy diffusion between internal toroidal stream lines of a moving drop in the presence of Marangoni convection	$\mathrm{Sh} = \alpha \left(\frac{\lambda_1}{128} \frac{\mathrm{ReSc}}{1+\frac{\mu_d}{\mu_c}} \right)$	(148)

4.3.3 Mass transfer in the continuous phase

A compilation of correlations for mass transfer in the continuous phase is shown in Table 17 (see pp. 121–122). Experimental correlations [252, 253, 347, 348] suggest that the viscous external mass transfer surrounding a rigid sphere can be expressed by

$$\mathrm{Sh} = 2 + B\,\mathrm{Re}^{1/2}\mathrm{Sc}^{1/3}\,, \tag{149}$$

where B is a constant. Based on an extensive literature review, Rowe *et al.* [348] suggested that B varies between 0.33 and 0.72 depending on the studied system. If the continuous phase is fully stagnant (Re = 0), correlations of the type shown in Eq. 149 reduce to Sh = 2; this is equivalent to mass transfer by diffusion only [1, 116, 288, 349]. The correlation proposed by Ihme *et al.* [350] (Eq. 153 in Table 17) has a slightly broader range of validity than those based on Eq. 149. Although Eqs. 150–152 (Table 17) were devised for mass transfer around individual rigid spheres, they can be used for particle clouds provided that the distance of the particles is much larger than the thickness of the diffusion boundary layer [1]. This condition is usually satisfied if the density of the particle cloud is low [1]. The effect of Re on Sh becomes larger in turbulent fluid flow, although the proportionality $\mathrm{Sh} \propto \mathrm{Sc}^{1/3}$ is retained. For example, the correlation for turbulent mass transfer in packed beds proposed by Calderband and Moo-Young [337] (Eq. 156 in Table 17) suggests that $\mathrm{Sh} \propto \mathrm{Re}^{2/3}$. In the case of solid particles in turbulent fluid flow, the mass transfer rate can be described using the correlation proposed by Sano *et al.* [351]. Their correlation (Eq. 155 in Table 17) relates the Sherwood number with the specific stirring energy.

It is worth noting that the mass transfer resistance of the continuous phase follows closely that reported for rigid spheres also in the circulating regime of internal flow [335]. As shown by Calderbank [352], the fluid flow around a fluid sphere at low Re values can be calculated by employing the Hadamard stream function; the proposed mass transfer correlation is shown in Eq. 157 (Table 17).

Outside the Stokes flow regime, a vortex forms behind the droplet and has an increasing effect on the external mass transfer rate [350]. Consequently, the significance of viscous forces decreases. At large $\mathrm{Pe_M}$ values the continuous phase mass transfer approaches uninhibited surface renewal, which can be described using the penetration model proposed by Higbie [226]. The expression shown in Eq. 158 (Table 17) represents a modification, which reduces to Sh = 2 when Re = 0 [1]. The correlations proposed by Calderbank and Moo-Young [337] for mass transfer around gas bubbles (Eq. 159)

differentiate between the regime of rigid sphere behaviour and that of uninhibited surface renewal. Baird and Davidson [244] proposed a mass transfer correlation (Eq. 160 in Table 17) for spherical-cap bubbles with planar rear surfaces and a half-angle of 50°. It can be seen that the exponent of the mass diffusivity in Eq. 160 corresponds to the exponent of the Schmidt number in the penetration model proposed by Higbie [226]. Lochiel and Calderbank [353] proposed a continuous phase mass transfer correlation for the frontal area of spherical-cap bubbles in the potential flow. The prefactor in Eq. 161 (Table 17) differs only slightly from the Higbie [226] penetration model.

An important factor to be considered is the presence of natural or forced convection. The effect of natural and forced convection is captured by the $\overline{\mathrm{Gr}}\mathrm{Sc}$ term in the Steinberg and Treybal [354] correlation (Eq. 162 in Table 17), which encompasses gas and liquid systems in a broad range of validity ($1 \leq \mathrm{Re} \leq 30000$; $0.6 \leq \mathrm{Sc} \leq 3000$). In metallurgical applications, the gas phase is often subject to high temperature gradients. The correlation proposed by Wu *et al.* [355] (Eq. 164 in Table 17) accounts for the effects of forced and natural convection as well as that of a high temperature gradient, but has a relatively narrow range of validity ($2 \leq \mathrm{Re} \leq 100$; $0.71 \leq \mathrm{Sc} \leq 0.73$).

Table 17. Mass transfer correlations for continuous phase.

Reference	Application	Equation	
Frössling [347]	Viscous fluid flow around a rigid sphere	$\mathrm{Sh} = 2 + 0.552\mathrm{Re}^{1/2}\mathrm{Sc}^{1/3}$	(150)
Ranz and Marschall [252, 253]	Viscous fluid flow around a rigid sphere	$\mathrm{Sh} = 2 + 0.6\mathrm{Re}^{1/2}\mathrm{Sc}^{1/3}$	(151)
Rowe *et al.* [348]	Viscous fluid flow around a rigid sphere	$\mathrm{Sh} = 2 + 0.72\mathrm{Re}^{1/2}\mathrm{Sc}^{1/3}$	(152)
Ihme *et al.* [350]	Viscous fluid flow around a rigid sphere	$\mathrm{Sh} = 2 + z_k \frac{(\mathrm{ReSc})^{1.7}}{1+(\mathrm{ReSc})^{1.2}}$	(153)
		where $z_k = \frac{0.66}{1+\mathrm{Sc}} + \frac{\mathrm{Sc}}{2.4+\mathrm{Sc}}\left(\frac{0.79}{\mathrm{Sc}^{1/6}}\right)$	(154)
Sano *et al.* [351]	Solid particles in turbulent fluid flow	$\mathrm{Sh} = \left[2 + 0.4\left(\frac{\dot{\varepsilon}_c d^4}{\nu_c^3}\right)^{1/4}\mathrm{Sc}^{1/3}\right]\phi$	(155)
Calderbank and Moo-Young [337]	Turbulent flow through packed beds	$\mathrm{Sh} = 0.69\mathrm{Re}^{2/3}\mathrm{Sc}^{1/3}$	(156)

Notes: $\dot{\varepsilon}_c$ = specific stirring energy of the continuous phase; ϕ = surface factor.

Table 17. (Continued)

Reference	Application	Equation	
Calderbank [352]	Viscous fluid flow around a fluid sphere (Re < 1)	$\mathrm{Sh} = 0.65\left(\frac{\mu_c}{\mu_c+\mu_d}\right)^{1/2}\mathrm{Re}^{1/2}\mathrm{Sc}^{1/2}$	(157)
Higbie [226]	Frictionless fluid flow	$\mathrm{Sh} = 2+\frac{2}{\sqrt{\pi}}\mathrm{Re}^{1/2}\mathrm{Sc}^{1/2}$	(158)
Calderbank and Moo-Young [337]	Viscous fluid flow around gas bubbles	$\mathrm{Sh} = \begin{cases} 0.31\mathrm{Gr}^{1/3}\mathrm{Sc}^{1/3} & \text{small bubbles } (d_b < 2.5 \text{ mm}) \\ 0.42\mathrm{Gr}^{1/3}\mathrm{Sc}^{1/2} & \text{large bubbles } (d_b > 2.5 \text{ mm}) \end{cases}$	(159)
Baird and Davidson [244]	Turbulent fluid flow around spherical-cap bubbles	$\mathrm{Sh} = 0.975 d_b^{3/4} D^{-1/2} g^{1/4}$	(160)
Lochiel and Calderbank [353]	Turbulent fluid flow around spherical-cap bubbles	$\mathrm{Sh} = 1.28\mathrm{Re}^{1/2}\mathrm{Sc}^{1/2}$	(161)
Steinberger and Treybal [354]	Viscous flow with natural and forced convection	$\mathrm{Sh} = \mathrm{Sh}_0 + 0.347(\mathrm{ReSc}^{1/2})^{0.62}$	(162)
		where $\mathrm{Sh}_0 = \begin{cases} 2+0.569(\overline{\mathrm{Gr}}\mathrm{Sc})^{1/4} & \text{for } \overline{\mathrm{Gr}}\mathrm{Sc} < 10^8 \\ 2+0.0254(\overline{\mathrm{Gr}}\mathrm{Sc})^{1/2}\mathrm{Sc}^{0.244} & \text{for } \overline{\mathrm{Gr}}\mathrm{Sc} > 10^8 \end{cases}$	(163)
Wu *et al.* [355]	Viscous flow with natural and forced convection; high temperature gradient (CO_2)	$\mathrm{Sh} = 2-0.317\left(\overline{\mathrm{Gr}}\mathrm{Sc}\right)^{1/4}+3\mathrm{Re}^{0.415}\mathrm{Sc}^{1/3}$	(164)

Notes: Eq. 158 is taken from [1].

4.3.4 Experimental considerations

Metal droplets in slag

The behaviour of metal droplets in slag is important for many metallurgical unit processes [356]. In this case, the dynamic viscosity of the continuous phase is considerably higher than that of the dispersed metal phase. Metal droplets with diameters in the range of 1 to 5 mm have Reynolds numbers in the slag between 100 and 1000 [356]. Under such circumstances the wake outside the metal droplet is accompanied by a circulatory pattern inside the metal droplet [356].

A case involving iron and copper droplets of 2–6 mm diameter in $CaO–SiO_2–Al_2O_3$ slag is discussed based on an example in [357].[22] In the first case, it was assumed that the mass transfer resistance lies solely in the dispersed metal phase (see Fig. 19a). The analytical solutions of Kronig and Brink [328] , Calderbank and Korchinski [335], and Newman [323] are in reasonable agreement with the measured mass transfer coefficients of Mn in Fe and Cu droplets. However, the measured mass transfer rate of S in Fe droplets is considerably larger than that predicted by the analytical correlations, being in the order of Sh = 100. On the other hand, Si in Fe droplets exhibit slower mass transfer than those obtained from the analytical solutions and are close to Sh = 1. Oeters [357] suggests that sulphur is likely to cause interfacial instability, which permits interfacial convection and thereby explains the observed high mass transfer rate. Moreover, it is suggested the slow mass transfer rate of Si in Fe droplets might be caused by the suppressing effect of Si on CO formation [357].

In the second case, it was assumed that the mass transfer limitation is solely in the surrounding slag phase, *i.e.* in the continuous phase (see Fig. 19b). The Higbie [226] correlation (Eq. 158) appears to overestimate the Sherwood number at low ReSc values, but converges towards the experimental values as the ReSc increases. The predictions obtained with the Calderbank correlation (Eq. 157) are in very good agreement with the experimental values; as stated earlier, this correlation assumes a laminar flow according to the Hadamard stream function. The Ranz-Marschall [252, 253] correlation (Eq. 151) underestimates the Sherwood number throughout the studied range, which suggests the assumption of rigid sphere behaviour holds poorly for external mass transfer in the

[22] The metal droplets were saturated with carbon and in some cases the metal droplets contained 0.5 wt-% S and the slag contained MnO [357]. The experiments were conducted at two temperatures: 1773 K (1500 °C) and 1873 K (1600 °C) [357].

studied droplet size range. However, all three correlations fail to describe the high mass transfer rate of S in Fe droplets.

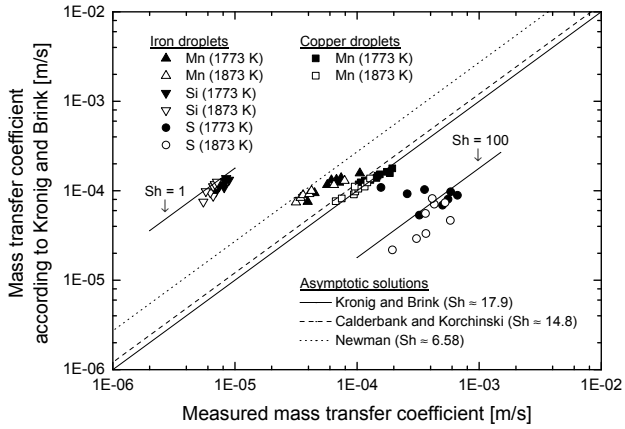

(a) Measured and calculated [323, 328, 335] internal mass transfer coefficients.

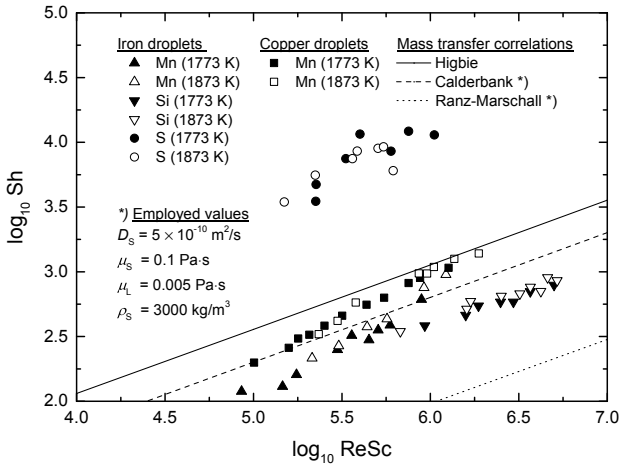

(b) Measured and calculated [226, 252, 253, 352] external Sherwood numbers.

Fig 19. Mass transfer rates of Mn, Si, and S in Fe droplets and Mn in Cu droplets. Adapted from [1].

Rhamdhani *et al.* [358] studied kinetics of reactions between Fe–Al alloy droplets and $CaO–SiO_2–Al_2O_3$ slag. In their study, dispersed phase mass transfer was suggested as the rate controlling step. Accounting for the changes in the interfacial area, the

measured mass transfer rate was found to be close to the asymptotic value of the Newman solution for mass transfer within a stagnant sphere.

In conclusion, it may be stated that that small metal droplets behave similarly to stagnant fluid spheres, while large metal droplets may exhibit a circulatory flow [1, 356]. It should be noted that the critical droplet diameter depends on the physical properties of the metal and slag phases as well as the amount of surface active elements. Nevertheless, the circulation is not as vigorous as in the case of aqueous and organic systems [356]. This deviation may be attributable to the high surface tension of liquid steel [356].

Metal droplets in gas flow

Wu *et al.* studied the decarburisation kinetics of levitated Fe–Cr–C droplets with top-blown O_2–Ar [359] and CO_2–Ar [355] gas mixtures. In both cases, the experimentally determined mass transfer rates (Sh < 2) at low Re values were lower than those permitted by pure diffusion alone or those predicted by the Steinberger-Treybal [354] correlation. However, in the case of CO_2–Ar gas with moderate Re values [355], the Ranz-Marschall [252, 253] and the Steinberger-Treybal [354] correlations were found to under predict the mass transfer in the gas phase (see Fig. 20).

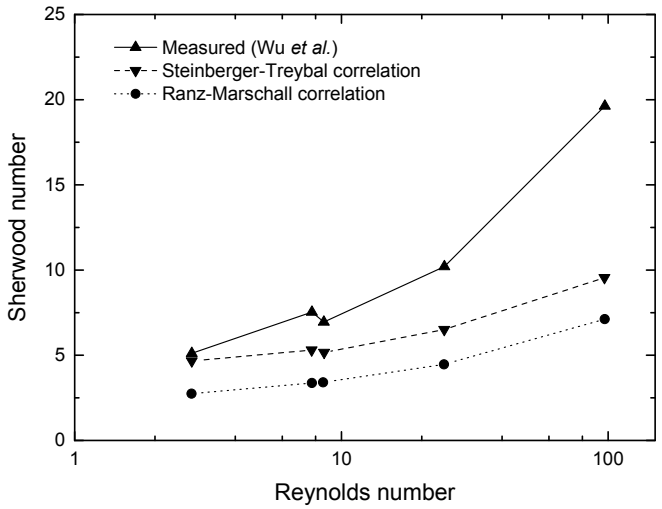

Fig 20. Measured and calculated [252, 253, 354] Sherwood numbers for CO_2 in CO_2–Ar gas surrounding Fe–Cr–C droplets. Adapted from [355].

Baker *et al.* studied levitated Fe–C droplets (0.7 g) with top-blown O_2–He [360] and CO_2–He [361] gas mixtures. They found that the predictions obtained with the Steinberger and Treybal [354] correlation were in very good agreement with the experimental values from experiments with CO_2–He [360] gas (see Table 18). However, in the case of O_2–He gas, the predicted mass transfer rates at high O_2 partial pressures were considerably lower than the experimentally measured values [360]. It was postulated that the discrepancy is caused by a CO combustion zone, which shrouds the specimen and increases the temperature of the gas [360]. An excellent agreement with the experimental values at high O_2 concentration was obtained when the gas film temperature was taken as equal to the temperature of the metal droplet [360]. Experiments similar to Baker *et al.* [360, 361] were conducted later by Distin *et al.* [362] with slightly larger metal droplets (1 g and 2 g). In the case of O_2 injection, the mass transfer coefficients obtained with the Steinberger-Treybal were much higher than the measured values [362]. The deviation decreased with higher gas flow rates [362].

Table 18. Decarburisation of levitated Fe–C droplets [360]. Adapted from [116].

Parameter	Unit	CO_2 tests			O_2 tests		
x_{CO_2}	–	0.0081	0.884	0.097	–	–	–
x_{O_2}	–	–	–	–	0.0078	0.926	0.942
x_{CO}	–	0.038	0.116	0.903	0.0043	0.074	0.058
x_{He}	–	0.988	–	–	0.988	–	–
p_G	atm	1	1	1	1	1	0.1
$\overline{Gr}$	–	5.12	236	155	4.43	183	1.83
Decarburisation rate							
Observed	$\frac{mol}{m^2 s} \times 10^2$	2.88	96	20.7	5.65	520	400
Predicted – a.)	$\frac{mol}{m^2 s} \times 10^2$	2.52	98	18.4	5.72	354	276
Predicted – b.)	$\frac{mol}{m^2 s} \times 10^2$	–	–	–	–	495	386

Gas properties defined at: a.) $T_G = 0.5 \cdot (T_{in} + T^*)$; b.) $T_G = T^*$.

El-Kaddah and Robertson [363] studied the kinetic of decarburisation of levitated Fe–C droplets in CO–CO_2 gas mixtures. With respect to mass transfer, the metal droplets behaved similarly to stagnant spheres [363]. A qualitative confirmation of the internal concentration gradients was obtained from microscope analysis of rapidly quenched metal droplets [363]. The effective diffusivity of carbon was found to be three times the molecular value [363], which corresponds to Sh $\approx$ 20. This value is in good agreement with the asymptotic value of the Kronig-Brink [328] solution (Sh $\approx$ 17.9) for rigid spheres with internal circulation.

Widlund *et al.* [364] studied the decarburisation of relatively large ($d_{md} \approx 8$ mm) Fe–C–Si droplets in O_2–He mixtures (10–20 % O_2). Their experimental results suggest that the mass transfer within metal droplets becomes a rate-limiting mechanism, when the carbon contents of the metal droplets decreases to less than 0.5 wt-% [364]. Based on their data it is possible to deduce that the Sherwood number of the internal mass transfer should be Sh > 100, which indicates rapid circulatory mixing within the droplets.

Slag droplets in a metal bath

Mietz *et al.* [365] studied emulsification and mass transfer in ladle metallurgy and found that the rate constant was increased by higher rates of gas injection. The increase was attributed to the higher emulsified volume of the top phase as well as to smaller droplet size, which enables faster mass transfer.

Nakasuga *et al.* [366, 367] found that the reduction of Cr_2O_3 from slag was controlled by mass transport in the slag phase. The overall rate was found to be higher with higher amounts of CaF_2 and lower with a high sulphur content in the metal bath [366]. In the case of solid Cr_2O_3, the overall rate was found to be controlled by a chemical reaction rate at the interface [366]. In contrast to this result, Sevinc and Elliott [368] found when using rotational cylinders that the rate-limiting step for the reduction of solid Cr_2O_3 by liquid Fe–Cr–C alloys was the mass transfer of oxygen in the metal phase. Fruehan [223] studied the rate of reaction of Cr_2O_3 particles with Fe–Cr–C alloys in Ar–O_2 gas mixtures, and postulated that the rate of reaction is controlled by the diffusive mass transfer of dissolved carbon.

Gas bubbles in liquid metal

In the case of reactions between rising gas bubbles and liquid metal, the mass transfer resistance of the gas phase can usually be ignored [369]. The exact treatment of the continuous phase mass transfer coefficient is possible for small bubbles which are roughly spherical and rise in straight paths [352, 369]. The shapes and rising paths of larger bubbles are irregular and vary over time; reasonable approximates of the mass transfer rate, however, can be obtained even if this behaviour is ignored [352, 369]. At high Reynolds numbers (Re > 5000), the gas bubbles rising in the metal bath are spherical caps and their rising velocity is virtually independent of the liquid metal properties [116]. The findings by Lochiel and Calderbank [353] were later confirmed

by Guthrie and Bradshaw [370], who found that the experimentally determined mass transfer coefficients for oxygen bubbles in liquid silver were in good agreement with predictions in which mass transfer was assumed to take place only through the front of the spherical cap.

The findings of Calderbank and Moo-Young [337] suggest that the diameter and free rising velocity of the bubbles have no effect on the continuous phase mass transfer coefficient in gas–liquid dispersions. This is due to the mutually compensating effect of bubble size and slip velocity [337]. However, a distinction can be made between small gas bubbles ($d_b < 2.5$ mm), which behave similarly to rigid spheres, and large gas bubbles ($d_b > 2.5$ mm), which exhibit unhindered surface renewal [337].

4.4 Kinetic treatment of parallel reactions

Chemical reactions which take place in a single phase are called *homogeneous*, while reactions involving more than one phase are called *heterogeneous* [116, 349]. The reaction rate of a homogeneous reaction is tied to the mass transfer rate via mass balance, because the transported substance is converted in all places [349]. In the case of a heterogeneous reaction, the reaction occurs only at the reaction interface [349]. The mathematical description of heterogeneous reactions is more complex, because both the mass transport and chemical reaction at the interface may form a rate limiting step [116].

In metallurgy, most reactions of are heterogeneous. In practice, heterogeneous reactions between gas, liquid metal, and slag phases are typically limited by the mass-transfer of species onto and from the reaction surface [1, 220, 371, 372]. The mass transfer resistance of a single reaction can be described using the boundary layer theory,[23] which assumes that mass transfer resistance exists only in a thin boundary layer [1, 322, 349].[24] The overall mass transfer resistance of the boundary layer of two phases can be treated similarly to resistors in a series; this approach is known as the Lewis-Whitman model [233].

In the case of *parallel* heterogeneous reactions, the description of mass transfer in the boundary layer needs to be coupled with a description of the competitive thermodynamic equilibrium at the interface [1, 249, 322, 373]. More specifically, the equilibrium state is characterised by the minimum Gibbs free energy at the given temperature

[23] The boundary layer theory is also known as the film theory.

[24] One of the first qualitative descriptions of the boundary layer theory was proposed by Nernst [219] in 1904, and hence the diffusion boundary layer is also known as the *Nernst boundary layer* [1].

and pressure [374]. Various methods are available for the mathematical treatment of the thermodynamic driving force in the case of parallel oxidation reactions. A short description of these methods is presented in the following sections.

Affinity based selectivity method

Wei and Zhu [49] calculated parallel competing reactions in an AOD converter during combined top- and side-blowing. The main assumption in their method is that all the species on the liquid metal phase have equal availability and the selectivity is linearly dependent on the affinity of the reactions. The drawback of this method is that it does not define the reaction rate directly, and for this reason, is not suitable for use with the control volume method as such. The advantage of this approach is the simplicity and that it does not require a separate solution for the equilibrium composition. As shown in Article VI, the method is relatively insensitive to mass transfer constraints of species other than that of dissolved carbon.

Effective equilibrium constant method

The effective equilibrium constant method, also known as the coupled reaction model, has been applied extensively for mathematical modelling of various processes in converter and ladle metallurgy [367, 375–385]. In this approach, the equilibrium constants are modified to an effective equilibrium constant, which in combination with an electro-neutrality condition, are employed to solve a system of parallel mass transfer limited reactions. The effective equilibrium constant of an arbitrary reaction can be defined as follows [375]:

$$K_{\text{eff}} = \frac{\prod\limits_{p} x_p^{\nu_p}}{a_{[\text{O}]}^{\nu_{[\text{O}]}} \prod\limits_{\substack{r \\ r\neq[\text{O}]}} x_r^{\nu_r}} = \frac{K \prod\limits_{p} \gamma_p^{\nu_p}}{\prod\limits_{\substack{r \\ r\neq[\text{O}]}} \gamma_r^{\nu_r}}\,, \tag{165}$$

where r denotes the reactants and p denotes the reaction products. The balance of electroneutrality is given by

$$\sum_{i=1}^{n_{\text{L}}} \nu_{[\text{O}],i} n_i'' = 0\,, \tag{166}$$

where n_{L} denotes the number of species dissolved in the metal phase, $\nu_{\text{O},i}$ is the

stoichiometric ratio of [O] to species i, and n_i'' is the molar flux of species i. The molar flux of species i of phase ψ is defined in relation to the driving force as follows:

$$n_i'' = F_i\left([\%\mathrm{i}] - [\%\mathrm{i}]^*\right) = \frac{\beta_i \rho_\psi}{100 M_i}\left([\%\mathrm{i}] - [\%\mathrm{i}]^*\right), \tag{167}$$

where F_i is the modified mass transfer coefficient for 1 wt-% driving force.

Constrained Gibbs free energy minimisation method

Koukkari and co-authors [386–388] proposed a method for calculating the constrained chemical equilibrium by means of introducing mass transfer constraints to a traditional Gibbs energy minimisation routine. This method suggests that every constraint is accompanied by a conjugate potential and thus will have several physical interpretations in addition to mere equilibrium chemical potentials. The calculation of the inhibited equilibria is calculated as follows [386]:

1. Introduction of an appropriate addition to the stoichiometric matrix of the system.
2. Calculation of an unrestricted equilibrium by using $a = 1$ for the introduced new species.
3. Determination of the degree of inhibition by applying any value between 0 and the value calculated in step 2 for the input amount of the "new species".

The result of the calculational procedure is the interfacial composition, which, however, is not the direct interest of models discussed in this work.

Constrained solubility method

Ding *et al.* [27] proposed a mathematical model for the VOD process. Two different oxygen distribution models were investigated for the metal–gas zone; the former approach corresponds to the incremental step method, while the latter is based on constrained solubility of oxygen. The results obtained with the two models were found to be very similar [27]. In comparison to the incremental step method, the constrained solubility method proceeds in reverse order by first determining the dissolution of oxygen based on the minimum dissolved oxygen concentration in equilibrium with other dissolved elements and then distributing the remaining oxygen to the oxidation reactions [27]:

$$Q_{\mathrm{O}}^{t}\Delta t = R^{t} + D^{t}\,, \tag{168}$$

where Q_{O}^{t} is the oxygen supply per time step, Δt is the time step, R^{t} is the oxygen consumed by the reactions and D^{t} is the oxygen dissolved in the liquid metal. The oxygen dissolved per time step can be calculated from the change in the dissolved oxygen content [27]:

$$D^{t} = \frac{\left([\%\mathrm{O}]^{t} - [\%\mathrm{O}]^{t-\Delta t}\right) m_{\mathrm{bath}}^{t}}{100}\,. \tag{169}$$

Coupled Gibbs free energy minimization and volume element method

Ersson *et al.* [218] and Andersson *et al.* [214] coupled CFD models of BOF and AOD converters, respectively, with computational thermodynamics. The composition of the local control volume is achieved from the chemical species present after each time step. The rate of phase mass change obtained from this is then used as a constant rate for solving the rate at the new time step. Therefore, in addition to the solution of the flow field, equilibrium calculations need to be carried at every time step. In order to save computational work, equilibrium calculations were carried out only in the cells that have more than one phase present. This method does not require information on the interfacial surface area as the whole cell is set to equilibrium if an interphase exists. On the other hand, the solution is inherently grid dependent.

Incremental step method

Jalkanen [389] and Virrankoski *et al.* [390] presented a mathematical model for the BOF process. The principal approach in their model is that the supplied oxygen is used momentarily only by a single reaction that has the highest affinity. Gaseous oxygen is supplied to the reaction surface in small step amounts and the composition of the reaction surface is constantly updated. When one species is rapidly depleted from the surface, its affinity decreases. The model has been reported to be sensitive to the employed parameters, especially to the amount and size of the oxygen steps supplied to the system [390].

5 Law of mass action based kinetic approach

In this work, a novel approach based on the law of mass action (LMA) was studied and developed further to provide a thermodynamically consistent treatment of parallel mass transfer controlled reactions in steelmaking contexts.[25] The law of mass action, proposed by Waage and Guldberg [391, 392] in 1864, is a mathematical expression of solutions in dynamic equilibrium. More specifically, it relates the thermodynamic equilibrium to reaction kinetics and implies that forward and backward reaction rates must be equal at equilibrium. A stoichiometric reversible reaction of species $A_1 \dots A_n$ to species $B_1 \dots B_n$ can be written as follows [374]:

$$\underbrace{\sum_r \nu_r A_r}_{\text{reactants}} \underset{k_\text{b}}{\overset{k_\text{f}}{\rightleftharpoons}} \underbrace{\sum_p \nu_p B_p}_{\text{products}} \quad \begin{cases} \text{endothermic} & \text{if} \quad \Delta H > 0 \\ \text{exothermic} & \text{if} \quad \Delta H < 0 \end{cases}, \tag{170}$$

where ν is the stoichiometric coefficient, r denotes reactants, p denotes reaction products, k_f is the forward reaction rate coefficient, and k_b is the backward reaction coefficient. According to the law of mass action, the corresponding reaction rate (mol/s) is expressed by [126, 311]:

$$\tilde{R} = \underbrace{k_\text{f} \prod_r c_r^{\nu_r}}_{\substack{\text{forward} \\ \text{reaction}}} - \underbrace{k_\text{b} \prod_p c_p^{\nu_p}}_{\substack{\text{backward} \\ \text{reaction}}}, \tag{171}$$

where c is the molar concentration.[26] The ratio of forward and backward reactions is described by the equilibrium constant, expressed below in terms of concentrations [126, 311, 393]:

$$K_\text{c} = \frac{k_\text{f}}{k_\text{b}} \left[= \frac{\prod_p c_p^{\nu_p}}{\prod_r c_r^{\nu_r}} \right]_{\substack{\text{only at} \\ \text{equilibrium}}}. \tag{172}$$

The expression shown in Eq. 172 above is valid only for ideal solutions [394]. In other cases, the effective concentration of species in a mixture can be described by

[25] The approach is referred to as the *LMA approach*.

[26] The unit of the reaction rate coefficients k_f and k_b depends on the stoichiometry. In this work, no differentiation is made between the reaction coefficients expressed in different units.

replacing concentrations with *activities* [394, 395]. The corresponding equilibrium constant is defined as follows:

$$K = \frac{k_\mathrm{f}}{k_\mathrm{b}} \left[= \frac{\prod\limits_p a_p^{\nu_p}}{\prod\limits_r a_r^{\nu_r}} \right]_{\substack{\text{only at} \\ \text{equilibrium}}} . \tag{173}$$

As for the activities of gaseous species, it is necessary to differentiate between *real* and *ideal* gases (see Eq. 174). The activity of real gases is expressed in terms of fugacity, which is an expression for effective pressure [393]. The assumption of an ideal gas behaviour is valid in most metallurgical applications due to low to moderate pressures. Under such conditions, gaseous mixtures typically obey the *Lewis-Randall rule*, which states that the properties of the mixture can be determined based on the properties of its pure components and composition of the mixture [393].

$$a_i = \begin{cases} \dfrac{\overline{f}_i}{f_i^\circ} & \text{(real gas)} \\ \dfrac{p_i}{p_i^\circ} & \text{(ideal gas)} \end{cases} , \tag{174}$$

where $\overline{f}$ is the partial fugacity, f° is the fugacity at the standard state, p is the partial pressure, and p° is the standard pressure. Typically, the standard state of an ideal gas is chosen as p° = 1 atm. A useful expression of the dynamic equilibrium can be obtained by expressing the law of mass action in terms of activities. Substituting Eq. 173 into Eq. 171 and expressing the reaction rate in relation to surface area yields:

$$\tilde{R}'' = k_\mathrm{f} \left(\prod_r a_r^{\nu_r} - \frac{\prod\limits_p a_p^{\nu_p}}{K} \right) , \tag{175}$$

where k_f has the unit mol/(m^2·s). Finally, the following expression is obtained for the reaction rate in kg/(m^2·s):

$$R'' = k_\mathrm{f} \left(\prod_r a_r^{\nu_r} - \frac{\prod\limits_p a_p^{\nu_p}}{K} \right) , \tag{176}$$

where k_f has the unit kg/(m^2·s). The expression shown in Eq. 176 is referred to here as the *modified law of mass action*. It suggests that the reaction rate and the resulting

equilibrium state are determined by the activities, stoichiometric coefficients, forward reaction rate coefficient, and the equilibrium constant. Following the *Le Chatelier's principle*, increasing the total temperature will shift the equilibrium towards the side with smaller number gas moles and *vice versa*, but if the number of gas moles on either side of the reaction is equal, the pressure of the system will not affect the equilibrium [394]. Although the equilibrium constant K and the rate constant k_{f} are independent of composition, both are temperature-dependent [311]. At a constant temperature, the equilibrium constant is defined by [311]:

$$K = \exp\left(-\frac{\Delta G^{\circ}}{RT}\right) \quad \text{where} \quad \Delta G^{\circ} = \Delta H^{\circ} - T\Delta S^{\circ}\,, \tag{177}$$

where ΔG° is the change in standard Gibbs free energy of reaction, R is the gas constant, T is the temperature, ΔH° is the change in standard enthalpy of reaction, and ΔS° is the change in standard entropy of reaction.

5.1 Rate of chemical reaction at the interface

Several theoretical equations have been proposed for calculating the rate of chemical reaction at the interface. The temperature dependency of the reaction rate coefficient can be expressed according to the *Arrhenius equation* shown in Eq. 178 [126, 257, 311, 396]. A somewhat analogous expression of the temperature dependency can be derived based on the transition state theory and is known as the *Eyring equation* (Eq. 179) [126, 311, 396].

$$k = A\exp\left(-\frac{E_{\mathrm{a}}}{RT}\right) \qquad \text{(Arrhenius equation)}\,, \tag{178}$$

$$k = \frac{k_{\mathrm{B}}T}{h}\exp\left(\frac{\Delta S_{\mathrm{a}}}{R}\right)\exp\left(-\frac{\Delta H_{\mathrm{a}}}{RT}\right) \qquad \text{(Eyring equation)}\,, \tag{179}$$

where A is the frequency factor, E_{a} is the activation energy, k_{B} is the Boltzmann's constant, h is the Planck's constant, ΔS_{a} is the entropy of activation, and ΔH_{a} is the enthalpy of activation. In the case of gas phase reactions, the reaction rate coefficient can be estimated using the collision theory (Eq. 180), which assumes that the reaction rate coefficient depends on the collision frequency between reactant molecules [126, 311, 396, 397]. Comparison with experimental data suggests that the collision theory based approach frequently over-estimates the reaction rate coefficient [126, 311, 396, 397].

This tendency can be compensated for an additional *probability* or *steric* factor P as shown in Eq. 181 [396, 397]. The steric factor is a measure of the deviation of an actual reaction rate from the ideal rate suggested by the collision theory [396, 397], but can also be interpreted as the ratio of the target area for the reaction to the target area of a simple non-reactive collision [396].[27]

$$k = Z_{\mathrm{AB}} \frac{10^3}{N_{\mathrm{a}}} \exp\left(-\frac{E_{\mathrm{a}}}{RT}\right) \qquad \text{(collision theory)}, \tag{180}$$

$$k = PZ_{\mathrm{AB}} \frac{10^3}{N_{\mathrm{a}}} \exp\left(-\frac{E_{\mathrm{a}}}{RT}\right) \qquad \text{(modified collision theory)}, \tag{181}$$

where Z_{AB} is the collision frequency between molecules A and B, and N_{a} is the Avogadro constant. Based on Eqs. 178–181 it can be deduced that the value of the reaction rate coefficient is likely to be very large at typical steelmaking temperatures.

Only a little experimental information on the rate of chemical reactions at the interface is available for metal–slag reactions. Because metal–slag reactions are electrochemical in nature, some authors have attempted to determine the interfacial reaction rate by measuring the exchange current density [398–401]. Pretnar and Schmalzried [399] studied the interfacial reaction rate of

$$[\mathrm{Si}] \rightleftharpoons (\mathrm{Si})^{4+} + 4\mathrm{e}^{-}, \tag{182}$$

using a galvanostatic pulse method. The obtained exchange current densities were approximately 240 A/m^2 [6.2·10^{-4} mol/(m^2·s)] at 1273 K (1000 °C) and 380 A/m^2 [9.8·10^{-4} mol/(m^2·s)] at 1373 K (1100 °C), suggesting that the mass transfer resistance and reaction resistance at the interface are of same magnitude [399]. When extrapolated to a temperature of 1600 °C (1873 K), the exchange current densities ranged from 1500 to 2600 A/m^2 depending on the value of activation energy employed [399]. However, it was found later that the exchange current density measured by Pretnar and Schmalzried [399] was not the pure exchange current density, because a concentration gradient had already formed, and thus the resistance of the interfacial reaction was estimated to be too high [1, 401]. Schwerdtfeger and Prange [401] studied the interfacial reaction rates of Eqs. 182 and 183 at 1873 K (1600 °C) and 1723 K (1450 °C), respectively, using single and double pulse techniques.

[27] The rate coefficients predicted by Eqs. 180 and 181 have the unit [mol/(l·s)] *i.e.* [kmol/(m^3·s)].

$$\mathrm{Fe_{(l)}} \rightleftharpoons (\mathrm{Fe})^{2+} + 2\mathrm{e}^- \,, \tag{183}$$

Schwerdtfeger and Prange [401] found that the interfacial reaction resistance was very small in comparison to the mass transfer resistance. The exchange current densities corresponding Eqs. 182 and 183 were measured to be approximately 200,000 A/m^2 [401] and 20,000 to 100,000 A/m^2 [400, 401], respectively; these values are considerably larger than those reported by Pretnar and Schmalzried [399]. Nagata and Goto [402] conducted similar experiments to study the reaction

$$\mathrm{Si_{(s)}} \rightleftharpoons (\mathrm{Si})^{4+} + 4\mathrm{e}^- \,, \tag{184}$$

and found that the overall reaction was controlled by diffusion in the slag. As suggested by Oeters [1], it appears reasonable to expect that the interfacial reaction rates of metal–slag reactions under steelmaking conditions are – with some reservations – very fast and do not affect the overall rate to a significant extent.

Similarly to metal–slag reactions, most metal–gas oxidation reactions are very fast. Notable examples of reactions controlled by the interfacial reaction rate include the absorption of nitrogen [138] and the dissociation of $\mathrm{CO_2}$ to CO by dissolved carbon [403]. In such cases, the description of the rate coefficient can be inserted into the modified law of mass action (see [44]).

5.2 Mathematical basis (Articles V and VI)

As discussed earlier, most heterogeneous reactions relevant to process metallurgy are effectively controlled by mass transport to the reaction interface. The principal proposition of this work is that the mathematical treatment of such reactions can then proceed as if the reaction interface were able to reach its equilibrium composition instantaneously. For this reason, it is assumed that the exact value of the forward reaction rate coefficient is irrelevant as long as it is sufficiently large. At first, only a single oxidation reaction is considered. Writing in terms of $\mathrm{O_2}$, the reaction equation can be written as follows:

$$\frac{i}{\nu_i} + \{\mathrm{O_2}\} \rightleftharpoons \frac{1}{\nu_i}\mathrm{iO}_{2\nu_i} \,, \tag{185}$$

where ν_i is the stoichiometric coefficient of species i. Considering oxygen as an ideal gas, the following rate expression is obtained:

$$R'' = k_\mathrm{f}\left(a_i^{1/\nu_i} p_{\mathrm{O}_2} - \frac{a_{i\mathrm{O}_{2\nu_i}}^{i/\nu_i}}{K}\right) = k_\mathrm{f}\left(a_i^{1/\nu_i} b y_{O_2} - \frac{a_{i\mathrm{O}_{2\nu_i}}^{i/\nu_i}}{K}\right), \tag{186}$$

where y is the mass fraction and b is the coefficient relating y to p. The conservation of oxygen at the reaction interface defined by

$$\underbrace{R'' = k_\mathrm{f}\left(a_i^{1/\nu_i} b y_{\mathrm{O}_2}^* - \frac{a_{i\mathrm{O}_{2\nu_i}}^{i/\nu_i}}{K}\right)}_{\text{reaction rate at the interface}} = \underbrace{\beta_\mathrm{G}\rho_\mathrm{G}\left(y_{\mathrm{O}_2} - y_{\mathrm{O}_2}^*\right)}_{\text{mass transport to the interface}}, \tag{187}$$

where β_G is the mass transfer coefficient of the gas phase, ρ_G is the density of the gas phase, y_i is the mass fraction of species i, and y_i^* is the interfacial mass fraction of species i. By solving the mass fraction of oxygen at the interface, it is found that the oxygen partial pressure at the interface approaches its equilibrium value $y_{\mathrm{O}_2,\mathrm{e}}$ as the reaction rate approaches infinity:

$$\lim_{k_\mathrm{f}\to\infty} y_{\mathrm{O}_2}^* = \frac{a_{i\mathrm{O}_{2\nu_i}}^{1/\nu_i}}{b a_i^{1/\nu_i} K} = y_{\mathrm{O}_2,\mathrm{e}}\,. \tag{188}$$

Consequently, the following limit is obtained for the reaction rate:

$$\lim_{k_\mathrm{f}\to\infty} R'' = \beta_\mathrm{G}\rho_\mathrm{G}\left(y_{\mathrm{O}_2} - \frac{a_{i\mathrm{O}_{2\nu_i}}^{1/\nu_i}}{b a_i^{1/\nu_i} K}\right) = \beta_\mathrm{G}\rho_\mathrm{G}\left(y_{\mathrm{O}_2} - y_{\mathrm{O}_2,\mathrm{e}}\right). \tag{189}$$

In the following, a case of n parallel reactions between oxygen and species dissolved in liquid steel is studied. Below, the reaction equations are written both in terms of dissolved species (Eq. 190) and with O_2 as the key component (Eq. 191).

$$i + \nu_i\{\mathrm{O}_2\} \rightleftharpoons i\mathrm{O}_{2\nu_i} \qquad \text{for} \quad i = 1,2\ldots n, \tag{190}$$

$$\frac{i}{\nu_i} + \{\mathrm{O}_2\} \rightleftharpoons \frac{i}{\nu_i} i\mathrm{O}_{2\nu_i} \qquad \text{for} \quad i = 1,2\ldots n, \tag{191}$$

where i denotes the key component used to define the rate expression and ν is the stoichiometric coefficient. The equilibrium constants corresponding to Eqs. 190 and 191 are given by Eqs. 192 and 193, respectively.

$$K_i = \exp\left(-\frac{\Delta G_i^\circ}{RT}\right) = \frac{a_{i\mathrm{O}_{2\nu_i}}}{a_i p_{\mathrm{O}_2}^{\nu_i}}\,. \tag{192}$$

$$K_i^{\mathrm{G}} = K_i^{1/\nu_i} = \exp\left(-\frac{\Delta G_i^\circ}{RT\,\nu_i}\right) = \frac{a_{i\mathrm{O}_{2\nu_i}}^{1/\nu_i}}{a_i^{1/\nu_i} p_{O_2}}\,. \tag{193}$$

As in the case of a single reaction system, the rate expressions were formulated according to the modified law of mass action in molar basis. For the sake of simplicity, the *stationary medium approach* [279] was employed and hence the bulk motion induced by density differences was not accounted for. Therefore, the mole balance of species i diffusing from the metal phase the bulk steel phase onto the reaction interface is defined by Eq. 194. The corresponding mole balance for O_2 is defined by Eq. 195.

$$\underbrace{\beta_{\mathrm{L}}\frac{c_{\mathrm{L}}}{M_{\mathrm{L}}}\left(x_i - x_i^*\right)}_{\substack{\text{mass transport}\\ \text{to the interface}}} = \underbrace{\beta_{\mathrm{L}}\frac{c_{\mathrm{L}}}{M_{\mathrm{L}}}\left(x_i - \frac{a_i}{\gamma_i}\right)}_{\substack{\text{mass transport}\\ \text{to the interface}}} = \underbrace{k_{\mathrm{f}}\left(a_i p_{\mathrm{O}_2}^{\nu_i} - \frac{a_{i\mathrm{O}_{2\nu_i}}}{K_i}\right)}_{\substack{\text{reaction rate}\\ \text{at the interface}}}, \tag{194}$$

$$\underbrace{\beta_{\mathrm{G}}\frac{p_{\mathrm{G}}}{RT}\left(x_{\mathrm{O}_2} - x_{\mathrm{O}_2}^*\right)}_{\substack{\text{mass transport}\\ \text{to the interface}}} = \underbrace{\beta_{\mathrm{G}}\frac{p_{\mathrm{G}}}{RT}\left(x_{\mathrm{O}_2} - \frac{p_{\mathrm{O}_2}}{\gamma_{\mathrm{O}_2}}\right)}_{\substack{\text{mass transport}\\ \text{to the interface}}} = \underbrace{\sum_{i=1}^{n} k_{\mathrm{f}}\left(a_i^{1/\nu_i} p_{\mathrm{O}_2} - \frac{a_{i\mathrm{O}_{2\nu_i}}^{1/\nu_i}}{K_i^{\mathrm{G}}}\right)}_{\substack{\text{reaction rate}\\ \text{at the interface}}}, \tag{195}$$

where β_{L} is the mass transfer coefficient of the liquid phase, c_{L} is the molar concentration of the liquid phase, M_{L} is the molar mass of the liquid phase, x is the mole fraction, γ is the activity coefficient, and p_{G} is the total pressure of the gas phase. As the considered the system consists of $n+1$ variables and $n+1$ equations, the system can be solved iteratively. The activities of the dissolved species and oxygen can be solved from Eqs. 196 and 197, respectively.

$$a_i = \frac{\dfrac{\beta_{\mathrm{L}} x_i}{k_{\mathrm{f}}}\dfrac{c_{\mathrm{L}}}{M_{\mathrm{L}}} + \dfrac{a_{i\mathrm{O}_{2\nu_i}}}{K_i}}{\dfrac{\beta_{\mathrm{L}}}{k_{\mathrm{f}}\gamma_i}\dfrac{c_{\mathrm{L}}}{M_{\mathrm{L}}} + a_{\mathrm{O}_2}^{\nu_i}} \qquad \text{for} \quad i = 1,2\ldots n\,. \tag{196}$$

$$p_{\mathrm{O}_2} = \frac{\dfrac{\beta_{\mathrm{G}} x_{\mathrm{O}_2}}{k_{\mathrm{f}}} \dfrac{p_{\mathrm{G}}}{RT} + \sum_{i=1}^{n} \left(\dfrac{a_{i\mathrm{O}_{2\nu_i}}^{1/\nu_i}}{K_i^{\mathrm{G}}} \right)}{\dfrac{\beta_{\mathrm{G}}}{k_{\mathrm{f}} \gamma_{O_2}} \dfrac{p_{\mathrm{G}}}{RT} + \sum_{i=1}^{n} \left(a_i^{1/\nu_i} \right)}. \tag{197}$$

By letting the forward reaction rate coefficients approach infinity, the following limits are obtained for the activities of the dissolved species and the partial pressure of oxygen at the reaction interface:

$$\lim_{k_{\mathrm{f}} \to \infty} a_i = \frac{a_{i\mathrm{O}_{2\nu_i}}}{K_i a_{\mathrm{O}_2}^{\nu_i}} = a_{i,\mathrm{e}} \qquad \text{for} \quad i = 1, 2 \ldots n, \tag{198}$$

$$\lim_{k_{\mathrm{f}} \to \infty} p_{\mathrm{O}_2} = \frac{\sum_{i=1}^{n} \left(\dfrac{a_{i\mathrm{O}_{2\nu_i}}^{1/\nu_i}}{K_i^{\mathrm{G}}} \right)}{\sum_{i=1}^{n} \left(a_i^{1/\nu_i} \right)} = p_{\mathrm{O}_2,\mathrm{e}}\,. \tag{199}$$

The limit shown in Eq. 198 satisfies the definition of the equilibrium constant, but the limit shown in Eq. 199 corresponds to the equilibrium oxygen partial pressure formed as a result of the competing oxidation reactions.

5.3 Implementation

It is important to understand that the equilibrium composition solved at the reaction interface is not the *full* chemical equilibrium that can be determined with traditional methods, such as the equilibrium constant method or Gibbs free energy minimisation, but rather a *dynamic* chemical equilibrium: the equilibrium permitted by the mass transfer rates onto and from the reaction interface. In essense, the law of mass action based method is *a rate expression for parallel mass transfer controlled reactions.*

As only finite values are permitted in numerical analysis, one of the most difficult tasks is to find forward reaction rate coefficients which are sufficiently large to bring the system close to equilibrium. In order to counter this problem, two methods were devised in the course of this work:

1. *A reaction quotient method*: a predefined small error is permitted in the reaction quotient by employing the concept of an equilibrium number. Owing to its simple

implementation, this method was used as the basis for the mathematical models for top-blowing and reduction of slag.

2. *A residual affinity method*: a predefined small error is permitted in the Gibbs free energy by using the concept of residual affinity. A simple decarburisation model was derived to illustrate this method.

The description of the two methods is provided in the following.

5.3.1 Reaction quotient method (Article I)

The aim of the reaction quotient method is to provide a numerical solution, which is very close to that dictated by the equilibrium constants. The Gibbs free energy of reaction is defined by [126]:

$$\Delta G = \Delta G^{\circ} + RT \ln Q, \tag{200}$$

where Q is the reaction quotient, which is defined as follows [126, 395]:

$$Q = \frac{\prod_p a_p^{\nu_p}}{\prod_r a_r^{\nu_r}}. \tag{201}$$

By definition, $Q = K$ at equilibrium [126, 395].[28] In order to provide a quantitative estimate of the error in the dynamic equilibrium, the concept of a dimensionless *equilibrium number* was introduced:

$$\mathrm{E} = \left| 1 - \frac{Q}{K} \right| = \frac{\text{absolute deviation from the equilibrium constant}}{\text{equilibrium constant}}, \tag{202}$$

where Q and K are the reaction quotient and the equilibrium constant, respectively. As a limit, E = 0 when $Q \to K$, E = 1 when $Q \to 0$, and $\mathrm{E} = \infty$ when $Q \to \infty$. Owing to these limits the equilibrium number is a convenient measure of the maximum allowed error in the equilibrium constants.

In this work, the numerical solution was executed so that the forward reaction rate coefficients k_f were increased periodically during iteration until the equilibrium number E of all reactions was smaller than a predefined maximum value. If the increment is too small, the solution is obtained at greater computational expense. On the other hand,

[28] This becomes evident by setting $\Delta G = 0$ and substituting Eq. 177 into Eq. 200.

overly large increments may cause numerical instability and prevent the numerical solution altogether. A reasonable compromise was obtained by defining the increment as a function of the equilibrium number so that large increments are employed when the error is large and *vice versa*.

5.3.2 Residual affinity method (Article VI)

The starting point for the residual affinity method is the notion that at equilibrium, the affinity (or the driving force) of the reactions at equilibrium should be equal to zero. This stems from the definition of the equilibrium constant. In a mass transfer limited setting, the affinity of a reaction is zero only when the forward reaction rate coefficient is equal to infinity. In order to find sufficiently large finite values, the concept of *residual affinity* is introduced and employed for setting the thermodynamic system at a predefined distance away from the exact solution, thus enabling the numerical solution of the problem. The residual affinities are defined according to

$$-A = \Delta G^\circ + RT \ln \left(\frac{\prod_p a_p^{\nu_p}}{\prod_r a_r^{\nu_r}} \right) . \tag{203}$$

If the residual affinity is small in comparison to the standard Gibbs free energies of the reactions, the resulting deviation from the exact solution is negligible. In the numerical solution, the formulations of the residual affinities are implemented as additional conservation equations; these should correspond to the form shown in Eq. 204. In addition, it may be necessary to define additional constraints for the activities.

$$\prod_r a_r^{\nu_r} - \frac{\prod_p a_p^{\nu_p}}{\exp\left(-\frac{A+\Delta G^\circ}{RT}\right)} = 0 . \tag{204}$$

In order to illustrate the LMA method, a simple model consisting of three oxidation reactions was developed. The observed reactions and the reference states of the species are as follows:

$$\mathrm{Si_{(l)}} + \{\mathrm{O_2}\} \rightleftharpoons \mathrm{SiO_{2\ (\beta\text{-cristobalite})}} , \tag{205}$$

$$\mathrm{Cr_{(l)}} + \frac{3}{4}\{\mathrm{O_2}\} \rightleftharpoons \frac{1}{2}\mathrm{Cr_2O_{3\ (s)}} , \tag{206}$$

$$\mathrm{C_{(graphite)}} + \frac{1}{2}\{\mathrm{O_2}\} \rightleftharpoons \{\mathrm{CO}\}\,. \tag{207}$$

The Raoultian reference state was employed for all the species, and the standard Gibbs free energy changes of the studied reactions were taken from the literature [404]. The calculations presented are related to a single moment in time only and hence the composition of the species in the bulk phases including the slag is assumed to be constant. The conservation of species i (Si, Cr, C) in the liquid phase and O_2 in the gas phase were defined by Eqs. 208 and 209, respectively.

$$\beta_\mathrm{L}\frac{\rho_\mathrm{L}}{M_\mathrm{L}}\left(x_i - a_i^\mathrm{R}\right) + \sum_{k=1}^{r} \nu_{i,k} k_{\mathrm{f},k}\left(\prod_r \left(a_r^\mathrm{R}\right)^{\nu_r} - \frac{\prod_p \left(a_p^\mathrm{R}\right)^{\nu_p}}{K_k}\right) = 0\,. \tag{208}$$

$$\begin{aligned}\beta_G\frac{p_G}{RT}\left(x_{\mathrm{O_2}} - p_{\mathrm{O_2}}\right) - \beta_\mathrm{L}\frac{\rho_\mathrm{L}}{M_\mathrm{L}}\left(x_\mathrm{Si} - a_\mathrm{Si}^\mathrm{R}\right)\\ - 0.75\beta_\mathrm{L}\frac{\rho_\mathrm{L}}{M_\mathrm{L}}\left(x_\mathrm{Cr} - a_\mathrm{Cr}^\mathrm{R}\right) - 0.5\beta_\mathrm{L}\frac{\rho_\mathrm{L}}{M_\mathrm{L}}\left(x_\mathrm{C} - a_\mathrm{C}^\mathrm{R}\right) = 0\,.\end{aligned} \tag{209}$$

It should be noted that the activities a_i^R are defined at the interfacial composition x_i^*. In addition to the equations for the conservation of mass, three conservation equations were defined for the residual affinities:

$$a_\mathrm{Si}^\mathrm{R} p_{\mathrm{O_2}} - \frac{a_{\mathrm{SiO_2}}^\mathrm{R}}{\exp\left(-\frac{A+\Delta G_0^\circ}{RT}\right)} = 0\,, \tag{210}$$

$$a_\mathrm{Cr}^\mathrm{R} p_{\mathrm{O_2}}^{0.75} - \frac{\left(a_{\mathrm{Cr_2O_3}}^\mathrm{R}\right)^{1/2}}{\exp\left(-\frac{A+\Delta G_1^\circ}{RT}\right)} = 0\,, \tag{211}$$

$$a_\mathrm{C}^\mathrm{R} p_{\mathrm{O_2}}^{0.5} - \frac{1 - p_\mathrm{CO}}{\exp\left(-\frac{A+\Delta G_2^\circ}{RT}\right)} = 0\,. \tag{212}$$

In addition, the constraints $p_\mathrm{CO} = 1 - p_{\mathrm{O_2}}$, $a_{\mathrm{SiO_2}}^\mathrm{R} = 0.5$ and $a_{\mathrm{Cr_2O_3}}^\mathrm{R} = 1 - a_{\mathrm{SiO_2}}^\mathrm{R}$ were set for the partial pressure of CO, activity of SiO_2 and activity of Cr_2O_3, respectively. The numerical solution for the non-linear system of seven conservation equations was calculated by employing Newton's method.

6 Mathematical modelling of the AOD process

The development of the *Converter Process Simulator* started from the mathematical model for reactions during side-blowing proposed by Järvinen *et al.* [44] (see p. 81). The simulator was programmed using C++ and features a graphical user interface developed using the Visual Basic programming language. In this work, the simulator was extended with two reaction models: a reduction stage model (Articles III and IV) and a top-blowing model (Articles I and II). Furthermore, the melting of alloying elements and refractory wear were added as sub-models. A schematic illustration of the material flows and interactions between phases is shown in Fig. 21. The graphical user interface was updated to accommodate the simulation of the new process stages.

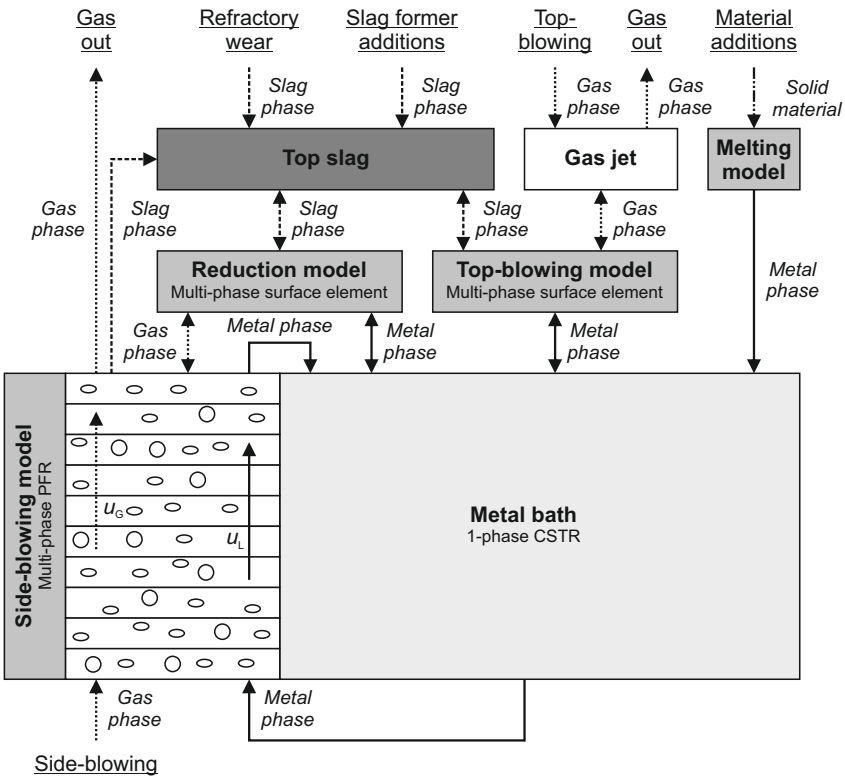

Fig 21. Schematic illustration of the Converter Process Simulator.

6.1 Work flow of the simulator

The work flow of the simulator is described briefly in the following. First, the model receives the input values from the user interface; these include (but are not limited to) metal bath and slag composition, metal bath mass, slag mass, converter geometry, blowing scheme, and material additions. The simulated process is divided into temporal increments, *i.e.* time steps. The structure of the calculation cycle depends on the studied process stage(s). At the beginning of each time step, the simulated process stage is detected based on the employed gas injection scheme. As shown in Fig. 22, three different routes can be identified: combined-blowing decarburisation, side-blowing decarburisation, and the reduction stage. Additions of scrap and slag formers, as well as their effect on the relevant compositions and temperatures are calculated analytically after the reaction modules. Finally, the program prints the results and proceeds on to a new time step. The calculation cycle is then repeated until the total process time studied is reached.

6.2 A model for reactions during top-blowing (Article I)

In the context of steelmaking converters, top-blowing denotes the injection of a gas mixture from a top lance, which is positioned perpendicular to the metal bath. Prior to impingement in the metal bath, the gas jet is in physico-chemical interaction with the converter atmosphere (see Section 2.1.2 on p. 40). Thereafter, the gas jet is in contact with the metal bath. The interaction of the gas jet with the metal bath is complicated by chemical reactions, which proceed very rapidly. Before the introduction of the model, a short review of the present knowledge of the reaction mechanisms is presented.

6.2.1 Reaction mechanisms

A considerable amount of research work has been devoted to identifying the reaction mechanisms in order to explain the high decarburisation rates observed in top-blowing steelmaking converters. Several reaction sites have been envisaged and are presented briefly in the following.

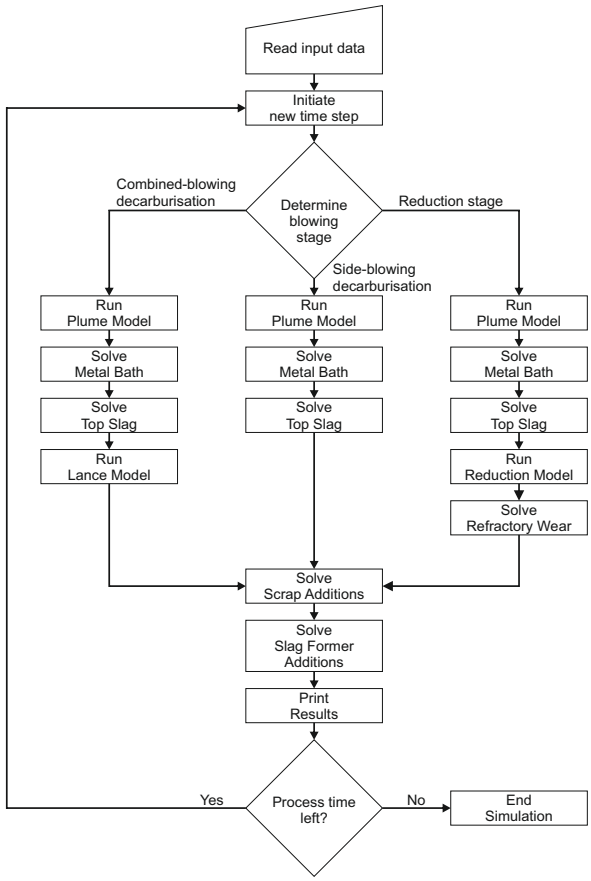

Fig 22. Flow chart of the simulator.

Impact area

The impact area of the gas jet forms a reaction site for direct oxidation reactions [1, 295, 405–420] and a local superheated reaction zone known as the *hot spot* [407, 415, 417, 419]. During the decarburisation of Fe–C melts, the temperature of the impact area can rise up to 2273–2773 K (2000–2500 °C) in the case of high specific oxygen top-blowing rates [407, 415, 417, 421]. These values have been obtained directly above the metal bath with pyrometers [407, 415, 417] or radiation spectroscopy [421], and correspond to an excess temperature of 500–800 K [407, 415, 417], while the largest temperature variations recorded with thermocouples are in the order of 100 K [414, 415].

Similar results have been obtained with radiation spectrometry. Both methods indicate that the superheat vanishes as the carbon content falls below a critical value [414, 415]. However, much smaller superheats have been reported for the decarburisation of Fe–C heats with low specific oxygen top-blowing rates of ≤ 2 Nm^3 O_2/(t·min) [422]. This finding is important, because the top-blowing rates employed in the AOD process are typically 1–1.6 Nm^3/(t·min) [80]. For example, Delhaes *et al.* [73] have estimated, based on vaporisation of Mn, that the average temperature of the hot spot should be approximately 2173 K (1900 °C) during pure-oxygen combined-blowing in the initial period of the AOD process; the proposed value denotes an excess temperature of 300–400 K. Tsujino *et al.* [423] reported a much higher average temperature of 2623 K (2350 °C) based on top- and combined-blowing decarburisation of stainless steel in a 100 kg furnace.

The initial understanding of the oxygen steelmaking processes was that all reactions would take place in the hot spot region [410, 424]. However, it was rapidly understood that the impact area alone was too small to be responsible for the high decarburisation rates observed in steelmaking converters with top-blowing [1, 408, 410–412, 414, 416, 419, 420, 424, 425]. Furthermore, the mass transfer rate at the cavity is not sufficiently high to compensate for the relatively small interfacial area [116, 294, 295, 297, 299, 414]; this effect becomes more pronounced at low carbon contents [413]. In experimental-scale vessels, however, decarburisation can take place almost entirely at the impact area due to the larger ratio of the surface area to the bath volume [1, 406, 411, 426].[29] The indirect oxidation of carbon at the impact zone may take place due to the reduction of iron oxide by carbon [382]. The kinetics of oxygen absorption by liquid iron have been studied in [429, 430]. The absorption kinetics were found to consist of two successive steps [429]: 1) rapid oxygen absorption, which is accompanied a rapid rise in temperature and continues until the solubility limit of oxygen is exceeded, and 2) formation of an oxide layer and the diffusion of oxygen through the layer into the melt. The formation of an oxide layer has also been observed in later studies [431]. The role of FeO as an intermediary product has received support in the literature regarding top-blowing in the AOD process [137].

[29] Some mathematical models [427, 428] have employed simplified descriptions which focus on the impact area and provide no description for the contribution of metal droplets to chemical reactions. Consequently, the values of the kinetic parameters employed in such models have limited physical meaning.

CO formation in the bath

High-speed films from hot experiments [413, 432] have confirmed that only limited formation of CO bubbles takes place in the lower part of the bath, *i.e.* outside the above-mentioned reaction areas. This is in agreement with thermodynamic considerations, which suggest that the homogeneous nucleation of CO in the metal bath is virtually impossible [433, 434]. In the case of reduction of FeO_n or MnO by carbon, however, the oxygen potential is typically sufficiently high to enable the spontaneous formation of CO bubbles [435].

Metal droplets

Numerous studies have established that metal droplets, which are generated due to the shear force of the gas jet impacting the metal surface, play a decisive role in defining the reaction rates due to their vast surface area [1, 156, 338, 408–412, 418–420, 424, 425, 436–443]. Furthermore, metal droplets can participate in reactions at different sites. One reaction site is the cavity area, where the metal droplets may react directly with atmosphere and top-blown gas [300, 405, 406, 411, 412, 414, 431, 444, 445]. In [431], the thickness of the oxide layer covering the oxidised droplets was determined to be approximately 60 μm. In physical experiments concerning top-blowing of CO_2 on water [300], the CO_2 concentration of the splashed water droplets was found to be 3–6 greater than that of the water bath. The maximum CO_2 absorption was found to occur halfway between the cavity and the walls of the vessel [300].

The metal droplets can emulsify in the top slag, where they react with slag species [412, 413, 418, 424, 443, 446]. If the slag is foamy, the metal droplets also react with the gas phase [412, 414]. Due to their higher density, the metal droplets exit the slag after a certain residence time due to gravity [447]. In [446], the quantity of metal droplets in the BOF slag was found to vary between 2.5 and 17.5 kg per ton of hot metal, while a considerably higher range of 68 to 780 kg per ton of hot metal was reported in [410]. Based on analysis of results from a 6 t BOF converter, Spooner *et al.* [443] reported that the amount of metal droplets in the BOF slag was 213 kg per ton of hot metal, while the average circulation rate was reported to be 15 kg/s per ton of hot metal. Simulations by Sarkar *et al.* [441] indicate a range of 2 to 300 kg of metal droplets in the emulsion per ton of hot metal and a droplet generation rate of 1 to 20 kg/s per ton of hot metal. The variance in the reported values stems to some extent from the sampling

method used. Based on laboratory-scale experiment it has been shown that the share of metal droplets in the immediate vicinity of the cavity can be much higher than the average value [431, 448]. The surface area of the metal droplets has been estimated to be in the order of thousands or tens of thousands of square meters [338, 410, 442, 446]. Some estimates of the residence times have been reported in the literature. The reported residence times of the metal droplets are only few seconds in periods without the foam, but vary approximately between 10 to 200 seconds in the presence of the foam during peak decarburisation [440, 443, 447].

Only a little experimental information is available about the contribution of metal droplets in the AOD process. However, foaming of slag similar to the BOF process has not been reported to occur during top-blowing in the AOD process. Therefore, the residence times of metal droplets induced by top-blowing are likely to be relatively short. Rubens and co-authors [156, 157] studied decarburisation slags from combined-blowing practice and analysed metal droplets found in the slag samples. The total amount of metal droplets in the slag was reported to be approximately 10–35 wt-% [157]. In the high carbon region – where combined-blowing was employed – the carbon content of the metal droplets (mm range) was found to be considerably below that of the metal bath (Fig. 23a). The observed difference in carbon content was found to decrease towards the end of the decarburisation stage. During combined-blowing, the chromium content of metal droplets in the mm-range was slightly higher than that of the metal bath, while the chromium content of fine metal droplets (μm-range) was considerably below the chromium content of the metal bath (Fig. 23b). These results indicate that the decarburisation of fine metal droplets takes place primarily in contact with gaseous oxygen, while larger metal droplets are decarburised mainly in contact with the top slag.

In addition to top-blowing, metal droplets are generated due to side-blowing. Lindstrand *et al.* [449] studied the metal droplets in decarburisation slags from side-blowing operation and found that their original composition corresponds to the composition of the metal bath and that they account for 2–7% of the slag mass.

Modelling approaches

Although the high mass exchange area created by metal droplets has been noted in the literature [4, 156, 157, 211], no definite answer has been given for the reaction mechanism(s) of decarburisation during top-blowing in the AOD process due to limited amount of experimental data.

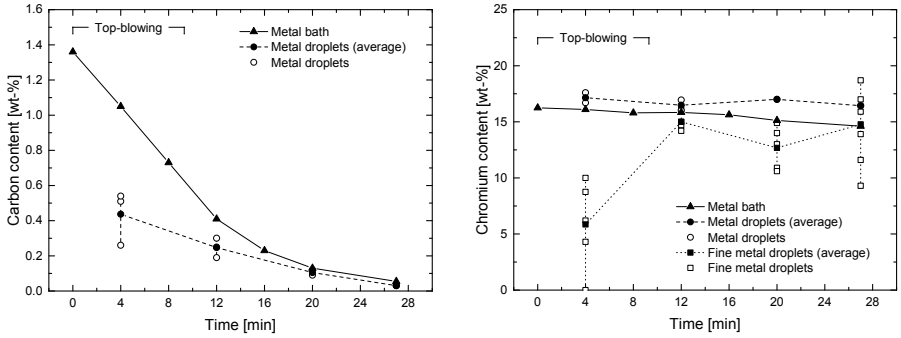

(a) Carbon content. **(b) Chromium content.**

Fig 23. Carbon and chromium content in the metal bath and metal droplets during the AOD process. Adapted from [156].

Scheller and Wahlers [134] studied reaction areas during combined-blowing and proposed that decarburisation takes place simultaneously in two reaction zones: inside the metal bath and on the surface of the bath, including metal droplets. The generation of metal droplets was thought to be caused by top-blowing and the bursting of gas bubbles at the bath surface [134]. Uchida *et al.* [211] conducted experiments on nitrogen top-blowing in the low carbon region and reported that the increased decarburisation rate was attributable not only to decreased partial pressure of CO and the promotion of slag–metal reactions by the stirring energy of the gas jet, but also due to the increase in the gas–metal reaction interface in the form of splashing. Zhu *et al.* [137, 144] postulated the following reaction mechanism:

– the top-blown oxygen dissolves into the bath primarily through the cavity and oxidises species dissolved in iron as well as iron itself. The oxide particles formed at the cavity are drawn into the metal bath by the gas jet and thus transfer oxygen, and
– the splashed metal droplets absorb part of the oxygen and oxidation of dissolved species takes place inside the droplets after integral iron-bearing slag films are generated on their surfaces.

Only a few approaches have been proposed for mathematical modelling reactions during top-blowing. Vercruyssen *et al.* [37] studied the refining of stainless steel in a combined-blowing MRP converter and assumed that the reactions take place at metal–slag, metal–gas, and slag–gas interfaces. Both the interfacial areas and the related mass transfer coefficients were employed as adjustable parameters. Based on

experimental data on oxygen top-blowing with simultaneous inert gas-stirring, the metal–slag, metal–gas, and slag–gas interfacial areas were estimated to be 200, 100, and 100 m^2, respectively. Kikuchi *et al.* [210, 211] assumed that reactions take place in the cavity created by the gas jet and at the metal–slag interface. The metal–slag interfacial was calculated based on the stirring energy produced by top-blowing. The surface area of the metal droplets was estimated to be in the order of 1000 m^2. Zhu *et al.* [137, 144] assumed that oxidation reactions take place simultaneously at the surface of the cavity and at the surface of the splashed metal droplets. The volume of the metal droplets was assumed to be equal to the volume of the sunken pit, while the average size of the metal droplets was employed as a fitting parameter [137]. However, the employed value of the average droplet diameter was not reported.

In this work, it was assumed that the reactions between gas, metal, and slag species take place simultaneously on the surface area of the cavity as well as on surface area of the metal droplets generated due to top-blowing. Owing to the high temperature, the reaction rates were assumed to be limited by mass transfer onto and from the reaction interfaces and hence the reaction interfaces are able to reach their constrained thermodynamic equilibrium at any given moment.

6.2.2 Conservation of species and mass

The rate expressions were defined according to the modified law of mass action, in which concentrations are replaced by activities (Eq. 176 on p. 134). The gas phase was taken as an ideal gas and hence the activities of gaseous species were replaced by their partial pressures. The parallel reversible reactions considered by the model were defined as follows:

$$\{O_2\} \rightleftharpoons 2[O], \tag{213}$$

$$[C] + \frac{1}{2}\{O_2\} \rightleftharpoons \{CO\}, \tag{214}$$

$$[C] + \{O_2\} \rightleftharpoons \{CO_2\}, \tag{215}$$

$$Fe_{(l)} + \frac{1}{2}\{O_2\} \rightleftharpoons (FeO), \tag{216}$$

$$2[Cr] + \frac{3}{2}\{O_2\} \rightleftharpoons (Cr_2O_3), \tag{217}$$

$$[Mn] + \frac{1}{2}\{O_2\} \rightleftharpoons (MnO), \tag{218}$$

$$[\mathrm{Si}] + \{\mathrm{O_2}\} \rightleftharpoons (\mathrm{SiO_2})\,. \tag{219}$$

In order to avoid the mathematical complexity of the Maxwell-Stefan equations and the generalized Fick's law, *an effective diffusion model* was employed, and hence only one effective diffusivity was assigned for each species [322]. The relation of effective and binary diffusivities can be expressed as follows [322]:

$$D_{i,\mathrm{eff}} = \sum_{k=1}^{n-i} D_{ik} \frac{\nabla x_k}{\nabla x_i}\,. \tag{220}$$

where D is the mass diffusivity and x is the mole fraction. A description of the treatment of effective diffusivities in this work is given in Section 6.4.3 (p. 186). The starting point for the derivation of the conservation equations is the definition of mass flux according to the Fick's First Law [116]:

$$m_i'' = \underbrace{\underbrace{-\rho D \nabla y_i}_{\text{diffusion}} + \underbrace{y_i \sum_{j=1}^{m} m_j''}_{\text{advection}}}_{\text{convection}}, \tag{221}$$

where ρ is the density, D is the (effective) mass diffusivity, y is the mass fraction, and m'' is the mass flux. The 1-dimensional mass flux of species i between the bulk composition y_i and interfacial composition y_i^*, which are separated by the boundary layer δ, can be expressed as follows [116, 450]:

$$m_i'' = \underbrace{\underbrace{-\rho D \frac{y_i - y_i^*}{\delta}}_{\text{diffusion}} + \underbrace{y_i \sum_{j=1}^{m} m_j''}_{\text{advection}}}_{\text{convection}}\,. \tag{222}$$

The accumulation of mass at the reaction interface is not permitted. By setting $y_i \sum_{j=1}^{m} m_j'' = 0$ and introducing chemical reactions at the reaction interface, the following expression is obtained:

$$\underbrace{\rho D \frac{y_i - y_i^*}{\delta}}_{\text{diffusion}} + \underbrace{\sum_{k=1}^{r} R_k'' \overline{\nu}_{i,k}}_{\text{chemical reactions}} = 0\,, \tag{223}$$

where R'' is the reaction rate flux and $\overline{\nu}_{i,k}$ is the mass-based stoichiometric coefficient of species i in reaction k. In order to describe the mass transfer onto and from the interface, it is often practical to employ the concept of a *mass transfer coefficient* [1, 116, 349, 450]:

$$\beta = \frac{D}{\delta_{\mathrm{N}}} = \frac{\text{molar flux}}{\text{molar concentration difference}} \equiv \frac{\text{mass flux}}{\text{mass concentration difference}}\,, \quad (224)$$

where δ_{N} is the thickness of the diffusion boundary layer, also known as the *Nernst boundary layer*. It should be noted that Eq. 224 does not imply that $\beta \propto D$, because δ_{N} is dependent on D [349]. Employing the definition given in Eq. 224, Eq. 223 transforms into

$$\underbrace{\beta\rho\,(y_i - y_i^*)}_{\text{mass transport}} \underbrace{+\sum_{k=1}^{r} R_k''\overline{\nu}_{i,k}}_{\text{chemical reactions}} = 0\,. \quad (225)$$

Chemical reactions may constitute a *mass sink* or a *mass source*, which is compensated for by mass transfer onto or from the interface [116]. The net production or net consumption of species due to chemical reactions induces bulk motion [372] also known as the *Stefan flow*. In the case of net consumption, the bulk motion is directed towards the reaction interface and its composition corresponds to that of the bulk phase, while in the case of net production the bulk motion is directed away from the reaction interface and its composition corresponds to that of the reaction interface [372]. If solutes are present in low concentrations, the effect of the bulk motion can often be ignored [116, 372]; this assumption is also known as the *stationary medium approach* [279]. The assumption of a stationary medium is usually valid for tramp elements in liquid steel [116]. In the case of an impinging gas jet, however, the conditions for a stationary medium approach are generally not fulfilled due to the imbalance of molar flows of gas species onto and from the interface [1, 298]. The same considerations also apply to metal and slag phases if the diffusing species are present in high concentrations.

In this work, the Stefan flow was taken into account for gas, liquid, and slag species and thus a net mass flow of species was incorporated into the conservation equations.[30]

[30] An alternative mathematical formulation is to introduce a *high mass flux correction factor* θ, which is employed as a multiplier of the mass transport rate induced by the concentration gradient [115, 268]. In this work, both approaches were found to yield the same results.

Employing the *first-order upwind method* for the Stefan flow, the conservation of species i in phase ψ at reaction interface ω is defined by

$$\underbrace{\beta_{i,\psi,\omega}\rho_{\psi,\omega}\left(y_{i,B}-y^*_{i,\omega}\right)}_{\text{mass transport}}+\underbrace{\max(m''_{\psi,\omega},0)y_{i,B}-\max(-m''_{\psi,\omega},0)y^*_{i,\omega}}_{\text{Stefan flow}}+\underbrace{\sum_{k=1}^{r}R''_{k,\omega}\overline{\nu}_{i,k}}_{\text{chemical reactions}}=0\,, \quad (226)$$

where B denotes the bulk phase and m'' is the total mass flux. It should be noted that all properties are specific to the reaction interface in question. In order to account for the conservation of mass within the metal droplets, the following expression is employed for species in the metal phase at the metal droplet interface:

$$\underbrace{\left(\frac{m_{\mathrm{md}}}{A_{\mathrm{md}}\bar{t}_{\mathrm{md}}}-m''_{\mathrm{L,md}}\right)\overline{\eta}_{i,\mathrm{M,md}}(y_{i,\mathrm{bath}}-y^*_{i,\mathrm{md}})}_{\text{mass transport}}+\underbrace{m''_{\mathrm{L,md}}y_{i,\mathrm{bath}}}_{\text{Stefan flow}}+\underbrace{\sum_{k=1}^{r}R''_{k,\mathrm{md}}\overline{\nu}_{i,k}}_{\text{chemical reactions}}=0\,, \quad (227)$$

where m_{md}, A_{md}, and $\bar{t}_{\mathrm{md}}$ are the mass, surface area, and average residence time of the metal droplets, respectively, and $\overline{\eta}_{i,\mathrm{M,md}}$ is the average microkinetic efficiency for the mass transfer of species i in the metal droplets. The average microkinetic efficiency was calculated based on the average residence time of the metal droplets:

$$\overline{\eta}_{i,\mathrm{M,md}}=\frac{y_{i,\mathrm{bath}}-y_{i_{\mathrm{md}}}}{y_{i,\mathrm{bath}}-y^*_{i_{\mathrm{md}}}}=1-\exp\left(-\beta_{i,\mathrm{L,md}}\frac{A_{\mathrm{md}}}{V_{\mathrm{md}}}\bar{t}_{\mathrm{md}}\right) \quad (228)$$

The total mass flux of phase ψ at the reaction interface ω is given by:

$$m''_{\psi,\omega}=-\sum_{i=1}^{n}\sum_{k=1}^{r}\Gamma_{i,\omega}R''_{k,\omega}\overline{\nu}_{i,k}\,, \quad (229)$$

where $\Gamma_{i,\psi}$ is a binary operator, which is defined as 1 if species i is in phase ψ and 0 otherwise. The differential equations for the conservation of mass were integrated with respect to time using the implicit Euler method, *i.e.* the backward Euler method, which is a first-order method and well-suited for stiff equations [451–453]. Explicit methods, such as the explicit Euler method or the fourth-order Runge-Kutta method, are

sensitive to the employed step size in the case of stiff equations. In general, higher-order methods exhibit smaller truncation errors than first-order methods, but require more function evaluations [451–453].[31] Accounting for the contributions of both interfaces, the conservation of species i in the metal bath, gas jet and top slag are expressed by Eqs. 230, 231 and 232, respectively.

$$\underbrace{-\beta_{i,\mathrm{L,cav}}\rho_{\mathrm{L,cav}}A_{\mathrm{cav}}\left(y_{i,\mathrm{bath}}-y^{*}_{i,\mathrm{cav}}\right)}_{\text{mass transport (cavity interface)}}$$

$$\underbrace{-\max(m''_{\mathrm{L,cav}},0)A_{\mathrm{cav}}y_{i,\mathrm{bath}}+\max(-m''_{\mathrm{L,cav}},0)A_{\mathrm{cav}}y^{*}_{i,\mathrm{cav}}}_{\text{Stefan flow (cavity interface)}}$$

$$\underbrace{-\left(\frac{m_{\mathrm{md}}}{\bar{t}_{\mathrm{md}}}-m''_{\mathrm{L,md}}A_{\mathrm{md}}\right)\overline{\eta}_{i,\mathrm{M,md}}\left(y_{i,\mathrm{bath}}-y^{*}_{i,\mathrm{md}}\right)}_{\text{mass transport (metal droplet interface)}}$$

$$\underbrace{-m''_{\mathrm{L,md}}A_{\mathrm{md}}y_{i,\mathrm{bath}}}_{\text{Stefan flow (metal droplet interface)}}\quad\underbrace{-\frac{m_{\mathrm{bath}}y_{i,\mathrm{bath}}-m^{\mathrm{t-\Delta t}}_{\mathrm{bath}}y^{\mathrm{t-\Delta t}}_{i,\mathrm{bath}}}{\Delta t}}_{\text{accumulation of mass}}=0\,, \tag{230}$$

$$\sum_{\omega}\Bigg[\underbrace{-\beta_{i,\mathrm{G},\omega}\rho_{\mathrm{G},\omega}A_{\omega}\left(y_{i,\mathrm{jet}}-y^{*}_{i,\omega}\right)}_{\text{mass transport}}\underbrace{-\max(m''_{\mathrm{G},\omega},0)A_{\omega}y_{i,\mathrm{jet}}+\max(-m''_{\mathrm{G},\omega},0)A_{\omega}y^{*}_{i,\omega}}_{\text{Stefan flow}}\Bigg]$$

$$\underbrace{+\dot{m}_{\mathrm{G,in,lance}}y_{i,\mathrm{in,lance}}+\dot{m}_{\mathrm{G,in,plume}}y_{i,\mathrm{in,plume}}}_{\text{gas input}}\underbrace{-\dot{m}_{\mathrm{G,out}}y_{i,\mathrm{jet}}}_{\text{gas exit}}\underbrace{-\frac{m_{\mathrm{jet}}y_{i,\mathrm{jet}}-m^{\mathrm{t-\Delta t}}_{\mathrm{jet}}y^{\mathrm{t-\Delta t}}_{i,\mathrm{jet}}}{\Delta t}}_{\text{accumulation of mass}}=0\,, \tag{231}$$

[31] Depending on the studied case, the smaller truncation errors need to be weighted against the higher computational expense depending on the studied case (see *e.g.* Meier *et al.* [454]). In the model presented here, the conservation of mass and energy are solved successively and hence relatively small time steps have to be used regardless of the employed time integration method.

$$\sum_{\omega}\Bigg[\underbrace{-\beta_{i,\mathrm{S},\omega}\rho_{\mathrm{S},\omega}A_{\omega}\left(y_{i,\mathrm{slag}}-y^{*}_{i,\omega}\right)}_{\text{mass transport}}\underbrace{-\max(m''_{\mathrm{S},\omega},0)A_{\omega}y_{i,\mathrm{slag}}+\max(-m''_{\mathrm{S},\omega},0)A_{\omega}y^{*}_{i,\omega}}_{\text{Stefan flow}}\Bigg]$$
$$\underbrace{-\frac{m_{\mathrm{slag}}y_{i,\mathrm{slag}}-m^{\mathrm{t}-\Delta\mathrm{t}}_{\mathrm{slag}}y^{\mathrm{t}-\Delta\mathrm{t}}_{i,\mathrm{slag}}}{\Delta t}}_{\text{accumulation of mass}}=0\,, \quad (232)$$

where A denotes the surface area, m_{bath} is the mass of the metal bath, m_{jet} is the mass of the gas jet, m_{slag} is the mass of the top slag, and Δt is the time step. The corresponding expressions for the conservation of the total mass in the metal bath, gas jet, and top slag are written simply by summation of the mass transport terms.

6.2.3 Conservation of energy

Following the formulation for the conservation of species and mass, the conservation of energy at the cavity interface was determined according to

$$\underbrace{\alpha_{\mathrm{L,cav}}\left(T_{\mathrm{bath}}-T^{*}_{\mathrm{cav}}\right)+\alpha_{\mathrm{G,cav}}\left(T_{\mathrm{jet}}-T^{*}_{\mathrm{cav}}\right)+\alpha_{\mathrm{S,cav}}\left(T_{\mathrm{slag}}-T^{*}_{\mathrm{cav}}\right)}_{\text{heat transport}}$$
$$\underbrace{-\sum_{k=1}^{r}R''_{k,\mathrm{cav}}\Delta h_{k}}_{\substack{\text{chemical}\\ \text{reactions}}}=0\,, \quad (233)$$

where α denotes the heat transfer coefficient, T_{bath} is the temperature of the metal bath, T_{jet} is the temperature of the gas jet, T_{slag} is the temperature of the top slag, T^{*}_{cav} is the interfacial temperature of the cavity, and Δh is the specific reaction enthalpy. The conservation of energy at the metal droplet interface was defined according to

$$\underbrace{\frac{m_{\mathrm{md}}}{A_{\mathrm{md}}\bar{t}_{\mathrm{md}}}c_{\mathrm{p,L}}\overline{\eta}_{\mathrm{H,md}}\left(T_{\mathrm{bath}}-T^{*}_{\mathrm{md}}\right)+\alpha_{\mathrm{G,md}}\left(T_{\mathrm{jet}}-T^{*}_{\mathrm{md}}\right)+\alpha_{\mathrm{S,md}}\left(T_{\mathrm{slag}}-T^{*}_{\mathrm{md}}\right)}_{\text{heat transport}}$$

$$\underbrace{-\sum_{k=1}^{r} R''_{k,\mathrm{md}} \Delta h_k}_{\substack{\text{chemical}\\ \text{reactions}}} = 0\,, \quad (234)$$

where T^*_{md} is the interfacial temperature of the metal droplets and $\overline{\eta}_{\mathrm{H,md}}$ is the average microkinetic efficiency of the heat transfer in the metal droplets:

$$\overline{\eta}_{\mathrm{H}} = \frac{T_{\mathrm{bath}} - T_{\mathrm{md}}}{T_{\mathrm{bath}} - T^*_{\mathrm{md}}} = 1 - \exp\left(-\alpha_{\mathrm{L,md}} \frac{A_{\mathrm{md}}}{m_{\mathrm{md}} c_{\mathrm{p,L}}} \bar{t}_{\mathrm{md}}\right). \quad (235)$$

where T_{md} is the temperature of the metal droplets. Using the implicit Euler method for time integration, conservation of energy in the metal bath, gas jet, and top slag is defined by Eqs. 236, 237, and 238, respectively.

$$\underbrace{-\alpha_{\mathrm{L,cav}} A_{\mathrm{cav}} \left(T_{\mathrm{bath}} - T^*_{\mathrm{cav}}\right)}_{\text{heat transport (cavity interface)}} \underbrace{-\frac{m_{\mathrm{md}}}{\bar{t}_{\mathrm{md}}} c_{\mathrm{p,L}} \overline{\eta}_{\mathrm{H,md}} \left(T_{\mathrm{bath}} - T^*_{\mathrm{md}}\right)}_{\text{heat transport (metal droplet interface)}}$$

$$\underbrace{-\sum_{\omega}\sum_{i=1}^{n}\sum_{k=1}^{r} \Gamma_{i,\mathrm{L}} R''_{k,\omega} \overline{\nu}_{i,k} A_{\omega} c_{\mathrm{p},i} \left(T_{\mathrm{bath}} - T^*_{\omega}\right)}_{\text{heating of species}}$$

$$\underbrace{-q_{\mathrm{lining}} A_{\mathrm{lining}}}_{\substack{\text{heat losses through}\\ \text{refractory lining}}} \underbrace{-m_{\mathrm{bath}} c_{\mathrm{p,bath}} \frac{T_{\mathrm{bath}} - T^{\mathrm{t-\Delta t}}_{\mathrm{bath}}}{\Delta t}}_{\text{accumulation of energy}} = 0\,, \quad (236)$$

$$\sum_{\omega} \left[\underbrace{-\alpha_{\mathrm{G},\omega} A_{\omega} \left(T_{\mathrm{jet}} - T^*_{\omega}\right)}_{\text{heat transport}} \underbrace{-\sum_{i=1}^{n}\sum_{k=1}^{r} \Gamma_{i,\mathrm{G}} R''_{k,\omega} \overline{\nu}_{i,k} A_{\omega} c_{\mathrm{p},i} \left(T_{\mathrm{jet}} - T^*_{\omega}\right)}_{\text{heating of species}} \right]$$

$$\underbrace{+\dot{m}_{\mathrm{G,in,lance}} \int_{T_{\mathrm{in,lance}}}^{T_{\mathrm{jet}}} c_{\mathrm{p,lance}}\, \mathrm{d}T + \dot{m}_{\mathrm{G,in,plume}} \int_{T_{\mathrm{plume}}}^{T_{\mathrm{jet}}} c_{\mathrm{p,plume}}\, \mathrm{d}T}_{\text{heating of injected gas}}$$

$$\underbrace{-\,m_{\mathrm{jet}}c_{\mathrm{p,jet}}\frac{T_{\mathrm{jet}}-T_{\mathrm{jet}}^{\mathrm{t}-\Delta\mathrm{t}}}{\Delta t}}_{\text{accumulation of energy}}=0\,, \quad (237)$$

$$\sum_{\omega}\Bigg[\underbrace{-\,\alpha_{\mathrm{S},\omega}A_{\omega}\left(T_{\mathrm{slag}}-T_{\omega}^{*}\right)}_{\text{heat transport}}\underbrace{-\sum_{i=1}^{n}\sum_{k=1}^{r}\Gamma_{i,\mathrm{S}}R_{k,\omega}''\overline{v}_{i,k}A_{\omega}c_{\mathrm{p},i}\left(T_{\mathrm{slag}}-T_{\omega}^{*}\right)}_{\text{heating of species}}\Bigg]$$

$$\underbrace{-\,q_{\mathrm{slag}}A_{\mathrm{slag}}}_{\substack{\text{heat losses}\\ \text{through slag}}}\underbrace{-\,m_{\mathrm{slag}}c_{\mathrm{p,slag}}\frac{T_{\mathrm{slag}}-T_{\mathrm{slag}}^{\mathrm{t}-\Delta\mathrm{t}}}{\Delta t}}_{\text{accumulation of energy}}=0\,, \quad (238)$$

where q_{lining} is the heat flux through the refractory materials, A_{lining} is the surface area of the refractory materials, q_{slag} is the heat flux through the top slag, and A_{slag} is the cross-sectional surface area of the top slag. The heat flux through the refractory lining was set to q_{lining} = 12500 W/m^2 as in [44]. The heat losses through the slag were determined on the basis of radiative heat transfer through the mouth of the vessel as described in Article I. The cooling effect of side-blowing is calculated separately by the earlier-proposed model for side-blowing [44].

6.2.4 Geometry of the cavity

Molloy [455] distinguished three cavity modes, namely *dimpling*, *splashing*, and *penetrating*. The cavity modes can be distinguished based on the frequency and amplitude of cavity oscillation [456].[32] Dimpling refers to a mere depression of the surface without droplet formation [455]. In this mode, practically no pulsation of the cavity takes place [458]. With higher dynamic pressure of the gas jet, the mode changes to a splashing mode and outwardly directed splashes start to form at the edges of the depression [455]. Moreover, the cavity starts to oscillate both in diameter and depth [432, 455, 458]. Fig. 24a illustrates the gas jet impact area with a 1-hole lance in splashing mode. A further increase in the dynamic pressure of gas jet leads to the penetrating mode [455]. The shift from splashing to penetrating mode is characterised

[32]The results of a recent study by Sabah and Brooks [457] suggests that the cavity modes can be distinguished also based on the amplitude and frequency of sound produced from the bath.

by deeper penetration, reduction of outwardly directed splashes, and more intense oscillation of the cavity [432, 458]. Nevertheless, Sabah and Brooks [459] have shown that irrespective of the cavity mode, most of the power of the gas jet is consumed in dissipation and splashing, whereas the formation of the cavity consumes a relatively small amount of energy. Okhotskii *et al.* [444] have suggested that the liquid metal might be entrapped and vaporised by the gas jet in the penetrating mode.

In the case of multi-hole lances, the gas jets may – depending on the inclination angle of the gas jets – either coalesce and form only one large cavity, or penetrate the bath surface as three separate jets, whereupon each gas jet will form its own cavity [460, 461]. It should be noted that even if the gas jets do not coalesce, the coalescence of cavities may occur if they are sufficiently close to each other [462]. A schematic illustration of the gas jet impact area is shown in Fig. 24b.

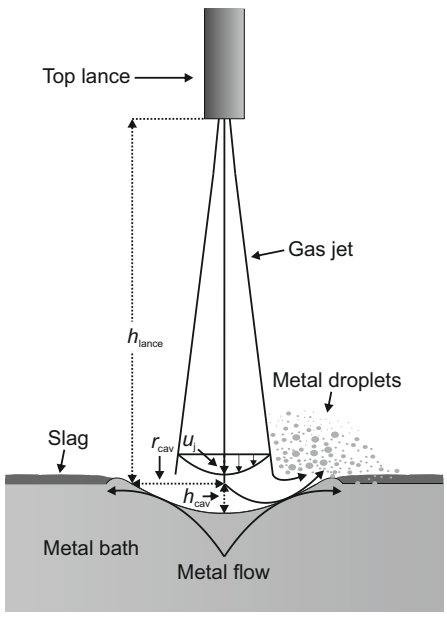

(a) 1-hole lance.

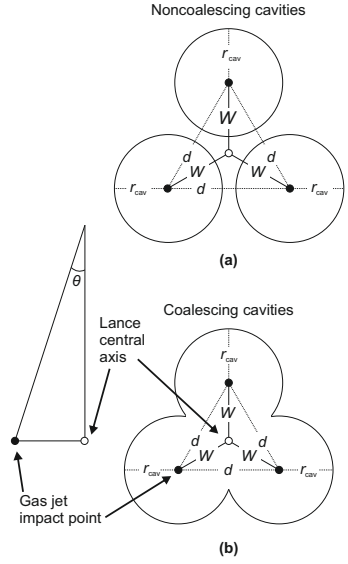

(b) 3-hole lance with noncoalescing cavities (top) and coalescing cavities (bottom).

Fig 24. Schematic illustration of the gas jet impact area. Reproduced from Article I by permission of Springer Nature.

The dimensions of the cavities caused by top-blowing have been studied extensively with hot models [462–464], cold models [294, 295, 464–478], and CFD models [276, 473, 474, 479–488]. Banks and Chandrasekhara [466] divided the analytical approaches into three categories:

1. *dimensional analysis*, which is used to produce a correlation between the factors affecting the cavity depth.
2. *stagnation pressure analysis*, which employs the dynamic pressure associated with the centreline velocity of a free, turbulent, incompressible gas jet, and ignores the effects of surface tension and shear on the cavity wall.
3. *displaced liquid analysis*, which assumes that the force exerted by the gas jet equals the weight of the displaced liquid. Moreover, it is assumed that the shape of the liquid surface does not significantly alter the velocity and pressure distributions of the gas flow.

Table 19 shows the proposed penetrability correlations along with their type corresponding to the categorisation proposed by Nordquist *et al.* [472]. Differences between the correlations are quite small, as many models are based on relatively similar assumptions. Most of the proposed models exclude the top slag entirely. Some authors [458, 469, 477, 478] have found that the presence of a top phase affects the penetration depth to some extent. However, Li *et al.* [478] suggested that the cavity diameter is insensitive to the gas flow rate through the top lance, but depends on the lance height, nozzle angle, and thickness of the top phase.

In order to simplify the treatment of the cavity, it was assumed that the number of cavities is equal to the number of the gas jets and that neither chemical reactions [479, 490, 491], nor the interference of top slag [491] affect the geometry of the cavity. Moreover, it was assumed that the geometry of the cavity follows the form of a paraboloid of revolution [444, 467]. The depth and diameter of the cavity were calculated using the correlations proposed by Koria and Lange [462]:

$$\frac{h_{\text{cav}}}{h_{\text{lance}}} = 4.469 \times \dot{M}_{\text{h}}^{0.66}, \tag{239}$$

$$\frac{d_{\text{cav}}}{h_{\text{lance}}} = 2.813 \times \dot{M}_{\text{d}}^{0.282}, \tag{240}$$

where h_{lance} is the lance height from the surface of the metal bath, while $\dot{M}_{\text{h}}$ and $\dot{M}_{\text{d}}$ represent the vertical and horizontal components of the dimensionless momentum

Table 19. Correlations for penetrability of gas jets.

Year	Study	Type	Studied system(s)
1954	Collins and Lubanska [465]	DLA	Air–H_2O
1962	Maatsch [489]	DLA	CO_2–Sn; O_2–H_2O; O_2–$ZnCl_2$ solution; CO_2–oil
1963	Banks and Chandrasekhara [466]	DLA	Air–H_2O
1966	Van der Lingen [490]	DLA	Air–H_2O; N_2–H_2O; H_2–H_2O; Air–Hg; N_2–cast iron; O_2–cast iron
1966	Wakelin [294]	SPA	Air–H_2O; Air–Hg; CO–H_2O, air–Hg
1966	Davenport *et al.* [295]	SPA	CO–H_2O
1967	Flinn *et al.* [463]	SPA	O_2–steel
1969	Cheslak *et al.* [467]	SPA	Air–H_2O; air–wet cement
1972	Chatterjee and Bradshaw [300]	SPA	Various gases (air, CO_2, H_2, He, SO_2, N_2) and liquids (H_2O, ethyl alcohol, toluene, acetone, glycerol–H_2O mixtures, Hg, Ag)
1973	Chatterjee *et al.* [468]	DLA	Air–H_2O
1975	Babtizmanskii *et al.* [464]	DA	Inert gas–H_2O; inert gas–pig iron; O_2–pig iron
1980	Chernyatevich *et al.* [458]	DLA	O_2–pig iron
1987	Koria and Lange [462]	DA	O_2–pig iron; O_2–steel
1996	Qian *et al.* [469]	SPA	Air–H_2O; air–kenosene–H_2O; air–corn oil–H_2O
2001	Kumagai and Iguchi [470]	DA	Air–H_2O
2002	Olivares *et al.* [471]	DA	Air–H_2O
2006	Nordquist *et al.* [472]	SPA	Air–H_2O
2012	Hwang and Irons [476]	SPA	Air–H_2O
2012	Ek and Sichen [477]	SPA	O_2–HCl–Ga-In-Sn alloy
2014	Dong *et al.* [485]	DA	O_2–steel
2016	Li *et al.* [478]	DA	Air–H_2O; air–H_2O–transformer oil

Notes: DLA = displaced liquid analysis; SPA = stagnation pressure analysis; DA = dimensional analysis.

flow rates. The correlations shown in Eqs. 239 and 240 are based on a dimensional analysis of a large set of experimental data on the penetration of oxygen jets in molten pig iron and pure iron-carbon alloys with single- and multi-hole lances. Results of other studies suggest that the penetration depth correlation given in Eq. 239 exhibits good agreement with CFD calculations for hot atmospheres [486], but poor agreement with cold experiments with water [472] or Ga-In-Sn alloy [477]. However, Eqs. 239 and 240 do not account for the effect of the top slag.

6.2.5 Splashing of metal droplets

If the momentum flux of the top-blown gas jet is sufficiently high, the liquid surface becomes unstable and the splashing of metal droplets occurs [411, 492]. Owing to similar physical properties of carbon and stainless steels, it is reasonable to expect that the mechanism of droplet generation due to top-blowing, excluding the foaming of slag, is essentially similar to the BOF process, for which quantitative descriptions are available in the literature [411, 420, 425, 437–441]. Standish and He [493] identified two regions of droplet generation:

1. *the dropping region*, in which single droplets are gradually formed and ejected. This is the mechanism of droplet generation, when the gas flow rate is relatively low.
2. *the swarming region*, in which not only single droplets but large tears of liquid phase are ejected from the bath. This mechanism takes place when the gas flow rate is increased past a certain limit.

The secondary break-up of the metal droplets can occur due to various reasons, *e.g.* due to the aerodynamic forces of the gas jet [494, 495], impact on the slag layer [496], bursting resulting from spontaneous CO nucleation within the droplet [410], or interfacial instability caused by chemical reactions involving surface-active elements [497]. On the other hand, the very smallest droplets are likely to be carried away with the flue gas [73, 498]. However, in the absence of suitable quantitative descriptions for the break-up mechanisms and due to uncertainties related to the trajectories of the droplets, the effect of the various break-up mechanisms on the droplet size distribution was not accounted for.

The generation of metal droplets is also caused by side-blowing through a mechanism referred to as bubble bursting [282, 320, 499–503]. This phenomenon occurs when a rising gas bubble reaches the surface of the steel and bursts creating very small metal droplets from the thin film of steel around the bubble [282, 320, 501–504]. A related mechanism is the entrainment of large droplets due to jet formation, which is caused by the collapsing of the cavity after the rupture of the iron film [320, 502]. The experimental results of Han and Holappa [503] suggest that the entrainment of metal droplets in slag increases as the bubble size increases, but decreases as the metal–slag interfacial tension and slag viscosity increase. In this work, it was assumed that the effect of these phenomena on the reaction rates is essentially captured by following the splashing generated by the top-blowing.

Trajectory

In this work, the lifespan of the metal droplets was assumed to consist of three successive steps. At first, the metal droplets are generated in the vicinity of the cavity, from which they are ejected onto a gas–metal–slag emulsion. This also includes metal droplets, which have been ejected into the atmosphere and land on the emulsion. Thereafter, the metal droplets pass though the emulsion layer, reacting simultaneously with gas and slag species. Finally, the metal droplets return to the metal bath, where they mix with the metal bath immediately. The metal droplets were assumed to be spherical in geometry; this assumption should hold well for small metal droplets [505], which make up most of the surface area. The total mass and surface area of the metal droplets residing in the emulsion were defined according to Eqs. 241 and 242, respectively.

$$m_{\mathrm{md}} = \sum_i m_{\mathrm{md},i}\,, \tag{241}$$

$$A_{\mathrm{md}} = \sum_i \frac{6 m_{\mathrm{md},i}}{d_{\mathrm{md},i}\rho_{\mathrm{L}}}\,, \tag{242}$$

where $m_{\mathrm{md},i}$ and $d_{\mathrm{md},i}$ are the mass and diameter of size class i, respectively. The mass of the metal droplets in the size class i residing in the emulsion can be solved from

$$m_{\mathrm{md},i} = f_{\mathrm{md},i}\dot{m}_{\mathrm{md}} \min\left(t_{\mathrm{md},i}, t\right)\,, \tag{243}$$

where $f_{\mathrm{md},i}$, $\dot{m}_{\mathrm{md}}$, and $t_{\mathrm{md},i}$ are the mass fraction of size class i at the place of origin, the metal droplet generation rate, and the residence time of size class i, respectively, and t is the time.[33] Because the terminal velocity of the droplets increases with increasing droplet size [507, 508], the residence time of large droplets is likely to be shorter than that of smaller droplets. In this work, the residence time of each size class was determined in relation to an ideal trajectory through the emulsion layer [509]. The terminal velocity of the metal droplets was calculated according to Subagyo and Brooks [507].

[33] The relation shown in Eq. 243 is essentially a reformulation of *Little's law* [506], which has been proven to hold for any stable and non-preemptive system.

Droplet generation rate

The concept of the blowing number has been employed for describing the onset of splashing. Block *et al.* [411] defined the blowing number as follows:

$$\tilde{N}_B = \frac{\dot{V}_{G,lance}}{d_{lance}(h_{cav} + h_{lance})}, \tag{244}$$

where $\dot{V}_{G,lance}$ is the volumetric gas flow rate through the top lance and d_{lance} is the nozzle diameter of the top lance. It should be noted that in Eq. 244, $\dot{V}_{G,lance}$ is in units of Nm^3/h, while d_{lance}, h_{cav}, and h_{lance} are in cm, and thus $\tilde{N}_B$ is expressed in $Nm^3/(h{\cdot}cm^2)$. Block *et al.* [411] suggested that splashing starts, when a critical value of the blowing number is exceeded. The critical blowing number was found to be dependent on the surface tension of the liquid phase so that in the case of molten steel, a typical value of the surface tension (1.5 N/m) yields a critical blowing number of $\tilde{N}_{B,crit} = 2.0\ Nm^3/(h{\cdot}cm^2)$. This value is in close agreement with the experimental values reported later by Koria [431] and Koch *et al.* [445]. According to Block *et al.* [411], the droplet generation rate (in kg/h) can be expressed as a function of the blowing number as follows [411]:

$$\dot{m}_{md} = K\dot{V}_{G,lance}\left(\tilde{N}_B - \tilde{N}_{B,crit}\right)^2, \tag{245}$$

where K is constant, which was reported to be 180 $kg{\cdot}h^2{\cdot}cm^4{\cdot}(Nm^3)^{-3}$ for liquid iron [411]. On the basis for the definitions of blowing number given in Eqs. 247 and 244 it can be deduced that – *ceteris paribus* – the intensity of splashing increases as the dynamic pressure of the gas phase increases, surface tension decreases, density of the metal phase decreases, gas flow rate increases, or lance height decreases.

Koria and Lange [431, 448] derived an expression for the generation rate of metal droplets based on hot modelling experiments. The droplet generation rate in the immediate vicinity of the cavity was expressed as follows [431, 448]:

$$\dot{m}_{md} = 0.8863 m_{bath}\left(\frac{\dot{m}_t \cos\theta}{n_{lance}\rho_L g h_{lance}^3}\right)^{0.4}, \tag{246}$$

where n_{lance} is the number of exit ports in the top lance, $\dot{m}_t$ is the total momentum flow rate of the gas jet, and θ is the inclination angle of the gas jet relative to the lance axis. It should be noted that a considerably lower prefactor of 0.0288 was calculated on the basis of slag samples collected from an industrial scale BOF vessel [431]. The large discrepancy between the calculated values was attributed to the sampling position [431].

Subagyo *et al.* [509] defined the blowing number as a dimensionless quantity, which relates the intensity of the jet momentum to the properties of the liquid steel and is defined by [509]:

$$\mathrm{N_B} = \frac{\rho_\mathrm{G} u_\mathrm{G}^2}{2\sqrt{\sigma_\mathrm{L} g \rho_\mathrm{L}}} = \frac{\eta^2 p_\mathrm{d}}{\sqrt{\sigma_\mathrm{L} g \rho_\mathrm{L}}} \quad \text{where} \quad \eta = \frac{u_\mathrm{G}}{u_\mathrm{j}}\,, \tag{247}$$

where u_G is the critical gas velocity, η is constant, and p_d is the dynamic pressure of the gas jet. $\mathrm{N_B}$ is essentially a reformulated Weber number (We), which is normalised for the context of metal droplet generation. The blowing number is defined so that $\mathrm{N_B}$ = 1 represents the criterion for the onset of droplet formation [509]. The results of other studies suggest that η is not independent of the lance height [510–514] or the gas jet angle [515]. Therefore, although splashing increases with the increasing blowing number in the splashing mode, an increase in the blowing number will lead to a decrease in the splashing rate if the cavity mode changes from a splashing mode to a penetrating mode [511–513, 516, 517]. Making use of the blowing number concept, Subagyo *et al.* [509] proposed a correlation, which applies to the splashing cavity mode and is based on hot- and cold modelling data:

$$\frac{\dot{m}_\mathrm{md}}{\dot{V}_\mathrm{G,lance}} = \frac{\left(\mathrm{N_B}\right)^{3.2}}{\left[2.6\times10^6 + 2.0\times10^{-4}\left(\mathrm{N_B}\right)^{12}\right]^{0.2}} \qquad (R^2 = 0.97)\,, \tag{248}$$

where $\dot{V}_\mathrm{G,lance}$ is the volumetric gas flow rate through the top lance (in $\mathrm{Nm^3/s}$). One of the main differences between Eqs. 244 and 247 is that the former suggests that the blowing number is dependent on the geometry of the cavity. As noted by Sarkar *et al.* [441] and Rout *et al.* [516], Eq. 248 yields droplet generation rates which are considerably below the values estimated from plant data. Rout *et al.* [516] have argued that the discrepancy is caused partly by the fact that Eq. 248 has been derived for conditions corresponding to room temperature.

In this work, the droplet generation rate was calculated according to a modified expression proposed by Rout *et al.* [516]. More specifically, Rout *et al.* [516] modified Eq. 248 so that the blowing number $\mathrm{N_B}$ and the volumetric gas flow rate $\dot{V}_\mathrm{G,lance}$ are temperature corrected for the conditions at the point of impact:

$$\frac{\dot{m}_\mathrm{md}}{\dot{V}'_\mathrm{G,lance}} = \frac{\left(\mathrm{N'_B}\right)^{3.2}}{\left[2.6\times10^6 + 2.0\times10^{-4}\left(\mathrm{N'_B}\right)^{12}\right]^{0.2}}\,, \tag{249}$$

where N'_B is the modified blowing number and $\dot{V}'_{G,lance}$ is the modified volumetric gas flow rate, which is calculated by converting $\dot{V}_{G,lance}$ to the pressure (p_G) and temperature (T_G) of the gas at the impact point. The modified blowing number N'_B can be obtained from Eq. 247 by employing the dynamic pressure at the point of impact. In this work, the dynamic pressure at the point of impact was calculated according to a correlation proposed by Deo and Boom [126]. Furthermore, the variation of η as a function of the gas jet angle was approximated by the method employed by Alam *et al.* [515].

Rout *et al.* [516] also suggested that due to the low lance height, the experiments conducted by Subagyo *et al.* [509] did not actually correspond to the splashing mode, but rather the penetrating mode of jet interaction, which – as noted earlier – is characterised by a lower droplet generation rate than the splashing mode. For this reason, the parameter J_{eff} was introduced similarly to Sarkar *et al.* [441] in order to calculate the effective droplet generation rate:

$$\dot{m}_{md,eff} = J_{eff} \cdot \dot{m}_{md} \,. \tag{250}$$

It needs to be kept in mind that the value of J_{eff} depends on the system observed, and is thus essentially a fitting parameter, which is evaluated based on plant data. In their BOF model, Sarkar *et al.* [441] calculated the droplet generation rate based on the expression shown in Eq. 248 and found that a reasonable agreement with the measured metal content of the emulsion in BOF processing was obtained with a value of J_{eff} = 15. Employing the same data, Rout *et al.* [516] found the modified expression (Eq. 249) yields comparable results without the parameter J_{eff}.

It should be noted that surface active elements can have a significant effect on the surface tension of the metal phase, thereby affecting the splashing behaviour. For example, sulphur may increase splashing in the case of Fe–C melts [518]. In this work, however, the effect of surface active elements on the splashing behaviour was not accounted for.

Size distribution

An important aspect of the splashing phenomenon is the size distribution of the metal droplets generated. A substantial contribution to understanding the interaction of molten metal and gas jets was published by Koria and Lange [280, 281, 431, 462, 494, 495, 519–523]. As a part of their work, they found that the size distribution of the metal droplets at their place of birth could be described well using a slightly modified version of the

Rosin-Rammler-Sperling (RRS) distribution [280]:[34]

$$RF = (0.001)^{\left(\frac{d_{\mathrm{md},i}}{d_{\mathrm{limit}}}\right)^{n}}, \tag{251}$$

where RF is the cumulative weight-fraction, n is a distribution parameter, and d_{limit} is the limiting diameter, which corresponds to $RF = 0.001$. More specifically, n describes the homogeneity of the droplet distribution, while d_{limit} is a measure of the fineness of the distribution [280]. In this work, Eq. 251 was employed for the size distribution of metal droplets at their place of origin. For the distribution exponent, a value of $n = 1.26$ was taken from Koria and Lange [280], because it represents an arithmetic mean for relatively large data. Modifying the expression presented by Deo *et al.* [437] to a more general form, the mass fraction of size class i at place of birth was calculated as follows:

$$f_{\mathrm{md},i} = -\ln(0.001)\, n\, RF \frac{d_{\mathrm{md},i}^{n-1}}{d_{\mathrm{limit}}^{n}}. \tag{252}$$

Following the assumption of non-coalescing jets, the limiting diameter was obtained from [281]:

$$d_{\mathrm{limit}} = 5.513 \times 10^{-6} \times \left[10 \left(\frac{d_{\mathrm{t}}^{2}}{h_{\mathrm{lance}}^{2}}\right) p_{\mathrm{amb}} \left(1.27 \frac{p_0}{p_{\mathrm{amb}}} - 1\right) \cos\theta\right]^{1.206}, \tag{253}$$

where p_0 and p_{amb} are the lance supply pressure (in Pa) and ambient pressure (in Pa), respectively.

6.2.6 Mass and heat transfer coefficients

The mass and heat transfer coefficients were defined in terms of the Sherwood number (Sh) and Nusselt number (Nu) as shown in Eqs. 254 and 255, respectively. The definitions of other dimensionless numbers are shown in the nomenclature and are not repeated here.

[34] The RRS distibution function is attributable to several studies on particle size measurement by Frechet [524] and Rosin *et al.* [525–527]. Later, Weibull [528, 529] showed that the distribution function could also be used in other fields of statistics. For this reason, the RRS distribution is more commonly known as the Weibull distribution [530].

$$\mathrm{Sh} = \frac{\text{mass transfer rate}}{\text{diffusive mass transfer rate}} = \frac{\beta L}{D}\,, \tag{254}$$

$$\mathrm{Nu} = \frac{\text{heat transfer rate}}{\text{conductive heat transfer rate}} = \frac{\alpha L}{\lambda}\,, \tag{255}$$

where D is the mass diffusivity, L is the characteristic length, and λ is the heat conductivity. In order to avoid excessive indexation, the employed correlations are – where possible – shown without reference to species, phases, or interfaces.

The cavity interface

At the cavity interface, the characteristic length (L) was set equal to the cavity radius (r_{cav}). In the absence of more suitable correlations, the mass transfer correlations employed for the gas jet were taken from Oeters [1]. His correlations are based on the experimental data for impinging air jet and water published by Lohe [297] and are shown in Eq. 256.[35] Similarly to Dogan *et al.* [420], the values of Re and Sc were defined based on the properties of the gas film at the impact surface. More specifically, the critical gas velocity, which can be calculated from the free axial velocity of the gas jet, was taken as the characteristic velocity for the gas phase mass transfer.

$$\mathrm{Sh} = \begin{cases} 1.41\mathrm{Re}^{0.51}\mathrm{Sc}^{0.33} & \text{when} \quad 2\times10^{3} \leq \mathrm{Re} \leq 3\times10^{4} \\ 0.41\mathrm{Re}^{0.75}\mathrm{Sc}^{0.33} & \text{when} \quad 3\times10^{4} \leq \mathrm{Re} \leq 2\times10^{5} \end{cases}. \tag{256}$$

The mass transfer coefficient of the metal phase in contact with the top-blown oxygen was determined based the turbulent mass transfer model proposed by Levich [290]. The turbulent diffusion boundary layer thickness and the corresponding Sherwood number were defined according to Eqs. 257 and 258, respectively [1, 287].

$$\delta_{\mathrm{N}} = \sqrt{\frac{D_{\mathrm{L}}\sigma_{\mathrm{equiv}}}{0.41\rho_{\mathrm{L}}u_{\tau}^{3}}}\,, \tag{257}$$

$$\mathrm{Sh} = \frac{r_{\mathrm{cav}}}{2\delta_{\mathrm{N}}}\,, \tag{258}$$

[35] It should be noted that the exponent of Sc in Eq. 256 at higher Re values was reported as 0.33 in the original version [1] and 0.53 in the newer English translation [357]. In this work, the exponent 0.33 was employed in the calculations as this value is more in keeping with the mass transfer theory and corresponding correlations [279]. Nevertheless, the predicted Sc $\approx$ 1 and hence the exponent of Sc has virtually no effect on the results.

where u_τ is the turbulent shear stress velocity and σ_{equiv} is the equivalent surface tension. The thickness of the thermal boundary layer (δ_{Pr}) can be obtained from Eq. 257 by replacing the mass diffusivity D_{L} with the ratio $\mu_{\text{L}}/\rho_{\text{L}}$, *i.e.* kinematic viscosity ν_{L}. As a first approximation, the mass transfer coefficients of the slag species were calculated similarly to the metal species, but using the properties of the slag species. The turbulent shear stress velocity was calculated on the basis of the momentum transfer between the gas jet and the metal bath similarly to Memoli *et al.* [480]. The heat transfer coefficients for gas, metal, and slag phases were derived from the mass transfer correlations according to the analogue of heat and mass transfer by replacing the Sherwood number (Sh) and the Schmidt number (Sc) with the Nusselt number (Nu) and the Prandtl number (Pr), respectively.

The metal droplet interface

At the metal droplet interface, the characteristic length L was set equal to the Sauter mean size of the metal droplets in the emulsion ($d_{32,\text{md}}$). The critical gas velocity (u_{G}) was defined as the characteristic velocity for the gas phase mass transfer, while the average terminal velocity of the metal droplets in the emulsion ($\overline{u}_{\text{md}}$) was employed as the characteristic velocity for the slag phase mass transfer. The mass transfer coefficients of the gas species were determined according to the Steinberger and Treybal [354] correlation (Eqs. 259 and 260), which accounts for the effects of both natural and forced convection.

$$\text{Sh} = \text{Sh}_0 + 0.347(\text{ReSc}^{1/2})^{0.62}, \tag{259}$$

$$\text{Sh}_0 = \begin{cases} 2 + 0.569(\overline{\text{Gr}}\text{Sc})^{1/4} & \text{for} \quad \overline{\text{Gr}}\text{Sc} < 10^8 \\ 2 + 0.0254(\overline{\text{Gr}}\text{Sc})^{1/2}\text{Sc}^{0.244} & \text{for} \quad \overline{\text{Gr}}\text{Sc} > 10^8 \end{cases}, \tag{260}$$

where $\overline{\text{Gr}}$ is the mean Grashof number. In small metal droplets, mass transfer takes place almost entirely by diffusion, while larger droplets may exhibit uninhibited circulatory flow [1, 338, 531]. In this work, it was assumed that only creeping laminar circulation takes place within the metal droplets, and hence the mass transfer coefficient was calculated according to the Kronig and Brink [328] solution (Eq. 261).[36] The mass transfer in the slag phase surrounding the metal droplets was calculated according to Eq.

[36]The expression shown in Eq. 261 was taken from Colombet *et al.* [324].

262, which is valid for fluid spheres in creeping flow [352].

$$\mathrm{Sh} = \frac{32}{3} \frac{\sum_{i=1}^{\infty} \left[A_i^2 \lambda_i \exp\left(-16 \lambda_i \mathrm{Fo_M}\right) \right]}{\sum_{i=1}^{\infty} \left[A_i^2 \exp\left(-16 \lambda_i \mathrm{Fo_M}\right) \right]}, \tag{261}$$

$$\mathrm{Sh} = 0.65 \left(\frac{\mu_\mathrm{S}}{\mu_\mathrm{S} + \mu_\mathrm{L}} \right)^{1/2} \mathrm{Re}^{1/2} \mathrm{Sc}^{1/2}, \tag{262}$$

where $\mathrm{Fo_M}$ is the Fourier number for mass transfer. The values for parameters A_i and λ_i were obtained from the literature [329]. Here, the average residence time of the metal droplets ($\bar{t}_\mathrm{md}$) was employed as the characteristic time in Fourier number for mass transfer ($\mathrm{Fo_M}$) and in the corresponding Fourier number for heat transfer ($\mathrm{Fo_H}$). By making use of the analogue of heat and mass transfer, the heat transfer correlations were obtained by substituting Sh, Sc, and $\mathrm{Fo_M}$ with Nu, Pr, and $\mathrm{Fo_H}$, respectively [279].

6.3 A model for the reduction stage (Article III)

The aim of the reduction stage is decrease the losses of valuable metallics to the top slag in order to improve the overall economy of the process. For this purpose, reductants and fluxes are added to the vessel [128]. Typical ferrous reductants have a density lower than that of iron (see Table 20) and are thus subject to buoyancy induced by the density difference. Reductants with a density higher than that of the top slag should, in principle, eventually settle between the metal and slag phases, while lighter reductants should rise on top of the slag phase. Nevertheless, the trajectories of the reductant particles are likely to be affected considerably by the fluid flows in the metal bath. In a physical modelling study of the reduction stage, Guthrie *et al.* [128] found that the wooden reductant particles were generally well-mixed in a "metal–slag" foam, *viz.* a mixture of the zinc chloride and silicone oil used to represent the metal and slag phases, respectively. The particles showed a tendency to return back to the plume along the sidewalls, only to be lifted by the plume back to the foam [128].

The reduction stage is characterised by efficient mixing induced by vigorous argon stirring [62, 99, 102, 103]. Physical [102, 128] and numerical [62, 101] modelling studies on the reduction stage of the AOD process suggest a relatively strong emulsification of the top slag. In this work, it was assumed that the reactions during the reduction stage of the AOD process take place solely between emulsified slag droplets and metal bath.

Table 20. Properties of ferrous reductants, liquid steel and slag.

Material	State	Density [kg/m^3]	Melting point [K]	Reference
50FeSi	Solid	6100	1683	[532]
75FeSi	Solid	2800	1589	[533]
SiMn	Solid	6120	1488	[533]
Steel (0.1 wt-% C)	Liquid (at 1873 K)	7050	1803	[533]
CaO-SiO_2-Cr_2O_3 slag	Liquid	3200–3500	1758	[533]

6.3.1 Conservation of species, mass, and energy

The parallel reversible reactions considered by the model are the same as in the top-blowing model, *i.e.* Eqs. 213–219 (p. 152), and are not repeated here. Because the reactions are formulated as reversible, the simple oxidation reactions form a complex reaction system, in which species with a higher oxygen affinity are able to reduce oxides of species with a lower oxygen affinity, thereby establishing a competitive equilibrium at the reaction interface. The rate expressions were formulated according to the modified law of mass action, while the forward reaction rate coefficients were treated according to the reaction quotient method. The mass transport terms were formulated according to the *stationary medium approach* [279]. Consequently, the conservation of species i in phase ψ at the slag droplet interface (sd) was defined as

$$\underbrace{\beta_{i,\psi,\mathrm{sd}}\rho_{\psi,\mathrm{sd}}\left(y_{i,B}-y^{*}_{i,\mathrm{sd}}\right)}_{\text{mass transport}}+\underbrace{\sum_{k=1}^{r}R''_{k,\mathrm{sd}}\overline{\nu}_{i,k}}_{\text{chemical reactions}}=0\,, \tag{263}$$

where β is the mass transfer coefficient, ρ is the density, y is the mass fraction, y^* is the interfacial mass fraction, $\overline{\nu}$ is the mass-based stoichiometric coefficient, and R'' is the reaction rate flux. Employing the *implicit Euler method* for time integration, the conservation of species i of phase ψ in bulk phase B was defined according to

$$\underbrace{-\beta_{i,\psi,\mathrm{sd}}\rho_{\psi,\mathrm{sd}}A_{\mathrm{sd}}\left(y_{i,B}-y^{*}_{i,\mathrm{sd}}\right)}_{\text{mass transport}}\underbrace{-\frac{m_B y_{i,B}-m_B^{\mathrm{t}-\Delta\mathrm{t}}y_{i,B}^{\mathrm{t}-\Delta\mathrm{t}}}{\Delta t}}_{\text{accumulation of mass}}=0\,, \tag{264}$$

where A is the reaction area and Δt is the time step. The conservation of total masses in the bulk phases was defined by summation of the mass transport terms of individual species. The conservation of heat at the slag droplet interface was defined as

$$\underbrace{\alpha_{\mathrm{L,sd}}\left(T_{\mathrm{bath}}-T_{\mathrm{sd}}^{*}\right)+\alpha_{\mathrm{G,sd}}\left(T_{\mathrm{plume}}-T_{\mathrm{sd}}^{*}\right)+\alpha_{\mathrm{S,sd}}\left(T_{\mathrm{slag}}-T_{\mathrm{sd}}^{*}\right)}_{\text{heat transport}}\underbrace{-\sum_{k=1}^{r}R''_{k,\mathrm{sd}}\Delta h_k}_{\text{chemical reactions}}=0\,, \tag{265}$$

where Δh_k is the specific enthalpy change of reaction k. In addition, the conservation of energy was defined in each of the bulk phases (metal bath, plume gas, and top slag). Their mathematical treatment, however, is not repeated here. The effect of refractory wear on the slag composition is calculated by assuming a fixed dissolution rate of refractory material into the slag. The dissolution rate is calculated from the loss of refractory lining thickness per heat.

6.3.2 Emulsification of slag

At the metal–slag interface, the turning flow of the molten metal can detach slag droplets, which brings about a considerable increase in the metal–slag interfacial area [1, 234–236, 534]. A schematic illustration of the emulsification mechanism is shown in Fig 25. Because the density of the slag droplets is much lower than that of molten steel, the buoyancy force eventually lifts the slag droplets back to the top slag [1, 234–236, 534]. There is little information on the size distributions and residence times of slag droplets in converter and ladle processes. Some useful experimental information has been provided by Lachmund *et al.* [535], who analysed slag droplet size distributions in a ladle treatment using a metal plate, which was lowered into the ladle. In contrast to the lack of data from actual processes, emulsification has been studied extensively with physical models [365, 534, 536–542]. Although the results are not directly applicable to industrial processes, these studies have provided valuable information on the physical properties and mechanisms affecting the emulsification phenomena. In recent years, CFD-based methods have also been applied for detailed studies of emulsification [234–236, 542, 543].

The description of emulsification employed in this work is based on the fundamental principles of emulsification proposed by Wei and Oeters [1, 534] and no consideration is given to periodic changes due to plume oscillation or possible disintegration of the slag droplets. The condition for droplet formation can be described according to the following force balance [1, 534]:

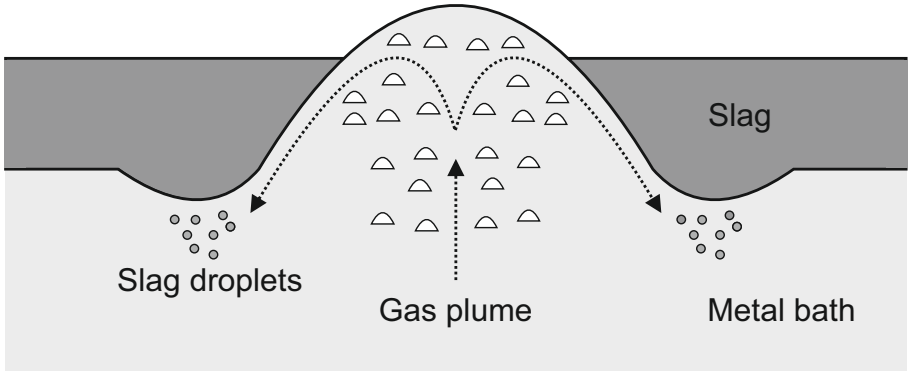

Fig 25. Schematic illustration of slag emulsification. Adapted from [1].

$$F_{\text{inertia}} \geq F_{\text{interface}} + F_{\text{buoyancy}} \cos\alpha\,, \tag{266}$$

where F_{inertia} is the inertial force of the slag, $F_{\text{interface}}$ is the interfacial force, F_{buoyancy} is the buoyancy force, and α is the angle between the buoyancy vector and the vertical axis; these are defined according to Eqs. 267, 268 and 269, respectively [1].

$$F_{\text{inertia}} = \frac{1}{2}\rho_{\text{S}} u_{\text{i}}^2 \frac{\pi}{4} d_{\text{sd}}^2\,, \tag{267}$$

$$F_{\text{interface}} = \sigma_{\text{L-S}} \pi d_{\text{sd}}\,, \tag{268}$$

$$F_{\text{buoyancy}} = g\,(\rho_{\text{L}} - \rho_{\text{S}})\,\frac{1}{6}\pi d_{\text{sd}}^3\,, \tag{269}$$

where d_{sd} is the diameter of the slag droplets and $\sigma_{\text{L–S}}$ is the metal–slag interfacial tension. The detachment of slag droplets takes place, if the velocity of the slag phase at the break away point, *i.e.* the interfacial velocity u_{i}, exceeds a critical value [1]. If the critical velocity is exceeded, the diameter of the droplets can be calculated as follows [1, 534]:

$$d_{\text{sd}} = \frac{3}{8}\frac{\rho_{\text{S}} u_{\text{i}}^2}{g(\rho_{\text{L}} - \rho_{\text{S}})}\left[1 - \left(1 - \frac{128\sigma_{\text{L–S}} g(\rho_{\text{L}} - \rho_{\text{S}})\cos\alpha}{3\rho_{\text{S}}^2 u_{\text{i}}^4}\right)^{1/2}\right]. \tag{270}$$

where α is the angle between the inertial and vertical force. The number of droplets generated per unit time can be calculated based on the energy balance of the work required to detach a single droplet and the kinetic energy supplied by the downwardly

flowing slag boundary layer [1]. The work required for detaching a single droplet (W_{sd}), the kinetic energy per time unit ($\dot{E}_{kin}$), and the total kinetic energy ($\dot{E}_{kin,tot}$) are given by Eqs. 271, 272, and 273, respectively [1].

$$W_{sd} = \pi d_{sd}^2 \sigma_{L\text{–}S} + \frac{1}{6}\pi d_{sd}^4 g\,(\rho_L - \rho_S)\cos\alpha\,, \tag{271}$$

$$\dot{E}_{kin} = \int_0^{\delta_S} \frac{1}{2} u_S^3 \rho_S d_{sd}\,\mathrm{d}x \approx 0.4153 d_{sd} \rho_S^{1/2} \mu_S^{1/2} L^{1/2} u_i^{5/2}\,, \tag{272}$$

$$\dot{E}_{kin,tot} = \dot{E}_{kin} \pi \frac{d_{plume}}{d_{sd}}\,, \tag{273}$$

where u_S is the velocity profile in the top slag at the height of the droplet detachment, L is the streamed length, and d_{plume} is the diameter of the plume at the metal–slag interface. The number of droplets generated per unit time can be obtained with the help of Eqs. 271, 272, and 273 [1]:

$$\dot{N}_{sd} = \frac{\dot{E}_{kin,tot}}{W_{sd}} = \frac{0.4153 d_{plume} \rho_S^{1/2} \mu_S^{1/2} L^{1/2} u_i^{5/2}}{d_{sd}^2 \sigma_{L\text{–}S} + \frac{1}{6}\pi d_{sd}^4 g (\rho_L - \rho_S)\cos\alpha}\,. \tag{274}$$

As seen from Eq. 274, the calculated droplet formation rate increases with increasing streamed length (*i.e.* thickening slag layer) and increasing interfacial velocity, respectively [1]. In this work, the streamed length (L) was taken as equal to the height of the slag layer (h_{slag}) similarly to Lachmund *et al.* [535]. The diameter of the gas plume in the studied converter was assumed to be d_{plume} = 1.5 m based on a CFD study [544], while the angle between the inertial and vertical force was assumed to be $\alpha = 30^\circ$ based on a physical modelling study [541]. The interfacial velocity u_i is determined iteratively from Eqs. 275–278 [1].

$$u_i = u_L \times U\,, \tag{275}$$

$$u_L = u_{L,0} + \frac{2}{3}\left[2g\left(1 - \frac{\rho_S}{\rho_L}\right) L \cos\alpha\right]^{1/2}, \tag{276}$$

$$U = 0.1367 \left(\frac{\rho_L}{\rho_S}\right)^{2/3} \left(\frac{u_L L}{\nu_S}\right)^{1/3} \left(\frac{u_L L}{\nu_L}\right)^{-2/15} \cdot \left[\Big(1 - U\Big)\Big(0.1108 - 0.0693U\Big)\right]^{2/15}, \tag{277}$$

$$u_{L,0} = \sqrt{2gh}\,, \tag{278}$$

where ν denotes the kinematic viscosity, h is the height of the top of plume above the surface slag, and U is the dimensionless velocity. Here, it was assumed that the spout does not rise above the level of the top slag and thus $h = 0$. It should be noted that some of the underlying assumptions [1, 534] of Eqs. 275–278 may be violated due to the highly turbulent conditions prevailing in the AOD process, and for this reason, the calculated interfacial velocity needs to be interpreted with care. The total surface area of the droplets at time $t = t_1$ was approximated as follows:[37]

$$A_{\mathrm{sd}}(t) = \int_{\max(t_1 - \bar{t}_{\mathrm{sd,max}}, 0)}^{t_1} \pi d_{\mathrm{sd}}^2(t) \dot{N}_{\mathrm{sd}}(t)\, \mathrm{d}t \approx \sum_{t=\max(t_1 - \bar{t}_{\mathrm{sd,max}}, 0)}^{t_1} \pi d_{\mathrm{sd}}^2(t) \dot{N}_{\mathrm{sd}}(t)\, \delta t\,, \quad (279)$$

where $\bar{t}_{\mathrm{sd,max}}$ is the maximum average residence time of the slag droplets, d_{sd} is the diameter of the slag droplets, $\dot{N}_{\mathrm{sd}}$ is the number of droplets generated per unit time, and δt is a small time increment, which was taken as δt = 1 s. The average residence time of the slag droplets is defined as $\bar{t}_{\mathrm{sd}} = \min(\bar{t}_{\mathrm{sd,max}}, t)$.

Some estimates on the validity of Eqs. 270 and 274 are available in the literature. Wei and Oeters [534] conducted physical modelling experiments, in which water and cyclohexane were used to represent steel and slag, respectively. Fig. 26 illustrates the average droplet diameter and droplet generation rate measured by Wei and Oeters [534] in comparison to the theoretical values calculated using Eqs. 270 and 274, respectively. The agreement between the measured and calculated droplet size is good at high water stream velocities, but poor at low velocities (Fig. 26a). At low water stream velocities, the calculated droplet generation rate is slightly higher than the measured values, while the opposite is true at high water stream velocities (Fig. 26b).

Using a CFD model, Sulasalmi *et al.* [234, 236] studied emulsification of slag in a geometry similar to that employed by Savolainen *et al.* [541] in their physical modelling study. For water–oil systems, the droplet sizes calculated with Eq. 270 were found to be slightly smaller than those measured by Savolainen *et al.* [541], but larger than those predicted by the CFD model [234]. The slag droplet generation rates calculated with Eq. 274 were in close agreement with the results obtained using CFD modelling [236].

[37] This approximation is permitted by the fact that $\int_a^b f(x)\, \mathrm{d}x = \lim_{\delta x \to 0} \sum_{x=a}^{b} f(x)\, \delta x$.

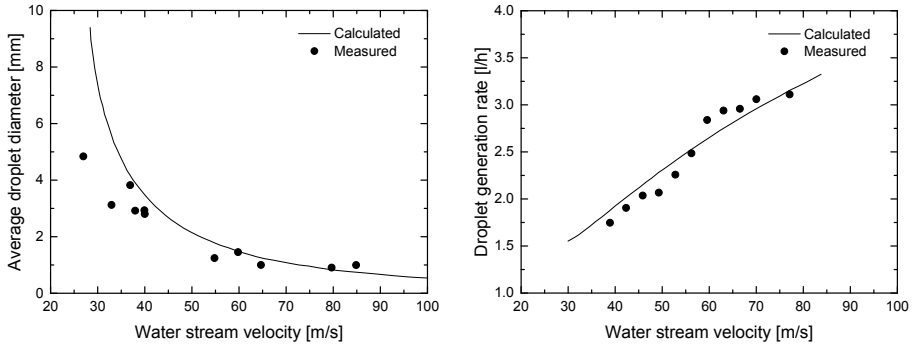

(a) Average droplet diameter. **(b) Droplet generation rate.**

Fig 26. Comparison of the calculated and measured average droplet diameter and droplet generation rate in a water-cyclohexane system. Adapted from [534].

6.3.3 Mass and heat transfer coefficients

The mass and heat transfer coefficients in the boundary layers on the outside of the slag droplets were estimated based on the penetration theory proposed by Higbie [226]. Moreover, it was assumed that the droplets behave like rigid spheres and the transport of species within the droplets takes place only by means of diffusion. The mass and heat transfer coefficients for metal, gas, and slag phases are given by Eqs. 280, 281, and 282.[38]

$$\beta_\mathrm{L} = \frac{2}{\sqrt{\pi}}\sqrt{\frac{D_\mathrm{L} u_\mathrm{sd}}{\overline{d}_\mathrm{sd}}} \qquad \alpha_\mathrm{L} = \frac{2}{\sqrt{\pi}}\rho_L c_{\mathrm{p,L}}\sqrt{\frac{\lambda_\mathrm{L} u_\mathrm{sd}}{\rho_\mathrm{L} c_{\mathrm{p,L}} \overline{d}_\mathrm{sd}}}\,. \tag{280}$$

$$\beta_\mathrm{G} = \frac{2}{\sqrt{\pi}}\sqrt{\frac{D_\mathrm{G} u_\mathrm{b}}{d_\mathrm{b}}} \qquad \alpha_\mathrm{G} = \frac{2}{\sqrt{\pi}}\rho_\mathrm{G} c_{\mathrm{p,G}}\sqrt{\frac{\lambda_\mathrm{G} u_\mathrm{b}}{\rho_\mathrm{G} c_{\mathrm{p,G}} d_\mathrm{b}}}\,, \tag{281}$$

$$\beta_\mathrm{S} = 12\frac{D_\mathrm{S}}{\overline{d}_\mathrm{sd}} \qquad \alpha_\mathrm{S} = 12\frac{\lambda_\mathrm{S}}{\overline{d}_\mathrm{sd}}\,, \tag{282}$$

where D, λ, and c_p denote the mass diffusivity, the heat conductivity, and the specific heat capacity, respectively, while u_sd is the terminal velocity of the slag droplets in the metal bath, $\overline{d}_\mathrm{sd}$ is the mean diameter of the slag droplets, d_b is the bubble diameter, and

[38] In Article III, Eqs. 280 and 281 were taken from Järvinen *et al.* [44], where the prefactor was given as 1.28. Unfortunately, this value corresponds to a correlation for spherical-cap bubbles [352] and the Higbie correlation [226] as stated in the text; the correct prefactor of the Higbie correlation is $\frac{2}{\sqrt{\pi}} \approx 1.128$. Here the equations are presented in their correct form.

u_b is the slip velocity of the gas bubbles in the metal bath. The bubble diameter d_b was calculated using the equation available in [44]. A detailed description of the calculation methods employed for the terminal velocities of slag droplets and gas bubbles are given in Appendix 1.

6.3.4 Modifications to the original model

Some of the assumptions of the reduction model leave room for criticism. For the internal mass transfer problem, the prefactor 12 in Eq. 282 was derived by assuming Sh = 2 and $L = 6/\bar{d}_{sd}$. The mass transfer coefficient resulting from this initial approximation is between the asymptotic solutions for rigid spheres [323] (Sh $\approx$ 6.6) and rigid spheres with laminar internal circulation [328] (Sh $\approx$ 17.9) solutions, but relatively close to effective laminar mass transfer in a rigid sphere [335] (Sh $\approx$ 14.8). Furthermore, the surface renewal model, which assumes frictionless mass transfer, overestimates the external mass transfer rate.

The metal–slag interfacial tension during the reduction stage was taken as σ_{L-S} = 0.49 N/m. However, this is a misunderstanding of the results reported by Fabritius *et al.* [313], as the value does not represent the interfacial tension between the steel and the slag, but rather the surface tension of the slag. Nevertheless, it is known that the interfacial tension can have low values during intense metal–slag reactions [545] and hence values in the order of σ_{L-S} = 0.5 N/m have often been employed in modelling work [235, 236, 535, 546].

With the above criticisms in mind, the reduction model was modified as follows:

1. The internal mass and heat transfer within a slag droplet was calculated according to the Newman solution [323] (Eq. 141 on p. 117). The average residence time of the slag droplets ($\bar{t}_{sd}$) in the metal bath was employed as the characteristic time for the mass and heat transfer within the droplets. The external mass and heat transfer around the slag droplets was described by the Ranz-Marschall correlation [252, 253] (Eq. 151 on p. 121). Here, the Sauter mean diameter of the slag droplets ($d_{32,sd}$) was employed as the characteristic lenght, while the terminal velocity of the slag droplets (u_{sd}) was employed as the characteristic velocity.
2. The mass and heat transport terms for the slag species were modified to account for conservation of mass and energy in the slag droplets. Furthermore, the Stefan flow term was introduced to the conservation equations of metal and slag species. At the

reaction interface, the conservation of slag species i in the metal and slag phases was formulated according to Eqs. 283 and 284, respectively. The conservation of mass in the bulk phases and the conservation of energy were formulated correspondingly.

$$\underbrace{\beta_{i,\mathrm{L,sd}}\rho_{\mathrm{L,sd}}\left(y_{i,\mathrm{bath}}-y^{*}_{i,\mathrm{sd}}\right)}_{\text{mass transport}}+\underbrace{\max(m''_{\mathrm{L,sd}},0)y_{i,\mathrm{bath}}-\max(-m''_{\mathrm{L,sd}},0)y^{*}_{i,\mathrm{sd}}}_{\text{Stefan flow}}+\underbrace{\sum_{k=1}^{r}R''_{k,\mathrm{sd}}\overline{\nu}_{i,k}}_{\text{chemical reactions}}=0\,, \quad (283)$$

$$\underbrace{\left(\frac{m_{\mathrm{sd}}}{A_{\mathrm{sd}}\bar{t}_{\mathrm{sd}}}-m''_{\mathrm{S,sd}}\right)\overline{\eta}_{i,\mathrm{M,sd}}\left(y_{i,\mathrm{slag}}-y^{*}_{i,\mathrm{sd}}\right)}_{\text{mass transport}}+\underbrace{m''_{\mathrm{S,sd}}y_{i,\mathrm{slag}}}_{\text{Stefan flow}}+\underbrace{\sum_{k=1}^{r}R''_{k,\mathrm{sd}}\overline{\nu}_{i,k}}_{\text{chemical reactions}}=0\,. \quad (284)$$

3. The effective metal–slag interfacial tension was assumed to be 50% of the nominal metal–slag interfacial tension, which was calculated on the basis of the Girifalco–Good equation [547]. Making use of the parameters applicable for the reduction stage [313], the resulting effective interfacial tension is $\sigma_{\mathrm{L–S}} \approx 0.56$ N/m. This value is slightly higher than that employed in Article IV.
4. The physical and thermochemical properties were determined as shown later in Table 22. With the exception of $\varepsilon^{\mathrm{Si}}_{\mathrm{Si}}$ and $\varepsilon^{\mathrm{Mn}}_{\mathrm{Mn}}$, the interaction parameters are the same as those employed in the top-blowing model. A higher value of $\varepsilon^{\mathrm{Si}}_{\mathrm{Si}}$ [548] was found to be necessary to achieve a sufficiently low final Si content of the metal bath, while the value of $\varepsilon^{\mathrm{Mn}}_{\mathrm{Mn}}$ was adjusted to provide a sufficiently high Mn content of the metal bath (see Appendix 1).
5. Similarly to the top-blowing model, the parameter J_{eff} was introduced for adjusting the slag droplet generation rate. More specifically, the effective number of droplets generated per unit time was calculated from

$$\dot{N}_{\mathrm{sd,eff}} = J_{\mathrm{eff}} \cdot \dot{N}_{\mathrm{sd}}\,. \quad (285)$$

6.4 Common functionalities

6.4.1 Material additions

Various additions of steel scrap, ferroalloy, slag formers, and flux are added during the AOD process. In the decarburisation stage, metal scrap can be used to cool the metal bath and to increase the batch size, while ferroalloys are employed primarily for alloying purposes. During the reduction stage, reductants are fed into the vessel in order to reduce chromium oxides in the slag; typical reductants include FeSi, SiMn, and Al. Two categories of ferroalloys can be distinguished [126]:

Class I Ferroalloys, which have a melting point *lower* than that of liquid steel [126]. When a cold alloy particle of Class I is added to the melt, a solid steel shell forms around the particle [1, 126, 549]. The steel shell eventually melts and the particle is heated to its melting point. Class I ferroalloys include FeSi, FeMn, SiMn, and FeCr [126].

Class II Ferroalloys, which have a melting point *higher* than that of liquid steel [126]. Their rate of dissolution is determined by the mass transfer in liquid steel and is generally much slower than that of class I ferroalloys [126]. Class II ferroalloys include Mo, V, Nb, and W [126].

Most of the ferrous reductants belong to class I ferroalloys (see Table 20 on p. 172). The melting and dissolution times of class I ferroalloys and other materials with melting points lower than that of steel were estimated by observing the melting time of spheres. The melting times of the additions were solved analytically from [550, 551]:

$$\tau_{\mathrm{m}} = \frac{d_{\mathrm{p}}^2 \rho_{\mathrm{p}} l_{\mathrm{m}}}{8 \lambda_{\mathrm{eff}} (T_{\mathrm{bath}} - T_{\mathrm{m}})}\,, \tag{286}$$

where d_{p} is the particle size, ρ_{p} is the density of the particle, l_{m} is the latent heat of melting, λ_{eff} is the effective heat conductivity of the material, and T_{m} is the melting temperature. In order to account for the effect of shell formation, the effective heat conductivities of the materials were fitted to the experimental melting times of 50FeSi [552], 75FeSi [533], SiMn [533], steel scrap [553], and nickel-bearing ferroalloys [554]. For particle sizes in the range of 50 mm, a reasonably good agreement with experimental data was achieved by assuming a linear dependency of the effective heat conductivity on the particle size. The feeding time of the additions was taken into account by employing

a constant feed rate separately for each batch of additions. The effect of material additions on the temperature of the metal bath was calculated explicitly. With respect to slag formers and fluxes, it was assumed that they dissolve and mix instantaneously with the top slag.

6.4.2 Thermodynamic properties

The equilibrium constants of the studied reactions were calculated at the temperature of the reaction interface:

$$K = \exp\left(-\frac{\Delta G^\circ}{RT^*}\right) \quad \text{where} \quad \Delta G^\circ = \Delta H^\circ - T^*\Delta S, \tag{287}$$

where ΔG°, ΔH°, and ΔS° are the changes in standard Gibbs free energy, enthalpy, and entropy of reaction, respectively. The Henrian standard state was employed for the species in the liquid metal phase (point B in Fig. 27), while the Raoultian standard state was employed for species in the slag phase (point A in Fig. 27). The non-ideality of the slag and gas species were taken into account by making use of available activity models; a more detailed description of these models is provided in the following sections. The detailed treatment of the thermochemical properties is described in Appendix 1.

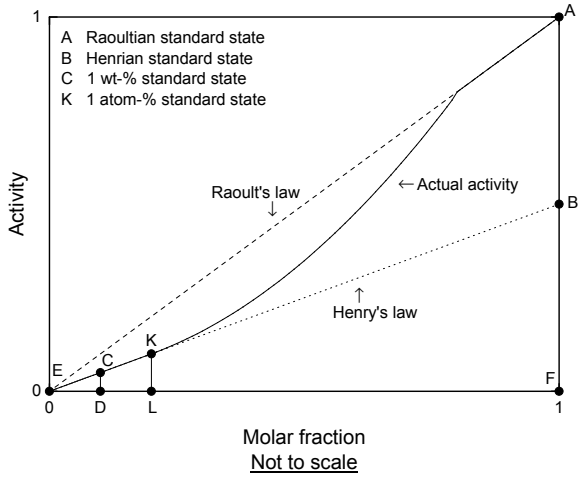

Fig 27. Thermodynamic standard states. Adapted from [404].

Gas partial pressures

The gas phase was assumed to obey the ideal gas law. Therefore, the partial pressures of species at the reaction interfaces can be obtained using Dalton's law [555]:

$$p_i = x_i^* p_{\mathrm{G}}\,, \tag{288}$$

where p_{G} is the total gas pressure (in atm). The pressure changes in a free gas jet are sufficiently small to be ignored [492] and therefore the total pressure at the cavity and metal droplet interfaces was defined as equal to the pressure of the surrounding atmosphere, $p_{\mathrm{G,cav}} = p_{\mathrm{G,md}} = p_{\mathrm{amb}}$. In the case of the reduction model, it was assumed that the ferrostatic pressure near the metal–slag interface is negligible and that the total pressure at the slag droplet interface is equal to the ambient pressure, $p_{\mathrm{G,sd}} = p_{\mathrm{amb}}$.

Activities of dissolved species

The Henrian activities of species dissolved in liquid iron can be expressed in terms of the mole fraction multiplied by the Henrian activity coefficient:

$$a_i^{\mathrm{H}} = \gamma_i^{\mathrm{H}} x_i\,. \tag{289}$$

The Wagner formalism represents the MacLaurin series expansion of the activity coefficient in terms of ε interaction parameters [556]. Consequently, the Henrian activity coefficient of species i can be expressed according to [556]:

$$\ln \gamma_i^{\mathrm{H}} = \ln\left(\frac{\gamma_i^{\mathrm{R}}}{\gamma_i^{\circ}}\right) = \underbrace{\sum_{j=2}^{n} \varepsilon_i^j x_j}_{\substack{\text{first-order}\\ \text{interactions}}} + \underbrace{\sum_{j=2}^{n} \rho_i^j x_j^2}_{\substack{\text{second-order}\\ \text{interactions}}} + \underbrace{\sum_{j=2}^{n-1}\sum_{k=j+1}^{n} \rho_i^{jk} x_j x_k}_{\substack{\text{second-order}\\ \text{cross-interactions}}} + \underbrace{R(x^3)}_{\substack{\text{error}\\ \text{term}}}\,, \tag{290}$$

where γ_i^{R} is the Raoultian activity coefficient, γ_i° is the activity coefficient at infinite dilution, ε is the molar first-order interaction parameter, ρ is the molar second-order interaction parameter, and $R(x^3)$ represents the sum of the terms higher than the third order. Because suitable higher-order parameters are rarely available, it is more common to truncate the MacLaurin series after the first-order terms [556]. As a result, the following well-known expression is obtained [556]:

$$\ln \gamma_i^{\mathrm{H}} = \ln\left(\frac{\gamma_i^{\mathrm{R}}}{\gamma_i^{\circ}}\right) = \sum_{j=2}^{n} \varepsilon_i^j x_j \,. \tag{291}$$

Although Eq. 291 is applicable for activity coefficients in the dilute region, the thermodynamic inconsistency of the truncated MacLaurin series can induce inaccuracy at high solute concentrations [254, 556, 557]. For this reason, the Wagner formalism is not recommendable for stainless steel melts [556]. Attempts have been made to extend the ε approach for concentrated solutions. Pelton and Bale [254] proposed the *unified interaction parameter* (UIP) formalism, which combines the *Wagner-Lupis-Elliott* (WLE) formalism [558], Darken's quadratic formalism [559, 560], and Margules formalism [561]; it reduces to WLE formalism at infinite dilution and to Darken's quadratic formalism in solutions. The Henrian activity coefficient of species i is expressed according to [254]:

$$\ln \gamma_i^{\mathrm{H}} = \ln\left(\frac{\gamma_i^{\mathrm{R}}}{\gamma_i^{\circ}}\right) = \underbrace{-0.5 \sum_{j=1}^{n} \sum_{k=1}^{n} \varepsilon_j^k x_j x_k}_{\substack{\text{interaction} \\ \text{with solvent}}} + \underbrace{\sum_{j=1}^{n} \varepsilon_i^j x_j}_{\substack{\text{interaction} \\ \text{with solutes}}} \,. \tag{292}$$

Ma *et al.* [557] proposed an ε formalism, which is thermodynamically consistent with the Gibbs-Duhem relationship. The Ma *et al.* [557] formalism has been employed particularly for stainless steel melts [556, 562, 563]. In comparison to the UIP formalism, it provides a more rigorous description for the effect of solvent on the activity of solutes [557, 564]. The Raoultian activity coefficient of the solvent and the Henrian activity coefficient of the solutes are expressed according to Eqs. 293 and 294.

$$\begin{aligned}
\ln \gamma_{\text{solvent}}^{\mathrm{R}} = & \sum_{i=2}^{m} \varepsilon_i^i \left[x_i + \ln(1-x_i)\right] \\
& - \sum_{j=2}^{m-1} \sum_{k=j+1}^{m} \varepsilon_j^k x_j x_k \left(1 + \frac{\ln(1-x_j)}{x_j} + \frac{\ln(1-x_k)}{x_k}\right) \\
& + \sum_{i=2}^{m} \sum_{k=2(k\neq i)}^{m} \varepsilon_i^k x_i x_k \left(1 + \frac{\ln(1-x_k)}{x_k} + \frac{1}{1-x_k}\right) \\
& + \frac{1}{2} \sum_{j=2}^{m-1} \sum_{k=j+1}^{m} \varepsilon_j^k x_j^2 x_k^2 \left(\frac{1}{1-x_j} + \frac{1}{1-x_k} - 1\right) \\
& - \sum_{i=2}^{m} \sum_{k=2(k\neq i)}^{m} \varepsilon_i^k x_i^2 x_k^2 \left(\frac{1}{1-x_i} + \frac{1}{1-x_k} + \frac{x_i}{2(1-x_i)^2} - 1\right) \,.
\end{aligned} \tag{293}$$

$$\ln \gamma_i^{\mathrm{H}} = \ln\left(\frac{\gamma_i^{\mathrm{R}}}{\gamma_i^{\circ}}\right) = \ln \gamma_{\mathrm{solvent}}^{\mathrm{R}} - \varepsilon_i^i \ln(1-x_i) - \sum_{k=2(k\neq i)}^{m} \varepsilon_i^k x_k \left[1 + \frac{\ln(1-x_i)}{x_k} - \frac{1}{1-x_i}\right] + \sum_{k=2(k\neq i)}^{m} \varepsilon_i^k x_k^2 x_i \left(\frac{1}{1-x_i} + \frac{1}{1-x_k} + \frac{x_i}{2(1-x_i)^2} - 1\right). \quad (294)$$

In this work, the activities of the dissolved species were calculated with the UIP formalism [254] based on the interfacial composition and hence x was replaced by x^* in Eq. 292. The employed molar first-order interaction parameters were obtained from the literature [548, 565–568] and are tabulated in Appendix 1. In order to find possible differences, the Wagner, UIP, and Ma *et al.* formalisms were compared for stainless steel melts. *Ceteris paribus*, the deviations in the predicted activities of the main species were found to be small even in the case of concentrated solutions such as liquid stainless steels.

Activities of slag species

Various models have been proposed for calculating activities in molten slags; these include the regular solution model [569], modified quasi-chemical model [570–574], reciprocal ionic liquid model [575], cell model [576], polymerisation model [577–580], the molecular interaction volume model [581, 582], and various empirical models [49, 583–585].[39] Regular solution models constitute one of the most simplistic types of slag models. The main assumptions of regular solution models are that the atoms are distributed randomly on the sites of a three-dimensional lattice (which has no vacancies) and that the energy of the system is defined as the sum of pairwise interactions [588]. In the regular solution model proposed by Ban-Ya [569], the Raoultian activity coefficients of the slag species are calculated as follows [569]:

$$RT \ln \gamma_i^{\mathrm{R}} = \underbrace{\sum_{\substack{j=1 \\ j\neq i}}^{n} \alpha_{ij} X_j^2}_{\text{first-order interactions}} + \underbrace{\sum_{\substack{j=1 \\ j\neq i}}^{n} \sum_{\substack{k=j+1 \\ k\neq i}}^{n} \left(\alpha_{ij} + \alpha_{ik} - \alpha_{jk}\right) X_j X_k}_{\text{second-order interactions}} + \underbrace{\Delta G_{i,\mathrm{conv}}}_{\text{conversion energy}}, \quad (295)$$

[39] More detailed reviews of the activity models are available in the literature [586, 587].

where α is the interaction energy between cations, X is the cation fraction, and ΔG_{conv} is the conversion energy of the activity coefficient between a hypothetical regular solution and a real solution. Although the parameters for chromium-containing slags are available in the literature [178], they are not applicable to the high basicity ratios typical for AOD processing.

In this work, the activity coefficients of slag species were calculated according to the model employed by Wei and Zhu [49]. The Raoultian activity coefficients of FeO, Cr_2O_3, MnO, and SiO_2 are given by Eqs. 296, 297, 298, and 299, respectively [49].

$$\begin{aligned}\log_{10}\gamma^{\text{R}}_{\text{FeO}} = {} & \frac{\varepsilon_1}{T^*}(x^*_{\text{CaO}} + x^*_{\text{MgO}})(x^*_{\text{SiO}_2} + 0.25x^*_{\text{AlO}_{1,5}}) \\ & + \frac{\varepsilon_2}{T^*}x^*_{\text{MnO}}(x^*_{\text{SiO}_2} + 0.45x^*_{\text{CrO}_{1.5}}) + \frac{\varepsilon_3}{T^*}x^*_{\text{AlO}_{1.5}}x^*_{\text{SiO}_2} \\ & + \frac{\varepsilon_4}{T^*}x^*_{\text{MnO}}x^*_{\text{AlO}_{1.5}} + \frac{\varepsilon_5}{T^*}x^*_{\text{CrO}_{1.5}}x^*_{\text{SiO}_2}\,, \end{aligned} \tag{296}$$

$$\log_{10}\gamma^{\text{R}}_{\text{Cr}_2\text{O}_3} = \log_{10}\gamma^{\text{R}}_{\text{FeO}} - \frac{\varepsilon_6}{T^*}(x^*_{\text{CaO}} + x^*_{\text{MgO}}) - \frac{\varepsilon_7}{T^*}x^*_{\text{MnO}} - \frac{\varepsilon_5}{T^*}x^*_{\text{SiO}_2}\,, \tag{297}$$

$$\log_{10}\gamma^{\text{R}}_{\text{MnO}} = \log_{10}\gamma^{\text{R}}_{\text{FeO}} - \frac{\varepsilon_2}{T^*}(x^*_{\text{SiO}_2} + 0.45x^*_{\text{CrO}_{1.5}}) - \frac{\varepsilon_4}{T^*}x^*_{\text{AlO}_{1.5}}\,, \tag{298}$$

$$\begin{aligned}\log_{10}\gamma^{\text{R}}_{\text{SiO}_2} = {} & \log_{10}\gamma^{\text{R}}_{\text{FeO}} - \frac{\varepsilon_1}{T^*}(x^*_{\text{CaO}} + x^*_{\text{MgO}}) \\ & - \frac{\varepsilon_2}{T^*}x^*_{\text{MnO}} - \frac{\varepsilon_3}{T^*}x^*_{\text{AlO}_{1.5}} - \frac{\varepsilon_5}{T^*}x^*_{\text{CrO}_{1.5}}\,, \end{aligned} \tag{299}$$

where $\varepsilon_1 \ldots \varepsilon_7$ are the interaction coefficients of the model. Table 21 shows the interaction coefficients reported by Wei and Zhu [49] for early and later periods of refining. The parameters for early refining are employed in the stages involving top-blowing, while the parameters for the later period of refining are employed in other stages, *e.g.* during the reduction stage.

Table 21. Interaction coefficients of the slag model. Adapted from [49].

	Interaction coefficients						
Stage	ε_1	ε_2	ε_3	ε_4	ε_5	ε_6	ε_7
Early period of refining	3540	1475	1068	36	593	1594	664
Later period of refining	4130	1720	1246	42	692	1859	774

In the top-blowing model it was assumed similarly to Wei and Zhu [49] that $a^{\text{R}}_{\text{Cr}_2\text{O}_3} = 1$ if the interfacial Cr_2O_3 content is greater than the maximum solubility of Cr_2O_3 in the slag. For this purpose, a simple regression equation for the solid fraction of the top slag

was derived with the help of the FactSage 7.0 computational thermodynamics software [589] (see Appendix 1).

6.4.3 Physical properties

A summary of the treatment of the physical properties is shown in Table 22. Where applicable, the properties were defined with respect to the composition and temperature of the considered reaction interface. The physical properties of the steel and slag phases were estimated at the temperature of the reaction interface, while the properties of the gas phase were defined at gas film temperatures. A more detailed description of the sub-models is presented in Appendix 1.

Table 22. Employed values and models for physical properties. Modified from Article I.

Property	Employed value or model	Notes	Reference
ρ_L	Temperature function	Stainless steel (AISI 304)	[590]
ρ_G	Ideal gas law	–	–
ρ_S	Partial molar volume method	–	[591]
μ_L	Temperature function	Stainless steel (AISI 304)	[590]
μ_G	Wilke equation	Gas mixture	[592]
$\mu_{i,G}$	Chapman–Enskog equation	Gas species	[115, 268, 593]
$\mu_{S(l)}$	Forsbacka *et al.* model	Liquid slag	[594]
$\mu_{S,rel}$	Thomas equation	Effect of solid particles	[595]
$D_{L,eff}$	Interdiffusion coefficients	Values in liquid iron	[596]
$D_{G,eff}$	$0.185 \cdot 10^{-4}$ m^2/s	O_2–CO binary at 273.0 K and 101325 Pa	[597]
$D_{S,eff}$	$5.0 \cdot 10^{-10}$ m^2/s	Estimated value (decarb.)	[598]
$D_{S,eff}$	$1.0 \cdot 10^{-9}$ m^2/s	Estimated value (reduction)	[598]
λ_L	Temperature function	Stainless steel (AISI 304)	[590]
λ_G	Mason–Saxena equation	Gas mixture	[268, 599]
$\lambda_{i,G}$	Eucken equation	Gas species	[268]
λ_S	1.0 W/(m·K)	Estimated value	[600]
$c_{p,L}$	Weight-averaged value	Liquid metal mixture	–
$c_{p,G}$	Weight-averaged value	Gas mixture	–
$c_{p,S}$	Weight-averaged value	Slag mixture	–
$c_{p,i}$	Shomate equation	Species	[200]

Table 22. (Continued)

Property	Employed value or model	Notes	Reference
σ_{L-S}	Girifalco–Good equation	Effective metal–slag interfacial tension assumed to be 50% of the nominal value	[547]
σ_L	1.5 N/m	Estimated value	[100]
σ_S	0.49 N/m	Reduction stage	[313]
ϕ	0.503	Reduction stage	[313]

6.4.4 Numerical solution

The objective of the numerical solution routine is to minimise the error in free variables, while minimising the error in thermodynamic equilibrium at the reaction interfaces. In this work, the conservation of mass and conservation of energy were solved successively in separate loops to obtain higher stability and better convergence. The resulting error is negligible when the employed time step is sufficiently small. The flowchart of the reduction and top-blowing models are similar and follow that shown in Fig. 28.

The conservation of mass and energy forms a highly non-linear system of differential equations, which needs to be solved using numerical methods. In this work, it was chosen to employ Newton's method, which approximates the target function with its tangent line [452]. Newton's method can be expressed in vector form as follows [322, 451]:

$$\mathbf{J}\Delta\mathbf{x} = -\mathbf{f}, \tag{300}$$

where $\mathbf{J}$ is the Jacobian matrix,[40] $\Delta\mathbf{x}$ is the correction vector, and $\mathbf{f}$ is the residual vector. An expanded form of Eq. 300 is shown below:

$$\underbrace{\begin{bmatrix} \frac{\partial f_1}{\partial x_1} & \cdots & \frac{\partial f_1}{\partial x_n} \\ \vdots & \ddots & \vdots \\ \frac{\partial f_n}{\partial x_1} & \cdots & \frac{\partial f_n}{\partial x_n} \end{bmatrix}}_{\text{Jacobian matrix}} \underbrace{\begin{bmatrix} \Delta x_1 \\ \vdots \\ \Delta x_n \end{bmatrix}}_{\text{correction vector}} = - \underbrace{\begin{bmatrix} f_1 \\ \vdots \\ f_n \end{bmatrix}}_{\text{residual vector}}, \tag{301}$$

where $f_1 \dots f_n$ are the residuals, $x_1 \dots x_n$ are the free variables, $\frac{\partial f_1}{\partial x_1} \dots \frac{\partial f_n}{\partial x_n}$ are the first-order differentiates of the residuals with respect to free variables, and $\Delta x_1 \dots \Delta x_n$

[40] A Jacobian matrix denotes a matrix of all first-order partial derivatives of a vector-valued function.

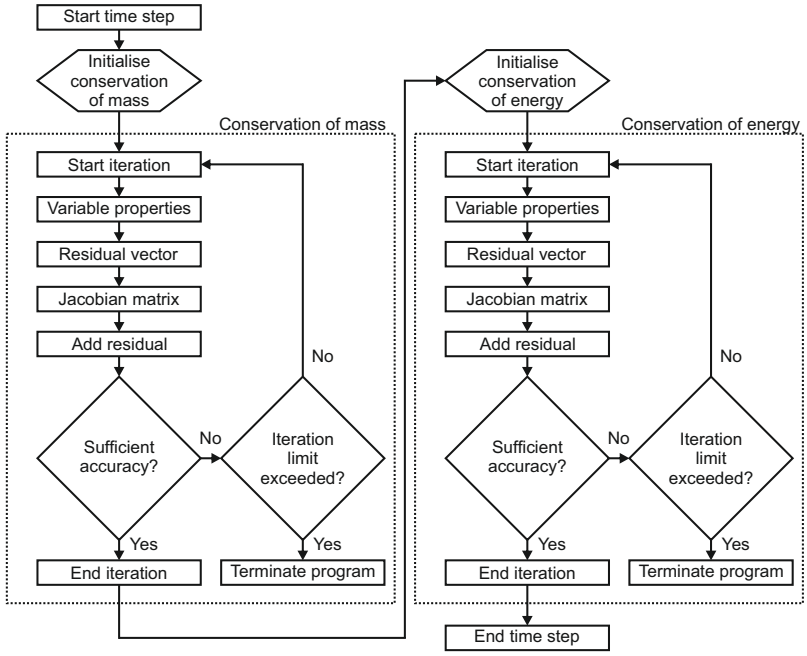

Fig 28. Flowchart of the top-blowing model. Modified from Article I.

are the corrections to the free variables. The system of linear equations defined by Eq. 301 is solved using Gauss–Jordan elimination.[41] The numerical convergence of Newton's method is rapid near the solution – being quadratic at best – but uncertain far away from it [451]. In fact, a poor initial approximation of the solution may prevent convergence altogether [451]. In order to improve the stability of the numerical solution, the vector of free variables is updated similarly to the *relaxed* Newton's method [602]:

$$\underbrace{\mathbf{x}_{k+1}}_{\substack{\text{new}\\\text{values}}} = \underbrace{\mathbf{x}_k}_{\substack{\text{old}\\\text{values}}} + \underbrace{\gamma \Delta \mathbf{x}_k}_{\substack{\text{relaxed}\\\text{corrections}}} \qquad \text{for} \quad n = 0, 1, 2 \ldots k_{\max}\,, \tag{302}$$

where k denotes the iteration number, γ is the relaxation factor, $k_{\max}$ is the maximum number of iterations, and $\mathbf{x}_0$ denotes the initial approximation of the solution. The calculation procedure is repeated until the numerical error is sufficiently small or the maximum number of iterations is exceeded. In the former case, the model proceeds to

[41] Detailed descriptions of the Gauss–Jordan elimination are available in the literature [451, 452]. In this work, the algorithm was implemented using the `gaussj` package [601].

the next time step, while in the latter case the numerical solution is terminated. The numerical error in residual vector **f** was measured using the l_1-, l_2-, and l_∞-norms; their definitions are given in Eqs. 303, 304, and 305, respectively [451]. The l_1-norm (*Taxicab norm*) describes the sum of absolute errors, the l_2-norm (*Euclidian norm*) is the Euclidian length of the residual vector, and the l_∞-norm (*Chebyshev norm*) measures the maximum residual in the residual vector. In this work, the l_2-norm was employed as the main criteria for convergence.

$$\|\Delta\mathbf{x}\|_1 \equiv \sum_{i=1}^{n} |\Delta x_i| \qquad (l_1\text{-norm}). \tag{303}$$

$$\|\Delta\mathbf{x}\|_2 \equiv \sqrt{\sum_{i=1}^{n} \Delta x_i^2} \qquad (l_2\text{-norm}). \tag{304}$$

$$\|\Delta\mathbf{x}\|_\infty \equiv \max\left(|\Delta x_1|, \ldots, |\Delta x_n|\right) \qquad (l_\infty\text{-norm}). \tag{305}$$

During the numerical solution, the interfacial composition asymptotically approaches the composition dictated by the equilibrium constants, provided the forward reaction rate constants (k_f) are sufficiently large. The fulfilment of the thermodynamic equilibrium at the reaction interfaces was assessed by employing the reaction quotient method described in Section 5.3.1 (p. 141). As a preliminary setting, the maximum allowed error was set to E = 0.1%, which translates to a maximum error of 0.1% in the equilibrium constants. During the numerical solution, the k_f values are increased periodically until the equilibrium numbers of all the reactions are below the maximum allowed error. In further work, it is recommendable to improve the robustness of this method.

7 Results and discussion

7.1 Application of the LMA approach (Articles V and VI)

7.1.1 Numerical results

The simple decarburisation model proposed in Section 5.3.2 (p. 142) was employed for studying the parallel oxidation of Si, Cr, and C in the case of liquid stainless steel surface exposed to O_2–CO gas. In order to identify different regimes of mass transfer control, the forward reaction rate coefficients and oxygen selectivity were calculated as a function of the ratio of gas and liquid side mass transfer rate assuming a constant residual affinity of $A = 0.001$ J/mol.The following parameters were employed in the calculations: $\beta_L = 5 \cdot 10^{-4}$ m/s, $T = 1873$ K (1600 °C), $x_C = 0.02$, $x_{Cr} = 0.17$, and $x_{Si} = 0.002$. The employed value of β_L was estimated based on the results of Chatterjee *et al.* [299] for liquid phase mass transfer coefficients during top-blowing of oxygen on liquid silver. The employed values of carbon mole fractions ($x_C = 0.04$ and $x_C = 0.01$) correspond roughly to the process conditions during the early stage of carbon removal in the AOD process. Fig. 29 shows that the both the forward reaction rate coefficients and the oxygen selectivity are sensitive to the mass transfer rate. Based on the results, three different regimes of mass transfer control can be identified:

Regime A Liquid phase mass transfer control. All species in the liquid phase are driven by their maximum diffusion rate towards the reaction interface and selectivity is defined by the molar composition of the bulk liquid and stoichiometry. The gas side mass transfer coefficient is much larger than the critical value.

Regime B Liquid phase mass transfer control with simultaneous reduction of Cr_2O_3. This regime occurs when the rate of oxygen mass transfer is close to or smaller than that of C and Si.

Regime C Gas phase mass transfer control. The selectivity of oxygen is defined by the combination of the equilibrium and the liquid side mass transfer rates. The oxygen mass transfer rate is smaller than the critical value.

The effect of the residual affinity A on the reaction rates was also studied. The employed parameters were defined similar to the previous case. Figs. 30a and 30b illustrate the dependency of the calculated forward reaction rate coefficients on the

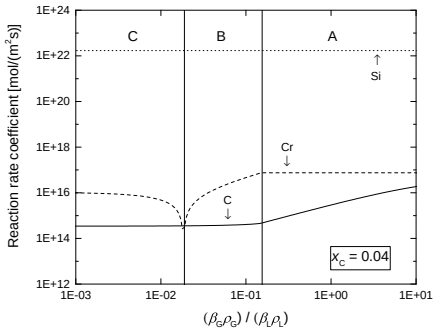

(a) Forward reaction rate (x_C = 0.04).

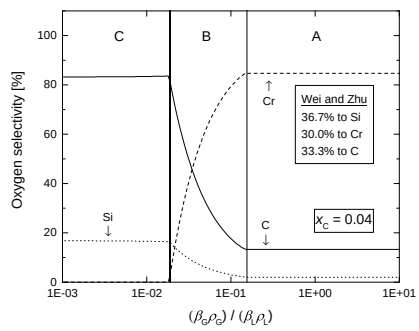

(b) Oxygen selectivity (x_C = 0.04).

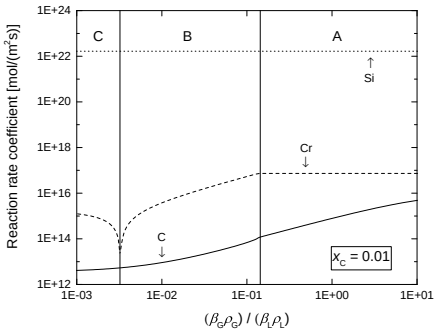

(c) Forward reaction rate (x_C = 0.01).

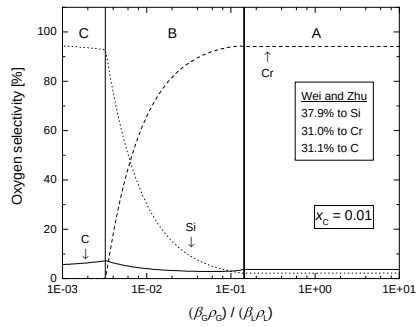

(d) Oxygen selectivity (x_C = 0.01).

Fig 29. Forward reaction rate coefficient and oxygen selectivity and as a function of mass transfer rate. Reproduced from Article VI by permission of the Iron and Steel Institute of Japan.

residual affinity using different mass transfer coefficients of the gas phase (β_G). It can be seen that the forward reaction rate coefficients depend not only on the residual affinity, but also on the mass transfer coefficient of the gas phase. From Figs. 30c and 30d it can be seen that above a certain threshold value the reaction rates are relatively insensitive to the residual affinity. However, the dependency of the reaction rate on the residual affinity is more pronounced for the oxidation of carbon and the oxidation of chromium than for the oxidation of silicon. For practical purposes, a sufficient degree of accuracy for the equilibrium is obtained when the residual affinity is smaller than 10 J/mol. At 1873 K (1600 °C), this value corresponds to E $\approx$ 0.1%, which is the value employed in the top-blowing and reduction models. For comparison, the reported ranges of error for ΔG° are typically greater than $\pm$ 1000 J/mol [394].

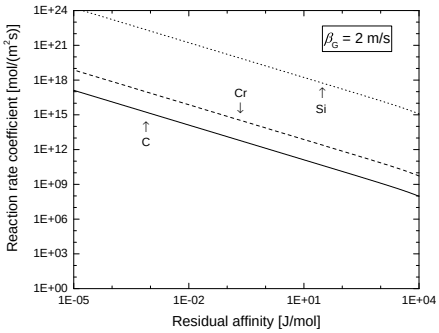

(a) Rate coefficients (β_G = 2 m/s).

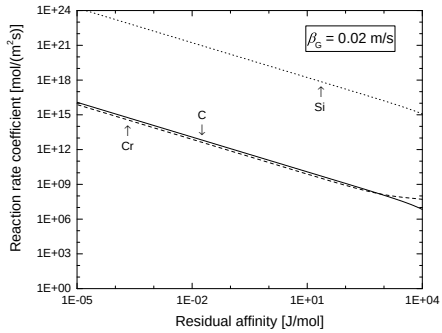

(b) Rate coefficients (β_G = 0.02 m/s).

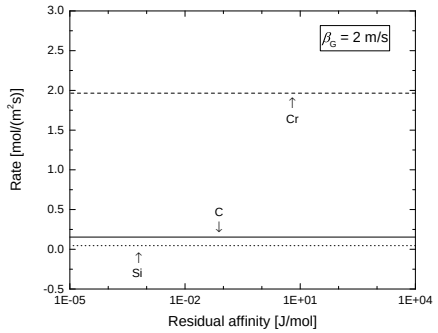

(c) Reaction rate (β_G = 2 m/s).

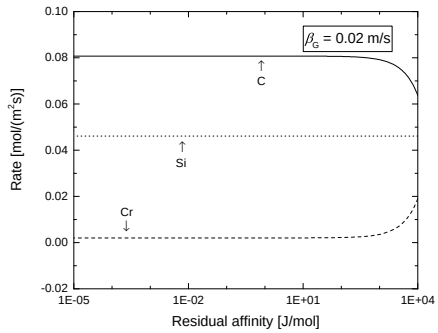

(d) Reaction rate (β_G = 0.02 m/s).

Fig 30. Calculated forward reaction rate coefficient and reaction rate as a function of residual affinity. Reproduced from Article VI by permission of the Iron and Steel Institute of Japan.

It is important to note that the residual affinity is essentially a measure of the error in the interfacial composition, which forms the boundary condition for the mass transport terms. If the interfacial mole fraction x_i^* is small compared to the bulk mole fraction x_i, the relative error in the concentration difference $x_i - x_i^*$ is considerably smaller than the relative error in the equilibrium constant K.

7.1.2 Comparison to other approaches

As discussed in Section 4.4 (p. 128), several methods are available for the treatment of parallel mass transfer limited reactions. A comparison of the proposed methods and their applications is shown in Table 23.

Table 23. Comparison of methods to calculate parallel oxidation reactions. Adapted from Article VI.

Method	References	Applications	Advantages	Drawbacks
Affinity based selectivity method				
Selectivity of oxygen corresponds to the oxygen affinity of species, additional constraints for mass transfer limitation.	[49, 137, 209, 245]	Parallel oxidation and reduction reactions in the AOD process.	Transparent, easy to implement, suitable for on-line applications	Cannot be derived from physical principles.
Effective equilibrium constant method				
The concentration changes of elements are determined based on effective equilibrium constant and electrical neutrality equation.	[367, 375–385]	Parallel oxidation and reduction reactions in converter and ladle treament processes.	Light computational effort.	
Constrained Gibbs free energy minimisation method				
Kinetic control considered through additional constraints in the Gibbs energy minimisation routine.	[386–388]	Numerous applications, including combustion, chemical engineering and metallurgy.	Commercial software available, combined with commercial library on thermodynamic properties, derived from physical principles, well-suited for process simulators.	Difficult implementation to CFD or complex mass transfer limited systems with diffusion, convection, and turbulence effects. Unsuitable for on-line applications.
Constrained solubility method				
Dissolved oxygen content is determined based on its solubility limit. Thereafter, the remaining oxygen is distributed so that the reaction with the largest oxygen affinity consumes all gaseous oxygen during a sub-time step.	[27]	Parallel oxidation and reduction reactions in the VOD process	Transparent, easy to implement, suitable for on-line applications.	Cannot be derived from physical principles. Solution is sensitive to model parameters, such as volumetric flow rates into and from the reaction zones.

Table 23. (Continued)

Method	References	Applications	Advantages	Drawbacks
Coupled Gibbs free energy minimisation and volume element method				
Volume cells with multiple phases are set into equilibrium.	[214, 218]	Parallel oxidation and reduction reactions in the AOD and BOF processes.	State of the art combination of CFD and equilibrium, uses commercial software in CFD and equilibrium solution	Treatment of the interface is unclear, the grid size needs to be very small near the reaction zone, cannot be used for on-line applications.
Incremental step method				
Time steps are divided into sub-steps, during which the reaction with the largest affinity consumes all available oxygen.	[389, 390]	Parallel oxidation and reduction reactions in the BOF process.	Transparent, easy to implement, possibly suitable for on-line applications	Solution is sensitive for model parameters, cannot be derived from physical principles, non-physical tuning parameters
Law of mass action based method				
Rate expressions are calculated from the modified law of mass action, predefined residual affinity or equilibrium number determines unknown forward reaction rate coefficients in an iterative procedure.	[44, 249, 255, 262, 264, 373, 546, 550, 551, 603, 604]	Parallel oxidation and reduction reactions in the AOD and CAS-OB processes.	Derived from physical principles, non-sensitive to model parameters, easy to implement, simultaneous solution of the mass transfer controlled rate and equilibrium composition, suitable for on-line applications.	No experience on suitability for CFD applications.

7.1.3 Summary of studied applications

The LMA approach enables the simultaneous solution of the thermodynamic equilibrium at the reaction surface and rate limiting mass transfer onto the reaction surface. The approach is sensitive to mass transfer conditions, which – particularly in the case of industrial processes – may vary during the process. Consequently, it is suggested that the LMA approach is well-suited for modelling mass-transfer controlled reversible reactions at high temperatures.

Table 24 presents a summary of the studied applications of the LMA approach. In this work, the side-blowing decarburisation model developed by Järvinen *et al.* [44, 45] was extended with reaction models for top-blowing (Articles I–II) and the reduction stage (Articles III–IV). The developed models can be applied to other metallurgical processes, provided that they have similar characteristics. In particular, the ferrochrome and VOD converters share many similarities with the AOD process; modelling these processes would be a fruitful topic for further work. In addition to the AOD process, the LMA approach has also been employed for modelling the CAS-OB process. The developed models share three basic geometries to describe the dominant reaction mechanisms:

Bubble spherical shape, negligible internal mass transfer resistance, transitory phase contact, complete emulsification of the gas phase.

Droplet spherical shape, significant internal and external mass transfer resistance, permanent phase contact, partial emulsification.

Plane plane surface, significant internal and external mass transfer resistance, permanent phase contact, no emulsification.

Table 24. Studied metallurgical applications. Adapted from Article V.

Application	References	Geometry	Phenomena	Gas input	Novelty
AOD process					
Rising gas bubble	[249]	Bubble	Reactions between gas bubble and metal bath	Gas bubble	Computationally efficient approach for mass transfer controlled reactions at high temperatures
Side-blowing	[44, 45, 255, 256]	Bubble	Reactions in the gas plume	Tuyères	Vertical variations of properties in the gas plume
Top-blowing	[136, 264]	Plane + droplet	Reactions in the cavity and at the metal droplets	Top lance	Effect of steel and slag properties, lance type, and employed top-blowing practice on the reaction rates
Reduction of slag	[262, 263]	Droplet	Reactions between metal bath and top slag	Tuyères	Effect of slag composition and properties on the reduction rate
CAS-OB process					
Heating stage	[550, 551, 603]	Plane + droplet	Reactions during chemical heating with aluminium, heat transfer within the bell and ladle structures	Top lance	Accurate chemical heating rates, heat storage to wall structures
Reduction of slag	[546]	Droplet	Reactions between metal bath and top slag	Bottom nozzles	Effect of gas injection rate, slag composition, and slag properties on the reduction rate

7.2 Top-blowing decarburisation (Article II)

7.2.1 Validation material

In Article II, twelve experimental heats were conducted with a 150-tonne AOD vessel at Outokumpu Stainless Oy in Tornio, Finland. The vessel is fitted with seven tuyères along the side wall and a supersonic top lance; more detailed technical descriptions of the employed vessel are available in the literature [605, 606].

In the studied heats, the last combined-blowing stage was altered so that oxygen was introduced from the top lance only. Four heats (Series A) were conducted using an oxygen–nitrogen mixture (1:1), while eight heats (Series B) were conducted with pure oxygen (see Table 25). The difference between the duration of the top-blowing and duration of the process stage is related to the tilting of the vessel from the sampling to operating position or *vice versa*. No reactions were assumed to take place during tilting, although the melting of added materials and the cooling effect of the gas stirring were taken into account in the simulations. The employed geometry parameters are available in Articles II and IV.

Table 25. Validation heats for the top-blowing model.

		Gas injection rate [$Nm^3/(t \cdot min)$]		Duration [min]	
Series	Heats	Top lance	Tuyères	Top-blowing	Total
Series A	4	1.27 O_2	0.79 N_2	7.6–7.9	9.5–10.1
Series B	8	0.63 O_2 + 0.63 O_2	0.79 N_2 or Ar	3.5–4.0	5.6–6.2

Note: the gas flow rates are expressed in relation to the nominal capacity of the vessel.

Metal and slag samples were taken before and after the blowing sequence (see Tables 27 and 28 on pp. 200 and 201, respectively). The samples were analysed with an optical emission spectrometer (OES) and an X-ray fluorescence (XRF) spectrometer. Because the oxygen content could not be determined from the metal samples, it was estimated based on literature data [38, 141]. In order to exclude the effect of metal droplets on the composition of the slag, the slag composition was re-calculated by excluding the Fe, Cr, Mn, and Si brought by the fine metal droplets. Similarly to Lindstrand *et al.* [449], the mass fraction of the metal phase in the slag sample was calculated based on the Ni content of the slag sample. The material additions are shown in Table 26. The additions were assumed to be perfectly mixed in a single silo. The employed feed rates were determined based on the measured feeding times.

Table 26. Additions during processing. Modified from Article II.

Series	Heat	Additions [kg] per 1 t of liquid metal					
		FeNi20	FeNi40	Ni90	Cu	Steel scrap	Stainless steel scrap
Series A	37826	0	0	0	0	11	42
	38032	8	0	0	1	36	0
	38034	19	0	0	1	32	0
	38036	0	0	0	0	0	42
Series B	54870	0	3	14	0	0	38
	54872	18	15	0	0	15	0
	54874	18	2	15	0	0	0
	54876	34	0	2	0	0	0
	54878	18	6	0	0	20	0
	54934	22	16	0	0	11	0
	54936	0	40	0	0	18	0
	54938	0	24	0	0	22	0

In order to account for the effect of different cavity modes, the effective metal droplet generation rate was calculated similarly to Sarkar *et al.* [441] by multiplying the nominal metal droplet generation rate by the parameter J_{eff} (see Eq. 250 on p. 167). The best results *vis-à-vis* the measured values were obtained with $J_{\text{eff}} = 1.75$ and hence this value was used in the simulations.[42] All the simulations were conducted with a time step of five seconds. The employed physical properties are given in Table 22 (p. 186).

7.2.2 Predicted compositions and temperatures

Table 27 shows a comparison of the predicted metal bath composition and temperature with the measured values. It can be seen that the model predictions for the species in the metal bath agree well with the measured values. A comparison of the predicted slag composition with the slag samples is shown in Table 28. Although the absolute deviations are relatively large, the agreement is qualitatively correct. It is realistic to expect that the main source of error is the distorting effect of undissolved lime found in the slag samples taken before the studied stage.

[42] In Articles I–II, the modified gas flow rate ($\dot{V}'_{\text{G,lance}}$) employed in Eq. 249 (p. 166) was calculated by converting the top-blowing rate ($\dot{V}_{\text{G,lance}}$) from 273.15 K (0 °C) to the temperature of the gas at the impact point (T_{G}). This differs slightly from the definition proposed by Rout *et al.* [516], who calculated $\dot{V}'_{\text{G,lance}}$ by converting $\dot{V}_{\text{G,lance}}$ from 298.15 K (25 °C) to T_{G}. Using their definition, the same results would be obtained with $J_{\text{eff}} = 1.75 \cdot (298.15\ \text{K}/273.15\ \text{K}) \approx 1.910$.

Table 27. Comparison of metal samples and predictions (top-blowing experiments). Reproduced from Article II.

		Composition [wt-%]					
Heat	Type	Cr	Mn	Si	C	Ni	T_{bath} [K (°C)]
Series A							
	Before	17.82	0.58	0.04	0.446	8.27	1953 (1680)
37826	After	17.35	0.52	0.02	0.138	8.26	1941 (1668)
	Prediction	17.22	0.57	0.04	0.130	8.25	1929 (1656)
	Before	18.42	0.81	0.06	0.447	8.40	1918 (1645)
38032	After	17.41	0.64	0.03	0.171	8.27	1913 (1640)
	Prediction	17.26	0.71	0.02	0.150	8.27	1913 (1640)
	Before	18.75	1.01	0.03	0.394	8.15	1957 (1684)
38034	After	17.51	0.80	0.01	0.114	8.21	1946 (1673)
	Prediction	17.36	0.84	0.03	0.117	8.20	1944 (1670)
	Before	17.55	0.89	0.01	0.466	8.21	1980 (1707)
38036	After	17.31	0.81	0.02	0.170	8.24	1973 (1700)
	Prediction	17.23	0.81	0.04	0.127	8.28	1964 (1691)
Series B							
	Before	16.98	0.74	0.04	0.381	9.66	1988 (1715)
54870	After	16.14	0.63	0.01	0.149	10.75	2011 (1738)
	Prediction	16.24	0.61	0.04	0.162	10.94	2009 (1736)
	Before	17.15	0.86	0.02	0.473	10.45	1980 (1707)
54872	After	15.88	0.77	0.05	0.221	10.91	2009 (1736)
	Prediction	15.96	0.67	0.02	0.210	10.89	2000 (1727)
	Before	17.19	0.78	0.04	0.405	8.94	1971 (1698)
54874	After	16.07	0.64	0.02	0.136	10.50	2013 (1740)
	Prediction	16.10	0.67	0.03	0.189	10.50	2010 (1737)
	Before	17.03	0.78	0.03	0.388	9.71	1988 (1715)
54876	After	16.04	0.68	0.02	0.153	10.35	2007 (1734)
	Prediction	15.94	0.66	0.03	0.184	10.30	2016 (1742)
	Before	17.23	0.78	0.03	0.407	10.22	1993 (1720)
54878	After	15.98	0.67	0.02	0.170	10.45	2005 (1732)
	Prediction	16.00	0.65	0.03	0.183	10.43	2011 (1737)
	Before	16.94	0.52	0.02	0.426	9.95	1996 (1723)
54934	After	15.76	0.45	0.01	0.142	10.51	2008 (1735)
	Prediction	15.62	0.44	0.03	0.187	10.50	2010 (1737)
	Before	17.07	0.69	0.02	0.391	9.77	2003 (1730)
54936	After	15.60	0.57	0.03	0.129	10.49	2022 (1749)
	Prediction	15.59	0.54	0.04	0.168	10.55	2013 (1740)
	Before	17.07	0.85	0.02	0.424	10.17	2021 (1748)
54938	After	15.71	0.72	0.02	0.186	10.52	2038 (1765)
	Prediction	15.92	0.64	0.03	0.174	10.56	2037 (1764)

Table 28. Comparison of slag samples and predictions (top-blowing experiments). Reproduced from Article II.

		Composition [wt-%]							
Heat	Type	FeO	Cr_2O_3	MnO	SiO_2	CaO	MgO	Al_2O_3	Other
Series A									
	Before	4.7	31.1	6.7	17.1	34.1	2.5	3.1	0.6
37826	After	4.5	29.5	6.2	14.4	40.2	1.9	2.7	0.5
	Prediction	2.3	43.4	7.0	15.0	27.4	2.0	2.5	0.6
	Before	5.7	30.6	8.0	8.5	44.0	2.0	1.0	0.1
38032	After	9.1	35.9	7.9	7.3	35.0	3.1	1.5	0.1
	Prediction	2.3	43.4	9.0	9.1	33.7	1.5	0.8	0.2
	Before	6.2	34.4	8.1	13.7	33.7	2.6	1.1	0.2
38034	After	5.1	31.3	8.2	8.9	43.4	1.8	1.2	0.1
	Prediction	2.4	49.9	10.5	10.6	23.7	1.8	0.8	0.3
	Before	3.5	28.2	7.9	21.0	35.2	2.2	1.4	0.5
38036	After	4.9	26.0	7.1	21.3	36.1	2.5	1.7	0.5
	Prediction	2.5	39.5	9.9	16.6	28.1	1.8	1.1	0.5
Series B									
	Before	2.2	15.8	4.1	24.1	48.3	4.6	0.5	0.5
54870	After	3.3	29.0	5.2	16.5	42.2	3.3	0.2	0.4
	Prediction	4.6	33.6	6.8	17.5	33.7	3.2	0.3	0.3
	Before	3.4	26.3	4.0	17.0	40.1	6.4	1.4	1.3
54872	After	4.8	39.5	4.6	13.7	30.9	4.7	0.8	0.9
	Prediction	4.4	38.6	7.6	12.9	29.7	4.7	1.0	1.0
	Before	5.6	33.6	7.0	15.1	31.0	6.5	0.7	0.5
54874	After	5.6	36.7	6.0	15.3	29.3	5.9	0.6	0.4
	Prediction	4.5	50.2	7.9	11.0	21.1	4.4	0.5	0.3
	Before	6.3	36.3	6.0	16.3	26.0	7.1	1.3	0.8
54876	After	5.2	36.1	5.8	17.3	26.6	6.3	1.8	0.9
	Prediction	4.6	51.9	7.9	11.5	17.9	4.9	0.9	0.5
	Before	4.0	26.7	5.7	17.8	40.8	3.2	0.9	0.7
54878	After	5.2	39.9	6.5	14.1	30.2	2.8	0.7	0.6
	Prediction	4.5	43.3	7.5	12.8	28.3	2.2	0.6	0.6
	Before	3.4	31.0	4.3	19.2	32.2	6.4	2.6	0.9
54934	After	7.1	40.6	3.3	10.4	32.4	4.5	1.0	0.6
	Prediction	4.4	46.0	5.2	14.0	23.3	4.6	1.9	0.7
	Before	2.5	22.5	4.2	24.3	34.2	8.8	2.5	1.1
54936	After	4.0	34.9	5.0	18.9	26.3	8.1	2.0	0.8
	Prediction	4.4	39.2	6.4	17.3	24.0	6.2	1.8	0.7
	Before	2.5	28.0	3.7	18.8	38.1	7.3	1.0	0.6
54938	After	3.1	37.5	5.0	15.6	31.3	6.3	0.7	0.4
	Prediction	5.2	37.4	7.4	14.4	28.9	5.5	0.8	0.5

Table 29 shows a statistical analysis of the results obtained. The mean absolute errors in the final Mn, Si, C, and Ni contents are less than or equal to 0.05 wt-%, while the MAE in the temperature is below 10 K. The MAE for chromium is somewhat larger, being approximately 0.1 wt-%. With respect to the final carbon content, a better agreement was achieved with experiments using an oxygen-nitrogen mixture as the top-blowing gas (Series A) than those with pure oxygen (Series B). With the exception of carbon and silicon, the R^2 values of other predicted variables are high. It is likely that the low R^2 of the predicted carbon content is explained to some extent by inaccuracies in the measurement data. These values compare reasonably well with other modelling studies concerning side-blowing or combined-blowing in a comparable carbon region [207, 209, 227, 232, 239, 245].

Table 29. Statistical indicators for the top-blowing model. Adapted from Article II.

Range of studied variables				Statistical indicators			
Variable	Start	End	Unit	n	R^2	RMSE	MAE
[C]	0.4 – 0.5	0.1 – 0.2	wt-%	12	0.23	0.029	0.024
[Cr]	16.9 – 18.8	15.6 – 17.5	wt-%	12	0.98	0.12	0.10
[Mn]	0.5 – 1.0	0.5 – 0.8	wt-%	12	0.81	0.05	0.04
[Si]	0.01 – 0.06	0.01 – 0.05	wt-%	12	0.09	0.02	0.01
[Ni]	8.15 – 10.45	8.21 – 10.91	wt-%	12	1.00	0.06	0.04
T	1918 – 2021	1913 – 2038	K	12	0.98	6.50	5.40

7.2.3 Dynamic changes in bath composition and temperature

Fig. 31a illustrates the simulated C, Cr, Mn, and Ni contents in heat 37826 (Series A). The two horizontal sections of the composition curves represent the tilting of the vessel to operating position (before top-blowing) and to sampling position (after top-blowing). It is seen that during top-blowing the predicted carbon content decreases according to first-order kinetics. Fig. 31b illustrates the predicted C, Cr, Mn, and Ni contents in heat 54878 (Series B).

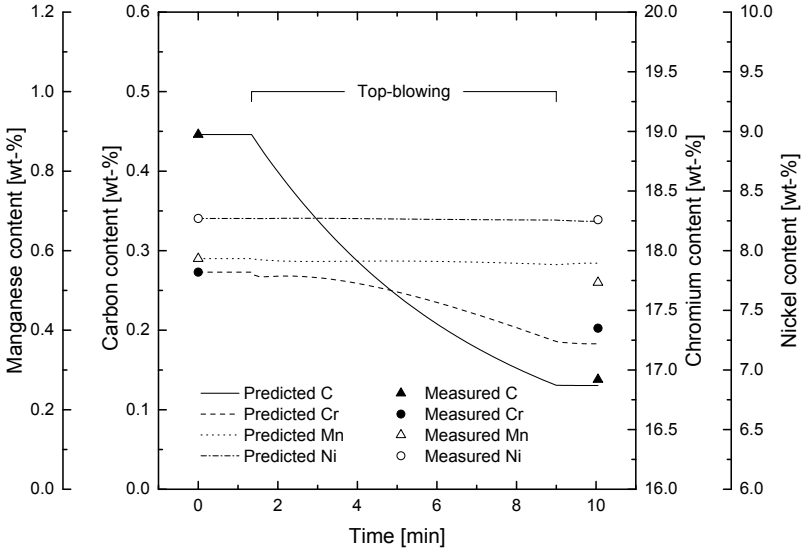

(a) Heat 37826.

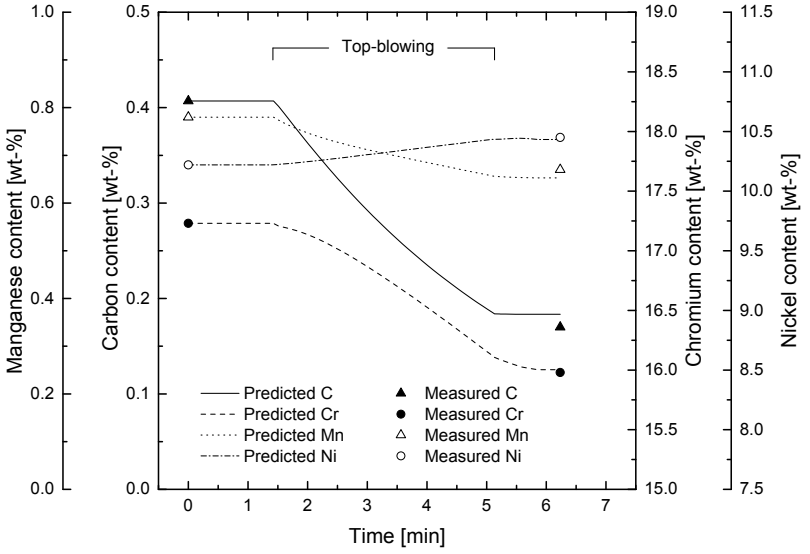

(b) Heat 54878.

Fig 31. Predicted and measured C, Cr, Mn, and Ni. Reproduced from Article II by permission of Springer Nature.

The simulated dynamic change in bath temperature in heat 38032 is illustrated in Fig. 32. The simulated bath temperature decreases until all of the additions and scrap have dissolved in the steel. After this, the predicted bath temperature rises rapidly due to oxidation of carbon and other elements.

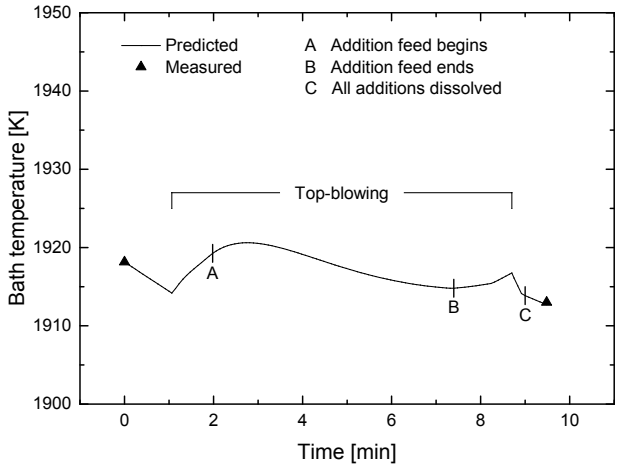

Fig 32. Predicted and measured bath temperature in heat 38032. Reproduced from Article II by permission of Springer Nature.

The calculated temperature of the cavity interface was roughly the same as that of the metal bath, while the calculated temperature of the metal droplet interface was significantly elevated, being lower in the case of heats with an oxygen–nitrogen mixture as the top-blowing gas (Series A) than those with pure oxygen (Series B). In the case of Series B, the calculated temperatures of the metal droplet interface varied in the range of 2000 K to 2200 K (1727 °C to 1927 °C). These results compare reasonably well with the hot spot temperature suggested by Delhaes *et al.* [73], but are lower than those reported by Tsujino *et al.* [423] for a 100 kg experimental furnace. Delhaes *et al.* [73] estimated based on vaporisation of Mn that the average temperature of the hot spot should be approximately 2173 K (1900 °C) during pure oxygen combined-blowing in the initial period of the AOD process. Based on analysis of hot spot spectra by two-color radiation thermometry, Tsujino *et al.* [423] reported an average temperature of 2623 K (2350 °C) for top-blowing and combined-blowing decarburisation of stainless steel in a 100 kg experimental furnace.

7.2.4 Carbon removal efficiency

In the case of oxygen–nitrogen mixtures (Series A), the predicted transient CRE value starts from close to or above 100% as the carbon reduces the slag species with lower oxygen affinity (see Fig. 33a). Because the dilution ratio of oxygen is higher in the studied process stage than in the preceding process stage, the top slag must settle into a new dynamic equilibrium with the metal phase. This finding is in agreement with the calculations by Swinbourne *et al.* [145] and Wijk [10] for side-blowing operation in comparable carbon ranges. In the case of pure oxygen-blowing (Series B), virtually no reduction of slag species takes place. In heat 54870, for example, the predicted transient CRE value remains below 100% throughout the studied stage (see Fig. 33b).

Based on the metal samples, the average CRE was approximately 51% for Series A and 44% for Series B. In the literature, the CRE values attributable to top-blowing vary in a broad range depending primarily on the carbon content and employed gas injection rates (see Table 30). In terms of the employed specific top-blowing rates and studied carbon range, the studies published by Koch *et al.* [157], Kuwano *et al.* [607], Masuda *et al.* [38], Schürmann and Rosenbach [141], and Gorges *et al.* [108] constitute the most reasonable experimental benchmark.

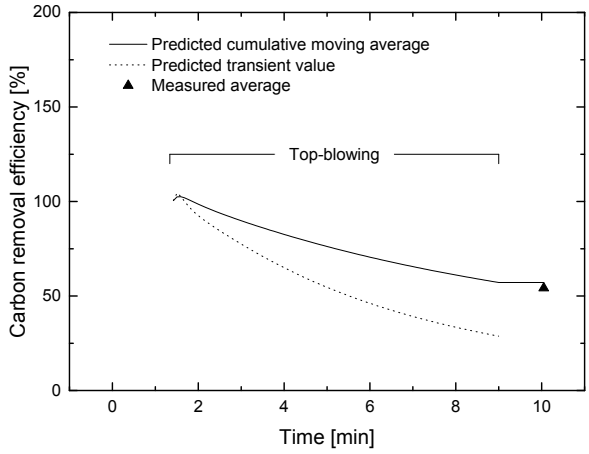

(a) Heat 37826.

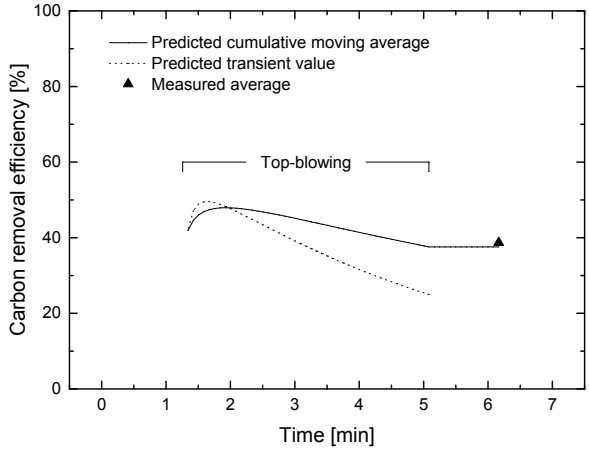

(b) Heat 54870.

Fig 33. Predicted and measured CRE in heats 37826 and 54870. Reproduced from Article II by permission of Springer Nature.

Table 30. Carbon removal efficiency attributable to top-blowing. Adapted from Article II.

Reference	Capacity [t]	Bottom-blowing [$Nm^3/(t \cdot min)$]	Top-blowing [$Nm^3/(t \cdot min)$]	n [–]	θ [°]	h_{lance}/d_t [–]	p_{amb} [kPa]	C [wt-%]	CRE [%]	Notes
Watanabe and Tohge [221]	0.0045	–	0.1 O_2	1	–	NA	21	0.2 – 0.3	7	
	0.0045	–	0.02 O_2 + 0.08 Ar	1	–	NA	8	0.2 – 0.3	53	
	0.0045	–	0.1 CO_2	1	–	NA	8	0.2 – 0.3	21	
Koch *et al.* [608]	0.01	–	0.13 – 0.51 O_2	1	–	7	p_{atm}	0.2 – 1.4	78	a)
	0.01	–	0.12 – 0.50 O_2	1	–	7	0.4	< 0.01 – 1.3	62	a)
	0.01	–	0.25 – 0.50 O_2	1	–	7	p_{atm}	0.03 – 0.8	17	b)
	0.01	–	0.25 – 0.50 O_2	1	–	7	0.4	0.01 – 0.9	47	b)
Kitamura *et al.* [609]	0.04	0.25 Ar	4.38 O_2	1	–	NA	p_{atm}	0.1 – 3.5	41	
	0.04	0.25 Ar	4.38 O_2	1	–	NA	p_{atm}	0.1 – 1.1	31	
Kuwano *et al.* [607]	0.1	–	0.04 – 0.93 O_2	1	–	10 – 20	p_{atm}	0.02 – 0.5	67	c)
	0.1	–	0.15 – 0.39 O_2 + 0.19 – 0.34 Ar	1	–	10	p_{atm}	0.04 – 0.5	30	c)
	0.1	–	0.10 – 0.55 O_2	1	–	10 – 20	p_{atm}	0.6 – 0.02	42	d)

Notes: a) Fe–C–10 Cr melt; b) Fe–C–18 Cr–Si melt; c) Fe–C–Cr–0.4 Si melt; d) Fe–C–Cr melt; NA = not available.

Table 30. (Continued)

Reference	Capacity [t]	Bottom-blowing [$Nm^3/(t \cdot min)$]	Top-blowing [$Nm^3/(t \cdot min)$]	n [–]	θ [°]	h_{lance}/d_t [–]	p_{amb} [kPa]	C [wt-%]	CRE [%]	Notes
Masuda *et al.* [38]	2.5	0.40 Ar	2.40 O_2	3	NA	98 – 107	p_{atm}	0.4 – 1.1	33	
	2.5	0.40 Ar	0.80 O_2	3	NA	98 – 107	p_{atm}	0.2 – 0.4	23	
	2.5	0.40 Ar	0.20 O_2	3	NA	98 – 107	p_{atm}	< 0.2	20	
Schürmann and Rosenbach [141]	8	0.21 Ar	0.68 O_2	1	–	NA	p_{atm}	0.07 – 0.3	22	
Yamada *et al.* [610]	30	1.03 O_2 + 0.35 Ar	0.33 O_2	NA	NA	NA	p_{atm}	0.2 – 3.5	25	e)
Tohge *et al.* [111]	70	0.74 O_2 + 0.19 Ar	0.36 O_2	1	–	92	p_{atm}	0.3 – 2.5	27	
	70	0.74 O_2 + 0.19 Ar	0.60 O_2	1	–	92	p_{atm}	0.3 – 2.5	28	
Gorges *et al.* [108]	80	0.16 Ar	1.25 O_2	NA	NA	38 – 50	p_{atm}	> 0.4	51	f)
	80	0.16 Ar	1.25 O_2	NA	NA	38 – 50	p_{atm}	> 0.4	63	g)
Li *et al.* [131]	118	0.85 O_2	0.86 O_2	1	–	84	p_{atm}	1 – 3	66	h)
	118	0.85 O_2	0.86 O_2	3	11	117	p_{atm}	1 – 3	76	h)
	118	0.85 O_2	0.86 O_2	3	15	117	p_{atm}	1 – 3	44	h)
This work (Series A)	150	0.79 N_2	0.63 O_2 + 0.63 N_2	3	11	78	p_{atm}	0.1 – 0.5	51	
This work (Series B)	150	0.79 N_2 or Ar	1.27 O_2	3	11	78	p_{atm}	0.1 – 0.5	44	

Notes: e) assuming that the CRE of the side-blowing corresponds to experiments without top-blowing; f) austenitic grades; g) ferritic grades; h) assuming the same CRE for side- and top-blowing; NA = not available.

7.2.5 Sensitivity analysis

After the main validation with the measurement data, the model was employed for a sensitivity analysis in heat 38034. The analysis was conducted *ceteris paribus* by changing either the lance height or the oxygen content of the top-blowing mixture. Fig. 34 illustrates the predicted effect of the oxygen content in the top-blowing gas mixture with O_2:N_2 ratios of 1:3, 1:1, and 3:1. As expected, the highest oxygen content in the gas mixture enables the lowest final carbon content. The predicted average CRE values corresponding to the O_2:N_2 ratios of 1:3, 1:1, and 3:1 were 87%, 50%, and 36%, respectively. Therefore, it is apparent that the increased decarburisation rate comes at the price of lower carbon removal efficiency.

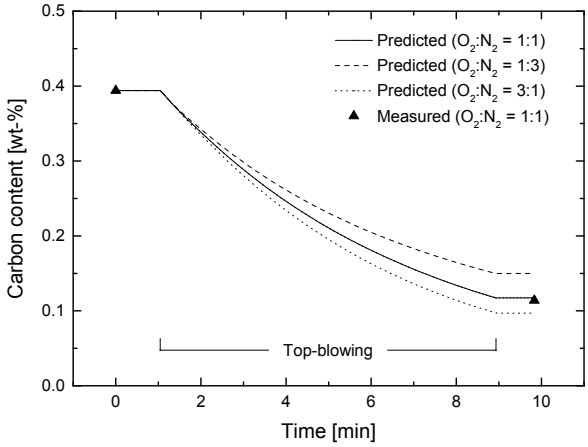

Fig 34. Effect of the top-blowing gas mixture on the predicted carbon content in heat 38034. Reproduced from Article II by permission of Springer Nature.

The effect of the lance height on the predicted carbon content is illustrated in Fig. 35. The results suggest that decreasing the lance height by 10% decreases the predicted final carbon content by approximately 0.03 wt-%, while increasing the lance height by 10% increases the predicted final carbon content by 0.05 wt-% *vis-à-vis* the normal lance position. The predicted CRE values corresponding to the lower, normal, and higher lance position were approximately 56%, 50%, and 40%, respectively. The effect of the lance position employed may be explained to a large extent by changes in the droplet generation rate and thus in the interfacial area available for mass exchange. However, the model does not account for the post-combustion of CO to CO_2 in the converter

atmosphere. It is likely that increased post-combustion would decrease the CRE even further in the case of the higher lance position. Based on the sensitivity analysis it appears that changing the lance position (within practical limitations) has a somewhat smaller effect on the predicted CRE than the oxygen content of the top-blowing gas mixture.

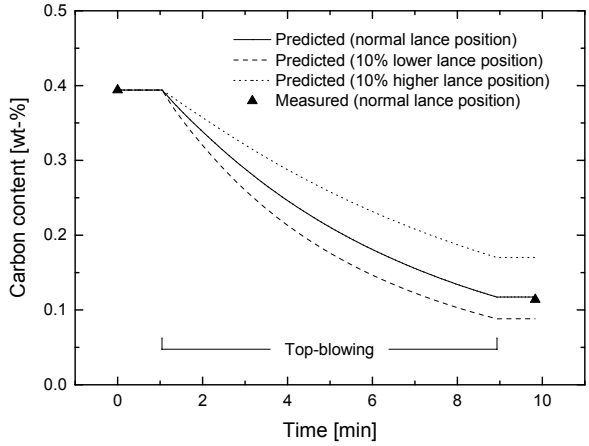

Fig 35. Effect of the top lance position on the predicted carbon content in heat 38034. Reproduced from Article II by permission of Springer Nature.

7.2.6 Rate-limiting factors

The top-blowing model proposed in Article I assumed that reactions take place simultaneously in the cavity and on the surface of the metal droplets which are ejected from the metal bath. In Article II, the majority of the carbon removal was predicted to take place via metal droplets owing to their large interfacial area. The generation rate of the metal droplets was determined according to the so-called *blowing number theory* [509], which links the metal droplet generation rate to a dimensionless *blowing number*: a ratio of the kinetic force of the gas jet to the surface force of the liquid phase. Despite some of its limitations, the theory has been applied to various top-blowing applications with a reasonable degree of success [440, 512, 515]. It should be noted that the blowing number theory does not explicitly account for the effect of top-blowing gas. Laboratory-scale tests suggest that splashing is more intense when O_2 is employed as a

top-blowing gas instead of CO_2 [518, 611]; the rationale behind this behaviour, however, is not yet fully understood. In this work, it is postulated that the increased splashing might be related to the following factors:

– The higher partial pressure of O_2 in the injected gas leads to a higher gas film temperature; this claim is supported by the findings of Baker *et al.* [360, 361].
– The higher gas film temperature enables a higher axial velocity and dynamic pressure of the gas jet [118, 612, 613].
– The higher dynamic pressure of the gas jet causes increased splashing, as suggested by the blowing number theory [509].

The residence times and trajectories of metal droplets have been the subject of numerous studies [447, 614–617], but no definitive answer is available for the conditions of the AOD process. In this work, it was assumed that the residence time of each size class equals the time required to pass through the gas–metal–slag emulsion at terminal falling velocity. The size distribution of the generated droplets was assumed to follow the RRS distribution function as suggested by Koria and Lange [280, 281].[43] The results of Article II suggest that the predicted Sauter mean diameter of the metal droplets *residing in the emulsion* is in the order of 1 mm (see Fig. 36), although the Sauter mean diameter of the metal droplets *at their place of origin* is in excess of 10 mm. Following the small size of the metal droplets in the emulsion, the predicted interfacial area is in the order of thousands of square meters.

The reason for the small droplet sizes predicted in this work is that the small metal droplets tend to have a very low terminal velocity, which results in long residence times. Therefore, the droplet size distribution in the emulsion shifts towards smaller droplets than at their place of origin. This conclusion is in line with the current understanding of surface area generation in top-blowing processes [280, 618]. However, certain precautions must to be made when interpreting the predicted size distribution and droplet generation rate:

1. The proposed model does not account for the interaction of top-blowing and side-blowing. Based on experimental studies on the interaction of top- and bottom-blowing [619–621], it would be reasonable to expect that simultaneous side-blowing would affect the droplet generation behaviour. As noted by Brooks *et al.* [622], none of the models proposed for predicting droplet generation have yet incorporated this effect.

[43] A normal distribution of metal droplets has also been proposed [493], but this finding has not received further attention in the literature.

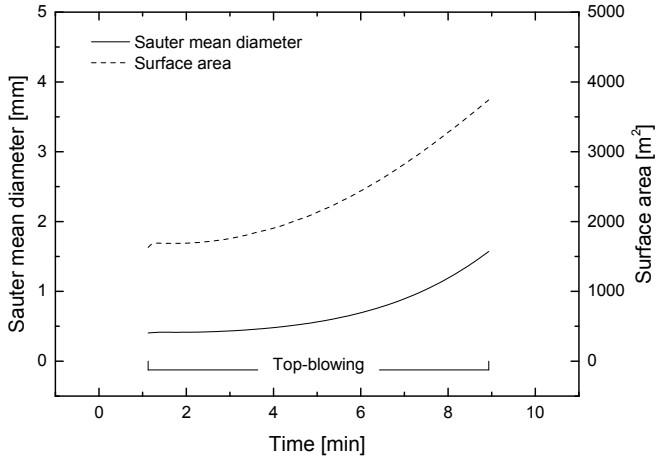

Fig 36. The predicted Sauter mean diameter and surface area of the metal droplets in heat 38034. Reproduced from Article II by permission of Springer Nature.

2. The proposed model assumes that all the generated metal droplets continue their trajectory into the emulsion undisturbed without any break-up or loss to flue gas. However, in the actual process various mechanisms may alter the droplet size distribution. Large droplets may disintegrate upon contact with the gas jet [495] or on impact with the slag [496], while the smallest metal droplets may be carried out of the vessel with the flue gas [73, 498]. With these considerations in mind, it is reasonable to expect that the actual size distribution of metal droplets in the slag at a given moment is not identical to the size distribution at birth, but is effectively cut off from both sides of the size distribution.
3. Nucleation of CO inside the metal droplets can reduce the apparent density of the metal droplets, thus increasing their residence time [440, 623]. Rao and Robertson [314] reported that impure Fe–18Cr–2C metal droplets exhibited CO boiling if the oxygen content of the gas was 67% or higher. In this work, the initial carbon content was much lower (approximately 0.4–0.5 wt-%) and although the oxygen content of the top-blown gas varied from 50% to 100%, the atmosphere contained a considerable amount of side-blown nitrogen or argon. Consequently, it is reasonable to expect that CO boiling is only of marginal importance in the studied process stage.

The *control factor* concept was introduced and employed for studying the rate-limiting mechanisms of microkinetics. The control factor C has a value of 1 when the

concentration gradient approaches its maximum value and 0 when the concentration gradient approaches zero. In mathematical terms, the control factor of species i is defined as follows:

$$C_i = \min\left(\left|1 - \frac{y_i^*}{y_i}\right|, \left|1 - \frac{y_i}{y_i^*}\right|\right), \tag{306}$$

where y_i^* is the mass fraction of species at the reaction interface and y_i is the mass fraction of species i in the corresponding bulk phase (metal bath, gas jet, or top slag). In the studied heats, the calculated partial pressures of oxygen at both reaction interfaces were between 10^{-7} to 10^{-10} atm, which indicates an almost total absence of oxygen. At the reaction interfaces, all the species are in equilibrium with each other according to the set of reversible reactions defined in the model. In the following, the competing oxidation reactions of carbon and chromium as well as the overall reaction defined by Eq. 307 are studied.

$$(Cr_2O_3) + 3[C] \rightleftharpoons 2[Cr] + 3\{CO\}. \tag{307}$$

The control factor of carbon at the cavity interface is initially much higher than that of CO, and hence the mass transfer of C is the controlling step for direct decarburisation (Fig. 37a). Considering the direct oxidation of chromium at the cavity interface, the mass transport of Cr_2O_3 forms a greater resistance than that of Cr. The overall rate defined by Eq. 307 is limited by the mass transfer of carbon.

Similarly to the cavity interface, the control factor for C at the metal droplet interface is much larger than that for CO (Fig. 37b). The control factor of Cr is larger than that for Cr_2O_3. It needs to be kept in mind that the reaction rates are defined by both macrokinetic and microkinetic factors. A closer examination of the predicted composition of the metal droplets reveals that the concentration gradients between the metal droplet interior and the interface are small, indicating that the oxidation reactions of C and Cr are not limited to a significant extent by the microkinetic mass transport rate. Consequently, the oxidation rates are defined primarily by the macrokinetic factors, most importantly the generation rate of the metal droplets. The same conclusion also applies to the overall rate described by Eq. 307.

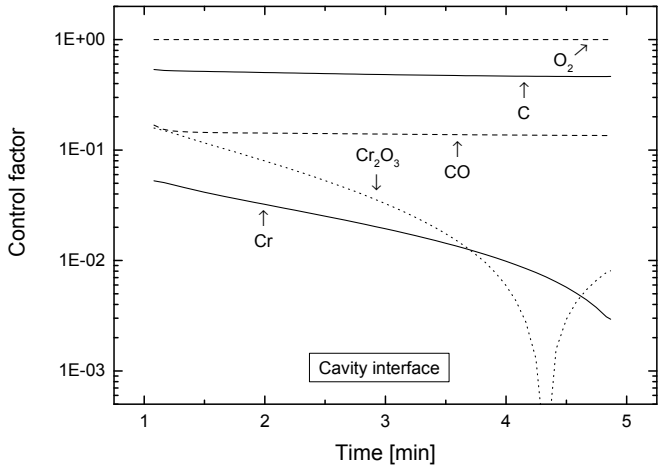

(a) Cavity interface.

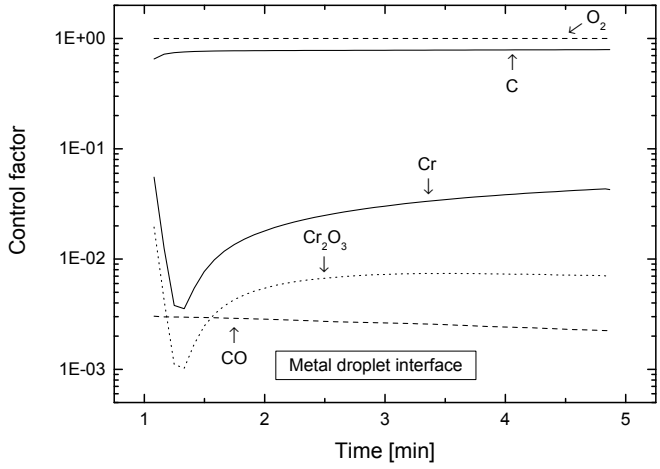

(b) Metal droplet interface.

Fig 37. Predicted control factors in heat 54872. Reproduced from Article II by permission of Springer Nature.

7.2.7 Experimental observations

In order to study the slag samples in more detail, micro-sections were prepared and analysed using light optical microscopy. The analysed cross-sectional surfaces were found to be qualitatively similar to those reported earlier in the literature [156, 158, 184, 185]. All the decarburisation slag samples contained a considerable number of

metal droplets (see Fig. 38). Most of the apparent surface area of the metal droplets was comprised of droplets in the range of 0.1 mm to 5 mm. Droplets with an equivalent diameter up to 1 mm were found to be mostly oval or spherical in shape (see Fig. 38b), while larger droplets were usually of irregular shape.

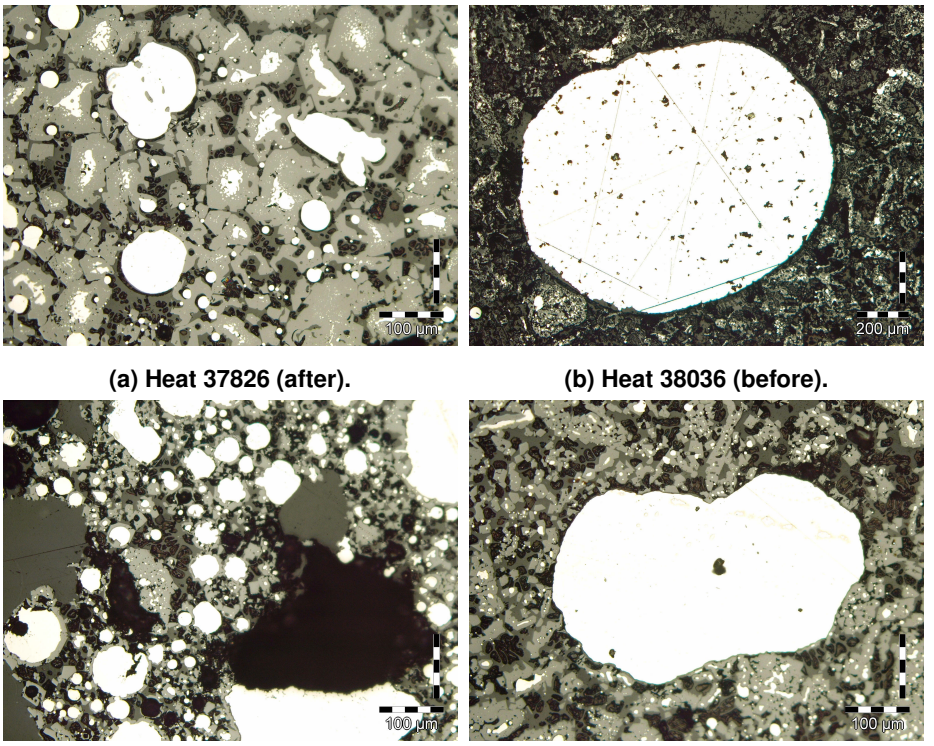

(a) Heat 37826 (after). **(b) Heat 38036 (before).**

(c) Heat 37826 (after). **(d) Heat 37826 (after).**

Fig 38. Metal droplets in cross-sections of slag samples before and after the studied process stage. Fig. 38b reproduced from Article II by permission of Springer Nature.

By comparing the slag samples with those presented by Rubens and co-authors [156, 158] and Ternstedt *et al.* [184], it appears likely that the white areas represent the metal alloy, light grey areas represent calcium chromate, and dark grey areas represent the silicate matrix. Similarly to [156, 158], the slag samples from the early parts of the decarburisation stage contained undissolved lime particles, which were covered by a solid shell. It has been suggested that the solid shell is dicalciumsilicate [156, 158].

7.3 Reduction stage (Article IV)

In Article IV, the reduction model was validated with measurement data from five heats conducted at Outokumpu Stainless Oy in Tornio, Finland. The simulated AOD converter had a nominal capacity of 150 tonnes and its technical details are available in [605, 606]. In this work, the cases studied in Article IV were recalculated using a modified version of the reduction model proposed in Article III.[44]

The starting point for the simulations was the beginning of the reduction stage, while the end point was the end of the reduction stage. In all of the studied heats, the length of the reduction stage was 6 minutes, while the argon injection rate was approximately 0.7 $Nm^3/(t \cdot min)$.[45] The metal and slag samples as well as the temperature measurements were taken both before and after the reduction stage (see Tables 32 and 33 on pp. 217 and 218, respectively). The samples were analysed with an OES and an XRF spectrometer. The additions were assumed to be fed from three silos with a feed rate of 2000 kg/min each (see Table 31). The employed geometry parameters are available in Article IV and are not repeated here.

Table 31. Material additions in the reduction stage. Modified from Article IV.

	Silo 1	Silo 2		Silo 3		
Feed rate [kg/min]	2000	2000		2000		
	Amount of addition [kg] per 1 kg of slag					
Heat	Lime	Dolomite	Fluorspar	75FeSi	SiMn	SST scrap
18552	0.15	0.16	0.09	0.16	0.08	0.00
18692	0.20	0.19	0.10	0.16	0.10	0.00
18694	0.18	0.17	0.09	0.17	0.09	0.00
18696	0.20	0.18	0.10	0.18	0.09	0.00
18698	0.23	0.17	0.08	0.15	0.12	0.10

Notes: SST = stainless steel.

The maximum average residence time of the slag droplets in the metal bath was assumed to be $\bar{t}_{sd,max} = 30$ s. The slag droplet generation rate was adjusted by multiplying the nominal slag droplet generation rate by the parameter J_{eff}. The best results with respect to the measured values were obtained with $J_{eff} = 15$ and consequently this value was employed in the simulations. All the simulations were conducted with a time step of one second. The employed physical properties are listed in Table 22 (p. 186).

[44] The modifications to the original model are outlined in Section 6.3.4 (p. 178).

[45] Expressed in relation to the nominal capacity of the vessel.

7.3.1 Predicted compositions and temperatures

In general, the predictions for the end composition of the metal bath agreed with the measurements taken after the reduction stage, as seen in Table 32. The results indicate that in most of the studied heats, the predicted Cr and Si contents were slightly higher than in the samples. The predicted C contents were also lower than the C contents found in the metal samples, which is partly due to the fact that the dissolution of carbon from the added lime was not taken into account in the simulations. It appears that the assumption of one average metal bath composition did not cause a significant error. This is most likely due to the efficient mixing in the AOD converter.

Table 32. Comparison of metal samples and predictions.

		Composition [wt-%]					
Heat	Type	Cr	Mn	Si	C	Ni	T_{bath} [K (°C)]
	Before	15.47	0.67	0.01	0.00876	8.43	1996 (1723) *
18552	After	18.02	1.49	0.38	0.0163	7.97	1991 (1718) *
	Predicted	18.16	1.49	0.35	0.0143	7.97	1929 (1656)
	Before	15.90	0.65	0.01	0.004	8.3	2039 (1766) *
18692	After	18.01	1.53	0.31	0.0152	7.95	1947 (1674) *
	Predicted	18.11	1.58	0.36	0.0100	7.88	1951 (1678)
	Before	15.90	0.66	0.02	0.00886	8.4	2034 (1761) *
18694	After	18.16	1.52	0.40	0.0166	8.00	1976 (1703) *
	Predicted	18.17	1.52	0.41	0.0141	7.98	1961 (1688)
	Before	15.90	0.74	0.01	0.00528	8.3	2035 (1762) *
18696	After	18.13	1.54	0.40	0.0198	7.97	1947 (1674) *
	Predicted	18.04	1.53	0.49	0.0108	7.89	1958 (1685)
	Before	16.30	0.64	0.01	0.00406	8.4	2039 (1766) *
18698	After	18.12	1.57	0.37	0.0162	7.99	1959 (1686) *
	Predicted	18.14	1.56	0.40	0.0092	8.02	1951 (1677)

* Highest temperature measured by the temperature probe.

The deviation of the predicted metal bath temperatures from the measured values varied from 4 to 62 K; in this respect, the predictive ability of the model is not as good as in the case of the metal bath composition. Nevertheless, it needs be kept in mind that the measured start and end temperatures were the highest temperatures measured by the temperature probe. Based on mass balance it can be deduced that the actual temperatures are likely to be less than 100 K higher. The effect of the initial temperature on the results was simulated and found to be small.

The overly high predicted Si contents of the metal bath were reflected in the overly

low predicted SiO_2 contents of the top slag (see Table 33). The predicted Cr_2O_3 and MnO contents were in satisfactory agreement with the measured values, while the predicted FeO contents of the slag are somewhat lower than the measured values.[46] Furthermore, the predicted CaO and MgO contents are lower than in the samples. The discrepancy in the CaO content is to large extent attributable to the XRF analysis, which did not differentiate between CaO and CaF_2, while in the simulations the CaF_2 was considered as a separate species in the modified reduction model.

Table 33. Comparison of slag samples and predictions.

		Composition [wt-%]							
Heat	Type	FeO	Cr_2O_3	MnO	SiO_2	CaO	MgO	Al_2O_3	Other
	Before	1.7	39.6	2.4	8.5	43.0	1.5	1.7	1.5
18552	After	1.1	1.6	0.3	29.7	56.4	8.5	1.6	0.6
	Predicted	0.1	1.1	0.4	27.4	54.0	6.6	1.4	8.9
	Before	2.3	37.3	3.1	10.7	40.6	2.2	2.1	1.7
18692	After	0.4	0.6	0.3	29.2	58.1	8.8	1.9	0.6
	Predicted	0.2	1.2	0.4	26.5	53.2	7.6	1.6	9.5
	Before	2.1	38.2	2.8	9.1	42.4	1.9	1.8	1.7
18694	After	0.8	1.0	0.4	29.9	56.7	8.9	1.7	0.6
	Predicted	0.2	1.1	0.3	26.9	54.2	6.9	1.4	9.1
	Before	2.6	37.6	2.7	8.2	43.4	2.2	1.5	1.7
18696	After	0.8	0.9	0.3	28.4	58.0	9.4	1.5	0.7
	Predicted	0.1	0.9	0.3	25.4	55.5	7.4	1.1	9.3
	Before	2.6	36.1	2.3	10.2	40.9	4.2	1.8	1.9
18698	After	1.4	4.4	0.4	27.2	55.5	8.8	1.6	0.7
	Predicted	0.2	1.3	0.3	25.6	54.5	8.4	1.3	8.3

The statistical indicators for the predicted end compositions are shown in Table 34. It can be seen that the MAE and RMSE of C, Cr, Mn, Si, and Ni are lower or equal to than their variation in the metal samples. The relatively large error in the predicted metal bath temperature is likely to be related to the problematic temperature measurements before the reduction stage. In view of the many uncertainties, the degree of accuracy can be considered as reasonably good.

[46]It should be noted that in Article IV, the initial FeO content was assumed to be equal to the Fe_2O_3 content of the slag sample. Although this assumption induces a minor distortion of the slag composition, it has virtually no effect on the results. Here, this assumption was retained in order to maintain comparability with the results obtained in Article IV.

Table 34. Statistical indicators for the reduction model.

Range of studied variables				Statistical indicators			
Variable	Start	End	Unit	n	R^2	RMSE	MAE
[C]	0.004 – 0.009	0.015 – 0.020	wt-%	5	0.00	0.006	0.005
[Cr]	15.5 – 16.3	18.0 – 18.2	wt-%	5	0.01	0.09	0.07
[Mn]	0.65 – 0.74	1.49 – 1.57	wt-%	5	0.54	0.02	0.02
[Si]	0.01 – 0.02	0.31 – 0.40	wt-%	5	0.39	0.05	0.04
[Ni]	8.30 – 8.43	7.95 – 8.00	wt-%	5	0.58	0.05	0.04
T	1996 – 2039	1947 – 1991	K	5	0.39	29.4	20.2

7.3.2 Dynamic changes in bath composition and temperature

Figs. 39a and 39b illustrate the predicted dynamic changes in the Cr, Mn, and Si contents of the metal bath during the reduction stage of heats 18692 and 18694, respectively. The metal samples taken before and after the reduction stage are shown for comparison. The Si content of the steel increases rapidly as a result of the FeSi and SiMn additions, starting the reduction of Fe, Cr, and Mn back to the metal bath. The reduction rate of the Cr decreases as the chromium oxide content of the slag approaches its equilibrium value. The Mn content of the metal bath rises not only as a result of the reduction of MnO, but also due to addition of SiMn, and reaches a plateau soon after the SiMn feed ends. The predicted changes in bath composition are in qualitative agreement with the results of Shi *et al.* [144] and Wei *et al.* [245].

Figs. 40a and 40b illustrate the predicted bath temperature and temperature measurements during the reduction stage of heats 18692 and 18694, respectively. Initially the temperature of the metal bath increases slightly, reaching its peak value at approximately 0.7 minutes. The temperature peak is associated with the reaction of Si not only with the oxide species in the top slag, but also with the oxygen dissolved in the metal bath. During the time interval from 1 to 3 minutes, the oxidation of Si starts to slow down and the bath temperature decreases rapidly as the feeding of reductants, slag formers, and fluxes continues. Thereafter, the bath temperature continues to decrease at a slow rate due to heat losses. The predicted evolution of the bath temperature is in qualitative agreement with the modelling results of Shi *et al.* [144] and Wei *et al.* [245].

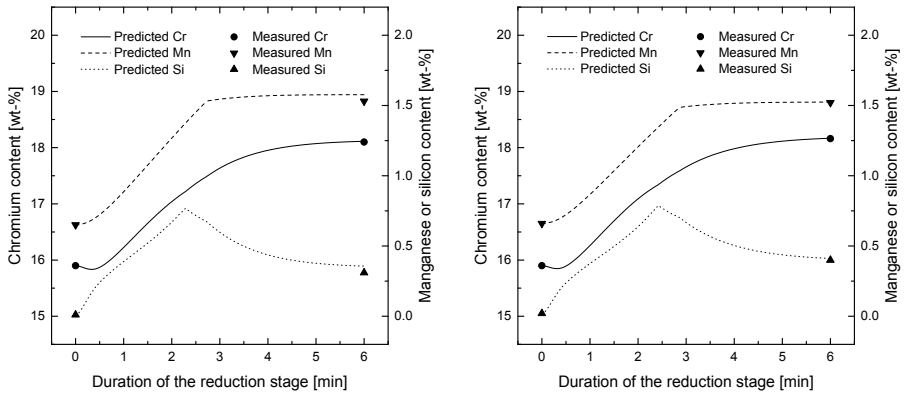

(a) Heat 18692. **(b) Heat 18694.**

Fig 39. Predicted bath composition during the reduction stage.

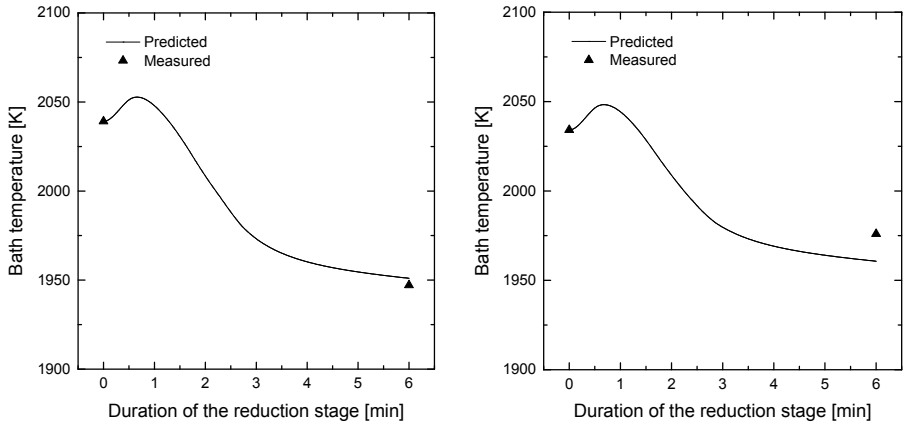

(a) Heat 18692. **(b) Heat 18694.**

Fig 40. Predicted bath temperature during the reduction stage.

7.3.3 Sensitivity analysis

It has been suggested that small 75FeSi particles should be preferred for their wider distribution, short melting time and large interfacial area [128]. The effect of a 75FeSi addition was simulated with three average particle sizes (40 mm, 50 mm, and 60 mm).

The total feed rate of the reductants (75FeSi and SiMn) from silo 3 was set to 2000 kg/min as in the previous calculations. As shown in Fig. 41a, the smaller particle size markedly decreased the amount of solid 75FeSi present in the metal bath at the beginning of the reduction stage. However, the effect on the reduction rate was found to be small. Corresponding results have been obtained with an actual AOD vessel [624]. In the light of these results, all of the studied particle sizes appear to be suitable.

The effect of the total feed rate of reductants (75FeSi and SiMn) was simulated with three total feed rates: 1500 kg/min, 2000 kg/min, and 2500 kg/min. It was found that increasing the feed rate resulted in a slighly faster reduction of the slag (see Fig. 41b). Such a change in the feed rate might also be realisable in practice.

Nakasuga *et al.* [366, 367] and Görnerup and Lahiri [14] have suggested that the reduction rate of Cr_2O_3 increases with increasing temperature. An increased incubation time was also reported [14]. In this work, the effect of temperature on the reduction rate was studied by simulating heat 18694 with three different initial bath temperatures: 1984 K (1711 °C), 2034 K (1761 °C), and 2084 K (1811 °C). The resulting differences in the reduction rate of chromium oxide were found to be negligibly small and no clear temperature dependency of the chromium reduction could be established (see Fig. 41c), although small deviations were found in the predicted final chromium contents. Finally, the effect of the blowing time was simulated. Prolonging the length of the reduction stage from 6 to 7 minutes or shortening it from 6 to 5 minutes had only a marginal effect on the composition of the metal bath (see Fig. 41d).

7.3.4 Emulsification of slag

The model for the reduction stage assumes that all reactions take place between the slag droplets and metal bath. The generation rate of the slag droplets is determined by energy balance, while the droplet size is calculated based on force balance [1]. Fig. 42a illustrates the average slag droplet size, interfacial velocity, and critical velocity as a function of time in heat 18694. The predicted interfacial velocity exceeds the predicted critical interfacial velocity throughout the process stage, which confirms that the conditions for emulsification are met.

Fig. 42b illustrates the simulated surface area of the emulsified slag droplets and the degree of emulsification in the same heat. The results suggest that the surface area of the emulsified droplets should be in the order of tens of thousands of square meters and thus considerably larger than the metal–slag interface around the plume eye. As expected,

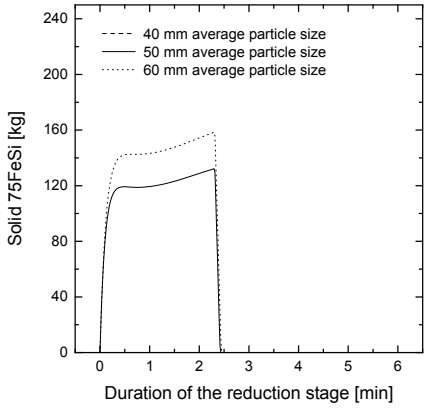

(a) Effect of average particle size on the amount of solid 75FeSi.

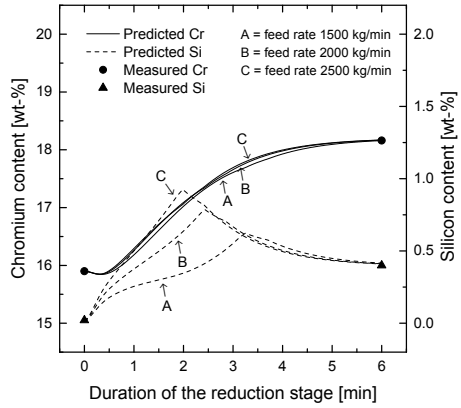

(b) Effect of the reductant feed rate on the predicted bath composition.

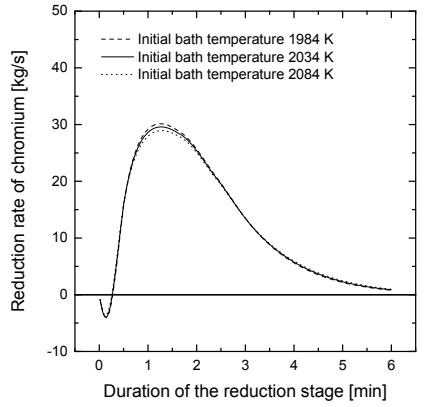

(c) Effect of the initial bath temperature on the predicted Cr reduction rate.

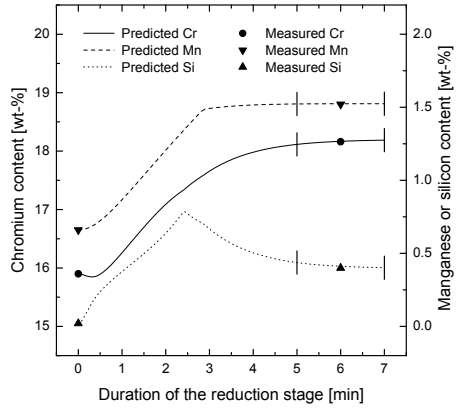

(d) Effect of the blowing time on the predicted bath composition.

Fig 41. Simulated effect of different parameters on the dynamics of the reduction stage in heat 18694.

the highest degree of emulsification was reached at the end of the reduction stage. It should be noted that the calculated surface area and degree of emulsification reflect the assumptions of the model. With respect to mass and heat transfer, the slag droplets were assumed to behave similar to rigid spheres – an assumption, which provides a fairly conservative estimate of the mass and heat transport rates. If it is assumed instead that a laminar circulation takes place within the slag droplets, comparable results can be obtained with a shorter average residence time of the droplets. By comparing the

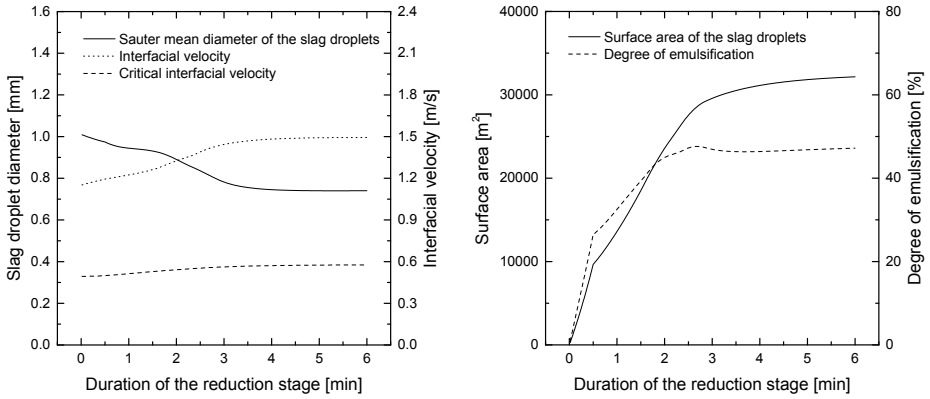

(a) Sauter mean diameter, interfacial velocity, and critical interfacial velocity.

(b) Surface area and degree of emulsification.

Fig 42. Predicted slag emulsification behaviour in heat 18694.

Newman [323] and Kronig-Brink [328] solutions, it can be deduced that the residence time required to obtain the same microkinetic efficiency would then need to be only roughly one third of the value employed in the present simulations. Consequently, the maximum degree of emulsification would be in the range of 15 to 20%.

As seen in Table 35, the predicted slag droplet diameter is in reasonable agreement with the experimental evidence [535] as well as the results of physical modelling [365, 534, 537, 541] and CFD modelling [101, 234, 236]. The results of Tilliander *et al.* [101] are the closest to the conditions of this work. They employed a three-dimensional three-phase model to study gas injection in a side-blowing AOD converter and suggested that the slag droplets should be in the order of 0.01–0.5 mm in diameter depending on the studied case [101]. Therefore, the interfacial area may be considerably larger than that predicted in this work.

The predicted degree of emulsification can be compared qualitatively with findings reported in the numerical [101] and physical [102, 128] modelling studies. The results of Tilliander *et al.* [101] suggest that the liquid slag can be dragged down to roughly one-third of the bath depth even in the case of a relatively mild blowing rate of 0.63 $Nm^3/(t \cdot min)$. In the case of a higher gas injection rate of 1.26 $Nm^3/(t \cdot min)$, part of the slag remained in the recirculation loops, while some of the slag droplets were dragged even deeper into the metal bath and also to the nozzle side of the vessel [101]. Guthrie *et al.* [128] studied the reduction stage by employing a physical model, in

Table 35. Studies on the emulsification of top slag. Modified from [236].

Study	Model type	Process	Droplet diameter [mm]	Droplet diameter Type	ϕ_{em} [%]
Mietz *et al.* [365]	Physical model	Ladle	–	–	6–100
Wei and Oeters [534]	Physical model	Ladle	1.7–5.2	$\overline{d}$	–
Lachmund *et al.* [535]	Experiment	Ladle	1	$\overline{d}$	4
Savolainen *et al.* [541]	Physical model	Ladle	3.1–8.19	$\overline{d}$	–
Sulasalmi *et al.* [234]	CFD model	Ladle	3.10–3.63	$\overline{d}$	–
Khajavi and Barati [625]	Physical model	Ladle	2–11	d_{32}	–
Sulasalmi *et al.* [236]	CFD model	Ladle	4–6	d_{32}	0.8–3
Frohberg *et al.* [537]	Physical model	BOF	1.6–4.25	d_{32}	–
Tilliander *et al.* [101]	CFD model	AOD	0.01–0.5	d	–
This work	Mathematical model	AOD	0.6 –1.2	d_{32}	0–56

which zinc chloride, silicone oil, and wooden particles were used to represent liquid metal, slag, and 75FeSi particles, respectively. They reported that the top phase was transferred to a foam [128], which indicates that the top phase was almost completely emulsified. In an earlier publication by the author [102], a physical model was employed for studying mixing times in the AOD process. In these experiments, it was found that the rapeseed oil employed for representing the top slag emulsified in the water bath to a large extent [102]. However, it should be kept in mind that owing to differences in physical properties,[47] the emulsification behaviour in the actual process is likely to be less intense than that observed in physical models. In conclusion, it can be stated that the predicted degree of emulsification is in qualitative agreement with the findings reported in [101, 102, 128].

7.3.5 Rate-limiting factors

The control factor concept was used to identify the rate-limiting mechanisms (see Eq. 306 on p. 213). Figs. 43a and 43b show the calculated control factors for Si and Cr_2O_3 in heats 18694 and 18698, respectively. It is observable that the reduction rate of Cr_2O_3 is controlled initially by the mass transfer of Si to the reaction surface. Subsequently, as the Si content of the bath increases and Cr_2O_3 content of the top slag simultaneously decreases, the diffusive mass transfer of Cr_2O_3 in the slag droplets begins to control the reduction rate. These results are in agreement with the results presented earlier by

[47] In particular, the density difference and interfacial tension of the bottom and top phases deviate considerably from that of liquid metal and slag.

Görnerup and Lahiri [14] and Nakasuga *et al.* [366, 367], who found that the reduction rate of Cr_2O_3 is controlled initially by the mass transfer of Si in the metal phase and subsequently by the mass transfer of Cr_2O_3 in the slag phase.

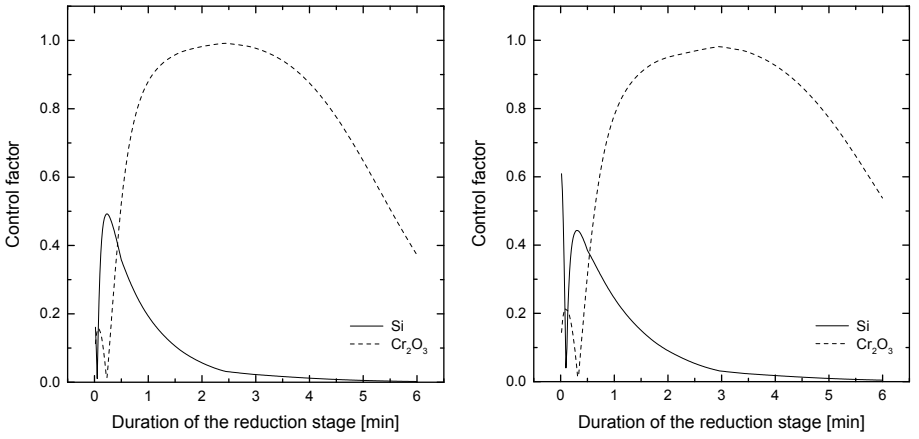

(a) Heat 18694. **(b) Heat 18698.**

Fig 43. Predicted control factors of Si and Cr_2O_3 during the reduction stage.

In the AOD process, violent stirring promotes short mixing times [58, 85, 94, 99, 102, 103, 274] and the effective dispersion of reductant additions [57]. As the availability of Si for reduction of Cr_2O_3 is controlled initially by the melting and dissolving of Si into the metal bath, it appears likely that the feeding and melting of the reductants form the rate-controlling step in the initial part of the reduction stage.

7.4 Further work

In this work, a law of mass action based method was employed for treatment of parallel mass transfer limited reactions was studied. A comparison of the computational efficiency of this method to other methods available in the literature would be an interesting topic for future work.

In the future, the increasing knowledge of the AOD process can be employed for improving the assumptions of the models developed in this work. For example, detailed studies on the interaction of gas jets and metal bath or emulsification of slag under the conditions of the AOD process would allow validation of the assumptions of the top-blowing model. In the reduction model, the size distribution of slag droplets

was considered through their Sauter mean diameter and hence the variation in the microkinetic efficiency of the droplets was ignored. In an earlier publication by the author [236], it was shown that the distribution of slag droplets in ladle treatments can be described reasonably well using the RRS function. The application of this distribution function to the conditions of the AOD process would enable a more detailed description of the emulsification behaviour and the microkinetics of the reduction stage. Furthermore, a description of desulphurisation during the reduction stage of the AOD process could be developed based on the sulphide capacity models available in the literature. To this end, some preliminary results have already been obtained.

In further work, the model needs to be validated for simulating complete AOD heats including combined-blowing decarburisation, side-blowing decarburisation, and the reduction stage. Some preliminary results on modelling of complete heats have been reported in [626]. In the standard process, it is possible to take samples only when the vessel is tilted, but modern instrumentation often includes a sublance, which can be employed for sampling and temperature measurements in the upright position [5, 627]. Nevertheless, one of the main challenges for the AOD process is to control the process without continuous steel and slag composition data. In this regard, transient metal and slag composition measurements from the AOD process could be used to validate and improve the accuracy of the models developed in this work. Some promising results of online steel [628] and slag [629–632] analysis have been obtained using *laser-induced breakdown spectroscopy* (LIBS).

An interesting topic would be to employ the top-blowing model for studying the use of alternative process gases. The use of CO_2 in the AOD process was already patented in the 1970s [633], but so far its industrial use has remained limited. Injected CO_2 decarburises the metal bath according to

$$[\mathrm{C}] + \{\mathrm{CO_2}\} = 2\{\mathrm{CO}\}\,. \tag{308}$$

The interfacial reaction kinetics of decarburisation with CO_2 have been the subject of numerous studies [403, 634–637]. Using mixed-control models, it has been established that the limiting step of the reaction given in Eq. 308 is the dissociation of CO_2 [403]. The reaction kinetics are thus very sensitive to surface active species, particularly to sulphur [403, 634–636]. Additional studies have been conducted to investigate the kinetic and thermodynamic aspects that are specific to the decarburisation of stainless steels [221, 251, 355, 635, 638, 639]. Wang *et al.* [639] have suggested that CO_2 is an

effective diluting and decarburisation gas at high carbon contents, but at low carbon contents ([%C] $\approx$ 0.25 wt-%) the decreased Cr losses were obtained at the expense of considerably slower decarburisation rate. As the reaction given in Eq. 308 is endothermic [639], less steel scrap is needed in order to cool the metal bath. Furthermore, the use of CO_2 might reduce dust formation similarly as in the BOF process [640].

Simulators are powerful tools for decision making and process optimisation [641]. In comparison to simplistic models, the more detailed description of the underlying phenomena allows prescriptive analysis of the AOD processes, thus increasing the economic value of the analysis (Fig. 44). The potential financial benefits of prescriptive mathematical modelling can be considerable. In [642], it was reported that the length of the AOD treatment of certain steel grades at Outokumpu Stainless Oy was reduced by 10% with the help of simulations with the Converter Process Simulator and automation system. However, at its present state, the converter simulator does not take any stand on the associated costs. With the help of a suitable function, which calculates the costs associated with a particular heat, further reductions in production costs may be achievable. An example of such a cost function has been proposed by Irving *et al.* [224]. Their equation accounts for the cost of replacing lost chromium, the cost of oxygen, the cost of argon, and the overhead running cost.

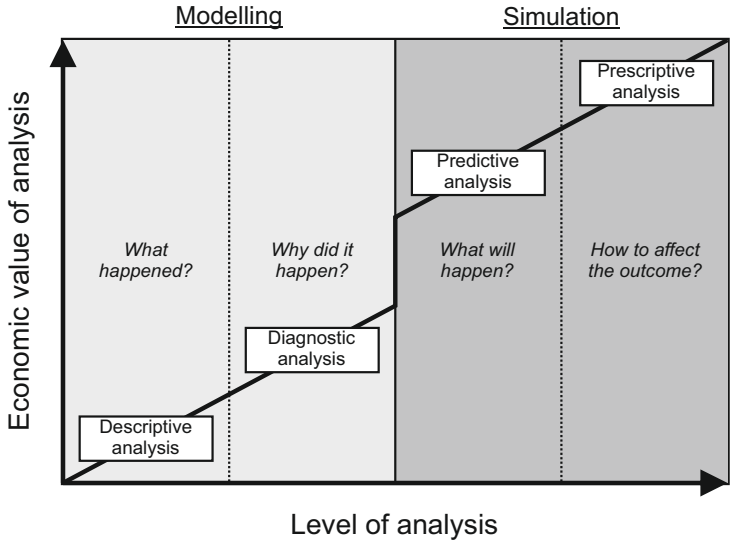

Fig 44. Economic value of mathematical analysis of unit processes.

8 Conclusions

The objective of this work was to study chemical kinetics and rate phenomena in the AOD process using mathematical modelling. For this aim, a review of the reaction models for the AOD process was conducted. The three main categories of the fundamental models are system free energy minimisation models, reaction volume models, and reaction interface models. The system free energy minimisation models deduce the reaction extent from the minimisation of the Gibbs free energy at the reaction zone. The reaction volume models assume that the rate-determining step is the mass exchange between the bulk volume and a reaction volume, in which a chemical equilibrium prevails. The reaction interface models are based on the boundary layer theory and assume that the rate-determining step is the mass transport between the bulk phase and the reaction interface, which are separated by a thin diffusion boundary layer. In comparison to thermodynamic factors, much less effort has been put into a detailed kinetic description of reactions in the AOD process. In the 21st century, there have been rigorous attempts to describe the process physics. Process mechanisms models employ experimental correlations to describe process physics, while finite volume reaction models solve the fluid flow field by means of computational fluid dynamics. Despite the increased computational resources, major simplifications are still needed to keep the computational expense of finite volume reaction models on a reasonable level. In conclusion, it can be stated that the reaction models have evolved from simplistic decarburisation models to comprehensive fundamental models, which account for dynamic reaction equilibria and local transport phenomena.

A literature review of the treatment of chemical kinetics under conditions relevant to the AOD process was conducted in order to form a synthesis of the current knowledge of the fundamentals. The main macrokinetic factors are the bath mixing, nature of the phase contact, as well as the distinction between dispersed and non-dispersed systems. The results of physical and numerical modelling studies suggest that the bath mixing resistance is of secondary importance in comparison to the microkinetic resistance. The main factors affecting the microkinetic efficiency are the mass transport rate, the ratio of interfacial area to volume, and the contact time. If the microkinetic efficiency is very low, the reaction operates far away from its equilibrium and the reaction rate is defined primarily by the mass transfer resistance and mass exchange area. On the other hand,

in case of high microkinetic efficiency the reaction rates are primarily a function of macrokinetic factors, such as bath mixing or the generation rate of the dispersion. In the case of low microkinetic efficiency, it may be permissible to ignore the conservation of mass in the dispersed phase and treat the dispersed system similarly to a non-dispersed system. However, because the resulting error approaches infinity as the microkinetic efficiency approaches 100%, the reaction rates in dispersed systems can be greatly overestimated if the conservation of mass in the dispersed phase is not accounted for.

The mathematical treatment of parallel oxidation-reduction reactions is an important aspect for modelling metallurgical unit processes. In this work, a novel approach based on a modified law of mass action was studied and further developed. The main advantage of the LMA approach is that it enables the simultaneous solution of chemical equilibrium and constraining mass transfer onto and from the reaction interface. The principal hypothesis of the LMA approach is that the reaction interface approaches its mass transfer constrained equilibrium as the forward reaction rate constants approach infinity. Two alternative methods, named the residual affinity method and the reaction quotient method, were suggested for determining the reaction rate coefficients in numerical modelling. The residual affinity method was illustrated with a simple reaction model, which was employed for studying the parallel oxidation of Si, Cr, and C in the case of liquid stainless steel surface exposed to O_2–CO gas. The results suggest that a sufficient degree of accuracy for the equilibrium is obtained when the residual affinity is smaller than 10 J/mol. The applicability of the LMA approach extends also to reactions, which are controlled by the surface reaction, as well as to non-metallurgical applications. The LMA approach is well-suited for dynamic models, which benefit from the transparent and direct determination of the reaction source term. The application of the LMA approach to CFD models could be a fruitful topic for further research.

Based on the LMA approach, a novel mathematical model was derived and validated for reactions during top-blowing. This model focuses on the local physico-chemical phenomena that control the rate phenomena during top-blowing. The approach employed complies automatically with the rate controlling mass and heat transfer mechanisms. In order to validate the model, composition and temperature data were collected from experimental heats, in which the last combined-blowing stage was modified such that oxygen was injected via the top lance only. The carbon removal efficiency of the top-blown oxygen was approximately the same as in reference heats with the combined top- and side-injection of oxygen. The collected slag samples were found to contain a considerable quantity of small metal droplets.

The results obtained with the top-blowing model suggest that the surface area of the cavity alone is too small to account for the high decarburisation rates associated with top-blowing. Consequently, it is suggested that both the direct and indirect oxidation of metal droplets play an important role in achieving the high decarburisation rates obtained in the AOD process. The results of a sensitivity analysis suggest that the oxygen content of the top-blown gas has a more significant effect on the decarburisation rate than the lance position. Finally, the model was employed for studying rate limiting factors during top-blowing. The predicted overall rate of decarburization was found to be limited by the mass transfer of carbon in the studied process stage. These findings agree with with previous studies available in the literature. In future work, the developed top-blowing model can be employed in combination with the side-blowing model developed by Järvinen *et al.* in order to predict changes in metal bath composition and temperature during combined side- and top-blowing.

Focusing on the reduction stage, a novel mathematical model was proposed based on the LMA approach. Here, it was assumed that the reduction reactions take place primarily between the metal bath and the emulsified slag droplets due to the large surface area of the droplets as well as their efficient mass transfer characteristics. The reduction of Cr_2O_3 does not commence before the addition and dissolving of reductants. It is suggested that the reduction rate of Cr_2O_3 is limited initially by the melting and dissolution of FeSi and subsequently by the transport of Cr_2O_3 to the reaction interface. The results of a sensitivity analysis suggests that in order to expedite the melting and dissolution of reductants into the metal bath, high reductant feed rates should be used during the reduction stage. In the studied cases, the particle size of 75FeSi had only a minor effect on the overall reduction rate of Cr_2O_3.

Finally, it should be pointed out that the small amount of data available of the process continues to define a practical limit for the accuracy of complex phenomena-based models. In particular, the heterogeneity of the slag poses a challenge because there are relatively large uncertainties in the sampled slag compositions. For a more detailed validation of the models, it would be necessary to obtain more information on the actual evolution of the metal and slag composition.

References

1. Oeters F (1989) Metallurgie der Stahlherstellung. Verlag Stahleisen mbH, Düsseldorf, Germany.
2. European Committee for Standardization (2002). EN 10020:2000, Definition and classification of stainless steel grades.
3. Erkkilä P (2004) Trends and challenges in the stainless steel industry. Ironmaking Steelmaking 31(4): 277–284.
4. Heinen K-H, Steffes B & Zörcher H (1997) Sekundärmetallurgie. In: Heinen KH (ed.) Elektrostahl-Erzeugung, pp. 513–571. Verlag Stahleisen GmbH, Düsseldorf, Germany.
5. Patil BV, Chan AH & Choulet RJ (1998) Refining of Stainless Steels. In: Fruehan RJ (ed.) The Making, Shaping and Treating of Steel. 11th Edition Steel Making and Refining, chapter 12, pp. 715–741. The AISE Steel Foundation, Pittsburg, USA.
6. Bleck W (2013) Materials Science of Steel – Textbook for Students at RWTH Aachen. Department of Ferrous Metallurgy, RWTH Aachen University, Aachen, Germany.
7. Cobb HM (2010) The History of Stainless Steel. ASM International, Materials Park, Ohio, USA.
8. International Stainless Steel Forum (2017). Meltshop production [e-publication, accessed on September 27, 2017]. URL: `http://www.worldstainless.org`.
9. Heikkinen E-P & Fabritius T (2012) Modelling of the Refining Processes in the Production of Ferrochrome and Stainless Steel. In: Nusheh M, Ahuett HG & Arrambide A (eds.) Recent Researches in Metallurgical Engineering - From Extraction to Forming, chapter 4, pp. 65–88. InTech, Rijeka, Croatia.
10. Wijk O (1992) Stainless Steelmaking in Converters. In: Engh TA (ed.) Principles of Metal Refining, pp. 280–301. Oxford University Press, Oxford, United Kingdom.
11. Jones JAT, Bowman B & Lefrank PA (1998) Electric Furnace Steelmaking. In: Fruehan RJ (ed.) The Making, Shaping and Treating of Steel. 11th Edition Steel Making and Refining, chapter 10, pp. 525–660. The AISE Steel Foundation, Pittsburg, USA.
12. Arh B & Tehovnik F (2007) The oxidation and reduction of chromium during the elaboration of stainless steels in an electric arc furnace. Mater. Tehnol. 41(5): 203–211.
13. Görnerup M & Lahiri AK (1998) Reduction of electric arc furnace slags in stainless steelmaking Part 1 Observations. Ironmaking Steelmaking 25(5): 317–322.
14. Görnerup M & Lahiri AK (1998) Reduction of electric arc furnace slags in stainless steelmaking Part 2 Mechanism of Cr_2O_3 reduction. Ironmaking Steelmaking 25(5): 382–386.
15. Kho TS, Swinbourne DR, Blanpain B, Arnout S & Langberg D (2010) Understanding stainless steelmaking through computational thermodynamics Part 1: electric arc furnace. Trans. Inst. Min. Metall. C 119(1): 1–7.
16. Toulouevski YN & Zinurov IY (2010) Innovation in Electric Arc Furnaces: Scientific Basis for Selection. Springer-Verlag Berlin Heidelberg.
17. Krivsky WA (1973) The Linde Orgon-Oxygen Process for Stainless Steel; A Case Study of Major Innovation in a Basic Industry. Metall. Trans. 4(6): 1439–1447.
18. Gorges H, Graf H, Lutz H, Oberhäuser P-G & Mülders H (1976) Erfahrungen mit dem AOD-Verfahren für die Erzeugung nichtrostender Stähle. Stahl Eisen 76(24): 1251–1258.

19. Kreutzer HW (1979) Die Entkohlung hochchromliegierter Stähle. Stahl Eisen 99(23): 1297–1301.
20. Chiappero A, Barozzi S & Barilati G (1997) A new high performance AOD converter. In: Proc. 2nd European Oxygen Steelmaking Congress, pp. 121–133. Associazione Italiana di Metallurgia, Taranto, Italy.
21. Dierstein H-A (1977) Experience with the AOD process at Fried. Krupp Hüttenwerke, Bochum. Ironmaking Steelmaking 4(2): 88–91.
22. Jalkanen H & Holappa L (2014) Converter Steelmaking. In: Seetharaman S, McLean A, Guthrie R & Sridhar S (eds.) Treatise on Process Metallurgy, Volume 3, Industrial Processes, pp. 223–270. Elsevier, Oxford, United Kingdom.
23. Lindenberg H-U, Schubert K-H & Zörcher H (1988) Developments in stainless steel melting process metallurgy. Metall. Plant Technol. Int. 11(1): 3–10.
24. Steffen R, Janke D, Schäfer K, Jacobi H, Hammer R & Hentrich R (2011) Steel, 2. Crude Steel Production. In: Ullmann's Encyclopedia of Industrial Chemistry, volume 34, pp. 157–213. Wiley-VCH Verlag GmbH, Weinheim, Germany.
25. Stolte G (2007) Secondary Metallurgy – Fundamentals, Processes, Applications. Verlag Stahleisen GmbH, Düsseldorf, Germany.
26. Reichel J & Szekely J (1995) Mathematical Models and Experimental Verification in the Decarburization of Industrial Scale Stainless Steel Melts. Iron Steelmaker 22(5): 41–48.
27. Ding R, Blanpain B, Jones PT & Wollants P (2000) Modeling of the Vacuum Oxygen Decarburization Refining Process. Metall. Mater. Trans. B 31(1): 197–206.
28. Wei J-H & Li Y (2015) Study on Mathematical Modeling of Combined Top and Bottom Blowing VOD Refining Process of Stainless Steel. Steel Res. Int. 86(3): 189–211.
29. Wei J-H & Zeng L (2012) Numerical Simulation of Fluid Flow in Bath during Combined Top and Bottom Blowing VOD Refining Process of Stainless Steel. Steel Res. Int. 83(11): 1053–1070.
30. Lindenberg H-U (1991) Spezielle Gesichtspunkte beim Stranggießen höherlegierter Stähle. In: Schwerdtfeger K (ed.) Metallurgie des Stranggießens – Gießen und Erstarren von Stahl, pp. 339–357. Verlag Stahleisen GmbH, Düsseldorf, Germany.
31. Odenthal H-J (2004) Physikalische und numerische Strömungssimulation kontinuierlicher Gießprozesse der Hochtemperaturtechnik. Habilitation thesis, Rheinisch-Westfälische Technische Hochschule Aachen, Aachen, Germany.
32. Rüttiger K, Diener A & Wagner K (1991) Einführung zur Technik des Stranggießens. In: Schwerdtfeger K (ed.) Metallurgie des Stranggießens – Gießen und Erstarren von Stahl, pp. 1–34. Verlag Stahleisen GmbH, Düsseldorf, Germany.
33. Morii K, Kumura S, Mori H, Shinkai M & Sakuma H (1993) Development of New Refining Process for Manufacture of Stainless Steel. Denki Seiko 64(1): 4–12.
34. Qian G, Cheng G, Li L, Li Y, Zhang J & Wang C (2015) Desulfurization Mechanism of Stainless Steel Produced by GOR Converter. In: Proc. 6th International Congress on the Science and Technology of Steelmaking, volume 2, pp. 1031–1034. The Chinese Society for Metals, Beijing, China.
35. Taoka K, Nomura H, Komamura K, Emoto K, Sudo F & Fujii T (1986) Progress in Stainless Steel Production by Top and Bottom Blown Converter. Kawasaki Steel Tech. Rep. (14): 12–22.
36. Liu FX, Hu YT, Li JM, Zhai Y, Mittag P, Shohl K & Flossmann G (2005) Stainless and carbon steel production via K-OBM-S. Millenium Steel pp. 90–94.

37. Vercruyssen C, Wollants P, Roos JR, Robertson DGC & Bertels L (1994) Mathematical modelling of refining of stainless steel in MRPA converter. Ironmaking Steelmaking 21(4): 287–296.
38. Masuda S, Taga M, Nakajima H & Ieda K (1986) Development of Oxygen Top Blowing and Argon Bottom Blowing Method in Refining of Stainless Steel. Tetsu-to-Hagané 72(9): 1301–1308.
39. Szekely J (1988) The Mathematical Modeling Revolution in Extractive Metallurgy. Metall. Trans. B 19(4): 525–540.
40. Velten K (2009) Mathematical Modeling and Simulation: Introduction for Scientists and Engineers. Wiley-VCH Verlag GmbH & Co. KGaA, Weinheim, Germany.
41. adn R E Crosbie SS, Gagné RE, Innis GS, Lalwani CS, Loch J, Sylvester RJ, Wright RD, Kheir N & Bartos D (1979) Terminology for model credibility. Simulation 32(3): 103–104.
42. Sargent RG (1988) A tutorial on validation and verification of simulation models. In: Abrams M, Haigh P & Comfort J (eds.) Proc. 1988 Winter Simulation Conference, pp. 33–39. San Diego, CA, USA.
43. Themelis NJ (1995) Transport and Chemical Rate Phenomena. Gordon and Breach Publishers, New York, NY, USA.
44. Järvinen MP, Pisilä S, Kärnä A, Ikäheimonen T, Kupari P & Fabritius T (2011) Fundamental Mathematical Model for AOD Process. Part I: Derivation of the Model. Steel Res. Int. 82(6): 638–649.
45. Pisilä SE, Järvinen MP, Kärnä A, Ikäheimonen T, Fabritius T & Kupari P (2011) Fundamental Mathematical Model for AOD Process. Part II: Model validation. Steel Res. Int. 82(6): 650–657.
46. Krivsky WA (1966). Preparation of metals and alloys. US Patent 3,252,790.
47. Choulet RJ, Death FS & Dokken RN (1971) Argon-oxygen refining of stainless steel. Can. Metall. Quart. 10(2): 129–136.
48. Hodge AL (1977) AOD process and its eighty-six months of growth. Ironmaking Steelmaking 4(2): 81–87.
49. Wei J-H & Zhu D-P (2002) Mathematical Modeling of the Argon-Oxygen Decarburization Refining Process of Stainless Steel: Part I. Mathematical Model of the Process. Metall. Mater. Trans. B 33(2): 111–119.
50. Saccomano JM, Choulet RJ & Ellis JD (1969) Making Stainless Steel in the Argon-Oxygen Reactor at Joslyn. J. Met. 21(2): 59–64.
51. Inomoto T, Matsuo M & Yano M (2015) Evaluation of the Chemical Vacuum Effect in Decarburization Treatment by Argon-injected Steel under Normal Atmosphere. ISIJ Int. 55(4): 723–726.
52. Rubens W & Oberhäuser P-G (1977) Anwendung technischer Gase bei der Herstellung von Edelstählen nach dem AOD-Verfahren. Techn. Mitt. Essen 70(2): 115–121.
53. Pastucha K, Spiess J, Dimitrinov S & Bruckner C (2007) Cost Optimization in the Production of Stainless and Special Steels in the AOD Converter by Using Oxidic Alloys. In: Proc. AISTech2007. Indianapolis, IN, USA.
54. Gorges H, Pulvermacher W, Rubens W & Dierstein H-A (1979) Einblasen von Nickeloxidsinter im AOD-Stahlwerk der Fried. Krupp Hüttenwerke AG, Bochum. Stahl Eisen 99(23): 1312–1314.
55. Mehlman SK (1991) Pneumatic Steelmaking: The AOD Process. Iron and Steel Society, Warrendale, Pennsylvania, USA.

56. Szekely J & El-Kaddah N (1984) Turbulence and Agitation in Ladle Metallurgical Operations. Iron Steelmaker 11(1): 22–29.
57. Szekely J, Evans JW & Brimacombe JK (1988) The Mathematical and Physical Modeling of Primary Metals Processing Operations. John Wiley & Sons, Inc., New York, USA.
58. Wei J-H, Zhu H-L, Chi H-B & Wang H-J (2010) Physical Modeling Study on Combined Side and Top Blowing AOD Refining Process of Stainless Steel: Fluid Mixing Characteristics in Bath. ISIJ Int. 50(1): 26–34.
59. Wuppermann C, Rückert A, Pfeifer H, Odenthal H-J, Reifferscheid M & Hovestädt E (2011) Numerical study of improvements of the flow simulation and the vessel vibration in the AOD-process. In: Proc. 4th International Conference on Modelling and Simulation of Metallurgical Processes in Steelmaking. Stahlinstitut VDEh, Düsseldorf, Germany.
60. Wuppermann C, Pfeifer H, Odenthal H-J, Jipnang E, Hovestädt E & Schlüter J (2012) Oscillation Phenomena during the AOD process. Stahl Eisen 132(6): 39–50.
61. Wuppermann C, Rückert A, Pfeifer H & Odenthal H-J (2013) Physical and Mathematical Modeling of the Vessel Oscillation in the AOD Process. ISIJ Int. 53(3): 441–449.
62. Odenthal H-J, Thiedemann U, Falkenreck U & Schlueter J (2010) Simulation of Fluid Flow and Oscillation of the Argon Oxygen Decarburization (AOD) Process. Metall. Mater. Trans. B 41(2): 396–413.
63. Aigner A, Pirker S & Wimmer G (2011) Modelling flow induced AOD-converter sloshing by analytical considerations, numerical simulation and cold water experiments. In: Proc. 4th International Conference on Modelling and Simulation of Metallurgical Processes in Steelmaking. Stahlinstitut VDEh, Düsseldorf, Germany.
64. Wimmer G & Voraberger B (2015) New damper system for reduction of AOD vibrations. In: Proc. 2nd European Steel Technology and Application Days. Steel Institute VDEh, Düsseldorf, Germany.
65. Fabritius TMJ, Mure PT & Härkki JJ (2003) The Determination of the Minimum and Operational Gas Flow Rates for Sidewall Blowing in the AOD-Converter. ISIJ Int. 43(8): 1177–1184.
66. Fabritius TMJ (2004) Modelling of combined blowing in steelmaking converters by physical models. Doctoral thesis, University of Oulu, Oulu, Finland.
67. Fabritius TMJ, Kurkinen PT, Mure PT & Härkki JJ (2005) Vibration of argon-oxygen decarburisation vessel during gas injection. Ironmaking Steelmaking 32(2): 113–119.
68. Shimizu K (2001) Wear of Refractories for AOD Furnace. J. Tech. Assoc. Refract. Jpn. 21(4): 258–263.
69. Oberbach M & Schmeiduch G (1997) Zustellung von Öfen und Pfannen. In: Heinen KH (ed.) Elektrostahl-Erzeugung, pp. 151–193. Verlag Stahleisen GmbH, Düsseldorf, Germany.
70. Leach JCC, Rodgers A & Sheehan G (1978) Operation of the AOD process in BSC. Ironmaking Steelmaking 5(3): 107–120.
71. Fabritius T, Vatanen J, Alamäki P & Härkki J (2000) Effect of sidewall blowing to the wear of the refractory lining in AOD. In: Proc. 6th Japan – Nordic Countries Steel Symposium, pp. 114–121. Iron and Steel Institute of Japan, Nagoya, Japan.
72. Koch K, Münchberg W, Stradtmann J, Niederau H-J & von der Crone G (2001) Optimierung der Blasbedingungen bei der Erzeugung hochchromhaltiger Stähle in einem bodenblasenden 10-t-AOD-Konverter. Stahl Eisen 121(11): 41–49.
73. Delhaes C, Hauck A & Neuschütz D (1993) Mechanisms of dust generation in a stainless steelmaking converter. Steel Res. 64(1): 22–27.

74. Zhan D-P, Zhang Y-P, Jiang Z-H, Wang D-W & Zhang H-S (2016) Chromium Recycling from Argon-oxygen Decarburization Dust in Hot Metal Pre-dephosphorization Process. J. Iron Steel Res. Int. 23(9): 867–873.
75. Song Z, Ersson M & Jönsson P (2014) A Study of Post-Combustion in an AOD Flue. Steel Res. Int. 85(7): 1173–1184.
76. Song Z (2013) Modeling of Gas flows in Steelmaking Decarburization Processes. Doctoral thesis, Royal Institute of Technology, Stockholm, Sweden.
77. Tang Y, Fabritius T & Härkki J (2004) Modelling of Nitrogen Intrusion into an AOD Converter at the Reduction Stage Caused by Suction Oscillation in the Ventilation Hood. Steel Res. Int. 75(6): 373–381.
78. Tang Y, Fabritius T & Härkki J (2005) Mathematical modeling of the argon oxygen decarburization converter exhaust gas system at the reduction stage. Appl. Math. Model. 29(5): 497–514.
79. Tilliander A, Jönsson PG & Jonsson L (2000) Effect of Ar/O_2 gas mixtures on heat-transfer and fluid-flow characteristics in AOD nozzles. Steel Res. 71(11): 429–434.
80. Staudinger G & Dimitrov S (2007) Latest Design Aspects of the AOD Steelmaking Converter. In: Proc. AISTech2007. Indianapolis, IN, USA.
81. Figueira RM & Szekely J (1985) Turbulent Fluid Flow Phenomena in a Water Model of an AOD System. Metall. Trans. B 16(1): 67–75.
82. Masterson IF (1986) Fluid dynamics and mixing time studies for AOD steelmaking using a water model. In: Proc. 5th International Iron and Steel Congress, volume 6, pp. 377–383. The Iron and Steel Society, Inc., Washington, DC, USA.
83. Povolotsky DY, Tokovoy OK & Zyryanov SV (1993) Physical Modeling of Hydrodynamic Effects in Argon-Oxygen Decarburization of Steel. Russ. Metall. (1): 20–24.
84. Zhu M-Y, Sawada I & Iguchi M (1998) Physical Characteristics of a Horizontally Injected Gas Jet and Turbulent Flow in Metallurgical Vessels. ISIJ Int. 38(5): 411–420.
85. Wei J-H, Ma J-C, Fan Y-Y, Yu N-W, Yang S-L, Xiang S-H & Zhu D-P (1999) Water modelling study of fluid flow and mixing characteristics in bath during AOD process. Ironmaking Steelmaking 26(5): 363–371.
86. Wei J-H, Ma J-C, Fan Y-Y, Yu N-W, Yang S-L & Xiang S-H (1999) Back-attack Phenomena of Gas Jets with Submerged Horizontally Blowing and Effects on Erosion and Wear of Refractory Lining. ISIJ Int. 39(8): 779–786.
87. Wei J-H, Xiang S-H, Fan Y-Y, Yu N-W, Ma J-C & Yang S-L (2000) Design and calculation of gas property parameters for constant area lance under conditions of friction flow with heating. Ironmaking Steelmaking 27(4): 294–301.
88. Tilliander A, Jonsson TLI & Jönsson PG (2001) A Mathematical Model of the Heat Transfer and Fluid Flow in AOD Nozzles and its Use to Study the Conditions at the Gas/Steel Interface. ISIJ Int. 41(10): 1156–1164.
89. Fabritius TMJ, Mure PT, Kupari PA, Juntunen VA & Härkki JJ (2001) Combined blowing with three - hole lance in a sidewall blowing converter. Steel Res. 72: 237–244.
90. Tilliander A, Jönsson PG, Jonsson TLI & Lille S (2000) An Experimental and Numerical Study of Fluid Flow in AOD Nozzles. Iron Steelmaker 29(2): 51–57.
91. Tilliander A, Jonsson TLI & Jönsson PG (2004) Fundamental Mathematical Modeling of Gas Injection in AOD Converters. ISIJ Int. 44(2): 326–333.
92. Bjurström M, Tilliander A, Iguchi M & Jönsson P (2006) Physical-modeling Study of Fluid Flow and Gas Penetration in a Side-blown AOD Converter. ISIJ Int. 46(4): 523–529.

93. Wei J-H & Zuo H-Y (2007) Study on Mass Transfer Characteristics in an AOD Converter Bath under Conditions of Combined Side and Top Blowing. Steel Res. Int. 78(12): 863–875.
94. Ternstedt P, Tilliander A, Jönsson PG & Iguchi M (2010) Mixing Time in a Side-Blown Converter. ISIJ Int. 50(5): 663–667.
95. Wei J-H, Zhu H-L, Chi H-B & Wang H-J (2010) Physical Modeling Study on Combined Side and Top Blowing AOD Refining Process of Stainless Steel: Gas Stirring and Fluid Flow Characteristics in Bath. ISIJ Int. 50(1): 17–25.
96. Wei J-H, Zhu H-L, Jiang Q-Y, Shi G-M, Chi H-B & Wang H-J (2010) Physical Modeling Study on Combined Side and Top Blowing AOD Refining Process of Stainless Steel: Back-attack Phenomenon of Gas Streams with Horizontal Side Blowing and Its Influence on Erosion and Wear of Refractory Lining. ISIJ Int. 50(10): 1347–1356.
97. Wei J-H, He Y & Shi G-M (2011) Mathematical Modeling of Fluid Flow in Bath during Combined Side and Top Blowing AOD Refining Process of Stainless Steel: Mathematical Model of the Fluid Flow. Steel Res. Int. 82(6): 703–709.
98. Wei J-H, He Y & Shi G-M (2011) Mathematical Modeling of Fluid Flow in Bath during Combined Side and Top Blowing AOD Refining Process of Stainless Steel: Application of the Model and Results. Steel Res. Int. 82(6): 693–702.
99. Wuppermann C, Giesselmann N, Rückert A, Pfeifer H, Odenthal H-J & Hovestädt E (2012) A Novel Approach to Determine the Mixing Time in a Water Model of an AOD Converter. ISIJ Int. 52(10): 1817–1823.
100. Wuppermann CF (2013) Mathematische Modellierung der fluidinduzierten Behälterschwingung beim AOD-Prozess. Doctoral thesis, Rheinisch-Westfälische Technische Hochschule Aachen, Aachen, Germany.
101. Tilliander A, Jonsson LTI & Jönsson PG (2014) A Three-Dimensional Three-Phase Model of Gas Injection in AOD Converters. Steel Res. Int. 85(3): 376–387.
102. Haas T, Visuri V-V, Isohookana E, Kärnä A, Sulasalmi P, Eriç RH, Pfeifer H & Fabritius T (2016) Physical Modelling of the Effect of Top Slag on Mixing in the AOD Process. In: Reddy RG, Chaubal P, Pistorius PC & Pal U (eds.) Proc. 10th International Conference on Molten Slags, Fluxes, and Salts, pp. 999–1008. The Minerals, Metals and Materials Society, Seattle, WA, USA.
103. Visuri V-V, Isohookana E, Kärnä A, Haas T, Eriç RH & Fabritius T (2016) A Physical Modelling Study of Mixing in an AOD Vessel. In: Proc. 5th International Conference on Process Development in Iron and Steelmaking. Swerea MEFOS, Luleå, Sweden.
104. Samuelsson P, Ternstedt P, Tilliander A, Appell A & Jönsson PG (2017) Use of physical modelling to study how to increase the production capacity by implementing a novel oblong AOD converter. Ironmaking Steelmaking, DOI 10.1080/03019233.2016.1265785.
105. Zhou X, Ersson M, Zhong L & Jönsson PG (2015) Numerical and Physical Simulations of a Combined Top-Bottom-Side Blown Converter. Steel. Res. Int. 85(11): 1328–1338.
106. Hoefele EO & Brimacombe JK (1979) Flow Regimes in Submerged Gas Injection. Metall. Trans. B 10(4): 631–648.
107. Aukrust E, Koros PJ & Meyer HW (1966) Process chemistry of basic oxygen stainless steelmaking. J. Met. 18(4): 433–439.
108. Gorges H, Pulvermacher W, Rubens W & Dierstein H-A (1978) Development and advantages of top blowing in combination with the AOD-process at Fried. Krupp Hüttenwerke AG. In: Proc. 3rd International Iron and Steel Congress, pp. 161–167. ASM International, Materials Park, OH, USA.

109. Gorges H, Pulvermacher W, Rubens W & Dierstein H-A (1979) Vorfrischen mit einer Aufblaslanze im AOD-Konverter der Fried. Krupp Hüttenwerke AG, Bochum. Stahl Eisen 99(23): 1310–1312.
110. Otani N, Shibata M, Asaho R, Hamada S, Yaji M & Kato Y (1983) Production of Stainless Steel by Top-and-Bottom-Blown Converter. Kawasaki Steel Tech. Rep. (8): 47–55.
111. Tohge T, Fujita Y & Watanabe T (1984) Some consideration on high blow rate AOD practice with top blowing system. In: 4th Process Technology Conference, pp. 129–136. Iron & Steel Society of AIME, Chicago, USA.
112. Anonymous (1987) Improved AOD Process by Adopting High Blow Rate Tuyere Practice together with Top Blowing. Trans. Iron Steel Inst. Jpn. 27(3): 241.
113. Courant R & Friedrichs KO (1976) Supersonic Flow and Shock Waves, volume 21 of *Applied Mathematical Sciences*. Springer Verlag, New York, NY, USA.
114. Odenthal H-J, Falkenreck U & Schlüter J (2006) CFD Simulation of Multiphase Melt Flows in Steelmaking Converters. In: Proc. European Conference on Computational Fluid Dynamics. Egmond aan Zee, The Netherlands.
115. Geiger GH & Poirier DR (1973) Transport Phenomena in Metallurgy. Addison-Wesley Publishing Company, Reading, MA, USA.
116. Szekely J & Themelis NJ (1971) Rate Phenomena in Process Metallurgy. John Wiley & Sons, Inc., New York, NY, USA.
117. Lange KW (1982) Physikalische und chemische Einflüsse beim Stoffübergang im Sauerstoffaufblasverfahren. In: Forschungsberichte des Landes Nordrhein-Westfalen, 3088. Westdeutscher Verlag, Opladen, Germany.
118. Song Z, Ersson M & Jönsson P (2011) Mathematical Modeling of VOD Oxygen Nozzle Jets. Steel Res. Int. 82(3): 249–259.
119. Song Z, Ersson M & Jönsson PG (2011) Mathematical Comparison of Two VOD Nozzle Jets. ISIJ Int. 51(10): 1637–1646.
120. Li Z-L, Zhang L-L & Cang D-Q (2017) Temperature Corrected Turbulence Model for Supersonic Oxygen Jet at High Ambient Temperature. ISIJ Int. 57(4): 602–608.
121. Odenthal H-J, Kempken J, Schlüter J & Emling WH (2007) Advantageous Numerical Simulation of the Converter Blowing Process. Iron Steel Technol. 4(11): 71–89.
122. Odenthal H-J, Schlüter J, Lachmund H & Bruckhaus R (2013) Verbesserte Blas- und Spülbedingungen im BOF-Prozess. Stahl Eisen 133(9): 43–59.
123. Odenthal H-J, Schlüter J & Uebber N (2014) Recent SMS Siemag Developments in BOF Steelmaking. In: Proc. 7th European Oxygen Steelmaking Conference. Czech Metallurgical Society, Třinec, Czech Republic.
124. Kärnä A, Järvinen M & Fabritius T (2013) Supersonic Lance Mass Transfer Modelling. Mater. Sci. Forum 762: 686–690.
125. Anderson AR & Johns FR (1955) Characteristics of Free Supersonic Jets Exhausting into Quiescent Air. Jet Propulsion 25(1): 13–15.
126. Deo B & Boom R (1993) Fundamentals of Steelmaking Metallurgy. Prentice Hall International, Hertfordshire, United Kingdom.
127. Inada S & Watanabe T (1977) Influence of Pressure in Surrounding Atmosphere on the Cavity Formation by Gas Jet. Tetsu-to-Hagané 63(6): 909–916.
128. Guthrie RIL, Isac M & Lin Z-H (2005) Fluid dynamics simulation of chromium recovery from AOD slags during reduction with ferrosilicon additions. Ironmaking Steelmaking 32(2): 133–140.

129. Office of Technology Assessment (1980) Technology and Steel Industry Competitiveness. Technical report, Washington, D.C., USA.
130. Li D, Chi H & Wei J (2008) The Applications of the Top and Side Combined Blowing in the AOD of Baosteel. In: Proc. AISTech2008. Association for Iron & Steel Technology, Pittsburgh, PA, USA.
131. Li D, Chi H & Shao S (2007) The Analysis of the Blowing Process with the Top Lance of the Argon Oxygen Decarburization (AOD) in Baosteel. Mater. Sci. Forum 561-565: 1039–1042.
132. Neuschütz D, Hauck A & Delhaes C (1996) Thermodynamische und kinetische Grundlagen der Entstehung und Verarbeitung von Rostfreistäuben. Abschlußbericht EUR 15594 DE, Amt für amtliche Veröffentlichungen der Europäischen Gemeinschaften, Luxembourg.
133. Stebner G, Ehrenputsch L, Moggee H, Stolz J, Maas J, Pastucha K, Vaillancourt D & Burzic D (2016) Performance of the new stainless steel melt shop of Outokumpu in the USA. Stahl Eisen 136(1): 37–43.
134. Scheller PR & Wahlers F-J (1996) Reaction Areas during Combined Blowing in the AOD-converter. ISIJ Int. 36(Supplement): S69–S72.
135. Patra S, Nayak J, Singhal LK & Pal S (2017) Prediction of Nitrogen Content of Steel Melt during Stainless Steel Making Using AOD Converter. Steel Res. Int. 88(5): 1–14.
136. Visuri V-V, Järvinen M, Kärnä A, Sulasalmi P, Heikkinen E-P, Kupari P & Fabritius T (2017) A Mathematical Model for Reactions During Top-Blowing in the AOD Process: Validation and Results. Metall. Mater. Trans. B 48(3): 1868–1884.
137. Zhu H-L, Wei J-H, Shi G-M, Shu J-G, Jiang Q-Y & Chi H-B (2007) Preliminary Investigation of Mathematical Modeling of Stainless Steelmaking in an AOD Converter: Mathematical Model of the Process. Steel Res. Int. 78(4): 305–310.
138. Riipi J, Fabritius T, Heikkinen E-P, Kupari P & Kärnä A (2009) Behaviour of Nitrogen During AOD Process. ISIJ Int. 49(10): 1068–1473.
139. Wijk O & Sjöberg P (1992) Reaction Model for Decarburization of Molten High-Chromium Steels in Converters. In: Proc. 6th International Conference on Refining Processes, pp. 5–26. MEFOS, Luleå, Sweden.
140. Hack K (2008) Thermochemical conditions for the production of low-carbon stainless steels. In: Hack K (ed.) The SGTE casebook - Thermodynamics at work, pp. 155–160. CRC Press, Boca Raton, FL, USA, second edition.
141. Schürmann E & Rosenbach K (1973) Herstellung von niedriggekohlten, nichtrostenden austenitischen Chrom-Nickel-Stählen nach dem Argon-Sauerstoff-Entkohlungsverfahren. Arch. Eisenhüttenwes. 44(10): 761–768.
142. Dierstein H-A (1978) Untersuchung der Kinetik des Entkohlungsvorganges in chrom- und nickelhaltigen Eisenschmelzen beim Durchblasen eines Gasgemisches aus Sauerstoff und Inertgas. Doctoral thesis, Rheinisch-Westfälische Technische Hochschule Aachen, Aachen, Germany.
143. Fruehan RJ (1976) Reaction Model for the AOD Process. Ironmaking Steelmaking 3(3): 153–158.
144. Shi G-M, Wei J-H, Zhu H-L, Shu J-H, Jiang Q-Y & Chi H-B (2007) Preliminary Investigation of Mathematical Modeling of Stainless Steelmaking in and AOD Converter: Application of the Model and Results. Steel Res. Int. 78(4): 311–317.
145. Swinbourne DR, Kho TS, Blanpain B, Arnout S & Langberg DE (2012) Understanding stainless steelmaking through computational thermodynamics: Part 3 - AOD converting.

Trans. Inst. Min. Metall. C 121(1): 23–31.
146. Brunner M (1998) Improved gas blowing program in AOD stainless steelmaking. Scand. J. Metall. 27: 37–43.
147. Kupari P & Hooli P (1999) Nitrogen Control in AOD Converter. Mater. Sci. Forum 318-320: 385–394.
148. Jiang Z, Li H, Chen Z, Huang Z, Zou D & Liang L (2005) The Nitrogen Solubility in Molten Stainless Steel. Steel Res. Int. 76(10): 740–745.
149. Gaye H, Huin D & Riboud PV (2000) Nitrogen Alloying of Carbon and Stainless Steels by Gas Injection. Metall. Mater. Trans. B 31(5): 905–912.
150. Kobayashi Y, Todoroki H & Shiga N (2014) Behaviour of nitrogen dissolution in Fe–Cr–Ni–Mo system stainless steels. Ironmaking Steelmaking 41(6): 459–463.
151. Small WM & Pehlke RD (1968) The Effect of Alloying Elements on the Solubility of Nitrogen in Liquid Iron-Chromium-Nickel Alloys. Trans. Metall. Soc. AIME 242(12): 2501–2505.
152. Ono H, Iuchi K, Morita K & Sano N (1996) Effects of Oxygen and Nitrogen on the Rate of Nitrogen Dissolution in Iron–Chromium and Iron–Vanadium Alloys. ISIJ Int. 36(10): 1245–1249.
153. Rao YK & Cho WD (1990) Rate of nitrogen absorption in molten iron–chromium alloys: Part 2 Mathematical model. Ironmaking Steelmaking 17(4): 273–281.
154. Chen J-B, Chen Q-Z, Huang Z-Z, Hu J-Y, Sun Y-Q & Pan J-Q (2010) Nitrogen Desorption in Molten Stainless Steel During Immersion Argon Blowing. J. Iron Steel Res. Int. 17(5): 1–5.
155. Wu WP, Lange KW & Janke D (1995) Effect of surface active elements on nitrogen reaction with iron melts. Ironmaking Steelmaking 22(4): 303–309.
156. Rubens W (1989) Untersuchung der Schlackenwege und des Verschleißes der feuerfesten Ausmauerung beim modifizierten AOD-Verfahren zur Erzeugung nichtrostender Stähle. Doctoral thesis, Technische Universität Clausthal, Clausthal-Zellerfeld, Germany.
157. Koch K, Münchberg W, Zörcher H & Rubens W (1992) Zusammensetzung von Metallbad, Schlacken und Granalien beim modifizierten AOD-Verfahren. Stahl Eisen 112(9): 91–99.
158. Münchberg W, Koch K, Zörcher H & Rubens W (1992) Verschleiß der feuerfesten Ausmauerung und Kalkauflösung beim modifizierten AOD-Verfahren. Stahl Eisen 112(11): 49–58.
159. Görnerup M & Sjöberg P (1999) AOD/CLU process modelling: optimum mixed reductants addition. Ironmaking Steelmaking 26(1): 58–63.
160. Koch K & Janke D (1984) Schlacken in der Metallurgie. Verlag Stahleisen mbH, Düsseldorf, Germany.
161. Song HS, Byun SM, Min DJ, Yoon SK & Ahn SY (1992) Optimization of the AOD Process at POSCO. In: Proc. 1st International Chromium Steel and Alloys Congress, volume 2, pp. 89–95. The Southern African Institute of Mining and Metallurgy, Johannesburg, South Africa.
162. Li L, Cheng G, Hu B, Wang C-S & Qian G (2017) Effect of Cr_2O_3 on the properties of stainless steel refining slags and desulfurization. Metall. Res. Technol. 114(1).
163. Richardson FD & Fincham CJB (1954) Sulphur in Silicate and Aluminate Slags. J. Iron Steel Inst. 178(9): 4–15.
164. Fincham CJB & Richardson FD (1954) The behaviour of sulphur in silicate and aluminate melts. Proc. Royal Society of London A 223(1152): 40–62.

165. Sosinsky DJ & Sommerville ID (1986) The Composition and Temperature Dependence of the Sulphide Capacity of Metallurgical Slags. Metall. Trans. B 17(2): 331–337.
166. Young RW, Duffy JA, Hassall GJ & Xu Z (1992) Use of optical basicity concept for determining phosphorus and sulphur slag–metal partitions. Ironmaking Steelmaking 19(3): 201–219.
167. Shankar A, Görnerup M, Lahiri AK & Seetharaman S (2006) Sulphide Capacity of High Alumina Blast Furnace Slags. Metall. Mater. Trans. B 37(6): 941–947.
168. Taniguchi Y, Sano N & Seetharaman S (2009) Sulphide Capacities of CaO–Al_2O_3–SiO_2–MgO–MnO Slags in the Temperature Range 1 673–1 773 K. ISIJ Int. 49(2): 156–163.
169. Taniguchi Y, Wang L, Sano N & Seetharaman S (2012) Sulfide Capacities of CaO-Al_2O_3-SiO_2 Slags in the Temperature Range 1673 K to 1773 K (1400 °C to 1500 °C). Metall. Mater. Trans. B 43(3): 477–484.
170. Duffy JA & Ingram MD (1971) Establishment of an Optical Scale for Lewis Basicity in Inorganic Oxyacids, Molten Salts, and Glasses. J. Am. Chem. Soc. 93(24): 6448–6454.
171. Reddy RG & Blander M (1987) Modeling of sulfide capacities of silicate melts. Metall. Mater. Trans. B 18(3): 591–596.
172. Shi C-B, Yang X-M, Jiao J-S, Li C & Guo H-J (2010) A Sulphide Capacity Prediction Model of CaO–SiO_2–MgO–Al_2O_3 Ironmaking Slags Based on the Ion and Molecule Coexistence Theory. ISIJ Int. 50(10): 1362–1372.
173. Yang X-M, Shi C-B, Zhang M, Chai G-M & Wang F (2011) A Thermodynamic Model of Sulfur Distribution Ratio between CaO–SiO_2–MgO–FeO–MnO–Al_2O_3 Slags and Molten Steel during LF Refining Process Based on the Ion and Molecule Coexistence Theory. Metall. Mater. Trans. B 42(6): 1150–1180.
174. Nzotta MM, Nilsson R, Sichen D & Seetharaman S (1997) Sulphide capacities in MgO-SiO_2 and CaO-MgO-SiO_2 slags. Ironmaking Steelmaking 24(4): 300–305.
175. Nzotta MM, Sichen D & Seetharaman S (1998) Sulphide Capacities in Some Multi Component Slag Systems. ISIJ Int. 38(11): 1170–1179.
176. Nzotta MM, Sichen D & Seetharaman S (1999) Study of the sulfide capacities of iron-oxide containing slags. Metall. Mater. Trans. B 30(5): 909–920.
177. Nzotta MM, Sichen D & Seetharaman S (1999) Sulphide Capacities of "FeO"-SiO_2, CaO-"FeO", and "FeO"-MnO Slags. ISIJ Int. 37(7): 657–663.
178. Xiao X, Holappa L & Reuter MA (2002) Oxidation State and Activities of Chromium Oxides in CaO-SiO_2-CrO_x Slag System. Metall. Mater. Trans. B 33(4): 595–603.
179. Pei W & Wijk O (1994) Experimental study on the activity of chromium oxide in the CaO-SiO_2-Al_2O_3-MgO_{sat}-CrO_x slag. Scand. J. Metall. 23(5-6): 228–235.
180. Coudurier L, Hopkins DW & Wilkomirsky I (1978) Fundamentals of Metallurgical Processes. Pergamon Press, Oxford, United Kingdom.
181. Forsbacka L & Holappa L (2004) Viscosity of CaO–CrO_x–SiO_2 slags in a relatively high oxygen partial pressure atmosphere. Scand. J. Metall. 33(5): 261–268.
182. Mills KC (1995) Structure of liquid slags. In: Verein Deutscher Eisenhüttenleute (ed.) Slag Atlas 2nd Edition, pp. 1–8. Verlag Stahleisen GmbH, Düsseldorf, Germany.
183. Adegoloye G, Beaucour A-L, Ortola S & Noumowe A (2016) Mineralogical composition of EAF slag and stabilised AOD slag aggregates and dimensional stability of slag aggregate concretes. Constr. Build. Mater. 115(6): 171–178.
184. Ternstedt P, Runnsjö G & Lindstrand G (2008) Top slag influence on the decarburization in the AOD process. In: Proc. 3rd International Conference on Process Development in

Iron and Steelmaking, volume 1, pp. 149–153. Metallurgical Research Institute AB, Luleå, Sweden.
185. Lindstrand G, Jönsson PG & Tilliander A (2012) Studies of AOD production decarburisation slags. In: Proc. 4th International Conference on Process Development in Iron and Steelmaking, volume 2, pp. 481–490. Swerea MEFOS, Luleå, Sweden.
186. Pretorius EB & Nunnington RC (2002) Stainless steel slag fundamentals: from furnace to tundish. Ironmaking Steelmaking 29(2): 133–139.
187. Mills KC (1995) Viscosities of molten slags. In: Verein Deutscher Eisenhüttenleute (ed.) Slag Atlas 2nd Edition, pp. 349–399. Verlag Stahleisen GmbH, Düsseldorf, Germany.
188. Dziggel K (1997) Zuschläge, Schlackenbildner. In: Heinen KH (ed.) Elektrostahl-Erzeugung, pp. 105–111. Verlag Stahleisen GmbH, Düsseldorf, Germany.
189. Yang Q, Xu A, Engström F, Han F, Xue P, He D & Björkman B (2014) Dissolution Behavior of Fluorine from AOD Slag after Treatments for Volume Stabilization. Appl. Mech. Mater. 587-589: 849–855.
190. Yingdong Y & Edström JO (1992) Dephosphorization of Crude Stainless Steel Melts Under Oxidising Conditions Using Lime-based Slags Containing BaO. In: Proc. 6th International Conference on Refining Processes, pp. 49–71. MEFOS, Luleå, Sweden.
191. Asai S & Szekely J (1974) Decarburisation of stainless steel: Part I. A mathematical model for laboratory scale results. Metall. Trans. 5(3): 651–657.
192. Szekely J & Asai S (1974) Decarburisation of stainless steel: Part II. A mathematical model and a process optimization for industrial scale systems. Metall. Trans. 5(7): 1573–1580.
193. Ohno T & Nishida T (1977) Reaction Model for the AOD Process. Tetsu-to-Hagané 63(13): 2094–2099.
194. Jonsson L, Jönsson P, Seetharaman S & Sichen D (2000) Process Models for Ladle Refining – A Fundamental Approach. In: Proc. 6th Japan-Nordic Countries Joint Symposium. The Iron and Steel Institute of Japan, Nagoya, Japan.
195. Tilliander A, Ersson M, Jonsson L & Jönsson P (2008) Fundamental mathematical modeling of metallurgical processes – current and future situation. In: Proc. 3th International Conference on Process Development in Iron and Steelmaking, volume 1, pp. 333–346. Swerea MEFOS, Luleå, Sweden.
196. Ersson M & Tilliander A (2017) Review on CFD Simulation and Modeling of Decarburization Processes. Steel Res. Int., DOI: 10.1002/srin.201700108.
197. Meier T (2016) Modellierung und Simulation des Elektrolichtbogenofens. Doctoral thesis, Rheinisch-Westfälische Technische Hochschule Aachen, Aachen, Germany.
198. Wang H, Xu A, Al L, Tian N & Du X (2012) An Integrated CBR Model for Predicting Endpoint Temperature of Molten Steel in AOD. ISIJ Int. 52(1): 80–86.
199. Bale CW, Chartrand P, Degterov SA, Eriksson G, Hack K, Mahfoud RB, Melançon J, Pelton AD & Peterssen S (2002) Calphad 26(2): 189–228.
200. Outotec Oyj (2015). HSC Chemistry 8.
201. Davies RH, Dinsdale AT, Gisby JA, Robinson JAJ & Martin SM (2002) MTDATA – Thermodynamic and Phase Equilibrium Software from the National Physical Laboratory. Calphad 26(2): 229–271.
202. Chen S-L, Daniel S, Zhang F, Chang YA, Yan X-Y, Xie F-Y, Schmidt-Fetzer R & Oates WA (2002) The PANDAT software package and its applications. Calphad 26(2): 175–188.
203. Andersson J-O, Helander T, Höglund L, Shi P & Sundman B (2002) Thermo-Calc & DICTRA, Computational Tools for Materials Science. Calphad 26(2): 273–312.

204. Swinbourne DR, Kho TS, Langberg D, Blanpain B & Arnout S (2010) Understanding stainless steelmaking through computational thermodynamics Part 2 - VOD converting. Trans. Inst. Min. Metall. C 119(2): 107–115.
205. Wendelstorf J (2015) Prozessmodellierung in der Hochtemperaturverfahrenstechnik. Habilitation thesis, Technische Universität Clausthal, Clausthal-Zellerfeld, Germany.
206. Kruskopf A & Visuri V-V (2017) A Gibbs Energy Minimization Approach for Modeling of Chemical Reactions in a Basic Oxygen Furnace. Metall. Mater. Trans. B, DOI: 10.1007/s11663-017-1074-x.
207. Semin AE, Pavlenko AP, Andzhum T & Shuklina EA (1983) Mathematical modelling of argon-oxygen decarburization of steel. Steel USSR 13(3): 95–97.
208. Görnerup M (1997) Studies of Slag Metallurgy in Stainless Steelmaking. Doctoral thesis, Royal Institute of Technology, Stockholm, Sweden.
209. Sjöberg P (1994) Some aspects on the scrap based production of stainless steels. Doctoral thesis, Royal Institute of Technology, Stockholm, Sweden.
210. Kikuchi N, Yamaguchi K, Kishimoto Y, Takeuchi S & Nishikawa H (2002) Influence of Slag Composition and Stirring Energy by Top Blowing on the Decarburization Rate of Stainless Steel in Combined Blowing Converter. Tetsu-to-Hagané 88(8): 32–39.
211. Uchida Y, Kikuchi N, Yamaguchi K, Kishimoto Y, Takeuchi S & Nishikawa H (2004) New decarburization technology for high-chromium hot metal in combined blowing converter with nitrogen top blowing. In: Proc. 2nd International Conference on Process Development in Iron and Steelmaking, volume 2, pp. 69–78. MEFOS, Luleå, Sweden.
212. Kärnä A, Hekkala L, Fabritius T, Riipi J & Järvinen M (2008) CFD model for nitrogen transfer in AOD converter. In: Proc. 3rd International Conference on Process Development in Iron and Steelmaking, volume 1, pp. 155–162. Swerea MEFOS, Luleå, Sweden.
213. Andersson NÅI, Tilliander A, Jonsson LTI & Jönsson PG (2012) An in-Depth Model-Based Analysis of Decarburization in the AOD Process. Steel Res. Int. 83(11): 1039–1052.
214. Andersson NÅI, Tilliander A, Jonsson LTI & Jönsson PG (2013) A Fundamental Decarburisation Model of AOD Process. Ironmaking Steelmaking 40(5): 390–397.
215. Andersson NÅI, Tilliander A, Jonsson LTI & Jönsson PG (2013) Investigating the Effect of Slag on Decarburization in an AOD Converter Using a Fundamental Model. Steel Res. Int. 84(2): 169–177.
216. Andersson NÅI, Tilliander A, Jonsson LTI & Jönsson PG (2013) Preliminary investigation of influence of temperature on decarburisation using fundamental AOD model. Ironmaking Steelmaking 40(7): 551–558.
217. Andersson NÅI (2012) Coupling of Fundamental Mathematical Modeling of Fluid Flow with Computational Thermodynamics to Study Decarburization in an AOD Converter. Doctoral thesis, KTH Royal Institute of Technology, Stockholm, Sweden.
218. Ersson M, Höglund L, Tilliander A, Jonsson L & Jönsson P (2008) Dynamic Coupling of Computational Fluid Dynamics and Thermodynamics Software: Applied on a Top Blown Converter. ISIJ Int. 48(2): 147–153.
219. Nernst W (1904) Theorie der Reaktionsgeschwindigkeit in heterogenen Systemen. Z. physik. Chem. 47: 52–55.
220. Coley KS (2013) Progress in the Kinetics of Slag-Metal-Gas Reactions, Past, Present and Future. J. Min. Metall. Sect. B-Metall. 49(2): 191–199.
221. Watanabe T & Tohge T (1973) The Study on the Mechanism of Decarburization for Liquid Stainless Steel under Reduced Pressure. Tetsu-to-Hagané 59(9): 1224–1236.

222. Fruehan RJ (1975) Nitrogenation and Decarburization of Stainless Steel. Metall. Trans. B 6(4): 573–578.
223. Fruehan RJ (1977) Rate of Reduction of Cr_2O_3 by Carbon and Carbon Dissolved in Liquid Iron Alloys. Metall. Trans. B 8(2): 429–433.
224. Irving MR, Boland FM & Nicholson H (1979) Optimal control of the argon-oxygen decarburising steelmaking process. Proc. IEE 126(2): 198–202.
225. Deb Roy T & Robertson DGC (1978) A mathematical model for stainless steelmaking: Part 1 Argon-Oxygen-Steam Mixtures. Ironmaking Steelmaking 5(5): 198–206.
226. Higbie R (1935) The rate of absorption of pure gas into a still-liquid during short periods of exposure. Trans. Am. Inst. Chem. Eng. 31(3): 365–389.
227. Deb Roy T, Robertson DGC & Leach JCC (1978) A mathematical model for stainless steelmaking: Part 2 application to AOD heats. Ironmaking Steelmaking 5(5): 207–210.
228. Reichel J, Köhle S, Schubert K-H, Wahlers F-J & Zörcher H (1993) Beobachtung und Steuerung des Frischens hochchromhaltiger Stähle nach dem KCB-S-Verfahren. Stahl Eisen 113(9): 83–89.
229. Reichel J, May R, Hahn B & Schönewolf G (1994) Computer-aided management and control of a VOD process. Metall. Plant Technol. Int. (3): 82–87.
230. Kleimt B, Lichterbeck R, Angelis VD, Paolis GD, Rinaldi M, Sabatini G & Burkat C (2006) Improvement of process control and refractory performance of the AOD converter. Report EUR 21974, European Commission, Luxembourg.
231. Kleimt B, Lichterbeck R & Burkat C (2006) Improved Dynamic Control of Carbon and Nitrogen Content in AOD Converter Process for Stainless Steelmaking on the Basis of Thermodynamic Process Models. In: Proc. 5th European Oxygen Steelmaking Conference, pp. 511–518. Steel Institute VDEh, Aachen, Germany.
232. Kleimt B, Lichterbeck R & Burkat C (2007) Modellbasierte dynamische Steuerung des AOD-Prozesses. Stahl Eisen 127(1): 35–41.
233. Lewis WK & Whitman WG (1924) Principles of Gas Absorption. Ind. Eng. Chem. 16(12): 1215–1220.
234. Sulasalmi P, Kärnä A, Fabritius T & Savolainen J (2009) CFD Model for Emulsification of Slag into the Steel. ISIJ Int. 49(11): 1661–1667.
235. Sulasalmi P, Visuri V-V & Fabritius T (2013) Effect of Interfacial Tension on the Emulsification – Considerations on the CFD Modelling of Dispersion. Mater. Sci. Forum 762: 242–247.
236. Sulasalmi P, Visuri V-V, Kärnä A & Fabritius T (2015) Simulation of the effect of steel flow velocity on the slag droplet distribution and interfacial area between steel and slag. Steel Res. Int. 86(3): 212–222.
237. Ternstedt P, Gyllenram R, Bengtsson J & Jönsson PG (2011) Using an AOD simulator workbench to support process control development. In: Proc. 4th International Conference on Modelling and Simulation of Metallurgical Processes in Steelmaking. Stahlinstitut VDEh, Düsseldorf, Germany.
238. Engholm M & Rick C-J (2011) Refining in AOD at high productivity with low environmental impact. In: Proc. 6th European Oxygen Steelmaking Conference. Jernkontoret, Stockholm, Sweden.
239. Wei J-H & Zhu D-P (2002) Mathematical Modeling of the Argon-Oxygen Decarburization Refining Process of Stainless Steel: Part II. Application of the Model to Industrial Practice. Metall. Mater. Trans. B 33(2): 121–127.

240. Wei J-H (1989) Oxidation of Alloying Elements during ESR of Stainless Steel. Chin. J. Met. Sci. Technol. 5: 235–246.
241. Wei J-H, Shu J-H, Zhu H-L, Shi G-M, Jiang Q-Y & Chi H-B (2006) Preliminary study on mathematical modelling of stainless steelmaking in aod converter. In: Proc. 5th European Oxygen Steelmaking Conference, pp. 440–453. Aachen, Germany.
242. Xiao X-G & Xie Y-G (1997) Basis of Metallurgical Reaction Engineering (in Chinese). Metallurgical Industry Press, Beijing, China.
243. Cai Z-P, Liang Y & Zhang C-X (2001) Experimental Investigation of Chemical and Metallurgical Models and Their Test Techniques (in Chinese). Metallurgical Industry Press, Beijing, China.
244. Baird MHI & Davidson JF (1962) Gas absorption by large rising bubbles. Chem. Eng. Sci. 17(2): 87–93.
245. Wei J-H, Cao Y, Zhu H-L & Chi H-B (2011) Mathematical Modeling Study on Combined Side and Top Blowing AOD Refining Process of Stainless Steel. ISIJ Int. 51(3): 365–374.
246. Chen J, Chen Z, Jiang Z & Huang Z (2006) Study on mathematical modeling for aod converter with top oxygen blowing. In: Proc. 5th European Oxygen Steelmaking Conference. Steel Institute VDEh, Aachen, Germany.
247. Chen Z-P (2007) Kinetic Model of Nitrogen during AOD Refining Process of Stainless Steel. In: Proc. AISTech2007. Indianapolis, IN, USA.
248. Ban-Ya S, Ishii F, Iguchi Y & Nagasaka T (1988) Rate of nitrogen desorption from liquid iron-carbon and iron-chromium alloys with argon. Metall. Trans. B 19(2): 233–242.
249. Järvinen MP, Kärna A & Fabritius T (2009) A Detailed Single Bubble Reaction Sub-Model for AOD Process. Steel Res. Int. 80(6): 429–436.
250. Wang H, Viswanathan NN, Ballal NB & Seetharaman S (2010) Modelling of Physico-Chemical Phenomena between Gas inside a Bubble and Liquid Metal during Injection of Oxidant Gas. Int. J. Chem. React. Eng. 8(1): 1–18.
251. Wang H, Viswanathan NN, Ballal NB & Seetharaman S (2009) Modeling of Reactions between Gas Bubble and Molten Metal Bath – Experimental Validation in the Case of Decarburization of Fe-Cr-C melts. High Temp. Mater. Proc. 28(6): 407–419.
252. Ranz WE & Marschall WR (1952) Evaporation from drops: Part I. Chem. Eng. Prog. 48(3): 141–146.
253. Ranz WE & Marschall WR (1952) Evaporation from drops: Part II. Chem. Eng. Prog. 48(4): 173–180.
254. Pelton AD & Bale CW (1986) A Modified Interaction Parameter Formalism for Non-Dilute Solutions. Metall. Trans. A 17(7): 1211–1215.
255. Järvinen M, Pisilä S, Kärnä A, Visuri V-V, Fabritius T, Ikäheimonen T & Kupari P (2011) Fundamental Mathematical Modelling of AOD Process. In: Proc. 4th International Conference on Modelling and Simulation of Metallurgical Processes in Steelmaking. Stahlinstitut VDEh, Düsseldorf, Germany.
256. Visuri V-V, Heikkinen E-P, Järvinen M, Kupari P & Fabritius T (2012) Phenomena-based model in AOD process improvement. In: Proc. 4th International Conference on Process Development in Iron and Steelmaking, volume 1, pp. 225–235. Swerea MEFOS, Luleå, Sweden.
257. Mazumdar D & Evans JW (2010) Modelling of Steelmaking Processes. CRC Press, Boca Raton, FL, USA.
258. Deo B & Srivastava V (2003) Process Control and Optimization of the AOD Process Using

Genetic Algorithm. Mater. Manuf. Process. 18(3): 401–408.
259. Deo B & Kumar S (2013) Dynamic On-line control of stainless steelmaking in AOD. Adv. Mat. Res. 794: 50–62.
260. Ma A, Mostaghel S & Chattopadhyay K (2017) Review of applicable desulphurization models for crude ferronickel refining. Trans. Inst. Min. Metall. C, pp. 1–21. http://dx.doi.org/10.1080/03719553.2016.1275449.
261. Teng X, Zhu M, Chen Z & Huang Z (2003) Mathematical Modeling of AOD-VOD Refining Process for Stainless Steelmaking I: Mathmatical Model of Process. In: China Iron and Steel Annual Conference Proceedings, pp. 692–698. Beijing, China.
262. Visuri V-V, Järvinen M, Sulasalmi P, Heikkinen E-P, Savolainen J & Fabritius T (2013) A Mathematical Model for the Reduction Stage of the AOD Process. Part I: Derivation of the Model. ISIJ Int. 53(4): 603–612.
263. Visuri V-V, Järvinen M, Savolainen J, Sulasalmi P, Heikkinen E-P & Fabritius T (2013) A Mathematical Model for the Reduction Stage of the AOD Process. Part II: Model Validation and Results. ISIJ Int. 53(4): 613–621.
264. Visuri V-V, Järvinen M, Kärnä A, Sulasalmi P, Heikkinen E-P, Kupari P & Fabritius T (2017) A Mathematical Model for Reactions During Top-Blowing in the AOD Process: Derivation of the Model. Metall. Mater. Trans. B 48(3): 1850–1867.
265. Mäkelä M, Soininen L, Tuomola S & Öistämö J (2015) Tekniikan kaavasto – Matematiikan, fysiikan, kemian ja lujuusopin peruskaavoja sekä SI-järjestelmä. Tammertekniikka, Tampere, Finland, 14. edition.
266. Kitamura S (2010) Importance of Kinetic Models in the Analysis of Steelmaking Reactions. Steel Res. Int. 81(9): 766–771.
267. Friedrichs HA (1974) Möglichkeiten der quantitativen Beschreibung metallurgischer Prozesse. Stahl Eisen 94(8): 315–325.
268. Bird RB, Stewart WE & Lightfoot EN (1960) Transport Phenomena. John Wiley & Sons, Inc., Singapore.
269. Oeters F (1985) Kinetic treatment of chemical reactions in emulsion metallurgy. Steel Res. 56(2): 69–74.
270. Oeters F (1989) Kinetik der Prozeßschritte bei der Stahlherstellung. Steel Res. 60(11): 485–495.
271. Schenk H, Steinmetz E & Frohberg MG (1963) Ableitungen zum Ausmaß chemischer Umsetzungen zwischen flüssigen Phasen in ruhendem und bewegtem Zustand. Arch. Eisenhüttenwes. 34(9): 659–672.
272. Schenk H (1964) Der Einfluß der Verfahrensweise auf den betriebstechnischen Wirkungsgrad der Reaktionen zwischen zwei Phasen, insbesondere Schlacke und Metall. Stahl Eisen 84(6): 311–326.
273. Steinmetz E (1968) Beitrag zur Behandlung des Stoffübergangs zwischen bewegten und ruhenden Phasen bei metallurgischen Prozessen. Arch. Eisenhüttenwes. 39(6): 421–432.
274. Rout BK, Singh OP & Mazumdar D (2015) Swirling Flows in Side Blowing Reactors and Possible Advantages. Trans. Indian Inst. Met. 68(5): 669–673.
275. Wei J-H, Zhu H-L, Yan S-L, Wang X-C, Ma J-C, Shi G-M, Jiang Q-Y, Chi H-B, Chi L-B, Che L-B & Zhang K (2005) Preliminary Investigation of Fluid Mixing Characteristics during Side and Top Combined Blowing AOD Refining Process of Stainless Steel. Steel Res. Int 76(5).
276. Zhou X, Ersson M, Zhong L, Yu J & Jönsson P (2014) Mathematical and Physical Simulation

of a Top Blown Converter. Steel Res. Int. 85(2): 273–281.
277. Reichel J & Rose L (2011) SMS Siemag – Innovations in Converter Process Measurement and Control. In: Proc. 6th European Oxygen Steelmaking Conference. Stockholm, Sweden.
278. Liu H, Qi Z & Xu M (2011) Numerical Simulation of Fluid Flow and Interfacial Behavior in Three-phase Argon-Stirred Ladles with One Plug and Dual Plugs. Steel Res. Int. 82(4): 440–458.
279. Incropera FP, Dewitt DP, Bergman TL & Lavine AS (2013) Principles of Heat and Mass Transfer. Seventh Edition. John Wiley & Sons Singapore Pte. Ltd., Singapore.
280. Koria SC & Lange KW (1984) A New Approach to Investigate the Drop Size Distribution in Basic Oxygen Steelmaking. Metall. Trans. B 15(1): 109–116.
281. Koria SC & Lange KW (1986) Estimation of drop sizes in impinging jet steelmaking. Ironmaking Steelmaking 13(5): 236–240.
282. Feiterna A, Huin D, Oeters F, Riboud P-V & Roth J-L (2000) Iron drop ejection into slags by bursting gas bubbles. Steel Res. 71(3): 61–69.
283. Visuri V-V & Sulasalmi P (2016) Hot metal desulphurisation simulator. In: DIMECC 9th Annual Seminar. DIMECC Oy, Helsinki, Finland. Poster presentation on November 14, 2016.
284. Xie Y, Orsten S & Oeters F (1992) Behaviour of Bubbles at Gas Blowing into Liquid Wood's Metal. ISIJ Int. 32(1): 66–75.
285. Oeters F, Strohmenger P & Pluschkell W (1973) Kinetik der Entschwefelung von Roheisenschmelzen mit Kalk und Erdgas. Arch. Eisenhüttenwes. 44(10): 727–733.
286. Crank J (1956) The Mathematics of Diffusion. Oxford University Press, Oxford, United Kingdom.
287. Davies JT (1972) Turbulence Phenomena. An Introduction to the Eddy Transfer of Momentum, Mass, and Heat, Particularly at Interfaces. Academic Press, Inc., New York, NY, USA.
288. Clift R, Grace JR & Weber ME (1978) Bubbles, Drops, and Particles. Academic Press, Inc., New York, NY, USA.
289. Danckwerts PV (1951) Significance of Liquid-Film Coefficients in Gas Absorption. Ind. Eng. Chem 43(6): 1460–1467.
290. Levich VG (1962) Physicochemical hydrodynamics. Prentice-Hall, Englewood Cliffs, NJ, USA.
291. Martin H (1977) Heat and Mass Transfer between Impinging Gas Jets and Solid Surfaces. Adv. Heat Transfer 13: 1–60.
292. Hrycak P (1983) Heat transfer from round impinging jets to a flat plate. Int. J. Heat Mass Transfer 26(12): 1857–1865.
293. Hofmann HM, Kind M & Martin H (2007) Measurements on steady state heat transfer and flow structure and new correlations for heat and mass transfer in submerged impinging jets. Int. J. Heat Mass Transfer 50(9): 3957–3965.
294. Wakelin DH (1966) The interaction between gas jets and the surfaces of liquids, including molten metals. Doctoral thesis, Imperial College, University of London, London, United Kingdom.
295. Davenport WG, Wakelin DH & Bradshaw AV (1966) Interaction of both Bubbles and Jets with Liquids. In: Proc. Symposium on Heat and Mass Transfer in Process Metallurgy, pp. 207–244. The Institution of Mining and Metallurgy, London, United Kingdom.
296. Lohe H (1966) Zum Wärme- und Stoffaustausch beim senkrechten Aufblasen von

Gasstrahlen auf Flüssigkeitsoberflächen. Chemie-Ing.-Techn. 38(3): 309–314.
297. Lohe H (1967) Wärme- und Stofftransport beim Aufblasen von Gasstrahlen auf Flüssigkeiten. Fortschr.-Ber. VDI-Z. 3(15): 1–59.
298. Löscher W (1970) Über die Entkohlung von schlackenfreien, kohlenstoffreichen Eisenschmelzen mittels aufgeblasenen Kohlendioxids. Hoesch Ber. Forsch. Entwickl. unserer Werke 5(2): 43–52.
299. Chatterjee A, Wakelin DH & Bradshaw AV (1972) Mass Transfer From an Oxygen Jet to Liquid Silver. Metall. Trans. 3(12): 3167–3172.
300. Chatterjee A & Bradshaw AV (1972) Break-up of a liquid surface by an impinging gas jet. J. Iron Steel Inst. 210(3): 179–187.
301. Chatterjee A & Bradshaw AV (1972) Die Wechselwirkung zwischen Gasstrahlen und Flüssigkeiten einschließlich flüssiger Metalle. In: Dahl W, Lange KW & Papamantellos D (eds.) Kinetik metallurgischer Vorgänge bei der Stahlherstellung, pp. 328–358. Verlag Stahleisen m.b.H., Düsseldorf, Germany.
302. Chatterjee A & Bradshaw AV (1973) The Influence of Gas Phase Resistance on Mass Transfer to a Liquid Metal. Metall. Trans. 4(5): 1359–1364.
303. Herbertson JG, Robertson DGC & Bradshaw AV (1983) Critical Experiments on the Role of Surface Tension Driven Flow in the Kinetics of Oxygen Transfer Between Gases and Liquid Silver. Can. Metall. Quart. 22(1): 1–8.
304. Kärnä A, Järvinen MP & Fabritius T (2015) CFD Modeling of a Supersonic Top Blown Lance in a CAS-OB Process: Development of Gas Heat and Mass Transfer Correlation. Steel. Res. Int. 86(11): 1370–1378.
305. Riboud PV & Olette M (1982) Mechanisms of some of the reactions involved in secondary refining. In: Proc. 7th International Conference on Vacuum Metallurgy, pp. 879–889. Iron and Steel Institute of Japan, Tokyo, Japan.
306. Hirasawa M, Mori K, Sano M, Hatanaka A, Shimatani Y & Okazaki Y (1987) Rate of Mass Transfer between Molten Slag and Metal under Gas Injection Stirring. Trans. Iron Steel Inst. Jpn 27(4): 277–282.
307. Hirasawa M, Mori K, Sano M, Shimatani Y & Okazaki Y (1987) Correlation Equations for Metal-side Mass Transfer in a Slag-Metal Reaction System with Gas Injection Stirring. Trans. Iron Steel Inst. Jpn 27(4): 283–290.
308. Oeters F & Xie H (1995) A contribution to the theoretical description of metal-slag reaction kinetics. Steel Res. 66(10): 409–415.
309. Xie H & Oeters F (1995) Kinetics of mass transfer of manganese and silicon between liquid iron and slags. Steel Res. 66(12): 501–508.
310. Xie H, Schulz M & Oeters F (1996) Kinetics of iron oxide reduction from CaO-MgO-FeO_n-SiO_2 slags by silicon dissolved in liquid iron. Steel Res. 67(8): 307–313.
311. Levenspiel O (1972) Chemical Reaction Engineering, 2nd Edition. John Wiley & Sons, Inc., New York, NY, USA.
312. Hayes P (2014) Reaction Kinetics. In: Seetharaman S, McLean A, Guthrie R & Sridhar S (eds.) Treatise on Process Metallurgy, Volume 1, Process Fundamentals, pp. 817–829. Elsevier, Oxford, United Kingdom.
313. Fabritius T, Riipi J, Järvinen M, Mattila O, Heikkinen E-P, Kärnä A, Kurikkala J, Sulasalmi P & Härkki J (2010) Interfacial Phenomena in Metal-Slag-Gas System during AOD Process. ISIJ Int. 50(6): 797–803.
314. Rao GS & Robertson DGC (2006) A Fundamental Study of Oxygen-Melt Reactions in

the AOD Process. In: Kongoli F & Reddy RG (eds.) Advanced Processing of Metals and Materials (Sohn International Symposium), Volume 2 - Thermo and Physicochemical Principles: Iron and Steel Making, pp. 325–342. The Minerals, Metals & Materials Society, San Diego, CA, USA.
315. Brunson RJ & Wellek RM (1970) Mass Transfer Within Oscillating Liquid Droplets. Can. J. Chem. Eng. 48(3): 247–274.
316. Altunok MY, Kalem M & Pfennig A (2012) Investigation of Mass Transfer on Single Droplets for the Reactive Extraction of Zinc with D2EHPA. AIChE J. 58(5): 1346–1355.
317. Hu S & Kintner RC (1955) The fall of single liquid drops through water. AIChE J. 1(1): 42–48.
318. Mendelson HD (1967) The prediction of bubble terminal velocities from wave theory. Am. Inst. Chem. Eng. J. 13(2): 250–253.
319. Xu Y, Ersson M & Jönsson P (2015) Numerical Simulation of Single Argon Bubble Rising in Molten Metal Under a Laminar Flow. Steel Res. Int. 86(11): 1289–1297.
320. Xu Y, Ersson M & Jönsson PG (2015) A Mathematical Modeling Study of Bubble Formations in a Molten Steel Bath. Metall. Mater. Trans. B 46(6): 2628–2638.
321. Wang G, Zhou H, Tian Q, Al X & Zhang L (in press) The Motion of Single Bubble and Interactions between Two Bubbles in Liquid Steel. ISIJ Int. DOI: 10.2355/isijinternational.ISIJINT-2016-670.
322. Taylor R & Krishna R (1993) Multicomponent Mass Transfer. John Wiley & Sons, Inc., New York, NY, USA.
323. Newman AB (1931) The drying of porous solids: diffusion and surface emission equations. Trans. Am. Inst. Chem. Eng. 27: 203–220.
324. Colombet D, Legendre D, Cockx A & Guiraud P (2013) Mass or heat transfer inside a spherical gas bubble at low to moderate Reynolds number. Int. J. Heat. Mass. Tran. 67: 1096–1105.
325. Danckwerts PV (1951) Absorption by simultaneous diffusion and chemical reaction into particles of various shapes and into falling drops. Trans. Faraday Soc. 47: 1014–1023.
326. Juncu G (2010) A numerical study of the unsteady heat/mass transfer inside a circulating sphere. Int. J. Heat Mass Transfer 53(15-16): 3006–3012.
327. Hill MJM (1894) On a Spherical Vortex. Philos. Trans. R. Soc. A 185: 213–245.
328. Kronig R & Brink JC (1951) On the theory of extraction from falling droplets. Appl. Sci. Res. 2(1): 142–154.
329. Heertjes PM, Holve WA & Talsma H (1954) Mass transfer between isobutanol and water in a spray column. Chem. Eng. Sci. 3(3): 122–142.
330. Hadamard JS (1911) Mouvement permanent lent d'une sphère liquide et visqueuse dans un liquide visqueux. C.R. Acad. Sci. Paris 152: 1735–1743.
331. Rybczynski W (1911) Über die fortschreitende Bewegung einer flüssigen Kugel in einem zähen Medium. Bull. Acad. Sci. Cracov., A 25: 40–46.
332. Sadhal SS, Ayyaswamy PS & Chung JN (1997) Transport Phenomena with Drops and Bubbles. Springer-Verlag New Work, Inc., New Work, NY, USA.
333. Brignell AS (1975) Solute extraction from an internally circulating spherical liquid drop. Int. J. Heat Mass Transfer 18(1): 61–68.
334. Johns LE & Beckmann RB (1966) Mechanism of Dispersed-Phase Mass Transfer in Viscous, Single-Drop Extraction Systems. Am. Inst. Chem. Eng. J. 12(1): 10–16.
335. Calderbank PH & Korchinski IJO (1956) Circulation in drops (A heat transfer study). Chem.

Eng. Sci. 6(2): 65–78.
336. Vermeulen T (1953) Theory for Irreversible and Constant-Pattern Solid Diffusion. Ind. Eng. Chem. 45(8): 1664–1670.
337. Calderbank PH & Moo-Young MB (1961) The continuous phase heat and mass-transfer properties of dispersions. Chem. Eng. Sci. 16(1-2): 39–54.
338. Lange KW (1971) Zur Kinetik des Sauerstoffaufblasverfahrens. Arch. Eisenhüttenwes. 42(4): 233–241.
339. Michaelides EE (2006) Particles, Bubbles & Drops – Their Motion, Heat and Mass Transfer. World Scientific Publishing Co. Pte. Ltd., Singapore.
340. Henschke M & Pfennig A (1999) Mass-Transfer Enhancement in Single-Drop Extraction Experiments. AIChE Journal 45(10): 2079–2086.
341. Handlos AE & Baron T (1957) Mass and heat transfer from drops in liquid-liquid extraction. Am. Inst. Chem. Eng. J. 3(1): 127–136.
342. Wellek RM & Skelland AHP (1965) Extraction with single turbulent droplets. AIChE J. 11(3): 557–560.
343. Olander DR (1966) The Handlos-Baron Drop Extraction Model. AIChE J. 12(5): 1018–1019.
344. Patel JM & Wellek RM (1967) Handlos and Baron model: Short contact times. AIChE J. 13(2): 384–386.
345. Wegener M & Paschedag AR (2011) Mass transfer enhancement at deformable droplets due to Marangoni convection. Int. J. Multiphas. Flow 37(1): 76–83.
346. Mills AF & Hoseyni MS (1988) Diffusive Deposition of Aerosols in a Rising Bubble. Aerosol Sci. Tech. 8(1): 103–105.
347. Frössling N (1938) Über die Verdunstung fallender Tropfen. Gerl. Beitr. Geophys. 52: 170–216.
348. Rowe PN, Claxton KT & Lewis JB (1965) Heat and mass transfer from a single sphere in an extensive flowing fluid. Trans Inst. Chem. Eng. 43: T14–T31.
349. Beek WJ & Muttzall KMK (1975) Transport Phenomena. John Wiley & Sons Ltd., London, United Kingdom.
350. Ihme F, Schmidt-Traub H & Brauer H (1972) Theoretische Untersuchung über die Umströmung und den Stoffübergang an Kugeln. Chemie-Ing.-Techn. 44(5): 306–313.
351. Sano Y, Yamaguchi N & Adachi T (1974) Mass Transfer Coefficients for Suspended Particles in Agitated Vessels and Bubble Columns. J. Chem. Eng. Jpn. 7(4): 255–261.
352. Calderbank PH (1967) Gas absorption from bubbles. Chem. Engr. 45(10): 209–233.
353. Lochiel AC & Calderbank PH (1964) Mass transfer in the continuous phase around axisymmetric bodies of revolution. Chem. Eng. Sci. 19(7): 471–484.
354. Steinberger RL & Treybal RE (1960) Mass Transfer from a Solid Soluble Sphere to a Flowing Liquid Stream. AIChE J. 6(2): 227–232.
355. Wu P, Yang Y, Barati M & McLean A (2014) Decarburization of Levitated Fe-Cr-C Droplets by Carbon Dioxide. Metall. Mater. Trans. B 45(6): 2211–2221.
356. Richardson FD (1971) Drops and Bubbles in Extractive Metallurgy. Metall. Trans 2(10): 2747–2756.
357. Oeters F (1994) Metallurgy of Steelmaking. Verlag Stahleisen mbH, Düsseldorf, Germany.
358. Rhamdhani MA, Brooks GA & Coley KS (2005) Kinetics of Metal/Slag Reactions during Spontaneous Emulsification. Metall. Mater. Trans. B 36(2): 219–227.
359. Wu P, Yang YD, Barati M & McLean A (2015) Influence of thermal diffusion on decarburi-

sation of iron–chromium alloy droplets by oxygen–argon gas mixture. Can. Metall. Q. 54(2): 177–184.
360. Baker LA, Warner NA & Jenkins AE (1967) Decarburization of a Levitated Iron Droplet in Oxygen. Trans. Met. Soc. AIME 239(6): 857–864.
361. Baker LA, Warner NA & Jenkins AE (1964) Kinetics of Decarburization of Liquid Iron in an Oxidizing Atmosphere Using the Levitation Technique. Trans. Met. Soc. AIME 230(10): 1228–1235.
362. Distin PA, Hallett GD & Richardson FD (1968) Some reactions between drops of iron and flowing gases. J. Iron Steel Inst. 206(8): 821–833.
363. El-Kaddah NH & Robertson DGC (1978) The Kinetics of Gas-Liquid Metal Reactions Involving Levitated Drops. Carburization and Decarburization of Molten Iron in CO-CO_2 Gas Mixtures at High Pressures. Metall. Trans. B. 9(2): 191–199.
364. Widlund D, Sarma DS & Jönsson PG (2006) Studies on Decarburisation and Desiliconisation of Levitated Fe–C–Si Alloy Droplets. ISIJ Int. 46(8): 1149–1157.
365. Mietz J, Schneider S & Oeters F (1991) Model experiments on mass transfer in ladle metallurgy. Steel Res. 62(1): 1–9.
366. Nakasuga T, Sun H, Nakashima K & Mori K (2001) Reduction Rate of Cr_2O_3 in a Solid Powder State and in CaO-SiO_2-Al_2O_3-CaF_2 Slags by Fe-C-Si Melts. ISIJ Int. 41(9): 937–944.
367. Nakasuga T, Nakashima K & Mori K (2004) Recovery Rate of Chromium from Stainless Slag by Iron Melts. ISIJ Int. 44(4): 665–672.
368. Sevinc N & Elliott JF (1976) Kinetics of reduction of Cr_2O_3 (s) by liquid Fe–Cr–C alloys. Ironmaking Steelmaking 3(5): 268–278.
369. Turkan S & Lange KW (1985) Digitale Simulation des Stofftransports in hintereinander aufsteigenden Gasblasen unter Berücksichtigung ihrer Entstehungsphase. Steel Res. 56(4): 199–209.
370. Guthrie RIL & Bradshaw AV (1969) The Behaviour of Large Bubbles Rising Through Molten Silver. Trans. Met. Soc. AIME 245(10): 2285–2292.
371. Oeters F (1972) Konvektive Diffusion mit chemischer Reaktion. In: Dahl W, Lange KW & Papamantellos D (eds.) Kinetik metallurgischer Vorgänge bei der Stahlherstellung, pp. 121–141. Verlag Stahleisen m.b.H., Düsseldorf, Germany.
372. Guthrie RIL (1989) Engineering in Process Metallurgy. Clarendon Press, Oxford, United Kingdom.
373. Järvinen M, Visuri V-V, Pisilä S, Kärnä A, Sulasalmi P, Heikkinen E-P & Fabritius T (2013) Advanced Methods in Modelling of Metallurgical Unit Operations. Mater. Sci. Forum 762: 236–241.
374. Walas SM (1985) Phase Equilibria in Chemical Engineering. Butterworth-Heinemann, Stoneham, MA, USA.
375. Ohguchi S, Robertson D, Deo B, Grieveson P & Jeffes J (1984) Simultaneous Dephosphorization and Desulphurization of Molten Pig Iron. Ironmaking Steelmaking 11(4): 202–213.
376. Kitamura S-Y, Kitamura T, Shibata K, Mizukami Y, Mukawa S & Nakagawa J (1991) Effect of Stirring Energy, Temperature and Flux Composition on Hot Metal Dephosphorization Kinetics 31(11): 1322–1328.
377. Kitamura S-Y, Kitamura T, Aida E, Sakomura R, Kaneko T & Nuibe T (1991) Development of Analysis and Control Method for Hot Metal Dephosphorization Process by Computer

Simulation. ISIJ Int. 31(11): 1329–1335.
378. Shibata E, Sun H & Mori K (1999) Kinetics of Simultaneous Reactions between Liquid Iron-Carbon Alloys and Slags Containing MnO. Metall. Mater. Trans. B. 30(2): 279–286.
379. Ishikawa M (2004) Analysis of Hot Metal Desiliconization Behaviour in Converter Experiments by Coupled Reaction Model. ISIJ Int. 44(2): 316–325.
380. Pahlevani F, Kitamura S, Shibata H & Maruoka N (2010) Simulation of Steel Refining Process in Converter. Steel Res. Int 81(8): 617–622.
381. Lytvynyuk Y, Schenk J, Hiebler M & Mizelli H (2011) Thermodynamic and Kinetic Modelling of the De-Vanadization Process in the Steelmaking Converter. In: Proc. 6th European Oxygen Steelmaking Conference. Jernkontoret, Stockholm, Sweden.
382. Lytvynyuk Y, Schenk J, Hiebler M & Sormann A (2014) Thermodynamic and Kinetic Model of the Converter Steelmaking Process. Part 1: The Description of the BOF Model. Steel Res. Int. 85(4): 537–543.
383. Lytvynyuk Y, Schenk J, Hiebler M & Sormann A (2014) Thermodynamic and Kinetic Model of the Converter Steelmaking Process. Part 2: The Model Validation. Steel Res. Int. 85(4): 544–563.
384. Harada A, Maruoka N, Shibata H & Kitamura S-Y (2013) A Kinetic Model to Predict the Compositions of Metal, Slag and Inclusions during Ladle Refining: Part 1. Basic Concept and Application. ISIJ Int. 53(12): 2110–2117.
385. Harada A, Maruoka N, Shibata H & Kitamura S-Y (2013) A Kinetic Model to Predict the Compositions of Metal, Slag and Inclusions during Ladle Refining: Part2. Condition to Control the Inclusion Composition. ISIJ Int. 53(12): 2118–2125.
386. Koukkari P, Pajarre R & Hack K (2001) Setting Kinetic Controls for Complex Equilibrium Calculations. Z. Metallkd. 92(10): 1151–1157.
387. Pajarre R, Blomberg P & Koukkari P (2008) Thermochemical multi-phase models applying the constrained gibbs energy method. In: Proc. 18th European Symposium on Computer Aided Process Engineering, volume 25, pp. 883–888.
388. Koukkari P & Pajarre R (2011) A Gibbs energy minimization method for constrained and partial equilibria. Pure Appl. Chem. 83(6): 1243–1254.
389. Jalkanen H (2006) Experiences in Physicochemical Modeling of Oxygen Converter Process (BOF). In: Kongoli F & Reddy RG (eds.) Proc. Sohn International Symposium, Advanced Processing of Metals and Materials, Volume 2 – Thermo and Physicochemical Principles: Iron and Steelmaking, pp. 541–554. The Minerals, Metals & Materials Society.
390. Virrankoski R, Oksanen T & Jalkanen H (2001) CONSIM 4.0 - happikonvertteriprosessin simulointiohjelma. Technical Report TKK-MK-121, Teknillinen korkeakoulu, Espoo, Finland.
391. Waage P & Guldberg CM (1864) Studies Concerning Affinity. In: Forhandlinger i Videnskabs-Selskabet i Christiania, p. 35.
392. Waage P & Guldberg CM (1986) Studies Concerning Affinity. J. Chem. Educ. 63(12): 1044–1047.
393. Balzhiser RE, Samuels MR & Eliassen JD (1972) Chemical Engineering Thermodynamics – The Study of Energy, Entropy, and Equilibrium. Prentice-Hall, Inc., Eaglewood Cliffs, NJ, USA.
394. Kubaschewski O & Alcock CB (1979) Metallurgical Thermochemistry 5th Edition. Pergamon Press Ltd., Oxford, United Kingdom.
395. Petrucci RH, Herring FG, Madura JD & Bissonnette C (2011) General Chemistry – Principles

and Modern Applications. Pearson Canada, Inc., Toronto, Canada.
396. Atkins PW (1994) Physical Chemistry. Oxford University Press, Oxford, United Kingdom.
397. Glassstone S, Laidler KJ & Eyring H (1941) The Theory of Rate Processes: The Kinetics of Chemical Reactions, Viscosity, Diffusion and Electrochemical Phenomena. McGraw-Hill Book Company, Inc., New York, NY, USA.
398. Streltsov AK, Esin OA & Toporishchev GA (1969) Investigation of reduction kinetics of silicon from molten oxides by potentiostatic method. Sov. Electrochem. 5(6): 145–150.
399. Pretnar B & Schmalzried H (1974) Elektrodenkinetische Untersuchungen zum Siliciumdurchtritt an der Phasengrenze zwischen einer kieselsäurehaltigen Oxidschmelze und einer siliciumhaltigen Metallschmelze. Arch. Eisenhüttenwes. 45(3): 185–191.
400. Prange R, Heusler K & Schwerdtfeger K (1984) Charge Transfer at Fe/FeO(CaF_2) Electrodes at 1450 °C: Exchange Current Density, Electrode Capacitance, Diffusivity. Metall. Trans. B 15(2): 281–288.
401. Schwerdtfeger K & Prange R (1984) Interface kinetics of slag-metal reactions. In: Fine HA & Gaskell DR (eds.) Proc. 2nd International Symposium on Metallurgical Slags and Fluxes, pp. 595–608. Metallurgical Society of AIME, Lake Tahoe, NV, USA.
402. Nagata K & Goto KS (1977) Electrochemical determination of quasi-binary interdiffusivity of CaO and SiO_2 in a blast-furnace type slag using a memory-type oscilloscope. Ironmaking Steelmaking 4(1): 23–28.
403. Mannion FJ & Fruehan RJ (1989) Decarburization Kinetics of Liquid Fe-C_{sat} Alloys by CO_2. Metall. Trans. B. 20(6): 853–861.
404. Rao YK (1985) Stoichiometry and Thermodynamics of Metallurgical Processes. Cambridge University Press, Cambridge, United Kingdom.
405. Kootz T (1960) The dynamics of the blowing process. J. Iron Steel Inst. (10): 253–259.
406. Kootz T, Behrens K, Maas H & Baumgarten P (1965) Zur Metallurgie der Sauerstoffaufblas-Verfahren. Stahl Eisen 85(14): 857–865.
407. Krainer H (1965) Zur Metallurgie des Sauerstoffaufblas-Verfahren. Stahl Eisen 85(15): 932–939.
408. Oeters F (1966) Zur Kinetik des Frischens unter besonderer Berücksichtigung des Sauerstoffaufblas-Verfahrens. Arch. Eisenhüttenwes. 37(3): 209–219.
409. Szekely J & Todd MR (1967) A Note on the Reaction Mechanism of Carbon Oxidation in Oxygen Steelmaking Processes. Trans. Met. Soc. AIME 239(10): 1664–1666.
410. Meyer HW, Porter WF, Smith GC & Szekely J (1968) Slag-Metal Emulsions and their Importance in BOF Steelmaking. J. Met. 20(6): 35–42.
411. Block F-R, Masui A & Stolzenberg G (1973) Physikalische Vorgänge im Sauerstoffaufblaskonverter. Arch. Eisenhüttenwes. 44(5): 357–361.
412. Urquhart RC & Davenport WG (1973) Foams and emulsions in oxygen steelmaking. Can. Metall. Quart. 12(4): 507–516.
413. Chernyatevich AG, Zarvin EY & Volovich MI (1975) Observation through a transparent wall of the behaviour of a basic oxygen furnace bath during injection. Steel USSR 5(2): 79–81.
414. Chatterjee A, Lindfors N-O & Wester J (1976) Process Metallurgy of LD steelmaking. Ironmaking Steelmaking 3(1): 21–32.
415. Koch K, Fix W & Valentin P (1976) Einsatz eines 50-kg-Aufblaskonverters zur Untersuchung der Entkohlung von Eisen-Kohlenstoff-Schmelzen. Arch. Eisenhüttenwes. 47(11): 659–663.
416. Koch K, Sittard J & Valentin P (1976) Entkohlung von Eisenschmelzen bei Sauerstoffangebot

über Schlacken- und Gasphase. Arch. Eisenhüttenwes. 47(10): 583–588.
417. Koch K, Fix W & Valentin P (1978) Kennzeichende Teilabschnitte der Entkohlungsreaktion beim O_2-Aufblasen auf Fe-C-Schmelzen. Arch. Eisenhüttenwes. 49(3): 109–114.
418. Schürmann E, Sperl H, Hammer R & Ender A (1986) Metallurgische Interpretation der CO_2-Gehalte des Konvertergases beim Sauerstoffaufblasverfahren. Stahl Eisen 106(23): 43–48.
419. Lee Y & Kolbeinsen L (2007) An Analysis of Hot Spot Phenomenon in BOF Process. ISIJ Int. 47(5): 764–765.
420. Dogan N, Brooks GA & Rhamdhani MA (2011) Comprehensive Model of Oxygen Steelmaking Part 3: Decarburization in Impact Zone. ISIJ Int. 51(7): 1102–1109.
421. Chiba K, Ono A, Saeki M, Yamauchi M, Kanamoto M & Ohno T (1993) Development of direct analysis method for molten iron in converter – hotspot radiation spectrometry. Ironmaking Steelmaking 20(3): 215–220.
422. Koch K, Fix W & Valentin P (1978) Entkohlungsreaktionen mit unruhigem Blasverhalten beim Aufblasen von Sauerstoff auf Fe-C-Schmelzen. Arch. Eisenhüttenwes. 49(4): 163–166.
423. Tsujino R, Nakao R, Kato K, Hisatomi R, Kitamura S-Y, Takano H, Morishige H & Hirata H (1994) Advances in Stainless Steelmaking Technology. Nippon Steel Tech. Rep. (61): 38–45.
424. Meyer HW (1969) Oxygen steelmaking: its control and future. J. Iron Steel Inst. 207(6): 781–789.
425. Dogan N, Brooks GA & Rhamdhani MA (2011) Comprehensive Model of Oxygen Steelmaking Part 1: Model Development and Validation. ISIJ Int. 51(7): 1086–1092.
426. Frenning A (2010) A Study of Top Blowing with Focus on the Penetration Region. Doctoral thesis, Royal Institute of Technology, Stockholm, Sweden.
427. Asai S & Muchi I (1970) Theoretical Analysis by the Use of Mathematical Model in LD Converter Operation. Trans. Iron Steel Inst. Jpn 10(4): 250–263.
428. Barron MA, Medina DY & Hilerio I (2014) Numerical Simulation of Decarburization in a Top-Blown Basic Oxygen Furnace. Model. Numer. Sim. Mater. Sci. 4(3): 94–103.
429. Emi T, Boorstein M & Pehlke RD (1974) Absorption of Gaseous Oxygen by Liquid Iron. Metall. Trans. 5(9): 1959–1966.
430. Radzilowski RH & Pehlke RD (1979) Gaseous Oxygen Absorption by Molten Iron and Some Fe-Al, Fe-Si, Fe-Ti, and Fe-V Alloys. Metall. Trans. B. 10(3): 341–348.
431. Koria SC (1981) Wechselwirkung zwischen einem Gasstrahl und flüssiger Metallschmelze. Doctoral thesis, RWTH Aachen University, Aachen, Germany.
432. Lange KW & Koria SC (1983) Wechselwirkung zwischen Sauerstoffstrahl und Roheisenschmelze beim Sauerstoffaufblasverfahren. Publ. Wiss. Film. Techn. Wiss./Naturw., Ser. 8, Nr. 9, Institut für den Wissenschaftlichen Film, Göttingen, Germany. Film D 1386.
433. von Bogdandy L, Hopp H-U & Stranski IN (1966) Entkohlungs- und Desoxydationsvorgänge im flüssigen Eisen. Arch. Eisenhüttenwes. 37(11): 841–845.
434. Breuer G, Trömel G & Engell H-J (1968) Beitrag zur Kenntnis der Entkohlung von Eisen-Kohlenstoff-Schmelzen. Arch. Eisenhüttenwes. 39(8): 553–557.
435. Pomfret RJ & Grieveson P (1978) Kinetics of fast initial stage of reduction of MnO from silicate slags by carbon in molten iron. Ironmaking Steelmaking 5(5): 191–197.
436. Steinmetz E & Lindenberg H-U (1970) Kinetik der Reaktionen zwischen Kohlenstoff und Sauerstoff bei der Stahlherstellung. Stahl Eisen 90(26): 1517–1525.
437. Deo B, Karamcheti A, Paul A, Singh P & Chhabra RP (1996) Characterization of Slag–Metal

Droplet–Gas Emulsion in Oxygen Steelmaking Converters. ISIJ Int. 36(6): 658–666.
438. Cicutti C, Valdez M, Pérez T, Petroni J, Gómez A, Donayo R & Ferro L (2000) Study of slag-metal reactions in an LD-LBE converter. In: Proc. 6th International Conference on Motel Slags, Fluxes and Salts. Stockholm, Sweden – Helsinki, Finland.
439. Dogan N, Brooks GA & Rhamdhani MA (2011) Analysis of bloated droplet theory using steelmaking process models. In: Proc. Chemeca 2011 – 39th Australasian Chemical Engineering Conference, pp. 1–14. Engineers Australia, Sydney, Australia.
440. Dogan N, Brooks GA & Rhamdhani MA (2011) Comprehensive Model of Oxygen Steelmaking Part 2: Application of Bloated Droplet Theory for Decarburization in Emulsion Zone. ISIJ Int. 51(7): 1093–1101.
441. Sarkar R, Gupta P, Basu S & Ballal NB (2015) Dynamic Modeling of LD Converter Steelmaking: Reaction Modeling Using Gibbs' Free Energy Minimization. Metall. Mater. Trans. B 46(2): 961–976.
442. Bundschuh P, Schenk J, Hiebler M, Sormann A & Panhofer H (2015) Effect of Interaction Area on the Thermodynamics and Kinetic Modelling of BOF Converter. In: Proc. 6th International Congress on the Science and Technology of Steelmaking, volume 1, pp. 151–154. The Chinese Society for Metals, Beijing, China.
443. Spooner S, Warnett JM, Bhagat R, Williams MA & Sridhar S (2016) Calculating the Macroscopic Dynamics of Gas/Metal/Slag Emulsion during Steelmaking. ISIJ Int. 56(12): 2171–2180.
444. Okhotskii VB, Chernyatevich AG & Prosvirin KS (1972) Studying the interaction between jets of oxygen and metal bath. Steel USSR 2(6): 443–444.
445. Koch K, Falkus J & Bruckhaus R (1993) Hot model experiments of the metal bath spraying effect during the decarburization of Fe-C melts through oxygen top-blowing. Steel Res. 64(1): 15–21.
446. Schürmann E, Mahn G, Schoop J & Resch W (1977) Betriebsuntersuchungen über den Verlauf der Entphosphorung und der Granalienbildung in der Schlacke beim Sauerstoffaufblasverfahren. Stahl Eisen 97(22): 1069–1074.
447. Brooks G, Pan Y, Subagyo & Coley K (2005) Modeling of Trajectory and Residence Time of Metal Droplets in Slag-Metal-Gas Emulsions in Oxygen Steelmaking. Metall. Mater. Trans. B 36(4): 525–535.
448. Koria SC & Lange KW (1986) Correlation between drop size distribution or total drop mass and oxygen top blowing parameters. In: Proc. 5th International Iron and Steel Congress, volume 6, pp. 353–356. The Iron and Steel Society, Inc., Washington, DC, USA.
449. Lindstrand G, Jönsson PG & Tilliander A (2013) Studies of Metal Droplets in AOD Production Decarburisation Slags. In: Proc. ISIJ-VDEh-Jernkontoret Joint Symposium, pp. 106–113. Iron and Steel Institute of Japan, Osaka, Japan.
450. Tosun I (2007) Modeling in Transport Phenomena: A Conceptual Approach (Second Edition). Elsevier.
451. Haataja J, Heikonen J, Leino Y, Rahola J, Ruokolainen J & Savolainen V (1999) Numeeriset menetelmät käytännössä. CSC - Tieteellinen laskenta Oy, Espoo, Finland.
452. Kreyszig E, Kreyszig H & Norminton EJ (2011) Advanced Engineering Mathematics 10th Edition. John Wiley & Sons, Inc.
453. Rice RG & Do DD (2012) Applied Mathematics and Modeling for Chemical Engineers. John Wiley & Sons, Inc., Hoboken, NJ, USA, 2nd edition.
454. Meier T, Logar V, Echterhof T, Škrjanc I & Pfeifer H (2016) Modelling and Simulation of

the Melting Process in Electric Arc Furnaces — Influence of Numerical Solution Methods. Steel Res. Int. 87(5): 581–588.
455. Molloy N (1970) Impinging jet flow in a two-phase system: the basic flow pattern. J. Iron Steel Inst. 208(10): 943–950.
456. Sabah S & Brooks G (2014) Splashing in Oxygen Steelmaking. ISIJ Int. 54(4): 836–844.
457. Sabah S & Brooks G (2016) Study of cavity modes in BOF by analysis of sound. Ironmaking Steelmaking 43: 473–480.
458. Chernyatevich AG, Shishov BI & Solomon GM (1980) Interaction between jet of oxygen and metal bath. Steel USSR 10(2): 70–72.
459. Sabah S & Brooks G (2016) Energy Balance Around Gas Injection into Oxygen Steelmaking. Metall. Mater. Trans. B 47(1): 458–466.
460. Lee CK, Neilson JH & Gilchrist A (1977) Correlation of the decay characteristics of jets from multi-nozzle oxygen lances with the performance of the charge in steel converters. Iron Steel Int. 50(3): 175–184.
461. Lee CK, Neilson JH & Gilchrist A (1977) Effects of nozzle angle on performance of multi-nozzle lances in steel converters. Ironmaking Steelmaking 4(6): 329–337.
462. Koria SC & Lange KW (1987) Penetrability of impinging gas jets in molten steel bath. Steel Res. 58(9): 421–426.
463. Flinn RA, Pehlke RD, Glass DR & Hays PO (1967) Jet Penetration And Bath Circulation In Basic Oxygen Furnace. Trans. Met. Soc. AIME 239(11): 1776–1791.
464. Baptizmanskii VI, Shchedrin GA & Prosvirin KS (1975) Dimensions of the reaction zone with oxygen top blowing. Communication 1. Steel USSR 5(10): 540–543.
465. Collins RD & Lubanska H (1954) The depression of liquid surfaces by gas jets. Brit. J. Appl. Phys. 5(1): 22–26.
466. Banks RB & Chandrasekhara DV (1963) Experimental investigation of the penetration of a high-velocity gas jet through a liquid surface. J. Fluid Mech. 15(1): 13–34.
467. Cheslak FR, Nicholls JA & Sichel M (1969) Cavities formed on liquid surfaces by impinging gaseous jets. J. Fluid Mech. 36(1): 55–63.
468. Chatterjee A (1973) On Some Aspects of Supersonic Jets of Interest in LD Steelmaking. Iron Steel 46(1): 38–40.
469. Qian F, Mutharasan R & Farouk B (1996) Studies of Interface Deformations in Single- and Multi-Layered Liquid Baths Due to an Impinging Gas Jet. Metall. Trans. B 27(6): 911–920.
470. Kumagai T & Iguchi M (2011) Instability Phenomena at Bath Surface Induced by Top Lance Gas Injection. ISIJ Int. 41(Supplement): S52–S55.
471. Olivares O, Elias A, Sánchez R, Díaz-Cruz M & Morales RD (2002) Physical and mathematical models of gas-liquid fluid dynamics in LD converters. Steel Res. 73(2): 44–51.
472. Nordquist A, Kumbhat N, Jonsson L & Jönsson P (2006) The Effect of Nozzle Diameter, Lance Height and Flow Rate on Penetration Depth in a Top-blown Water Model. Steel Res. Int. 77(2): 82–90.
473. Asahara N, Naito K-I, Kitagawa I, Matsuo M, Kumakura M & Iwasaki M (2011) Fundamental Study on Interaction between Top Blown Jet and Liquid Bath. Steel Res. Int. 82(5): 587–594.
474. Solórzano-López J, Zenit R & Ramírez-Argáez M (2011) Mathematical and physical simulation of the interaction between a gas jet and a liquid free surface. Appl. Math. Model. 35(10): 4991–5005.
475. Pericleous K, Lebon B, Djambazov G & Patel M (2012) Mathematical modeling of a

compressible oxygen jet interfacing with a free surface in a basic oxygen furnace for steel production. In: Nastac L, Zhang L, Thomas BG, Sabau A, E-Kaddah N, Powell AC & Combeau H (eds.) CFD Modeling in Materials, pp. 287–294. The Minerals, Metals & Materials Society.
476. Hwang HY & Irons GA (2012) A Water Model Study of Impinging Gas Jets on Liquid Surfaces. Metall. Mater. Trans. B 43(2): 302–315.
477. Ek M & Sichen D (2012) Study of Penetration Depth and Droplet Behavior in the Case of a Gas Jet Impinging on the Surface of Molten Metal usin Liquid Ga-In-Sn. Steel Res. Int. 83(7): 678–685.
478. Li M, Li Q, Kuang S & Zou Z (2016) Determination of Cavity Dimensions Induced by Impingement of Gas Jets onto a Liquid Bath. Metall. Mater. Trans. B. 47(1): 116–126.
479. Nakazono D, Abe K-I, Nishida M & Kurita K (2004) Supersonic O_2-jet Impingement on Liquid Iron with Surface Chemistry. ISIJ Int. 44(1): 91–99.
480. Memoli F, Mapelli C, Ravanelli P & Corbella M (2004) Simulation of Oxygen Penetration and Decarburisation in EAF Using Supersonic Injection System. ISIJ Int. 44(8): 1342–1349.
481. Ersson M, Tilliander A, Jonsson L & Jönsson P (2008) A Mathematical Model of an Impinging Air Jet on a Water Surface. ISIJ Int. 48(4): 377–384.
482. Hwang HY & Irons GA (2011) Mathematical Modeling of Impinging Gas Jets on Liquid Surfaces. Metall. Mater. Trans. B 42(3): 575–591.
483. Lv M, Zhu R, Guo Y-G & Wang Y-W (2013) Simulation of Flow Fluid in the BOF Steelmaking Process. Metall. Mater. Trans. B 44(6): 1560–1571.
484. Li Q, Li M, Kuang SB & Zou Z (2014) Computational study on the behaviours of supersonic jets and their impingement onto molten liquid free surface in BOF steelmaking. Can. Met. Quart. 53(3): 340–351.
485. Dong K, Zhu R, Gao W & Liu F-H (2014) Simulation of three-phase flow and lance height effect on the cavity shape. Int. J. Miner. Metall. Mater. 21(6): 523–530.
486. Brosse G, Ghazal G & Huber J-C (2014) Oxygen Jet Penetration Depth in BOF. In: Proc. 7th European Oxygen Steelmaking Conference. Czech Metallurgical Society, Třinec, Czech Republic.
487. Li Q, Li M, Kuang S & Zou Z (2015) Numerical Simulation of the Interaction Between Supersonic Oxygen Jets and Molten Slag–Metal Bath in Steelmaking BOF Process. Metall. Mater. Trans. B 46(3): 1494–1509.
488. Li M, Li Q, Kuang S & Zuo Z (2016) Transferring Characteristics of Momentum/Energy during Oxygen Jetting into the Molten Bath in BOFs: A Computational Exploration. Steel. Res. Int. 87(3): 288–300.
489. Maatsch J (1962) Über das Eindringen eines freien Gasstrahles in eine Flüssigkeitsoberfläche. Techn. Mitt. Krupp Forsch.-Ber. 20(1): 1–9.
490. van der Lingen TW (1966) Penetration of inclined gas jets into liquid baths. J. Iron Steel Inst. 204(4): 320–325.
491. Sharma SK, Hlinka JW & Kern DW (1977) The Bath Circulation, Jet Penetration and High-Temperature Reaction Zone in BOF Steelmaking. Iron Steelmaker 24(7): 7–18.
492. Turkdogan ET (1966) Fluid dynamics of gas jets impinging on surface of liquids. Chem. Eng. Sci. 21: 1133–1144.
493. Standish N & He QL (1989) Drop Generation due to an Impinging Jet and the Effect of Bottom Blowing in the Steelmaking Vessel. ISIJ Int. 29(6): 455–461.
494. Koria SC & Lange KW (1979) Breakup of iron–carbon drops by a high velocity oxygen gas

jet. Can. Metall. Quart. 18(2): 131–143.
495. Koria SC & Lange KW (1983) Disintegration of iron–carbon drop by high-velocity gas jet. Ironmaking Steelmaking 10(4): 160–168.
496. Lee K-Y, Lee H-G & Hayes PC (1998) Critical Falling Heights for the First Break-up of Liquid Drops Impacting on Immiscible Liquids. ISIJ Int. 38(11): 1242–1247.
497. Assis AN, Warnett J, Spooner S, Fruehan RJ, Williams MA & Sridhar S (2015) Spontaneous Emulsification of a Metal Drop Immersed in Slag Due to Dephosphorization: Surface Area Quantification. Metall. Mater. Trans. B 46(2): 568–576.
498. Lange KW & Rees H (1973) Ermittlung der zum Überlaufen von Sauerstoffaufblaskonvertern führenden Aufblasgeschwindigkeiten sowie der Größe fluider Partikeln in Gasströmen. Arch. Eisenhüttenwes. 44(11): 813–821.
499. Reiter G & Schwerdtfeger K (1992) Observations of Physical Phenomena Occurring during Passage of Bubbles through Liquid/Liquid Interfaces. ISIJ Int. 32(1): 50–56.
500. Reiter G & Schwerdtfeger K (1992) Characteristics of Entrainment and Liquid/Liquid Interfaces due to Rising Bubbles. ISIJ Int. 32(1): 57–65.
501. Hahn I (1999) Untersuchungen zum Verspritzen von Schmelze in sekundärmetallurgischen Anlagen. Doctoral thesis, Rheinisch-Westfälische Technische Hochschule Aachen, Aachen, Germany.
502. Han Z & Holappa L (2003) Mechanisms of Iron Entrainment into Slag due to Rising Gas Bubbles. ISIJ Int. 43(3): 292–297.
503. Han Z & Holappa L (2003) Characteristics of Iron Entrainment into Slag Due to Rising Gas Bubbles. ISIJ Int. 43(11): 1698–1704.
504. Li X, Bao Y-P, Wang M & Lin L (2016) Simulation study on factors influencing the entrainment behavior of liquid steel as bubbles pass through the steel/slag interface. Int. J. Miner. Metall. Mater. 23(5): 511–519.
505. Nordquist A, Tilliander A, Grönlund K, Runnsjö G & Jönsson P (2009) Characterisation of metal droplets sampled during top lance blowing. Ironmaking Steelmaking 36(6): 421–431.
506. Little JDC (1961) A Proof for the Queuing Formula: $L = \lambda W$. Oper. Res. 9(3): 383–387.
507. Subagyo & Brooks GA (2002) An Improved Correlation for Predicting Terminal Velocity of Droplets and Bubbles in Slag-Metal-Gas Emulsion. ISIJ Int. 42(10): 1182–1184.
508. Kamble S, Song D-Y, Dhavamani A, Gupta GS, Maruoka N, Kitamura S-Y & Shibata H (2013) Modelling of metal-slag emulsion. High Temp.-High Press. 42(3): 227–236.
509. Subagyo, Brooks GA, Coley KS & Irons GA (2003) Generation of Droplets in Slag–Metal Emulsions through Top Gas Blowing. ISIJ Int. 43(7): 983–989.
510. Kleppe W & Oeters F (1977) Untersuchung der Abreißbedingungen von Flüssigkeitstropfen durch einen auf eine Flüssigkeitsoberfläche auftreffenden Gasstrahl. Arch. Eisenhüttenwes. 48(3): 139–143.
511. Sabah S, Alam M, Brooks G & Naser J (2012) Droplet Generation in Steelmaking. In: Proc. 4th International Conference on Process Development in Iron and Steelmaking, volume 2, pp. 125–134. Swerea MEFOS, Luleå, Sweden.
512. Alam M, Naser J, Brooks G & Fontana A (2012) A Computational Fluid Dynamics Model of Shrouded Supersonic Jet Impingement on a Water Surface. ISIJ Int. 52(6): 1026–1035.
513. Sabah S & Brooks G (2015) Splash Distribution in Oxygen Steelmaking. Metall. Mater. Trans. B 46(2): 863–872.
514. Sabah S & Brooks G (2015) Splash Distribution in Oxygen Steelmaking. Metall. Mater. Trans. B 46(2): 863–872.

515. Alam M, Irons G, Brooks G, Fontana A & Naser J (2011) Inclined Jetting and Splashing in Electric Arc Furnace Steelmaking. ISIJ Int. 51(9): 1439–1447.
516. Rout BK, Brooks G, Subagyo, Rhamdhani MA & Li Z (2016) Modeling of Droplet Generation in a Top Blowing Steelmaking Process. Metall. Mater. Trans. B. 47(6): 3350–3361.
517. Li M, Li Q, Kuang S & Zou Z (2016) Computational Investigation of the Splashing Phenomenon Induced by the Impingement of Multiple Supersonic Jets onto a Molten Slag–Metal Bath. Ind. Eng. Chem. Res. 55(12): 3630–3640.
518. Zughbi HD (2004) Decarburization of Fe/C melts in a crucible: Effects of bath sulfur level and bath surface area. Scand. J. Metall. 33(4): 242–250.
519. Koria SC & Lange KW (1984) Mixing-time correlation in top gas stirred melts. Arch. Eisenhüttenwes. 55(3): 97–100.
520. Koria SC & Lange KW (1984) An experimental study on the behaviour of an underexpanded supersonic gas jet. Arch. Eisenhüttenwes. 55(9): 427–432.
521. Koria SC & Lange KW (1984) Effect of top blowing parameters on drop size and drop size distribution in BOF steelmaking. Arch. Eisenhüttenwes. 55(12): 581–584.
522. Koria SC (1988) Nozzle design in impinging jet steelmaking process. Steel Res. 59(5): 104–109.
523. Koria SC (1988) Dynamic variations of lance height distance in impinging jet steelmaking practice. Steel Res. 59(6): 257–262.
524. Fréchet M (1927) Sur la loi de probabilité de l'écart maximum. Ann. Soc. Polon. Math. 6: 93–116.
525. Rosin P & Rammler E (1933) The Laws Governing the Fineness of Powdered Coal. J. Inst. Fuel 7(31): 29–36.
526. Rosin P, Rammler E & Sperling K (1933) Korngrößenprobleme des Kohlenstaubes und ihre Bedeutung für die Vermahlung. Bericht C 52 des Reichskohlenrates, Berlin, Germany.
527. Bennett JG (1936) Broken coal. J. Inst. Fuel 10: 22–39.
528. Weibull W (1939) A Statistical Theory of the Strenght of Materials. In: Ingeniörsvetenskapsakademiens handlingar Nr 151. Generalstabens litografiska anstalts förlag, Stockholm, Sweden.
529. Weibull W (1951) A statistical distribution function of wide applicability. J. Appl. Mech.-Trans. ASME 18(3): 293–297.
530. Stoyan D (2013) Weibull, RRSB or extreme-valued theorists? Metrika 76(2): 153–159.
531. Lange KW (1972) Disperse Systeme und Stofftransport. In: Dahl W, Lange KW & Papamantellos D (eds.) Kinetik metallurgischer Vorgänge bei der Stahlherstellung, pp. 359–375. Verlag Stahleisen m.b.H., Düsseldorf, Germany.
532. Barin I (1989) Thermochemical Data of Pure Substances Part I. VCH Verlagsgesellschaft mbH, Weinheim, Germany.
533. Lee YE, Berg H & Jensen B (1995) Dissolution kinetics of ferroalloys in steelmaking process. Ironmaking Steelmaking 22(6): 486–494.
534. Wei T & Oeters F (1992) A model test for emulsion in gas-stirred ladles. Steel Res. 63(2): 60–68.
535. Lachmund H, Xie Y, Buhles T & Pluschkell W (2003) Slag Emulsification during Liquid Steel Desulphurisation by Gas Injection into the Ladle. Steel Res. 74(2): 77–85.
536. Mietz J & Brühl M (1990) Model calculations for mass transfer with mixing in ladle metallurgy. Steel Res. 61(3): 105–112.

537. Frohberg MG, Gerlach F & Handschuh G (1990) Investigations of drop-size-distribution and mass transfer in gas-stirred liquid-liquid systems. Steel Res. 61(4): 151–156.
538. Mietz J, Schneider S & Oeters F (1991) Emulsification and mass transfer in ladle metallurgy. Steel Res. 62(1): 10–15.
539. Akdogan G & Eric RH (2004) Physical modelling of slag-metal dispersion. J. S. Afr. I. Min. Metall. 104(10): 589–595.
540. Kabezya K & Eric RH (2008) Study of dispersion phenomena in creusot loire uddeholm reactor. Miner. Eng. 21(2): 138–142.
541. Savolainen J, Fabritius T & Mattila O (2009) Effect of Fluid Physical Properties on the Emulsification. ISIJ Int. 49(1): 29–36.
542. Huang A, Harmuth H, Doletschek M, Vollmann S & Feng X (2015) Toward CFD Modeling of Slag Entrainment in Gas Stirred Ladles. Steel Res. Int. 86(12): 1447–1454.
543. Irons G, Senguttuvan A & Krishnapisharody K (2015) Recent Advances in the Fluid Dynamics of Ladle Metallurgy. ISIJ Int. 55(1): 1–6.
544. Kärnä A, Fabritius T & Hekkala L (2007) AOD-konvertterin virtausmalli. Report 327, University of Oulu, Department of Process and Environmental Engineering, Oulu, Finland.
545. Tanaka T, Goto H, Nakamoto M, Suyuki M, Hanao M, Zeze M, Zamamura H & Yoskihawa T (2016) Dynamic Changes in Interfacial Tension between Liquid Fe Alloy and Molten Slag Induced by Chemical Reactions. ISIJ Int. 56(6): 944–952.
546. Sulasalmi P, Visuri V-V, Kärnä A, Järvinen M, Ollila S & Fabritius T (2016) A Mathematical Model for the Reduction Stage of the CAS-OB Process. Metall. Mater. Trans. B 47(6): 3544–3556.
547. Girifalco LA & Good RJ (1957) A Theory for the Estimation of Surface and Interfacial Energies. I. Derivation and Application to Interfacial Tension. J. Phys. Chem. 61(7): 904–909.
548. Slye WE & Fruehan RJ (1999) The Activity of Silicon in Liquid Fe-Si and Fe-Si-Cr alloys at 1600 °C. In: Proc. 57th Electric Furnace Conference, pp. 401–412. Iron & Steel Society, Pittsburgh, PA, USA.
549. Zhang L & Oeters F (2006) Melting and mixing of alloying agents in steel melts. Methods of mathematical modelling. Verlag Stahleisen GmbH, Düsseldorf, Germany.
550. Järvinen M, Kärnä A, Ollila S & Fabritius T (2012) A novel approach for numerical modeling of the CAS-OB process. In: Proc. 4th International Conference on Process Development in Iron and Steelmaking, volume 1, pp. 79–88. Swerea MEFOS, Luleå, Sweden.
551. Järvinen M, Kärnä A, Visuri V-V, Sulasalmi P, Heikkinen E-P, Pääskylä K, De Blasio C, Ollila S & Fabritius T (2014) A Novel Approach for Numerical Modeling of the CAS-OB Process: Process Model for the Heat-Up Stage. ISIJ Int. 54(10): 2263–2272.
552. Argyropoulos SA & Guthrie RIL (1979) The Exothermic Dissolution of 50 wt.% Ferro-Silicon in Molten Steel. Can. Metall. Quart. 18(3): 267–281.
553. Li J, Brooks G & Provatas N (2005) Kinetics of Scrap Melting in Liquid Steel. Metall. Mater. Trans. B 36(2): 293–302.
554. Zayakin OV, Zhuchkov VI & Lozovaya EY (2007) Melting time of nickel-bearing ferroalloys in steel. Steel Transl. 37(5): 416–418.
555. Turkdogan ET (1996) Fundamentals of Steelmaking. The Institute of Materials, London, United Kingdom.
556. Ma Z & Janke D (2003) Thermodynamic Assessment to Chromium Oxidation in the

Production of Stainless Steel. Steel Res. 74(2): 99–103.
557. Ma ZT, Ohser J & Janke D (1997) Thermodynamic Treatment of Multicomponent Systems using Interaction Parameters. Acta Metall. Sin. 10(5): 375–385.
558. Lupis CHP & Elliott JF (1966) Generalised Interaction Coefficients. Acta Metall. 14(4): 529–538.
559. Darken LS (1967) Thermodynamics of Binary Metallic Solutions. Trans. Metall. Soc. AIME 239(1): 80–89.
560. Darken LS (1967) Thermodynamics of Ternary Metallic Solutions. Trans. Metall. Soc. AIME 239(1): 90–96.
561. Margules M (1895) Über die Zusammensetzung der gesättigten Dämpfe von Mischungen. Sitzb. d. mathem.-naturw. Cl. 104(2a): 1243–1278.
562. Ma Z & Janke D (1999) Activities of carbon and nitrogen in Fe-Cr and Fe-Cr-Ni melts. Steel Res. 70(12): 491–495.
563. Ma Z & Janke D (1999) Oxygen and nitrogen reactions inf Fe-X and Fe-Cr-Ni-X melts. 1999 70(10): 395–402.
564. Ma ZT & Janke D (1998) Thermodynamic Properties of Nitrogen in Fe-Cr-Ni Alloys at 1873K. Acta Metall. Sin. 11(4): 235–240.
565. Sigworth GK & Elliott JF (1974) The Thermodynamics of Liquid Dilute Iron Alloys. Met. Sci. 8(1): 298–310.
566. Ueno S, Waseda Y, Jacob TK & Tamaki S (1988) Theoretical treatment of interaction parameters in multicomponent metallic solutions. Steel Res. 59(11): 474–483.
567. Malyutin KV & Paderin SN (2007) Interaction Parameters of Carbon in Liquid Iron and the Thermodynamics of Carbon and Oxygen in Alloyed Iron Melts. Russ. Metall. 2007(7): 545–551.
568. Alpatov AV & Paderin SN (2010) Thermodynamic Models of Liquid Multicomponent Metallic Solutions. Russ. Metall. 2010(6): 557–564.
569. Ban-Ya S (1993) Mathematical Expression of Slag-Metal Reactions in Steelmaking Process by Ouadratic Formalism Based on the Regular Solution Model. ISIJ Int. 33(1): 2–11.
570. Pelton AD & Blander M (1986) Thermodynamic Analysis of Ordered Liquid Solutions by a Modified Quasichemical Approach – Application to Silicate Slags. Metall. Trans. B 17(6): 805–815.
571. Pelton AD, Degterov SA, Eriksson G, Robelin C & Dessureault Y (2000) The Modified Quasichemical Model I – Binary Solutions. Metall. Mater. Trans. B 31(4): 651–659.
572. Pelton AD & Chartrand P (2001) The Modified Quasi-Chemical Model: Part II. Multicomponent Solutions. Metall. Mater. Trans. A. 32(6): 1355–1360.
573. Chartrand P & Pelton AD (2001) The Modified Quasi-chemical Model: Part III. Two Sublattices. Metall. Mater. Trans. A 32(6): 1397–1407.
574. Pelton AD, Chartrand P & Eriksson G (2001) The Modified Quasi-chemical Model: Part IV. Two Sublattice Quadruplet Approximation. Metall. Mater. Trans. A 32(6): 1409–1416.
575. Hillert M, Jansson B, Sundman B & Ågren J (1985) A Two Sublattice Model for Molten Solutions with Different Tendency for Ionization. Metall. Trans. A 16(2): 261–266.
576. Kapoor ML & Frohberg MG (1971) Theoretical treatment of activities in silicate melts. In: Proc. Symposium on Chemical Metallurgy of Iron and Steel, pp. 17–25. The Iron and Steel Institute, London, United Kingdom.
577. Toop G & Samis C (1962) Activities of ions in silicate melts. Trans. Met. Soc. AIME 224: 878–887.

578. Masson CR (1965) An approach to the problem of ionic distribution in liquid silicates. Proc. R. Soc. London Ser. A 287: 201–221.
579. Masson CR, Smith IB & Whiteway SG (1970) Activities and ionic distributions in liquid silicates: application of polymer theory. Can. J. Chem. 48(9): 1456–1464.
580. Whiteway WG, Smith IB & Masson CR (1970) Theory of molecular size distribution in multichain polymers. Can. J. Chem. 48(1): 33–45.
581. Tao DP (2004) A Comparison of the Molecular Interaction Volume Model with the Subregular Solution Model in Multicomponent Liquid Alloys. Metall. Mater. Trans. A 35(2): 419–424.
582. Tao DP (2006) Prediction of Activities of Three Components in the ernary Molten Slag CaO-FeO-SiO_2 by the Molecular Interaction Volume Model. Metall. Mater. Trans. B 37(6): 1091–1097.
583. Ohta H & Suito H (1995) Activities of MnO in CaO-SiO_2-Al_2O_3-MnO (<10 Pct)-Fe_tO (<3 Pct) Slags Saturated with Liquid Iron. Metall. Mater. Trans. B 26(2): 295–303.
584. Ohta H & Suito H (1996) Activities in MnO-SiO_2-Al_2O_3 Slags and Deoxidation Equilibria of Mn and Si. Metall. Mater. Trans. B 27(2): 263–270.
585. Ohta H & Suito H (1998) Activities of SiO_2 and Al_2O_3 and Activity Coefficients of Fe_tO and MnO in CaO-SiO_2-Al_2O_3-MgO Slags. Metall. Mater. Trans. B 29(1): 119–129.
586. Li H, Morris AE & Robertson DGC (1998) Thermodynamic Model for MnO-Containing Slags and Gas-Slag-Metal Equilibrium in Ferromanganese Smelting. Metall. Mater. Trans. B. 29(6): 1181–1191.
587. Jung I-H (2010) Overview of the applications of thermodynamic databases to steelmaking processes. CALPHAD 34(3): 332–362.
588. Iguchi Y (1990) The thermochemistry of ferrous melts. In: The Elliott Symposium on Chemical Process Metallurgy, pp. 129–147. The Iron and Steel Society, Warrendale, PA, USA.
589. GTT-Technologies GmbH (2015). FactSage 7.0.
590. IAEA (2008) Thermophysical Properties of Materials for Nuclear Engineering: A Tutorial and Collection of Data. International Atomic Energy Agency, Vienna, Austria.
591. Keene BJ & Mills KC (1995) Densities of molten slags. In: Verein Deutscher Eisenhüttenleute (ed.) Slag Atlas 2nd Edition, pp. 313–348. Verlag Stahleisen GmbH, Düsseldorf, Germany.
592. Wilke CR (1950) A Viscosity Equation for Gas Mixtures. J. Chem. Phys. 18(4): 517–519.
593. Cloutman LD (1993) A Database of Selected Transport Coefficients for Combustion Studies. Lawrence Livermore National Laboratory, Livermore, CA, USA.
594. Forsbacka L, Holappa L, Kondratiev A & Jak E (2007) Experimental Study and Modelling of Chromium Containing Slags. Steel Res. Int. 78(9): 676–684.
595. Thomas DG (1965) Transport characteristics of suspension: VIII. A note on the viscosity of Newtonian suspensions of uniform spherical particles. J. Colloid Sci. 20: 267–277.
596. Nagata K, Ono Y, Ejima T & Yamamura T (1988) Diffusion. In: Kawai Y & Shiraishi Y (eds.) Handbook of Physico-chemical Properties at High Temperatures, pp. 181–204. The Iron and Steel Institute of Japan, Tokyo, Japan.
597. Wilke CR & Lee CY (1955) Estimation of Diffusion Coefficients for Gases and Vapors. Ind. Eng. Chem. 47(6): 1253–1257.
598. Mills KC (1995) Diffusion coefficients in molten slags. In: Verein Deutscher Eisenhüttenleute (ed.) Slag Atlas 2nd Edition, pp. 541–556. Verlag Stahleisen GmbH, Düsseldorf,

Germany.
599. Mason EA & Saxena SC (1958) Approximate Formula for the Thermal Conductivity of Gas Mixtures. Phys. Fluids 1(5): 361–369.
600. Mills KC & Susa M (1995) Thermal conductivities of slags. In: Verein Deutscher Eisenhüttenleute (ed.) Slag Atlas 2nd Edition, pp. 591–600. Verlag Stahleisen GmbH, Düsseldorf, Germany.
601. Press WH, Teukolsky SA, Vetterling WT & Flannery BP (2002) Numerical Recipes in C – The Art of Scientific Computing. Press Syndicate of the University of Cambridge, Cambridge, UK, 2. edition.
602. Argyros IK & Hilout S (2013) Computational Methods in Nonlinear Analysis – Efficient Algorithms, Fixed Point Theory and Applications. World Scientific Publishing Co. Pte. Ltd., Singapore.
603. Visuri V-V, Järvinen M, Pääskylä K, Kärnä A, Sulasalmi P, De Blasio C, Ollila S & Fabritius T (2014) Preliminary validation of a numerical model for the CAS-OB process. In: Proc. 7th European Oxygen Steelmaking Conference. Czech Metallurgical Society, Třinec, Czech Republic.
604. Järvinen M, Visuri V-V, Heikkinen E-P, Kärnä A, Sulasalmi P, De Blasio C & Fabritius T (2016) Law of Mass Action Based Kinetic Approach for the Modelling of Parallel Mass Transfer Limited Reactions: Application to Metallurgical Systems. ISIJ Int. 56(9): 1543–1552.
605. Spiess J, Lempradi H, Staudinger G & Zipp P (2005) Technological challenges in stainless steel production at Outokumpu Stainless. Rev. Met. Paris 102(4): 329–335.
606. Roininen J, Kupari P & Parviainen T (2011) Ruostumattoman teräksenvalmistuksen kuonat. In: Kuonat prosessimetallurgiassa. POHTO, Oulu, Finland.
607. Kuwano T, Maruhashi S & Aoyama Y (1973) Decarburization of Molten High Chromium Steel under Reduced Pressure. Tetsu-to-Hagané 59(7): 863–873.
608. Koch K, Hahn F-J, Maas H & Schmöle P (1983) Reaktionen beim Aufblasen von Sauerstoff auf C-Cr-Si-haltige Eisenschmelzen unter normalem und vermintertem Druck. Arch. Eisenhüttenwes. 54(3): 99–102.
609. Kitamura S-Y, Okohira K & Tanaka A (1986) Influence of Bath Stirring Intensity and Top Blown Oxygen Supply Rate on Decarburization of High Chromium Molten Iron. Trans. Iron Steel Inst. Jpn. 26(1): 33–39.
610. Yamada K, Azuma H, Hiyama T & Nishimae N (1983) Direct Stainless Steelmaking by AOD Process with Top Blowing from Molten Fe-Ni and Fe-Cr Materials. Tetsu-to-Hagané 69(7): 775–781.
611. Zughbi HD (2003) Decarburization of Fe/C melts in a crucible: Effect of gas flow rate and composition. Scand. J. Metall. 32(4): 194–202.
612. Sumi I, Kishimoto Y, Kikuchi Y & Igarashi H (2006) Effect of High-temperature Field on Supersonic Oxygen Jet Behaviour. ISIJ Int. 46(9): 1312–1317.
613. Alam M, Naser J & Brooks G (2010) Computational Fluid Dynamics Simulation of Supersonic Oxygen Jet Behavior at Steelmaking Temperature. Metall. Mater. Trans. B 41(3): 636–645.
614. He QL & Standish N (1990) A Model Study of Residence Time of Metal Droplets in the Slag in BOF Steelmaking. ISIJ Int. 30(5): 356–361.
615. Subagyo, Brooks GA & Coley KS (2002) Interfacial area in top blown oxygen steelmaking. In: Proc. 61st Ironmaking Conference, pp. 837–850. Iron and Steel Society, Nashville, TN,

USA.
616. Subagyo, Brooks GA & Coley KS (2005) Residence time of metal droplets in slag-metal-gas emulsions through top gas blowing. Can. Metall. Quart. 44(1): 119–130.
617. Ghosh S, Ballal NB & Nasu S (2015) Modelling of the Slag-Gas-Metal Foam in the BOF – Recent Insights. In: Proc. 6th International Congress on the Science and Technology of Steelmaking, volume 1, pp. 116–119. The Chinese Society for Metals, Beijing, China.
618. Ji F, Rhamdhani M, Subagyo, Barati M, Coley KS, Brooks GA, Irons GA & Nightingale S (2003) Treatment of Transient Phenomena in Analysis of Slag-Metal-Gas Reaction Kinetics. High Temp. Mater. Proc. 22(5-6): 359–367.
619. Turner G & Jahanshahi S (1987) A Model Investigation on Emulsification of Metal Droplets in the Basic Oxygen Steelmaking Processes. Trans. Iron Steel Inst. Jpn. 27(9): 734–739.
620. He QL & Standish N (1990) A Model Study of Droplet Generation in the BOF Steelmaking. ISIJ Int. 30(4): 305–309.
621. Fabritius TMJ, Luomala MJ, Virtanen EO, Tenkku H, Fabritius TLJ, Siivola TP & Härkki JJ (2002) Effect of Bottom Nozzle Arrangement on Splashing and Spitting in Combined Blowing Converter. ISIJ Int. 42(8): 861–867.
622. Brooks G, Sabah S, Rout B & Li Z (2017) Splash Generation in Oxygen Steelmaking: What is Known? In: Proc. AISTech 2017, pp. 1253–1260. Association for Iron & Steel Technology, Nashville, TN, USA.
623. Gao K, Sahajwalla V, Sun H, Wheatley C & Dry R (2000) Influence of Sulfur Content and Temperature on the Carbon Boil and CO Generation in Fe–C–S Drops. ISIJ Int. (4): 301–308.
624. Lee YE, Klevan OS & Guthrie RIL (1992) A Model Study to Examine the Reactions during Reduction Period of AOD Process. In: Proc. 11th Process Technology Division Conference, pp. 131–138. Iron and Steel Society, Atlanta, GA, USA.
625. Khajavi LT & Barati M (2010) Cold Model Study of Emulsification Behavior in Bottom Blown Metallurgical Baths Covered with Thick Slag. ISIJ Int. 50(5): 654–662.
626. Kivelä V (2016) AOD-prosessimallien hyödyntäminen mellotuksen kehittämisessä. Master's thesis, University of Oulu.
627. Holzhauser J-F, Scheller PR, Wiedemeier F-J & Zörcher H (1992) Prozeßführung und Qualitätssicherung für nichtrostende Stähle im Stahlwerk Bochum der Krupp Stahl AG. Stahl Eisen 112(6): 97–102.
628. Noll R, Bette H, Brysch A, Kraushaar M, Mönch I, Peter L & Sturm V (2001) Laser-induced breakdown spectrometry - Applications for production control and quality assurance in the steel industry. Spectrochim. Acta B 56(6): 637–649.
629. Wiens O (2005) Entwicklung eines in situ LIBS-Messverfahrens für eine quantitative Analyse prozessrelevanter Komponenten in flüssiger Schlacke. Doctoral thesis, Rheinisch-Westfälische Technische Hochschule Aachen, Aachen, Germany.
630. Pilz K (2012) Online-Analytik zur Prozesskontrolle in der voestalpine Stahl GmbH. Berg-Hüttenmänn. Monatsh. 157(8): 250–257.
631. Noll R, Fricke-Begemann C, Brunk M, Connemann S, Meinhardt C, Scharun M, Sturm V, Makowe J & Gehlen C (2014) Laser-induced breakdown spectroscopy expands into industrial applications. Spectrochim. Acta B 93: 41–51.
632. Sturm V, Feige R, De Kanter M, Leitner R, Pilz K, Fischer D, Hubmer G & Noll R (2014) Laser-induced breakdown spectroscopy for 24/7 automatic liquid slag analysis at a steel works. Anal. Chem. 86(19): 9687–9692.

633. Heise BH & Dokken RN (1978). Use of CO_2 in argon-oxygen refining of molten metal. United States Patent Re 29,584.
634. Sain DR & Belton GR (1976) Interfacial Reaction Kinetics in the Decarburization of Liquid Iron by Carbon Dioxide. Metall. Trans. B. 7(3): 235–244.
635. Petit CP & Fruehan RJ (1997) Influence of Chromium and Nickel on the Dissociation of CO_2 on Carbon-Saturated Liquid Iron. Metall. Mater. Trans. B 28(4): 639–645.
636. Simento N, Lee H-G & Hayes P (1998) Kinetics of decarburisation of levitating liquid iron drops by carbon dioxide. Steel Res. 69(8): 318–324.
637. Simento NJ, Lee H-G & Hayes PC (1999) Decarburisation of Liquid Fe–C–S Drops using Multiple Oxidants of O_2, CO_2 and H_2O. ISIJ Int. 39(12): 1217–1223.
638. Wang H, Teng L & Seetharaman S (2012) Investigation of the Oxidation Kinetics of Fe-Cr and Fe-Cr-C Melts under Controlled Oxygen Partial Pressures. Metall. Mater. Trans. B 43(6): 1476–1487.
639. Wang H, Nzotta MM, Teng L & Seetharaman S (2013) Decarburization of ferrochrome and high alloy steels with optimized gas and slag phases towards improved Cr retention. J. Min. Metall. Sect. B Metall. 49(2): 175–181.
640. Lv M, Zhu R, Wei X, Wang H & Bi X (2012) Research on Top and Bottom Mixed Blowing CO_2 in Converter Steelmaking Process. Steel Res. Int. 83(1): 11–15.
641. Heikkinen E-P, Visuri V-V, Suopajärvi H, Kemppainen A, Aula M, Sulasalmi P & Fabritius T (2017) Selected research focus areas for energy and material improvements in reduction and refining metallurgy. In: Proc. 2nd ISIJ-VDEh-Jernkontoret Joint Symposium, pp. 24–33. Jernkontoret, Stockholm, Sweden.
642. Visuri V-V, Sulasalmi P & Kärnä A (2016) Simulators for the AOD and CAS-OB processes. In: DIMECC 9th Annual Seminar. DIMECC Oy, Helsinki, Finland. Poster presentation on November 14, 2016.

Appendix 1 Description of properties

As for the mathematical treatment of mass and heat transfer, the physical properties of the steel and slag phases were estimated at the temperature, pressure, and composition of the reaction interface in question, while the properties of the gas phase were evaluated at the gas film temperature, which was approximated as follows [1]:

$$T_{\mathrm{G}} = 0.5 \cdot \left(T^{*} + T_{\mathrm{gas}}\right) , \tag{A1.1}$$

where T^{*} is the temperature of the reaction interface and T_{gas} is the temperature of the bulk gas phase. The pressure changes in the gas jet are small enough to be ignored [2] and hence the total gas pressure at the cavity and metal droplet interfaces was taken as equal to the ambient pressure, $p_{\mathrm{G,cav}} = p_{\mathrm{G,md}} = p_{\mathrm{amb}}$. Similarly, the total pressure at the slag-droplet interface was set to be equal to the ambient pressure, $p_{\mathrm{G,sd}} = p_{\mathrm{amb}}$. For the conditions of the AOD process, a value of p_{amb} = 1 atm (101325 Pa) was employed. It should be noted that this value can be changed in the user interface, thus allowing for the simulation of reactions under vacuum conditions.

1.1 Physical properties

1.1.1 Density

The density of liquid stainless steel (AISI 304) was calculated according to [3]:

$$\rho_{\mathrm{L}} = 7433 + 0.0393T - 1.80110^{-4}T^{2} . \tag{A1.2}$$

The equation of state for an ideal gas is given by [4]:

$$p_{\mathrm{G}}V = nRT . \tag{A1.3}$$

where p_{G} is the pressure. By substituting $\rho_{\mathrm{G}} = \frac{nM}{V}$ and $p_i = x_i p_{\mathrm{G}}$ (Dalton's law) into Eq. A1.3, the following expression is obtained for the density of an ideal gas mixture:

$$\rho_{\mathrm{G}} = \underbrace{\frac{p_{\mathrm{G}} M_{\mathrm{G}}}{\sum_{i}^{n_{\mathrm{G}}} RT x_i}}_{\text{molar basis}} = \underbrace{\frac{p_{\mathrm{G}}}{\sum_{i}^{n_{\mathrm{G}}} RT \frac{y_i}{M_i}}}_{\text{mass basis}} , \tag{A1.4}$$

where M_G is the molar mass of the gas mixture. The density of the slag phase was calculated based on the partial molar volume method [5]:

$$\rho_S = \frac{M_S}{\sum_i^{n_S} x_i \overline{V}_i}, \tag{A1.5}$$

where M_S is the molar mass of the slag phase and $\overline{V}_i$ is the partial molar volume of species i. The partial molar volumes of the slag species were obtained from the literature [5, 6] and their temperature dependency was treated similarly to Hanao *et al.* [7].

1.1.2 Viscosity

The viscosity of the liquid stainless steel (AISI 304) was calculated according to [3]:

$$\log_{10} \mu_L = \frac{2385.2}{T} - 3.5958, \tag{A1.6}$$

where T is the temperature. The viscosity of the gas mixture was calculated according to the equation proposed by Wilke [8]. A slightly modified formulation of the Wilke equation was obtained from Bird *et al.* [9]:

$$\mu_G = \sum_i^{n_G} \frac{x_i \mu_i}{\sum_j^{n_G} x_j \Phi_{ij}}, \tag{A1.7}$$

in which

$$\Phi_{ij} = \frac{1}{\sqrt{8}} \left(1 + \frac{M_i}{M_j}\right)^{-0.5} \left[1 + \left(\frac{\mu_i}{\mu_j}\right)^{0.5} \left(\frac{M_j}{M_i}\right)^{0.25}\right]^2. \tag{A1.8}$$

The dynamic viscosity of gaseous species (in Pa·s) was calculated according to the Chapman-Enskog equation [9]:

$$\mu = 2.6693 \cdot 10^{-6} \frac{\sqrt{1000MT}}{\sigma^2 \Omega_\mu}, \tag{A1.9}$$

where σ is the collision diameter and Ω_μ is the collision integral of the molecule. The collision integral was estimated as follows [10, 11]:

$$\Omega_\mu = 1.147 \left(\frac{k_B T}{\varepsilon}\right)^{-0.145} + \left(\frac{k_B T}{\varepsilon} + 0.5\right)^{-2}, \tag{A1.10}$$

where k_B is the Boltzmann constant and ε is the Lennard-Jones potential well depth. The Lennard-Jones parameters σ and ε/k_B of the relevant species were taken from the literature [12] and are shown in Table 1.

Table 1. Lennard-Jones parameters for gaseous species [12].

	Species				
Property	O_2	CO	CO_2	N_2	Ar
σ [Å]	3.433	3.590	3.996	3.681	3.418
ε/k_B [K]	113.0	110.0	190.0	91.5	124.0

During decarburization, the top slag consists of a molten slag phase saturated with chromium oxide and a solid chromium oxide phase [13]. An exhaustive review of the viscosity models for molten slags is available in the literature [14] and is not repeated here. In this work, the viscosity of the liquid part ($\mu_{S(l)}$) was calculated using the viscosity model proposed by Forsbacka *et al.* [15], which is an extension of the modified Urbain model [16] for the Al_2O_3–CaO-CrO–Cr_2O_3–'FeO'–MgO–SiO_2 system. The dynamic viscosity (in Pa·s) is given by the Weymann-Frenkel relation [15]:

$$\mu_{S(l)} = 0.1 \cdot AT \exp\left(\frac{1000B}{T}\right), \tag{A1.11}$$

The parameters A, m, B, and α are defined according to Eqs. A1.12, A1.13, A1.14, and A1.15, respectively [15].

$$-\ln A = mB + n, \tag{A1.12}$$

$$\begin{aligned} m = {} & m_{Al_2O_3} X_{Al_2O_3} + m_{CaO} X_{CaO} + m_{FeO} X_{FeO} \\ & + m_{Cr_2O_3} X_{Cr_2O_3} + m_{MgO} X_{MgO} + m_{SiO_2} X_{SiO_2}, \end{aligned} \tag{A1.13}$$

$$\begin{aligned} B = {} & \sum_{i=0}^{3} b_i^0 X_{SiO_2}^i + \sum_{i=0}^{3}\sum_{j=1}^{2} \Bigg[b_i^{CaO,j} \frac{X_{CaO}}{X_{CaO} + X_{FeO} + X_{Cr_2O_3} + X_{MgO}} \\ & + b_i^{FeO,j} \frac{X_{FeO}}{X_{CaO} + X_{FeO} + X_{Cr_2O_3} + X_{MgO}} \\ & + b_i^{Cr_2O_3,j} \frac{X_{Cr_2O_3}}{X_{CaO} + X_{FeO} + X_{Cr_2O_3} + X_{MgO}} \\ & + b_i^{MgO,j} \frac{X_{MgO}}{X_{CaO} + X_{FeO} + X_{Cr_2O_3} + X_{MgO}} \Bigg] \alpha^j X_{SiO_2}^i, \end{aligned} \tag{A1.14}$$

$$\alpha = \frac{X_{CaO} + X_{FeO} + X_{Cr_2O_3} + X_{MgO}}{X_{Al_2O_3} + X_{CaO} + X_{FeO} + X_{Cr_2O_3} + X_{MgO}}, \tag{A1.15}$$

where X is the cation fraction, while n and b are constants available in Ref. [15]. The cation fractions were calculated according to [17]:

$$X_i = \frac{x_i N_{O,i}}{\sum_j^n x_j N_{O,j}}, \tag{A1.16}$$

where x_i is the mole fraction of species i and $N_{O,i}$ is the number of oxygen atoms in one molecule of species i. The effect of solid particles on the effective viscosity of slag in the decarburisation stage was taken into account by employing the concept of *relative viscosity*:

$$\mu_S = \mu_{S(l)} \mu_{S,rel}, \tag{A1.17}$$

where $\mu_{S(l)}$ is the viscosity of the liquid part and $\mu_{S,rel}$ is the relative viscosity. Numerous models have been proposed for calculating the relative viscosity based on the volume fraction of solids [18–25]. In this work, the relative viscosity was calculated according to Thomas [25]:

$$\mu_{S,rel} = 1 + 2.5\phi + 10.05\phi^2 + 0.00237 \times \exp(16.6\phi), \tag{A1.18}$$

where ϕ is the solid fraction. In this work, it was assumed that the volume fraction of solids in the slag is equal to their weight-fraction, *i.e.* $\phi_{(s)} = y_{(s)}$. The weight-fraction of the solids was defined as a linear function of the weight-fraction of solid Cr_2O_3 in the slag:

$$y_{(s)} = A \cdot y_{Cr_2O_3\,(s)}, \tag{A1.19}$$

where A is a fitting parameter and $y_{Cr_2O_3}$ is the weight-fraction of solid Cr_2O_3 in the slag. The weight-fraction of solid Cr_2O_3 was calculated as follows:

$$y_{Cr_2O_3\,(s)} = \max\left(y_{Cr_2O_3} - y_{Cr_2O_3\,(l)}, 0\right), \tag{A1.20}$$

where $y_{Cr_2O_3}$is the total weight-fraction of Cr_2O_3 in the slag and $y_{Cr_2O_3\,(l)}$ is the maximum weight-fraction of soluble Cr_2O_3 in the liquid slag. The solid fractions of the slag samples taken in this work were calculated with the FactSage 7.0 thermodynamic software [26] at the temperature measured from metal bath at corresponding occasions. With the help of the results of these calculations, the values of $y_{Cr_2O_3\,(l)}$ and A were determined based on the method of least squares. The best agreement was obtained with

$y_{Cr_2O_3\,(l)} = 0.078$ (*i.e.* 7.8 wt-%) and $A = 1.55$. It should be noted that the employed value of Cr_2O_3 solubility is quite close to the value of $y_{Cr_2O_3\,(l)} = 0.05$ (*i.e.* 5 wt-%) employed by Wei and Zhu [27].

1.1.3 Mass diffusivity

In view of the relatively dilute concentrations of species dissolved in the steel bath [28], the effective mass diffusivities of species in the metal phase were assumed to be equal to their interdiffusivity in liquid iron. Where possible, their temperature dependency was described by an Arrhenius type relationship [29]:

$$D_L = D_0 \exp\left(-\frac{E_D}{RT}\right), \tag{A1.21}$$

where D_0 is the maximum mass diffusivity and E_D is the activity energy of diffusion. The effective mass diffusivities of species in the gas phase were assumed to be equal to the binary mass diffusivity of O_2 in O_2–CO system, for which a value of $D_{G,eff} = 0.185 \times 10^{-4}$ m^2/s at 273.0 K (–0.15°C) and 101325 Pa was extracted from Wilke and Lee [30]. As shown by Taylor and Krishna [28], this assumption holds well for the O_2–N_2–CO system. The effect of pressure and temperature on the mass diffusivity of gaseous species was treated similarly as by Järvinen *et al.* [31]:

$$D_G = D_{G,eff} \cdot \left(\frac{T_G}{T_{ref}}\right)^{1.5} \left(\frac{p_{ref}}{p_G}\right), \tag{A1.22}$$

where $D_{G,eff}$ is the effective mass diffusivity at ambient pressure, T_{ref} is the reference temperature of the effective mass diffusivity, p_{ref} is the reference pressure, and p_G is the total gas pressure. The species in the slag phase were assigned an equal effective diffusivity. In the top-blowing model, the effective diffusivity was estimated to be $5.0 \cdot 10^{-10}$ m^2/s at 1873 K (1600 °C) based on a compilation of experimental data by Mills [32]. To account for the effect of lower slag viscosity on the diffusivity, a slightly higher value of $1.0 \cdot 10^{-9}$ m^2/s was employed in the reduction model.

1.1.4 Thermal conductivity

The description for the thermal conductivity of the liquid steel (AISI 304) was taken from Ref. [3] and can be expressed as follows:

$$\lambda_{\mathrm{L}} = 12.41 + 0.003279T\,. \tag{A1.23}$$

The thermal conductivity of the gas mixture was calculated according to the Mason–Saxena equation [33]. A slightly modified form of this equation can be presented as follows [9]:

$$\lambda_{\mathrm{G}} = \sum_{i}^{n_{\mathrm{G}}} \frac{x_i \lambda_i}{\sum\limits_{i}^{n_{\mathrm{G}}} x_j \Phi_{ij}}\,, \tag{A1.24}$$

where λ_i is the thermal conductivity of species i. The parameter Φ_{ij} was calculated based on the Chapman-Enskog theory (see Eq. A1.8). The thermal conductivity polyatomic gaseous species at low density can be calculated with the Eucken equation [34], which was obtained from Bird *et al.* [9]:

$$\lambda = \left(c_{\mathrm{p}} + \frac{5}{4}\frac{R}{M}\right)\mu\,. \tag{A1.25}$$

It should be noted that Eq. A1.25 includes monoatomic gases as a special case [9]. The thermal conductivity of the slag phase was assigned a value of λ_{S} = 1.0 W/(m·K), which represents a rough estimate based on the compilation of thermal conductivity data by Mills and Susa [35].

1.1.5 Interfacial tension

The effective metal–slag interfacial tension was assumed to be 50% of the nominal metal–slag interfacial tension. The nominal metal–slag interfacial tension can be calculated according to the Girifalco–Good equation [36]:

$$\sigma_{\mathrm{L\text{–}S}} = \sigma_{\mathrm{L}} + \sigma_{\mathrm{S}} - 2\phi\left(\sigma_{\mathrm{L}} \cdot \sigma_{\mathrm{S}}\right)^{1/2}, \tag{A1.26}$$

where ϕ is the proportionality factor. The values applicable for the reduction stage are σ_{L} = 1.5 N/m [37], σ_{S} = 0.49 N/m [38], and ϕ = 0.503 [38]. Substituting the aforementioned values to Eq. A1.26 yields a nominal interfacial tension of $\sigma_{\mathrm{L\text{–}S}} \approx 1.13$ N/m. The resulting effective interfacial tension is $\sigma_{\mathrm{L\text{–}S}} \approx 0.56$ N/m.

1.2 Thermodynamic properties

1.2.1 Interaction parameters

The molar first-order interaction parameters employed in the top-blowing and reduction models are shown in Tables 2 and 3, respectively. With the exception of $\varepsilon_{\mathrm{Si}}^{\mathrm{Si}}$ and $\varepsilon_{\mathrm{Mn}}^{\mathrm{Mn}}$, the parameters employed in the reduction model are the same as those employed in the top-blowing model. A higher value of $\varepsilon_{\mathrm{Si}}^{\mathrm{Si}}$ was employed to obtain a sufficient oxidation of Si, while the value of $\varepsilon_{\mathrm{Mn}}^{\mathrm{Mn}}$ was adjusted to enable sufficient reduction of MnO.

Table 2. Molar first-order interaction parameters employed in the top-blowing model. Reproduced from Article I.

ε_i^j	Fe	Cr	Mn	Si	C
Fe	–	–	–	–	–
Cr	–	0.00475 [39]	–	1.73 [40]	–4.9 [41]
Mn	–	–	–0.642 [39]	–3.3 [41]	–1.9 [41]
Si	–	1.73 [40]	–3.3 [41]	12.0 [41]	9.8 [41]
C	–	–4.9 [41]	–1.9 [41]	9.8 [41]	13 [41]
O	–	–4.84 [42]	–4.7 [42]	–7.1 [42]	–20 [42]
N	–	–9.8 [41]	–4.5 [41]	6.1 [41]	7.2 [41]
Ni	–	–0.0027 [41]	–1.8 [41]	1.2 [41]	2.4 [41]
Al	–	–	–	7.0 [41]	5.3 [41]
S	–	–2.2 [39]	–5.9 [39]	9.2 [39]	6.3 [39]
ε_i^j	O	N	Ni	Al	S
Fe	–	–	–	–	–
Cr	–4.84 [42]	–9.8 [41]	–0.0027 [41]	–	–2.2 [39]
Mn	–4.7 [42]	–4.5 [41]	–1.8 [41]	–	–5.9 [39]
Si	–7.1 [42]	6.1 [41]	1.2 [41]	7.0 [41]	9.2 [39]
C	–20.0 [42]	7.2 [41]	2.4 [41]	5.3 [41]	6.3 [39]
O	–10.7 [42]	4.0 [43]	2.4 [42]	–434.2 [43]	–17.1 [43]
N	4.0 [43]	0.75 [41]	1.6 [41]	1.6 [41]	1.4 [43]
Ni	2.4 [42]	1.6 [41]	0.17 [43]	–	0 [42]
Al	–434.2 [43]	1.6 [41]	–	5.5 [43]	4.4 [43]
S	–17.1 [43]	1.4 [43]	0 [42]	4.4 [43]	–5.6 [39]

Table 3. Molar first-order interaction parameters employed in the modified reduction model.

ε_i^j	Fe	Cr	Mn	Si	C
Fe	–	–	–	–	–
Cr	–	0.00475 [39]	–	1.73 [40]	–4.9 [41]
Mn	–	–	–100	–3.3 [41]	–1.9 [41]
Si	–	1.73 [40]	–3.3 [41]	126.6 [40]	9.8 [41]
C	–	–4.9 [41]	–1.9 [41]	9.8 [41]	13 [41]
O	–	–4.84 [42]	–4.7 [42]	–7.1 [42]	–20 [42]
N	–	–9.8 [41]	–4.5 [41]	6.1 [41]	7.2 [41]
Ni	–	–0.0027 [41]	–1.8 [41]	1.2 [41]	2.4 [41]
Al	–	–	–	7.0 [41]	5.3 [41]
S	–	–2.2 [39]	–5.9 [39]	9.2 [39]	6.3 [39]
ε_i^j	O	N	Ni	Al	S
Fe	–	–	–	–	–
Cr	–4.84 [42]	–9.8 [41]	–0.0027 [41]	–	–2.2 [39]
Mn	–4.7 [42]	–4.5 [41]	–1.8 [41]	–	–5.9 [39]
Si	–7.1 [42]	6.1 [41]	1.2 [41]	7.0 [41]	9.2 [39]
C	–20.0 [42]	7.2 [41]	2.4 [41]	5.3 [41]	6.3 [39]
O	–10.7 [42]	4.0 [43]	2.4 [42]	–434.2 [43]	–17.1 [43]
N	4.0 [43]	0.75 [41]	1.6 [41]	1.6 [41]	1.4 [43]
Ni	2.4 [42]	1.6 [41]	0.17 [43]	–	0 [42]
Al	–434.2 [43]	1.6 [41]	–	5.5 [43]	4.4 [43]
S	–17.1 [43]	1.4 [43]	0 [42]	4.4 [43]	–5.6 [39]

1.2.2 Thermochemical properties

According to Hess's law, the heat content change in a chemical reaction at constant temperature and pressure is independent of the number of stages between the initial and final state [44]. Consequently, the reaction enthalpy and reaction entropy can be calculated according to Eqs. A1.27 and A1.28, respectively.

$$\Delta H^\circ = \sum_{i=1}^{n} \nu_i H_i^\circ \,, \tag{A1.27}$$

$$\Delta S^\circ = \sum_{i=1}^{n} \nu_i S_i^\circ \,, \tag{A1.28}$$

where ν_i, ΔH°, and ΔS° are the stoichiometric coefficient, enthalpy, and entropy of species i. The values of ΔH° and ΔS° at temperature T were calculated as follows:

$$H^\circ = H^\circ_{298.15\ \mathrm{K}} + \int_{298.15\ \mathrm{K}}^{T} C_\mathrm{p}\ \mathrm{d}T + H^\circ_{\mathrm{tr},T} + H^\circ_\mathrm{dis}\,, \tag{A1.29}$$

$$S^\circ = S^\circ_{298.15\ \mathrm{K}} + \int_{298.15\ \mathrm{K}}^{T} \frac{C_\mathrm{p}}{T}\ \mathrm{d}T + S^\circ_{\mathrm{tr},T} + S^\circ_\mathrm{dis}\,, \tag{A1.30}$$

where $H^\circ_{298.15\ \mathrm{K}}$ is the enthalpy at 298.15 K (25 °C), $C_{\mathrm{p},i}$ is the molar heat capacity, H°_tr is the total enthalpy of phase transformations from 298.15 K (25 °C) to T, H°_dis is the enthalpy of dissolution, $S^\circ_{298.15\ \mathrm{K}}$ is the entropy at 298.15 K (25 °C), S°_tr is the total entropy of the phase transformations from 298.15 K (25 °C) to T, and S°_dis is the entropy of dissolution. The enthalpies H°_i and entropies S°_i correspond to the following standard states: the Henrian standard state for the species dissolved in the steel bath and the Raoultian standard state for the gas and slag species. For the dissolved species, the relevant values of H°_dis and S°_dis were obtained from Sigworth and Elliott [43]; for the gas and slag species H°_dis and S°_dis were set to zero. The molar heat capacity at temperature T is calculated on the basis of the Shomate equation [45]:

$$C_\mathrm{p} = A + B\cdot 10^{-3}T + C\cdot 10^{5}T^{-2} + D\cdot 10^{-6}T^{2}\,, \tag{A1.31}$$

where A, B, C, and D are the fitting parameters applicable to a certain temperature interval. A comprehensive database of the Shomate equation parameters was taken from HSC Chemistry [45]; for the studied species, the data covers temperatures from room temperature (or lower) to at least 4000 K (3727 °C). The specific heat capacities of species i and phase ψ at temperature T are defined by Eqs. A1.32 and A1.33, respectively.

$$c_{\mathrm{p},i}(T) = \frac{C_{\mathrm{p},i}(T)}{M_i}\,, \tag{A1.32}$$

$$c_{\mathrm{p},\psi}(T) = \sum_{i}^{n_\psi} y_{i,\psi}\, c_{\mathrm{p},i}(T)\,, \tag{A1.33}$$

where M is the molar mass and $y_{i,\psi}$ is the mass fraction of species i in phase ψ.

1.3 Other properties

1.3.1 Terminal velocity

Gas bubbles

The terminal velocity of the gas bubbles was calculated according to Mendelson [46]:

$$u_{\mathrm{b}} = \left(\frac{2\sigma_{\mathrm{L}}}{\rho_{\mathrm{L}} d_{\mathrm{b}}} + \frac{g d_{\mathrm{b}}}{2} \right)^{1/2}, \tag{A1.34}$$

where σ_{L} is the surface tension of liquid metal, ρ_{L} is the density of liquid metal, and d_{b} is the bubble diameter. In [47] it was found that Eq. A1.34 could be used to correlate experimental data from argon bubbles in liquid mercury to the precision of the experiments. Therefore, the application of Eq. A1.34 for liquid steel appears to be justified. The bubble diameter was obtained from [31]:

$$d_{\mathrm{b}} = 0.168 \sqrt{\frac{\sigma_{\mathrm{L}}}{\rho_{\mathrm{L}}^{2/3}}}. \tag{A1.35}$$

Metal droplets

In order to define the terminal velocity of the metal droplets in a slag–metal–gas emulsion, the metal phase was taken as the dispersed phase, while the slag–gas continuum was taken as the continuous phase. The terminal velocity was calculated for each size class by making use of the equation proposed by Subagyo and Brooks [48]:

$$u_{\mathrm{t}} = \begin{cases} \frac{1}{18} \frac{(\rho_{\mathrm{L}} - \rho_{\mathrm{SG}}) g d_{\mathrm{md}}^2}{\mu_{\mathrm{SG}}} \mathfrak{R} & \text{if} \quad \mathrm{Re} < 1 \\ 0.1528 \left[\frac{(\rho_{\mathrm{L}} - \rho_{\mathrm{SG}}) g d_{\mathrm{md}}}{\rho_{\mathrm{SG}}} \left(\frac{\rho_{\mathrm{SG}} d_{\mathrm{md}}}{\mu_{\mathrm{SG}}} \right)^{0.6} \mathfrak{R} \right]^{0.7143} & \text{if} \quad 1 \leq \mathrm{Re} < 10^3 \\ 1.7408 \left[\frac{(\rho_{\mathrm{L}} - \rho_{\mathrm{SG}}) g d_{\mathrm{md}}}{\rho_{\mathrm{SG}}} \mathfrak{R} \right]^{0.5} & \text{if} \quad 10^3 \leq \mathrm{Re} < 10^4 \end{cases}, \tag{A1.36}$$

where ρ_{SG} is the density of the slag–gas continuum, μ_{SG} is the dynamic viscosity of the slag–gas continuum, and $\mathfrak{R}$ is a correction factor, which relates the terminal velocity of a fluid sphere to the velocity of a spherical body moving in a fluid by gravitational force. For Eq. A1.36, the Reynolds number of each size class was evaluated as follows:

$$\mathrm{Re} = \frac{\rho_{\mathrm{SG}} u_{\mathrm{t}} d_{\mathrm{md}}}{\mu_{\mathrm{SG}}} \,. \tag{A1.37}$$

Similarly to Subagyo and Brooks [48], the parameters ρ_{SG}, μ_{SG}, and $\mathfrak{R}$ were solved from Eqs. A1.38, A1.39, and A1.40, respectively.

$$\rho_{\mathrm{SG}} = \rho_{\mathrm{S}} \left(1 - \phi_{\mathrm{G}}\right) , \tag{A1.38}$$

$$\mu_{\mathrm{SG}} = \frac{2}{3} \frac{\mu_{\mathrm{S}} \left(1 - \phi_{\mathrm{G}}\right)}{\left(1 - \phi_{\mathrm{G}}^{1/3}\right)} , \tag{A1.39}$$

$$\mathfrak{R} = \frac{3\mu_{\mathrm{SG}} \left(1 - \phi_{\mathrm{L}}^{1/3}\right) \left(1 - \phi_{\mathrm{L}}^{5/3}\right) + \left[3 - \frac{9}{2}\left(\phi_{\mathrm{L}}^{1/3} - \phi_{\mathrm{L}}^{5/3}\right) - 3\phi_{\mathrm{L}}^{2}\right] \mu_{\mathrm{L}}}{2\mu_{\mathrm{SG}} \left(1 - \phi_{\mathrm{L}}^{5/3}\right) + \left(3 + \phi_{\mathrm{L}}^{5/3}\right) \mu_{\mathrm{L}}} , \tag{A1.40}$$

where ϕ_{S}, ϕ_{G}, and ϕ_{L} are the volume fractions of the slag, gas, and metal phases. The volume fraction of metal droplets in the emulsion was defined as

$$\phi_{\mathrm{L}} = \frac{V_{\mathrm{L}}}{V_{\mathrm{L}} + V_{\mathrm{G}} + V_{\mathrm{S}}} \quad \text{where} \quad V_{\mathrm{G}} = \frac{\phi_{\mathrm{G}}}{1 - \phi_{\mathrm{G}}} \left(V_{\mathrm{L}} + V_{\mathrm{S}}\right) . \tag{A1.41}$$

The volume-fraction of gas in the emulsion was solved numerically from the correlation proposed by Gou *et al.* [49]:

$$\frac{\phi_{\mathrm{G}}^{2}}{1 - \phi_{\mathrm{G}}} = 0.91 u_{\mathrm{s}}^{0.57} , \tag{A1.42}$$

where u_{s} is the superficial velocity. The superficial velocity was defined as the ratio of the gas flow rate from the plume and the cross sectional area of the slag layer, *i.e.* $u_{\mathrm{s}} = \dot{V}_{\mathrm{G,plume}} / A_{\mathrm{slag}}$.

Slag droplets

The slip velocity between the steel bath and the slag droplets was taken to equal the terminal velocity of the slag droplets in the vertical direction. At the terminal velocity, the following force balance must hold:

$$F_{\mathrm{buoyancy}} = F_{\mathrm{drag}} + F_{\mathrm{gravitation}} , \tag{A1.43}$$

where F_{buoyancy}, F_{drag} and $F_{\mathrm{gravitation}}$ are the buoyancy force, drag force, and gravitation acting on the slag droplet. Solving the force balance for the terminal velocity corresponding the Sauter mean diameter ($d_{32,\mathrm{sd}}$) yields [50]:

$$u_{\mathrm{sd}} = \sqrt{\frac{4gd_{32,\mathrm{sd}}}{3C_{\mathrm{d}}}\frac{(\rho_{\mathrm{L}}-\rho_{\mathrm{S}})}{\rho_{\mathrm{L}}}}\,, \tag{A1.44}$$

where C_{d} is the drag coefficient. In this work, the drag coefficient of a slag droplet in liquid metal was solved according to the Lapple correlation (Eq. A1.45), which is valid for Re $<$ 1000 within +5% to –8% range of deviation [51].

$$C_{\mathrm{d}} = \frac{24}{\mathrm{Re}}\left(1+0.125\mathrm{Re}^{0.72}\right) \quad \text{where} \quad \mathrm{Re} = \frac{u_{\mathrm{sd}}d_{32,\mathrm{sd}}\rho_{\mathrm{L}}}{\mu_{\mathrm{L}}}\,, \tag{A1.45}$$

where C_{d} is the drag coefficient. The terminal velocity is solved numerically from Eqs. A1.44 and A1.45 using the Newton's method.

Fluid spheres

The terminal velocities of fluid spheres can be calculated as follows [50]:

$$u_{\mathrm{t}} = \sqrt{\frac{4gd_{\mathrm{p}}}{3C_{\mathrm{d}}}\frac{\Delta\rho}{\rho_{\mathrm{c}}}}\,, \tag{A1.46}$$

where the subscript c indicates the properties of the continuous phase. Here, the drag coefficient was calculated according to the empirical equations proposed by Hu and Kintner [52]:

$$C_{\mathrm{d}} = 1.661C^{-0.038}\,, \tag{A1.47}$$

in which C is a substance specific constant, which is defined according to

$$C = \frac{3}{4}\frac{\mathrm{Re}^4}{C_{\mathrm{d}}\mathrm{We}^3} = \frac{\rho_{\mathrm{c}}\sigma^3}{g\mu_{\mathrm{c}}\Delta\rho}\,. \tag{A1.48}$$

The value of the Weber number was assumed to have a constant value of We = 3.58.

1.3.2 Geometry of the cavity

The geometry of the cavity was determined based on the following assumptions:

– Because the cavity is in oscillating motion, the analysis is based on quasi-steady state flow conditions [53, 54].

– Individual cavities follow the form of a paraboloid of revolution [55, 56]. In the case of multihole lances, it is assumed that the cavities are non-coalescing, and hence the number of cavities is equal to the number of the gas jets. Observations with high-speed cameras [57] suggest that this assumption is valid when the inclination angle is greater than 10°.
– Neither chemical reactions [58–60] or the interference of top slag [59] affect the geometry of the cavity.

The surface area of a single cavity, *i.e.* a paraboloid of revolution excluding its base, can be calculated from [61]:

$$A_{\mathrm{cav},1} = \frac{\pi}{6}\frac{r_{\mathrm{cav}}}{h_{\mathrm{cav}}^2}\left[\left(r_{\mathrm{cav}}^2 + 4h_{\mathrm{cav}}^2\right)^{3/2} - r_{\mathrm{cav}}^3\right], \tag{A1.49}$$

where h_{cav} is the depth of the cavity and r_{cav} is the top radius of the cavity. The total surface area of the cavities caused by a multi-hole lance was calculated simply by multiplying the surface area of a single cavity by the number of exit ports in the top lance [62, 63]:

$$A_{\mathrm{cav}} = n_{\mathrm{lance}} \cdot A_{\mathrm{cav},1}\,, \tag{A1.50}$$

where n_{lance} is the number of holes in the nozzle. The mathematical description for h_{cav} and r_{cav} was adopted from Koria and Lange [64]:

$$h_{\mathrm{cav}} = 4.469\dot{M}_{\mathrm{h}}^{0.66} h_{\mathrm{lance}}\,, \tag{A1.51}$$

$$r_{\mathrm{cav}} = 0.5 \cdot 2.813\dot{M}_{\mathrm{d}}^{0.282} h_{\mathrm{lance}}\,, \tag{A1.52}$$

where h_{lance} is the lance height, $\dot{M}_{\mathrm{d}}$ is the horizontal component of the dimensionless momentum flow rate, and $\dot{M}_{\mathrm{h}}$ is the vertical component of the dimensionless momentum flow rate. The definitions of $\dot{M}_{\mathrm{h}}$ and $\dot{M}_{\mathrm{d}}$ are given in Eqs. A1.53 and A1.54, respectively. Due to the assumption of non-coalescing cavities, $\dot{M}_{\mathrm{d}}$ was calculated for a single cavity.

$$\dot{M}_{\mathrm{h}} = \frac{\dot{m}_{\mathrm{n}}\cos\theta}{\rho_{\mathrm{L}} g h_{\mathrm{lance}}^3}\,, \tag{A1.53}$$

$$\dot{M}_{\mathrm{d}} = \begin{cases} \dfrac{\dot{m}_{\mathrm{t}}}{\rho_{\mathrm{L}} g h_{\mathrm{lance}}^3}(1+\sin\theta) & \text{(for the diameter of a single cavity)} \\ \dfrac{n_{\mathrm{lance}}\dot{m}_{\mathrm{n}}\sin\theta}{\rho_{\mathrm{L}} g h_{\mathrm{lance}}^3} & \text{(for the diameter of multiple cavities)} \end{cases}, \tag{A1.54}$$

where θ is the inclination angle of the nozzle holes relative to the central axis, ρ_{L} is the density of the metal phase, and g is the acceleration due to gravity. According to Koria and Lange [64], the dimensionless momentum flow rates $\dot{m}_{\mathrm{n}}$ and $\dot{m}_{\mathrm{t}}$ are defined by Eqs. A1.55 and A1.56, respectively.

$$\dot{m}_{\mathrm{n}} = \frac{m_{\mathrm{t}}}{n_{\mathrm{lance}}}, \tag{A1.55}$$

$$\dot{m}_{\mathrm{t}} = 0.7854 n_{\mathrm{lance}} d_{\mathrm{t}}^2 p_{\mathrm{amb}} \left(1.27 \frac{p_0}{p_{\mathrm{amb}}} - 1 \right), \tag{A1.56}$$

where p_{amb} is the ambient pressure (in Pa), d_{t} is the throat diameter of the nozzle and p_0 is the supply pressure (in Pa). However, Eq. A1.56 is applicable only for diatomic gases. In the case of non-diatomic gases, a more general expression for $\dot{m}_{\mathrm{t}}$ can be derived based on the equations presented by Koria [65]:

$$\dot{m}_{\mathrm{t}} = \frac{1}{4} \pi d_{\mathrm{t}}^2 n_{\mathrm{lance}} \left[p_0 \left(\frac{2\gamma^2}{\gamma+1} \right)^{0.5} \left(\frac{2}{\gamma+1} \right)^{\frac{\gamma+1}{2(\gamma-1)}} + (0.53 p_0 - p_{\mathrm{amb}}) \right], \tag{A1.57}$$

where γ is the isentropic expansion factor of the gas mixture. In the case of gas mixtures, an average value of γ can be calculated based on the molar composition:

$$\gamma_{\mathrm{G}} = \sum_{i=0}^{n_{\mathrm{G}}} \gamma_i x_i . \tag{A1.58}$$

In accordance with the ideal gas law, the isentropic expansion factors of individual molecules were calculated based on their degrees of freedom:

$$\gamma = 1 + \frac{2}{f}, \tag{A1.59}$$

where f denotes the degree of freedom. The degrees of freedom consist of translational, rotational and vibrational degrees of freedom. Due to low temperature of the gas injected, the vibrational degrees of freedom can be ignored. Hence, the degrees of freedom were defined as $f = 3$ for monoatomic gases (Ar), $f = 5$ for diatomic gases (O_2, N_2 and CO) and $f = 6$ for triatomic gases (CO_2).

References

1. Szekely J & Themelis NJ (1971) Rate Phenomena in Process Metallurgy. John Wiley & Sons, Inc., New York, NY, USA.
2. Turkdogan ET (1966) Fluid dynamics of gas jets impinging on surface of liquids. Chem. Eng. Sci. 21: 1133–1144.
3. IAEA (2008) Thermophysical Properties of Materials for Nuclear Engineering: A Tutorial and Collection of Data. International Atomic Energy Agency, Vienna, Austria.
4. Turkdogan ET (1996) Fundamentals of Steelmaking. The Institute of Materials, London, United Kingdom.
5. Keene BJ & Mills KC (1995) Densities of molten slags. In: Verein Deutscher Eisenhüttenleute (ed.) Slag Atlas 2nd Edition, pp. 313–348. Verlag Stahleisen GmbH, Düsseldorf, Germany.
6. Penttilä K (2014) Modelling of Thermophysical Properties In EAF-Process And Steelmaking. VTT-R-00514-14, VTT Technical Research Centre of Finland, Espoo, Finland.
7. Hanao M, Tanaka T, Kawamoto M & Takatani K (2007) Evaluation of Surface Tension of Molten Slag in Multi-component Systems. ISIJ Int. 47(7): 935–939.
8. Wilke CR (1950) A Viscosity Equation for Gas Mixtures. J. Chem. Phys. 18(4): 517–519.
9. Bird RB, Stewart WE & Lightfoot EN (1960) Transport Phenomena. John Wiley & Sons, Inc., Singapore.
10. Cloutman LD (1993) A Database of Selected Transport Coefficients for Combustion Studies. Lawrence Livermore National Laboratory, Livermore, CA, USA.
11. Dogan N, Brooks GA & Rhamdhani MA (2011) Comprehensive Model of Oxygen Steelmaking Part 3: Decarburization in Impact Zone. ISIJ Int. 51(7): 1102–1109.
12. Geiger GH & Poirier DR (1973) Transport Phenomena in Metallurgy. Addison-Wesley Publishing Company, Reading, MA, USA.
13. Wijk O (1992) Stainless Steelmaking in Converters. In: Engh TA (ed.) Principles of Metal Refining, pp. 280–301. Oxford University Press, Oxford, United Kingdom.
14. Kekkonen M, Oghbasilasie H & Louhenkilpi S (2012) Viscosity Models for Molten Slags. Technical report, Aalto University, Department of Materials Science and Engineering.
15. Forsbacka L, Holappa L, Kondratiev A & Jak E (2007) Experimental Study and Modelling of Chromium Containing Slags. Steel Res. Int. 78(9): 676–684.
16. Urbain G (1987) Viscosity estimation of slags. Steel Res. 58(3): 111–116.
17. Sosinsky DJ & Sommerville ID (1986) The Composition and Temperature Dependence of the Sulphide Capacity of Metallurgical Slags. Metall. Trans. B 17(2): 331–337.
18. Einstein A (1906) Eine neue Bestimmung der Moleküldimensionen. Ann. Phys. (Berlin) 19(2): 289–306.
19. Guth E & Simha R (1936) Untersuchungen über die Viskosität von Suspensionen und Lösungen. 3. Über die Viskosität von Kugelsuspensionen. Kolloid Z. 74(3): 266–275.
20. Smallwood HM (1944) Limiting Law of the Reinforcement of Rubber. J. Appl. Phys. 10(15): 758–766.
21. Guth E (1945) Theory of Filler Reinforcement. J. Appl. Phys. 16(1): 20–25.
22. Brinkman HC (1952) The Viscosity of Concentrated Suspensions and Solutions. J. Chem. Phys. 20(4): 571.
23. Happel J (1957) Viscosity of Suspensions of Uniform Spheres. J. Appl. Phys. 28(11):

1288–1292.
24. Kitano T, Kataoka T & Shirota T (1981) An empirical equation of the relative viscosity of polymer melts filled with various inorganic fillers. Rheol. Acta 20(2): 207–209.
25. Thomas DG (1965) Transport characteristics of suspension: VIII. A note on the viscosity of Newtonian suspensions of uniform spherical particles. J. Colloid Sci. 20: 267–277.
26. GTT-Technologies GmbH (2015). FactSage 7.0.
27. Wei J-H & Zhu D-P (2002) Mathematical Modeling of the Argon-Oxygen Decarburization Refining Process of Stainless Steel: Part I. Mathematical Model of the Process. Metall. Mater. Trans. B 33(2): 111–119.
28. Taylor R & Krishna R (1993) Multicomponent Mass Transfer. John Wiley & Sons, Inc., New York, NY, USA.
29. Nagata K, Ono Y, Ejima T & Yamamura T (1988) Diffusion. In: Kawai Y & Shiraishi Y (eds.) Handbook of Physico-chemical Properties at High Temperatures, pp. 181–204. The Iron and Steel Institute of Japan, Tokyo, Japan.
30. Wilke CR & Lee CY (1955) Estimation of Diffusion Coefficients for Gases and Vapors. Ind. Eng. Chem. 47(6): 1253–1257.
31. Järvinen MP, Pisilä S, Kärnä A, Ikäheimonen T, Kupari P & Fabritius T (2011) Fundamental Mathematical Model for AOD Process. Part I: Derivation of the Model. Steel Res. Int. 82(6): 638–649.
32. Mills KC (1995) Diffusion coefficients in molten slags. In: Verein Deutscher Eisenhüttenleute (ed.) Slag Atlas 2nd Edition, pp. 541–556. Verlag Stahleisen GmbH, Düsseldorf, Germany.
33. Mason EA & Saxena SC (1958) Approximate Formula for the Thermal Conductivity of Gas Mixtures. Phys. Fluids 1(5): 361–369.
34. Eucken A (1913) Über das Wärmeleitvermögen, die spezifische Wärme und die innere Reibung der Gase. Physik. Z. 14(8): 324–332.
35. Mills KC & Susa M (1995) Thermal conductivities of slags. In: Verein Deutscher Eisenhüttenleute (ed.) Slag Atlas 2nd Edition, pp. 591–600. Verlag Stahleisen GmbH, Düsseldorf, Germany.
36. Girifalco LA & Good RJ (1957) A Theory for the Estimation of Surface and Interfacial Energies. I. Derivation and Application to Interfacial Tension. J. Phys. Chem. 61(7): 904–909.
37. Wuppermann CF (2013) Mathematische Modellierung der fluidinduzierten Behälterschwingung beim AOD-Prozess. Doctoral thesis, Rheinisch-Westfälische Technische Hochschule Aachen, Aachen, Germany.
38. Fabritius T, Riipi J, Järvinen M, Mattila O, Heikkinen E-P, Kärnä A, Kurikkala J, Sulasalmi P & Härkki J (2010) Interfacial Phenomena in Metal-Slag-Gas System during AOD Process. ISIJ Int. 50(6): 797–803.
39. Alpatov AV & Paderin SN (2010) Thermodynamic Models of Liquid Multicomponent Metallic Solutions. Russ. Metall. 2010(6): 557–564.
40. Slye WE & Fruehan RJ (1999) The Activity of Silicon in Liquid Fe-Si and Fe-Si-Cr alloys at 1600 °C. In: Proc. 57th Electric Furnace Conference, pp. 401–412. Iron & Steel Society, Pittsburgh, PA, USA.
41. Ueno S, Waseda Y, Jacob TK & Tamaki S (1988) Theoretical treatment of interaction parameters in multicomponent metallic solutions. Steel Res. 59(11): 474–483.
42. Malyutin KV & Paderin SN (2007) Interaction Parameters of Carbon in Liquid Iron and the Thermodynamics of Carbon and Oxygen in Alloyed Iron Melts. Russ. Metall. 2007(7): 545–551.

43. Sigworth GK & Elliott JF (1974) The Thermodynamics of Liquid Dilute Iron Alloys. Met. Sci. 8(1): 298–310.
44. Upadhyaya GS & Dube RK (1977) Problems in Metallurgical Thermodynamics and Kinetics. Pergamon Press, London, United Kingdom.
45. Outotec Oyj (2015). HSC Chemistry 8.
46. Mendelson HD (1967) The prediction of bubble terminal velocities from wave theory. Am. Inst. Chem. Eng. J. 13(2): 250–253.
47. Schwerdtfeger K (1968) Velocity of rise of argon bubble in mercury. Chem. Eng. Sci 23(8): 937–938.
48. Subagyo & Brooks GA (2002) An Improved Correlation for Predicting Terminal Velocity of Droplets and Bubbles in Slag-Metal-Gas Emulsion. ISIJ Int. 42(10): 1182–1184.
49. Gou H, Irons GA & Lu W-K (1996) A Multiphase Fluid Mechanics Approach to Gas Holdup in Bath Smelting Processes. Metall. Mater. Trans. B 27(2): 195–201.
50. Oeters F (1989) Metallurgie der Stahlherstellung. Verlag Stahleisen mbH, Düsseldorf, Germany.
51. Clift R, Grace JR & Weber ME (1978) Bubbles, Drops, and Particles. Academic Press, Inc., New York, NY, USA.
52. Hu S & Kintner RC (1955) The fall of single liquid drops through water. AIChE J. 1(1): 42–48.
53. Odenthal H-J, Falkenreck U & Schlüter J (2006) CFD Simulation of Multiphase Melt Flows in Steelmaking Converters. In: Proc. European Conference on Computational Fluid Dynamics. Egmond aan Zee, The Netherlands.
54. Zhou X, Ersson M, Zhong L, Yu J & Jönsson P (2014) Mathematical and Physical Simulation of a Top Blown Converter. Steel Res. Int. 85(2): 273–281.
55. Cheslak FR, Nicholls JA & Sichel M (1969) Cavities formed on liquid surfaces by impinging gaseous jets. J. Fluid Mech. 36(1): 55–63.
56. Okhotskii VB, Chernyatevich AG & Prosvirin KS (1972) Studying the interaction between jets of oxygen and metal bath. Steel USSR 2(6): 443–444.
57. Lange KW & Koria SC (1983) Wechselwirkung zwischen Sauerstoffstrahl und Roheisenschmelze beim Sauerstoffaufblasverfahren. Publ. Wiss. Film. Techn. Wiss./Naturw., Ser. 8, Nr. 9, Institut für den Wissenschaftlichen Film, Göttingen, Germany. Film D 1386.
58. van der Lingen TW (1966) Penetration of inclined gas jets into liquid baths. J. Iron Steel Inst. 204(4): 320–325.
59. Sharma SK, Hlinka JW & Kern DW (1977) The Bath Circulation, Jet Penetration and High-Temperature Reaction Zone in BOF Steelmaking. Iron Steelmaker 24(7): 7–18.
60. Nakazono D, Abe K-I, Nishida M & Kurita K (2004) Supersonic O_2-jet Impingement on Liquid Iron with Surface Chemistry. ISIJ Int. 44(1): 91–99.
61. Krivoshapko SN & Ivanov VN (2015) Encyclopedia of Analytical Surfaces. Springer International Publishing, Cham, Switzerland.
62. Deo B & Boom R (1993) Fundamentals of Steelmaking Metallurgy. Prentice Hall International, Hertfordshire, United Kingdom.
63. Wei J-H & Zeng L (2012) Numerical Simulation of Fluid Flow in Bath during Combined Top and Bottom Blowing VOD Refining Process of Stainless Steel. Steel Res. Int. 83(11): 1053–1070.
64. Koria SC & Lange KW (1987) Penetrability of impinging gas jets in molten steel bath. Steel Res. 58(9): 421–426.

65. Koria SC (1981) Wechselwirkung zwischen einem Gasstrahl und flüssiger Metallschmelze. Doctoral thesis, RWTH Aachen University, Aachen, Germany.

Original articles

I Visuri V-V, Järvinen M, Kärnä A, Sulasalmi P, Heikkinen E-P, Kupari P & Fabritius T (2017) A Mathematical Model for Reactions During Top-Blowing in the AOD Process: Derivation of the Model. Metall. Mater. Trans. B 48(3): 1850–1867

II Visuri V-V, Järvinen M, Kärnä A, Sulasalmi P, Heikkinen E-P, Kupari P & Fabritius T (2017) A Mathematical Model for Reactions During Top-Blowing in the AOD Process: Validation and Results. Metall. Mater. Trans. B 48(3): 1868–1884

III Visuri V-V, Järvinen M, Sulasalmi P, Heikkinen E-P, Savolainen J & Fabritius T (2013) A Mathematical Model for the Reduction Stage of the AOD Process. Part I: Derivation of the Model. ISIJ Int. 53(4): 603–612

IV Visuri V-V, Järvinen M, Savolainen J, Sulasalmi P, Heikkinen E-P & Fabritius T (2013) A Mathematical Model for the Reduction Stage of the AOD Process. Part II: Model Validation and Results. ISIJ Int. 53(4): 613–621

V Järvinen M, Visuri V-V, Pisilä S, Kärnä A, Sulasalmi P, Heikkinen E-P & Fabritius T (2013) Advanced Methods in Modelling of Metallurgical Unit Operations. Mater. Sci. Forum 762: 236–241

VI Järvinen M, Visuri V-V, Heikkinen E-P, Kärnä A, Sulasalmi P, De Blasio C & Fabritius T (2016) Law of Mass Action Based Kinetic Approach for the Modelling of Parallel Mass Transfer Limited Reactions: Application to Metallurgical Systems. ISIJ Int. 56(9): 1543–1552

Original publications are not included in the electronic version of the dissertation.

607. Niemelä, Ville (2017) Evaluations and analysis of IR-UWB receivers for personal medical communications

608. Keränen, Anni (2017) Water treatment by quaternized lignocellulose

609. Jutila, Mirjami (2017) Adaptive traffic management in heterogeneous communication networks

610. Shahmarichatghieh, Marzieh (2017) Product development sourcing strategies over technology life cycle in high-tech industry

611. Ylitalo, Pekka (2017) Value creation metrics in systematic idea generation

612. Hietajärvi, Anna-Maija (2017) Capabilities for managing project alliances

613. Kangas, Maria (2017) Stability analysis of new paradigms in wireless networks

614. Roivainen, Antti (2017) Three-dimensional geometry-based radio channel model : parametrization and validation at 10 GHz

615. Chen, Mei-Yu (2017) Ultra-low sintering temperature glass ceramic compositions based on bismuth-zinc borosilicate glass

616. Yliniemi, Juho (2017) Alkali activation-granulation of fluidized bed combustion fly ashes

617. Iljana, Mikko (2017) Iron ore pellet properties under simulated blast furnace conditions : investigation on reducibility, swelling and softening

618. Jokinen, Karoliina (2017) Color tuning of organic light emitting devices

619. Schuss, Christian (2017) Measurement techniques and results aiding the design of photovoltaic energy harvesting systems

620. Mämmelä, Olli (2017) Algorithms for efficient and energy-aware network resource management in autonomous communications systems

621. Matilainen, Matti (2017) Embedded computer vision methods for human activity recognition

622. Li, Xiaobai (2017) Reading subtle information from human faces

623. Luoto, Markus (2017) Managing control information in autonomic wireless networking

624. Mustonen, Miia (2017) Analysis of recent spectrum sharing concepts in policy making

Book orders:
Granum: Virtual book store
http://granum.uta.fi/granum/

UNIVERSITY OF OULU P.O. Box 8000 FI-90014 UNIVERSITY OF OULU FINLAND

ACTA UNIVERSITATIS OULUENSIS

UNIVERSITY of OULU
OULUN YLIOPISTO

ISBN 978-952-62-1670-6 (Paperback)
ISBN 978-952-62-1671-3 (PDF)
ISSN 0355-3213 (Print)
ISSN 1796-2226 (Online)